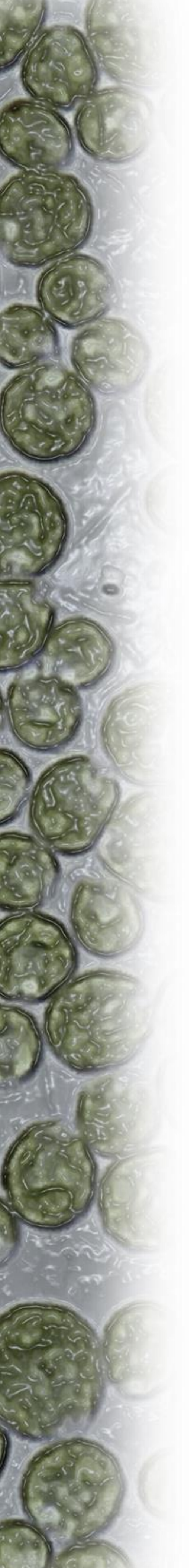

LIÈGE université
Sciences

University of Liege (BE) — Faculty of Sciences
Laboratory of Genetics and Physiology of Microalgae

Photosynthetic variation within *Chlamydomonas reinhardtii*: a multidisciplinary approach to learn from biodiversity.

A thesis submitted in fulfilment of the requirements for the degree of Doctor in Philosophy in Sciences

Fabrizio Iacono

Promoter: Pierre Cardol
Co-promoter: Tom Druet

Liege, May 2023

Doctoral training program: Biochemistry, Molecular and Cell Biology, Bioinformatics and Modelling

Date of the public oral examination: May 23rd, 2023

Members of the jury:

- Prof. Marc Hanikenne (University of Liege, Liege, BE) (President)
- Prof. Claire Remacle (University of Liege, Liege, BE)
- Dr. Olivier Vallon (Institut de Biologie Physico-chimique, Paris, FR)
- Dr. Dimitris Petroutsos (CEA Grenoble, FR)
- Dr. Xenie Johnson (Institut Biosciences et Biotechnologies d'Aix-Marseille, FR)
- Dr. Yannic Lara (University of Liege, Liege, BE)
- Dr. Tom Druet (University of Liege, Liege, BE) (Co-promoter)
- Dr. Pierre Cardol (University of Liege, Liege, BE) (Promoter)

“We are all trapped in our own way of thinking, trapped in our own way of relating to people. We get so used to seeing the world our way that we come to think that the world is the way we see it.”

From “A Curious Mind” of Brian Grazer.

Summary

The complex regulation of cell metabolism challenges the development of novel biotechnologies driving a more efficient use of natural resources. For instance, microalgae are considered sustainable sources of proteins, biomaterials, nutraceuticals, and biofuels, but their large-scale adoption is limited by their low cost-efficiency. The deeper understanding of algal metabolism and investigation of its natural variants occupy a central role in the development of algal biotechnologies. In this thesis, I explored and exploited the natural diversity present among divergent strains of *Chlamydomonas reinhardtii*, providing new insights about the multilevel regulation of the photosynthetic metabolism and its response to photo-oxidative stress. This study includes a comprehensive fluorescence-based phenotypic description of 25 wild-type strains partitioned into 14 laboratory isolates and 11 field-isolates. The presence of phenotypic divergence between the two groups with respect to their photosynthetic and photoprotective efficiency, particularly under mixotrophic condition is discussed. An in-depth multimethodological comparison between the laboratory-isolate CC-1010 and the field-isolate CC-2936 revealed the presence of wide intraspecific diversity in proton-motive force regulation and accumulation of low-CO_2-inducible transcripts and proteins. Shotgun proteomics was used to provide a thorough overview of the two strains' physiological response to photo-oxidative stress, showcasing the extent of intraspecific diversity in *C. reinhardtii*. Mating efficiency, genomics, and phenotypic data were used to select a subset of 8 strains to use as parental lines for the construction of a Multiparent Advanced Generation Inter-Cross (MAGIC) design. A detailed genomic analysis of the resulting 768 F8-lines was performed to track recombination events and unravel the population's structure. The optimization of the fluorescence-based mass-phenotyping method used to characterise the MAGIC population is also described. Several parameters describing the photochemical and non-photochemical chloroplastic activity were measured under photo-autotrophic and mixotrophic growth. The large size of the phenotypic dataset was exploited to investigate covariance among photosynthetic traits. The complex relationship between photochemistry and photoprotection in presence/absence of acetate is discussed. Heritability and genetic correlation were computed for each trait, providing a fresh view on the link between genetics and fluorescence-derived parameters. Finally, the genomic and phenotypic datasets were used to develop a quantitative genetics study, mapping genomic loci associated to the different photosynthetic traits. A total of 26 quantitative-trait loci (QTLs) were found to be associated to Photosystem II's quantum yield and non-photochemical quenching-related parameters. Our fine-mapping analysis found the presence of several major candidate-genes among some of the confidence intervals, providing strong bases for the development of future scientific studies targeting to the identification and exploitation of natural genetic variants. Overall, this thesis describes why the MAGIC population represents a landmark resource in the scientific history of *C. reinhardtii*'s community, and how the use of fluorescence-based high-throughput phenotyping is a powerful tool to help us understand and master photosynthetic cells' physiology.

Table of Contents

Chapter 1

1.1 Introduction

The notorious Australian scientist Robert M. May (8 January 1936 – 28 April 2020) pointed out that, if aliens asked humans: “*How many distinct life forms/species does your planet have?*”, our answer would be embarrassingly random (May, 2010).

Life thrives on planet Earth. From the fertile Amazon rainforest to the harshest corners of our planet, an astonishing variety of living organisms has developed through the course of time. Global biodiversity is the result of about 3.95 billion years (Gyr) of evolution, dating back to the appearance of the Last Universal Common Ancestor (LUCA) (Tashiro et al., 2017). During the slow evolutionary process, several steps were pivotal for the development of life as we know it. Some examples are the development of a more compartmentalized intracellular organization, the incorporation of the mitochondrion and the plastid, the appearance of the multicellular organization, etcetera. Among the milestones of evolution, one event drastically shaped the fate of all life-forms on our planet. There is no common agreement about the exact moment in history, but sometime earlier than 2.4 Gyr ago, a group of bacteria evolved the ability to photo-oxidize water molecules into hydrogen ions (H^+) and molecular oxygen (O_2) in order to produce biochemical energy (Canfield, 2005). Today, this process is known as oxygenic photosynthesis. About 2.4 to 2 Gyr ago, photosynthetically generated O_2 gradually accumulated in the environment turning Earth’s reducing atmosphere into an oxidizing one. This event is known as the Great Oxidation Event (GOE), and it shaped the geochemistry of Earth’s surface and shallow waters (Holland, 2006; Lyons et al., 2014) as well as the course of evolution of all the organisms that inhabited the planet at that time (Kerr, 2005). Sedimentological and biogeochemical evidences suggest that the GOE caused a 80% reduction in Earth’s primary productivity due to an O_2-driven nutrients depletion (Anbar and Knoll, 2002; Hodgskiss et al., 2019), creating a biological depression that lasted for at least 0.5 Gyr. Despite this initial recession, the increase of O_2 levels in the atmosphere boosted the development of all organisms who were able to use it as an electron acceptor within the so-called aerobic respiration, leading to the evolution of the complex eukaryotic life-forms that nowadays populate our planet. Today, the great majority of the alive biomass on the planet relies on O_2 for its survival, and virtually all life on Earth relies on photosynthesis as a source of primary production. It is therefore essential to understand every aspect of photosynthesis; how it appeared and evolved through the tree of life, its functioning and ecology, and its response to anthropogenic climatic and geochemical changes. Moreover, the world population is growing at a high rate and it will reach 10 billion people by 2050 (United Nations et al., 2019). Global food security is one of the biggest challenges of the 21st century, in the context of a planet already unsettled by climate change and famines. One of the strategies to address the challenge is the human-driven improvement of photosynthesis to increase crops’ photosynthetic efficiency and yield (Kang et al., 2009; Evans, 2013; Vecchi et al., 2020). Complementary strategies are the development of more sustainable agricultural systems such as aquaponic, vertical and urban agriculture, and the inclusion of new phototrophs like algae and cyanobacteria into our daily diet. The accomplishment of these goals can be achieved only through the understanding of photosynthesis together with the safeguard and sustainable exploitation of global biodiversity.

1.1.1 The early research and establishment of the photosynthetic equation

Photosynthesis, from the Greek *phōs* (light) and *sunthesis* (putting together), is the process that enables photoautotrophs to feed on light energy. The discovery of photosynthesis arrived quite late in the human history, and the understanding of its fundamentals required the contribution of many scientists who designed landmark experiments (Blankenship, 2002). The first report of an experiment aimed to understand plants growth dates to the 1640s, when the Belgian physician Jan Baptista van Helmont (1577–1644) conducted a simple 5-years experiment on a willow tree. Van Helmont initially potted the tree into a container full of topsoil, which weighed about 90 kg, and watered it for 5 years. At the end of the experiment, he pulled the tree from the pot, weighed the biomass and added the weight of all the leaves that the plant had lost during every fall. He finally weighed the pot full of substrate, of which weight was almost unchanged. Van Helmont concluded that the tree's biomass was generated from water rather than from soil, which is indeed only partially correct. Nonetheless, the experimental design was extremely advanced for that age, and the concept of weighting will be adopted by the French chemist Antoine Lavoisier (1743-1794) a hundred years later to prove the law of conservation of matter within a chemical reaction. It was during that century that Lavoisier, the Swedish chemist Carl Scheel (1742–1786) and the English chemist Joseph Priestley (1733-1804), discovered oxygen, proving that water is a compound made of oxygen combined with another inflammable element (hydrogen), and that plants produce oxygen as they grow while mice consume it for living (respiration). The importance of light remained unproved until 1779, when the Dutch physician Jan Ingenhousz (1730–1799), inspired by the experiments of Priestley and the new chemistry of Lavoisier, studied the effects of plants on the air composition under dark and light condition. During his research, he discovered the central role of light in photosynthesis, and the process of plants respiration. He published the results in the form of a book entitled: "*Experiments upon Vegetables, discovering Their Great Power of Purifying the Common Air in Sunshine and Injuring it in the Shade and At Night*". Ingenhousz also shared with his Swiss rival, Jean Senebier (1742–1809), the understanding of the importance of carbon dioxide during photosynthesis. A first contribution to the understanding of CO_2 fixation came from the Swiss scientist Nicolas de Saussure (1767–1845) and his weighting experiments demonstrating that the increase in dry weight of plants is significantly higher than the weight of CO_2 they uptake. He brilliantly proposed that the exceeding weight came from the incorporation of water molecules into plant's dry matter. De Saussure also proved that plants need minerals to grow and that the chemicals are uptaken from the soil. By the beginning of the 1800s, the first equation of photosynthesis was established as:

$$\text{carbon dioxide} + \text{water} + \text{light} \rightarrow \text{organic matter} + \text{oxygen}$$

More scientific effort was required to rewrite the equation using unambiguous chemical formulas. After several decades, Jean Baptiste Boussingault (1802–1887) estimated through the calculation of the photosynthetic quotient (assimilated CO_2/evolved O_2) that uptaken CO_2 was fixed into carbohydrates. The German botanist Julius von Sachs (1832-1897) demonstrated in parallel the accumulation of starch only in the areas of a leaf exposed to light. Finally, it was proposed by the German physician and physicist Julius Robert Mayer (1814–1878), one of the fathers of thermodynamics, that in photosynthesis light energy is converted to chemical energy. The time was ripe for the complete equation of photosynthesis to be established:

$$CO_2 + H_2O + \text{light} \rightarrow (CH_2O) + O_2$$

Where CH_2O (formaldehyde) represents just the building block of carbohydrates such as glucose, which is the most abundant aldohexose monosaccharide:

$$6\ CO_2 + 6\ H_2O \rightarrow C_6H_{12}O_6 + 6\ O_2$$

Once the unbreakable link between photosynthesis, oxygen and life was uncovered, scientific interest grew in photosynthetic and plants research leading to the elucidation of the main components and mechanistic aspects of this central process.

1.1.2 The chloroplast

If the mitochondrion is the catabolism-driven powerhouse of the heterotrophic metabolism, the chloroplast can be compared to a solar power plant, where light energy is turned into chemical energy and used to drive cells' anabolism. Plastids originated somewhere between 1.2 to 1.7 Gyr ago from the establishment of a mutualistic endosymbiosis between a cyanobacterium and a heterotrophic eukaryotic host. The relationship became obligatory when endosymbiont-to-host gene transfer, coupled to the evolution of a dedicated membrane transport system, would allow the cyanobacterial-gene products to be synthetized by the host and imported into the symbiont when required. Due to this dependency, chloroplasts are today considered as fully integrated organelles of the eukaryotic photoautotrophs' cell. The primary endosymbiotic event gave rise to the *Archaeplastida* taxon, including *Glaucophyta* (glaucophyte algae), *Rhodophyta* (red algae), and *Chloroplastida* (green algae and land-plants) (Cenci et al., 2015). A general description of *Chloroplastida*'s chloroplasts will be provided in the following sections of this chapter.

Chloroplasts are highly compartmentalized organelles. From the outer layer inward, the first compartment is the intermembrane space, delimited by the outer and the inner membranes of the chloroplast envelope. The second compartment is the stroma, delimited by the inner membrane and the thylakoid membrane. The last compartment is the lumen, fully surrounded by the thylakoid membrane. All compartments are filled with an aqueous matrix. While the inner and outer membranes are mostly organized into linear sheets of lipid bilayers, the thylakoid membrane presents a rather heterogeneous ultrastructure in land plants, where the thylakoids organize into cylindric structures (grana) composed of several layers of disk-shaped thylakoid vesicles (granal lamellae). One side of each lipid bilayer is exposed to the thylakoid lumen, while the other side is in close contact (appressed) with the next lipid bilayer. All granal lamellae share the same lumen as they are connected by membrane bridges called "frets". These structures do not just connect each vesicle of a single grana, but extroflect into the stromal matrix creating areas of thylakoids in contact with both stroma and lumen (stroma lamellae), that interconnect different grana stacks (Kirchhoff, 2019).

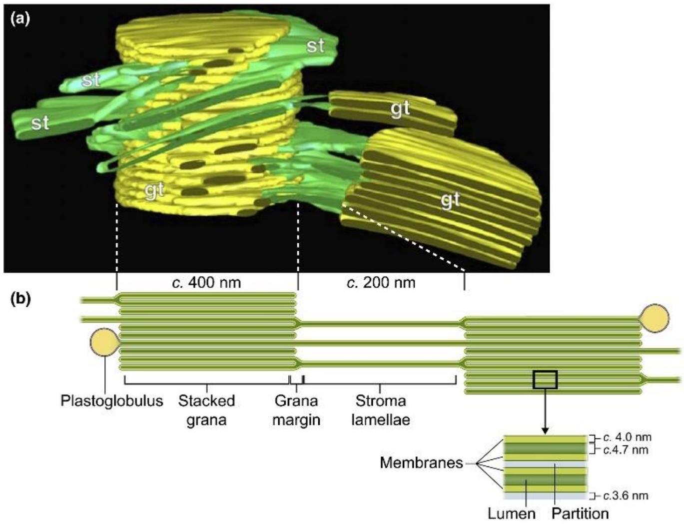

Figure 1. 1: Ultrastructure of the thylakoid membrane system of land plants. (a) 3D reconstruction of the thylakoid architecture derived from electron tomography (ET) data. (b) In-scale model of a thylakoid membrane cross section (Kirchhoff, 2019).

The envelope's outer membrane is generally described as a low-selectivity membrane. It is composed of phospholipids and glycolipids, and it shows a high lipids-to-proteins (W/W) ratio (Inoue, 2007). On the contrary, the other two membranes display a much lower lipids-to-proteins ratio, and they are mainly composed of glycolipids such as the highly unsaturated monogalactosyl diacylglycerols (MGDG), which can form non-bilayer structures, and digalactosyl diacylglycerols (DGDG) (Gounaris and Barber, 1983).

The high concentration of MGDG confers high fluidity to the thylakoids, facilitating the reorganization of the grana stacking in response to the environmental stimuli. Both inner membrane and thylakoids are highly selective membranes. Thus, the transport of ions, proteins and other molecules in and out the compartments is tightly regulated by a battery of transporters and channels embedded in the lipid bilayer (Marchand et al., 2018).

The photosynthetic apparatus is embedded in the thylakoid membrane, and it consists of large protein-pigment complexes of which building blocks are mainly encoded in the nuclear genome. The next paragraphs will focus on the molecular aspects of photosynthesis and its regulation.

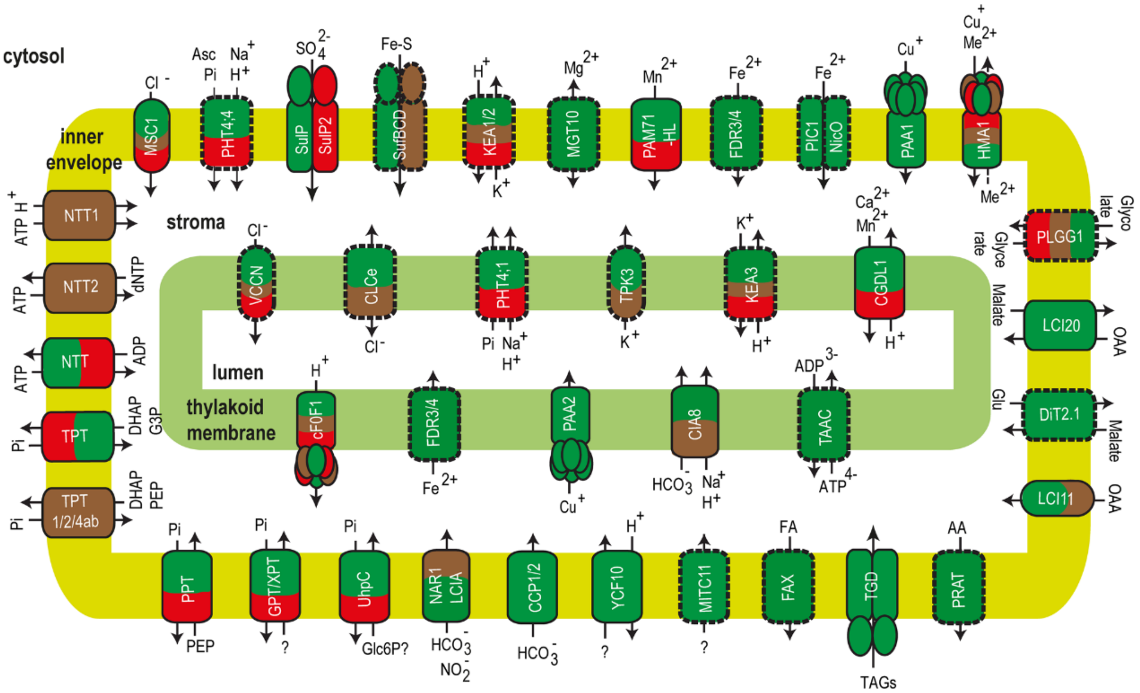

Figure 1. 2: Ion and metabolite transport proteins of the chloroplast envelope and thylakoid membrane from algae. Proteins identified or characterized in at least one algal model are framed with continuous line. Plant homologous genes coding for putative transporters in algae are framed with broken lines. Green algae, red algae and diatoms are represented in green, red and brown, respectively. Figure from (Marchand et al., 2018).

1.1.3 Light trapping and energy conversion

Light is composed of elementary particles called photons, that can be imagined as energy packets of electromagnetic radiation. The amount of energy enclosed into each photon can be described by its wavelength, with the lower wavelengths of the light spectrum being more energetic than the higher ones. The part of the light spectrum driving photosynthesis is called Photosynthetically Active Radiation (PAR), and it corresponds to the portion of the spectrum visible to the human eye (400-700nm). Photosynthesis starts with the capture of the light energy by the photosynthetic antennae and its transfer to the reaction center (RC) of the photosystems. Plants and green algae's antennae are composed of proteins belonging to the same Light-Harvesting Complex (LHC) protein superfamily. This class of membrane proteins contains pigments like chlorophyll a, chlorophyll b, carotenoids (e.g., lutein), embedded into their structure. The pigments are essential for the correct folding and functioning of LHC proteins. The antenna associated with photosystem I (PSI) is named LHCI (or LHCA), and the one associated with photosystem II (PSII) is named LHCII (or LHCB). The major components of LHCII are organized in trimers surrounding the PSII core complex, while LHCI has a belt-like configuration, and it is asymmetrically bound to PSI. Extensive interspecific variability in the antennae structure is present within the green lineage with respect to the number of LHC subunits and their overall cross-section, but the physical aspects of light trapping remain well conserved. When a photon is absorbed by a pigment, its energy boosts the ground energy level of the molecule to the excited (singlet) state. The excited state of a pigment is very unstable, and if an excited chromophore is close enough to a lower-energy (more red-shifted) chromophore, its excitation energy will be transferred to the other. In this way, excitation energy can be funneled from the peripheral area of the antennae to the PS-RCs (Mirkovic et al., 2017). Chlorophylls are the most abundant pigments in nature, and they are the main actors in the process of light-trapping, energy transfer and conversion. Once the excitation energy reaches the photosynthetic RCs, a special pair of chlorophyll molecules (P680 in PSII-RC and P700 in PSI-RC) undergoes charge separation reducing the nearest electron acceptor. Electrons flowing out of P680 create the energy gap needed for water photolysis, that takes place within the O_2-evolving complex (OEC) in the stromal side of PSII. Four charge-separation events lead to the photolysis of 2 water molecules, freeing one O_2 and four H^+ molecules while re-reducing the oxidized P680 ($P680^+$) (Lubitz et al., 2019). Electrons coming from P680 are transferred along a set of acceptor molecules, exiting PSII complex through the reduction of the mobile electron carrier plastoquinone (PQ) into plastoquinol (PQH_2). The PQH_2 diffuses within the lipid bilayer of the thylakoid membrane and binds Cytochrome b_6f complex (Cyt b_6f) which catalyzes the transfer of electrons from the PQ-pool to a second mobile carrier, plastocyanin (PC), located in the lumen. The latter shuttles electrons between Cyt b_6f and PSI-RC reducing $P700^+$. Electrons generated by the light-driven P700 oxidation are transported out of the RC and transferred to the last electron acceptor of the photosynthetic chain: the iron-sulfur protein ferredoxin (Fdx). In the stroma, Fdx functions as an electron donor for the reduction of oxidized nicotinamide-adenine-dinucleotide-phosphate ($NADP^+$) into NADPH, mediated by a ferredoxin-NADP reductase (FNR). In this way, electrons extracted from H_2O molecules are used to produce NADPH during the above-described Linear Electron Flow (LEF). Moreover, electron-transport through Cyt b_6f results in the release of stroma-derived H^+ ions into the lumen. This light-driven activity, together with the release of hydrogen ions by the OEC, provides the energy needed to power the chloroplastic ATP-synthase, driving the production of adenosine triphosphate (ATP). This energy was identified by Mitchell (Mitchell, 1961) to be conserved in the form of an electrical ($\Delta\Psi$) and a chemical (ΔpH) gradient across the thylakoids, of which sum is referred to as proton-motive force (*pmf*).

1.1.4 Carbon reactions and photorespiration

The carbon reactions are the ones related to CO_2 reduction into sugars, and they are powered by the ATP and NADPH produced during the light reactions. They are commonly known under the name of “light-independent” or “dark” reactions, but this nomenclature was repeatedly reported as misleading as certain enzymes of the carbon reactions are directly regulated by light-driven phenomena (Buchanan, 2016). CO_2 fixation takes place in the stromal compartment and its pathway was first elucidated by Melvin Calvin, Andrew Benson, and James Bassham from whom it takes its name (Calvin-Benson-Bassham cycle, or CBB cycle) (Bassham et al., 1950). The cycle starts with the carboxylation phase, consisting in the incorporation of one molecule of CO_2 and one of H_2O into a molecule of ribulose-1,5-biphospate (RuBP). This reaction is catalyzed by ribulose-1,5-bisphosphate carboxylase/oxygenase (RuBisCO), the most abundant soluble enzyme on Earth. The product is a very unstable 6-carbons intermediate (2-carboxy 3-keto 1,5-biphosphoribotol) that spontaneously splits into two molecules of 3-phosphoglycerate (3-PGA). The second phase is the phosphorylation and reduction of 3-PGA molecules resulting in the formation of an equivalent number of glyceraldehyde 3-phosphate (GAP) and the consumption of 1 ATP + 1 NADPH per molecule. GAP is considered the primary product of photosynthesis, and it is used as substrate for the biosynthesis of mono- and polysaccharides. Within the CBB cycle, only a small part of GAP molecules (1 out of 6) enters sugars biosynthetic pathways. The rest is used by the chloroplast to regenerate the pool of RuBP molecules following the stoichiometry: $5\ GAP + 3\ ATP \rightarrow 3\ RuBP + 3\ ADP + 3\ P_i$. Therefore, the fixation of 3 CO_2 molecules leads to the overall consumption of 6 NADPH and 9 ATP (ATP/NADPH = 1.5). The energy requirements of CBB can be dramatically impacted by the high affinity of the enzyme RuBisCO for O_2. The phenomenon is known as “oxygenation”, and its frequency depends on the O_2/CO_2 ratio in the proximity of RuBisCO. It was estimated (Sharkey, 1988) that at atmospheric levels of O_2 (209500 ppm) and CO_2 (420 ppm), the ratio oxygenation/carboxylation ≥ 0.2. The oxygenation of RuBP produces only one molecule of GAP to feed the CBB cycle, while a second molecule of 2-phosphoglycollate (2PG) is produced. The latter is a problematical molecule for plant metabolism as its accumulation strongly inhibits the activity of the chloroplastic triose-phosphate isomerase (Anderson, 1971) and phosphofructo-kinase (Kelly and Latzko, 1976), both important enzymes within the carbohydrates’ metabolism. Photorespiration is the pathway evolved by photosynthetic organisms to detoxify 2PG, and it involves: i) a set of oxidative reactions in the peroxisome resulting in the production of hydrogen peroxide (H_2O_2) and its detoxification, ii) a decarboxylation step in the mitochondrion resulting in the loss of CO_2 and production of ammonia (NH_3), iii) the synthesis of glycerate in the peroxisome and its phosphorylation into the chloroplast to regenerate 1 molecule of GAP. This process costs the cell an overall loss of 0.5 molecules of CO_2, 2 NADPH and 3.5 ATP (ATP/NADPH = 1.75) for each oxygenation event (Walker et al., 2016), drastically reducing the overall efficiency of light energy conversion into biomass.

As CBB cycle and photorespiration require an ATP/NADPH ratio of 1.5 and 1.75 respectively, one could imagine that LEF’s net production were equaling or outdoing such stoichiometry. Following the water oxidation cycle’s (Kok et al., 1970) stoichiometry, 4 charge separation events at P680 (4 e^-) result in the production of 2 NADPH molecules, and releases 4 H^+ through the photolysis of two water molecules + 8 H^+ through the Q-cycle into the lumen (Tikhonov, 2018). Considering the fourteen-fold rotational symmetry of the chloroplast CF_o ATP-synthase (Seelert et al., 2000), 12/14 protons drive CF_o through only 0.857 of a rotation, that would result in the equivalent phosphorylation of 2.56 ATP molecules. Thus, LEF results in a ATP/NADPH ratio of ≈1.28, failing to meet the energetic demand of CBB cycle and photorespiration. Such gap between ATP production and demand would be deleterious for the cell resulting in an acceptor-side limitation, over-reduction of the electron-transport chain (ETC) and damage of its components (Leister, 2020). As the intensity and spectrum quality of solar radiation, and the O_2/CO_2 ratio are subjected to continuous fluctuations in natural environments, photosynthetic organisms have evolved an efficient set of structural, biochemical, biophysical pathways to adjust the ATP/NADPH ratio to fulfill the metabolic demand while avoiding the overload of the ETC. Two main categories will be discussed in the following paragraphs: the alternative electron pathways and the non-photochemical quenching (NPQ) pathways. The first category includes all sorts of electron flows that are not linear (H_2O-to-NADPH). The second category will focus on the photoprotection pathways, responsible for poising the ETC's redox state upon high-light regimes. Some of the innate structural features contributing to this redox poising do not fall into any of these two categories, such as: a 14-20% higher concentration of chlorophylls in PSI compared to PSII, and a PSI/PSII ratio > 1 (Allen, 2002). The importance of such features will be highlighted during the paragraph about photoprotection.

1.1.5 Alternative electron transport pathways

To achieve the ATP/NADPH ratio needed for carbon fixation, photosynthetic organisms rely on the activity of secondary pathways that contribute to the H^+-gradient across the thylakoids without resulting in the production of NADPH. The most iconic alternative electron pathway is the cyclic electron-flow (CEF), in which electrons exiting PSI are shuttled back to Cyt b_6f and reinjected into the ETC, thus favoring lumen acidification and ATP over NADPH production. Two CEF mechanisms have been discovered (Nawrocki et al., 2019b), the main involving the interaction of reduced Fdx with the two proteins PGR5 and PGRL1, of which mode of action remains rather unclear. Main differences in the molecular machinery's organization are observed between plants and green algae for this pathway, and the contribution of PGRL1 remains still controversial (Nawrocki et al., 2019a). The second and minor route involves the interaction between Fdx and the chloroplast-localized NADH dehydrogenase–like (NDH) complex, proposed to work as a ferredoxin-dependent plastoquinone reductase. Such complex is mostly not present in green algae, where chlororespiration is carried out by a type II NAD(P)H dehydrogenase-like (NDA2) interacting directly with NADPH molecules. CEF pathways are still reason of debate among the photosynthetic community, and the wide diversity observed within different branches of the green lineage hinders the affirmation of a general working model. Nonetheless, a common agreement exists about the general physiological role of CEF in plants and green algae. As well summarized by Yamori and Shikanai (2016), numerous studies reported that CEF-mutants of *Arabidopsis thaliana* and *Chlamydomonas reinhardtii* display a slow-growth phenotype and higher sensibility to high-light stress, temperature stress, water stress as well as lower affinity for CO_2. Most of these phenotypes are linked to the mutants' incapacity to adjust (lower) their luminal pH, with harsh consequences for ATP production and other pathways that are tightly regulated by the light-driven *pmf* formation (DalCorso et al., 2008; Johnson et al., 2014; Wang et al., 2015; Yamori et al., 2015).

Oxygen is an important alternative electron acceptor, and several pathways lead to its photoreduction into water molecules. Thus, electrons coming from water photolysis contribute to the proton-gradient formation while eventually returning to water (water-water cycle). An example is the pathway dependent on the activity of the plastid terminal oxidase (PTOX), present in both plants and algae. This peripheral membrane protein, homologous of the mitochondrial alternative oxidase (AOX), catalyzes the reaction: $O_2 + 2PQH_2 \rightarrow 2H_2O + 2PQ$. A low value of PTOX-dependent electron transport rate was observed in *Chlamydomonas reinhardtii* ($5\ e^- s^{-1}$ per PSII) (Houille-Vernes et al., 2011), and even a lower value ($0.3\ e^- s^{-1}$ per PSII) was reported for vascular plants (Trouillard et al., 2012). Many physiological roles have been suggested for PTOX, including its involvement in chloroplast development, chlororespiration, carotenoid biosynthesis, reactive oxygen species (ROS) signaling, light and temperature stress responses (Nawrocki et al., 2015). Moreover, as for CEF, wide interspecific diversity occurs among plants and algae about the functioning and activity of this pathway.

Oxygen photoreduction happens also at the exit of PSI through the Mehler reaction, leading to the production of hydrogen-peroxide (H_2O_2) in the stroma, where the ascorbate peroxidase-cycle detoxifies it into H_2O. The physiological function of this pathway is still under open discussion, and the existing literature suggests multiple roles for this alternative electron pathway (Curien et al., 2016). In green algae, another water-to-water cycle is mediated by the flavodiiron proteins (FLVs), proposed to buffer the stromal side of PSI and avoid ROS formation upon transition between dark and light (Rochaix, 2016).

As mentioned before, the alternative electron pathways are mostly electrogenic and their activity results in an increased acidification of the lumen over the stroma (*ΔpH*), and polarization of the thylakoid membrane (*ΔΨ*). Both gradients are thermodynamically equivalent at driving ATP-synthesis, but the extent of each *pmf*'s component also regulates the thermodynamics of the photosynthetic ETC in many other ways. For instance, the light-driven alkalinization of the stroma provides the optimal pH for the functioning of several key enzymes of the CBB, while the acidification of the lumen is essential for the activation of the photoprotection mechanisms that prevent PSI photodamage and ROS formation. On the other hand, the *ΔΨ* controls the activity of the voltage-dependent transport system and the diffusion of counterions and enzymatic cofactors across membranes.

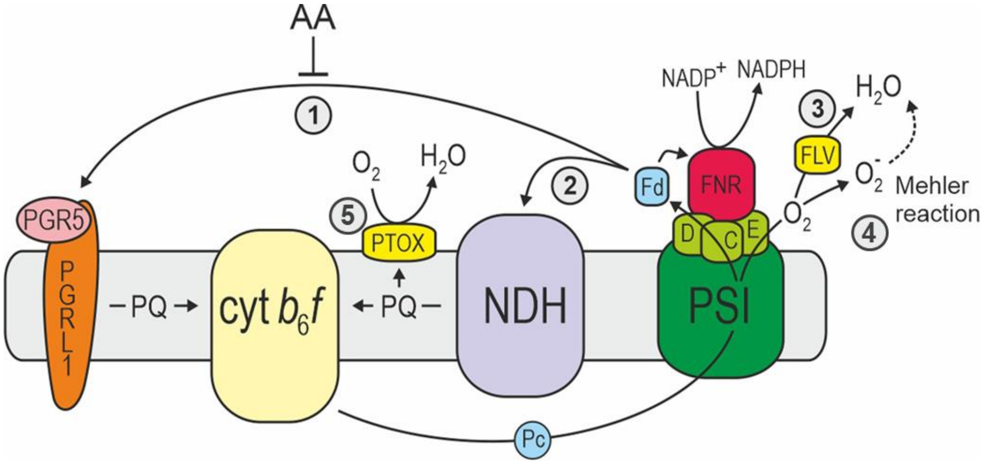

Figure 1. 3: A schematic representation of photosynthetic alternative electron pathways in plants. (1) PGRL1/PGR5-dependent and antimycin A (AA)-sensitive CEF. (2) NDH-dependent and AA-insensitive CEF. (3) FLV-dependent oxygen photoreduction. (4) PSI-dependent oxygen photoreduction. (5) PTOX-dependent oxygen photoreduction. Thioredoxins and hydrogenases (in some algae) also receive electrons from PSI (not shown). Readapted from (Leister, 2020).

1.1.6 Non-photochemical quenching

As we addressed how the chloroplast adjusts the ATP/NADPH ratio to the demand of CBB cycle, we shall now wonder what happens when the photosynthetic electron-transport rate (ETR) exceeds the demand of the CBB cycle. Upon an average sunny day, the photon flux reaching the leaves' surface is about 2000 µmol of photons m^{-2} s^{-1}. Under such conditions, the ETR is not limited by the availability of excitation energy, but rather by the availability of CO_2 in the proximity of RuBisCO resulting in the over-reduction of the pool of photosynthetic electron carriers. Despite the lack of electron-acceptors, light-harvesting never stops, and the excitation energy transferred to the RCs lingers within the special pair of chlorophyll molecules extending the lifetime of their excited singlet state (^{1}Chl*). The absence of photochemical quenching causes the slow decay of ^{1}Chl* and formation of chlorophyll excited triplet states (^{3}Chl*), that interact with O_2 yielding singlet oxygen ($^1O_2$): the forefather of ROS. These strong oxidizing agents are highly unstable and their overaccumulation results in the photodegradation of proteins, lipids and nucleic acids, leading to cell death. Given the fluctuating nature of the environmental factors, photoautotrophs had to come up with a strategy that could protect them from sudden changes in light intensity, without overruling their primary metabolism. Besides, an efficient ROS detoxification pathway was developed to minimize the lifetime of the dangerous molecules. The non-photochemical quenching (NPQ) of chlorophyll *a* fluorescence includes a set of pathways that reduce the pressure on the photosynthetic RCs through the modulation of light harvesting, and feedback regulation of energy valves which limit the formation of ^{3}chl*. Even if some differences are present among algae and plants, the main components of the NPQ are well conserved among the green lineage, highlighting the important role such

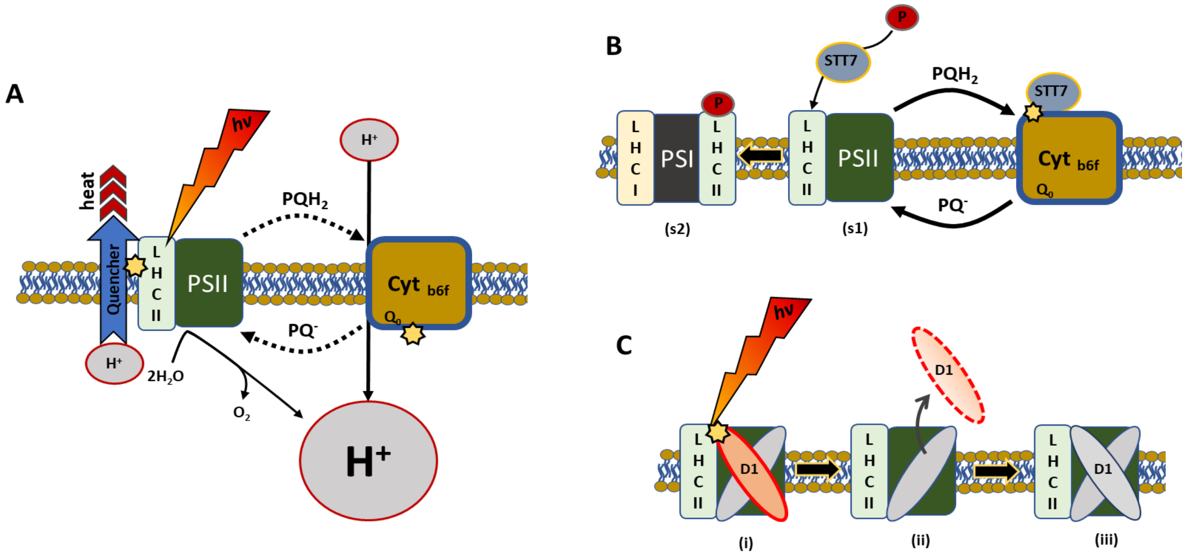

Figure 1. 4: Representation of the main regulatory processes acting on the donor side of the electron-transport chain to reduce the pressure on PSI. (A) The light-dependent acidification of the lumen induces a decrease in Cyt b6f turnover (photosynthetic control) and the activation of the energy-dependent component (qE) of the NPQ. (B) The overreduction of the PQ-pool triggers the activation of the thylakoid-associated protein kinase (STT7 in C. reinhardtii) that phosphorylates the LHCII bounded to PSII (s1 or state 1) inducing its migration and association with PSI (s2 or state 2). (C) The PSII photoinhibition/repair cycle starting with *i*) the photoinhibited PSII in a quenched state (qI), following with *ii*) the disassembly of the damaged D1 core subunit and *iii*) replacement with a new copy of the protein.

mechanisms along the process of evolution. The fastest and strongest form of NPQ is the ΔpH-dependent energy quenching (qE). It is well established that upon saturating light exposure, the pmf is mainly stored as ΔpH (Wilson et al., 2021). Upon this condition, some transmembrane proteins of which lumen-exposed glutamates residues act as pH-sensors, trigger the dissipation of excess energy in the form of heat. In both plants and algae, qE happens at the level of the LHCII-PSII supercomplex, but the molecular players involved in the process differ among the two groups. A process that is often associated with qE is the xanthophyll cycle (XC), consisting in the pH-dependent violaxanthin deepoxidation into zeaxanthin. It was demonstrated that in certain species, XC is essential for the activity of qE, while in others, no presence of a XC-dependent qE was found. In *Chlamydomonas reinhardtii*, XC seems not to be a major player in the development of qE (Bonente et al., 2011; Lacour et al., 2020). A second NPQ component is state transition (qT), a mechanism consisting in the reversible association of a percentage of total LHCIIs to the PSI-LHCI super-complexes (state 2). The conformational change is triggered by a serine/threonine protein kinase which is associated with the thylakoid membrane and regulated by the redox state of the intersystem electron-carriers. As PSI's absorbance peak is more red-shifted than PSII's, the role of state transition is to change the absorption proprieties of the ETC, limiting the energy transfer to PSII and favoring the oxidation of the intermediate electron carriers. The importance of qT is still a topic of discussion, above all in flowering plants where only a small percentage (25%) of LHCII is involved in such process with respect to green algae (85%) (Eberhard et al., 2008). A third NPQ component is the controlled photoinhibition (qI) of PSII reaction centers. Within the photosynthetic process, most of the ROS are formed in the proximity of PSII damaging one of the two main subunits of the PSII-RC (the D1 protein). It was reported that the turnover of this protein is very fast, and large amounts of D1 are synthetized even under low-light (LL). In parallel, an efficient mechanism of PSII-repair allows the damaged PSII to be quickly repaired through the degradation of the old D1 subunit and replacement with a new one. A substantial difference in recovery rate exists for PSI, where photodamage leads to a long-lasting decrease in productivity due to the much slower turnover of its core subunits. PSII photoinhibition was reported to protect PSI under high-light (HL) conditions by reducing the flux of electrons directed to P700. For this reason PSII photoinhibition is considered as an essential photoprotective mechanism (Sonoike, 2011). The acidification of the lumen is another important factor for the protection of PSI due to its role in the redox regulation of Cyt b*6*f turnover. The name "photosynthetic control" refers to the pH-dependent decrease in PH_2 oxidation rate at the Q_o-site of Cyt b_6f, thus resulting in a more reduced PQ-pool and a lower ETR toward PSI (Kramer et al., 1999). This mechanism is one of the most important feedback control factors of the photosynthetic electron transport (Tikhonov, 2013).

1.1.7 The model organism *C. reinhardtii*

Viridiplantae is a monophyletic group of eukaryotic organisms including both land plants and green algae. The group includes an estimated 450,000–500,000 species displaying high morphological and ecological diversity as they are scattered over land and marine environments (Leebens-Mack et al., 2019). Among all species, some have gained more scientific interest over time, becoming the subjects of countless research projects that deeply boosted our understanding of many processes spanning from the molecular to the ecological level. One good example is the green alga *Chlamydomonas reinhardtii* (hereafter: *C. reinhardtii*) which was first described by Dangeard in 1888. Its early involvement in genetic studies highlighted the suitability of this species to be grown under standard laboratory conditions and subjected to manipulations. *C. reinhardtii* is gifted with many qualities which, during its scientific history, led to its appreciation as subject of study for the investigation of many biological aspects. Some of these features are its fast growth rate, its capacity to perform sexual reproduction, its simplicity to be synchronized through a day-night cycle, its ability to form mature chloroplasts in the dark, while feeding on organic carbon sources.

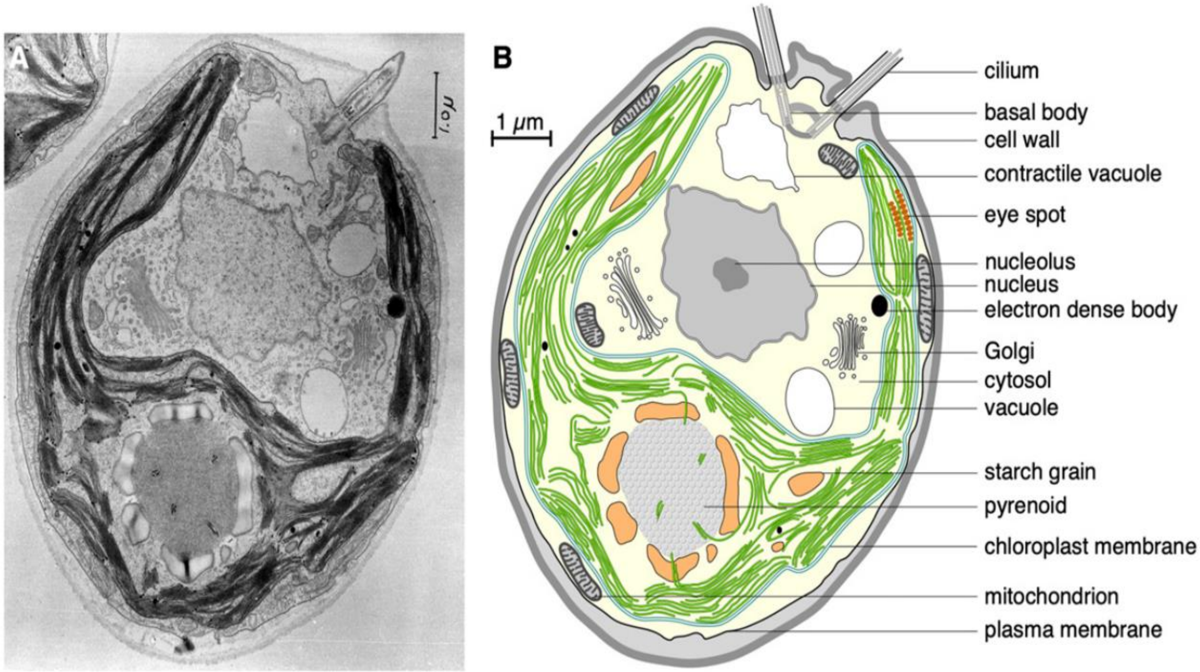

Figure 1. 5: Anatomy of Chlamydomonas reinhardtii. (A) Transmission electron micrograph (TEM) available on the Cell Image Library website (CIL:37252, C reinhardtii. CIL. Data set). (B) Drawing of a C. reinhardtii cell based on the TEM image in (A) realized by (Salomé and Merchant, 2019).

This chlorophyte is a single-celled photosynthetic biflagellate of which egg-shaped cell measures 5-10 μm of diameter and presents a single cup-shaped chloroplast that occupies most of the cell’s volume. The two anterior cilia devoted to mobility and sexual reproduction have been studied for decades to dissect the genetics and functioning of the intraflagellar transport machinery, leading to landmark discoveries in the field of human ciliopathies (Pazour et al., 2000; Li et al., 2004). *C. reinhardtii*'s cell wall is composed of hydroxyproline-rich glycoproteins and carbohydrates organized into 5 distinguishable layers (Goodenough and Heuser, 1985). Beneath the external coat, a selective membrane (plasma membrane) encloses the cytoplasm and all the organelles. As water can passively enter the cell, the tonicity of the protoplast is maintained by the channeling of excess water through the aquaporins, into the contractile vacuoles. The latter expel their content outside the cell by fusing with the plasma membrane. The nucleus is located at the center of the cell, mainly surrounded by the chloroplast, and it contains a haploid genome of about 111-114 Mb (size subjected to intraspecific variation) (Craig et al., 2022) arranged into 17 chromosomes. Golgi bodies, endoplasmic reticulum and cytoplasmic ribosomes are also found within the cavity formed by the cup-shaped chloroplast, submerged in the water-based cytoplasmic matrix. Multiple mitochondria are present in one cell, and they are generally localized in proximity of the chloroplast (Geraghty and Spalding, 1996). Mitochondria enclose a small genome of 15.8 Kb presenting a linear organization and encoding for 8 proteins, 15 rRNA and 3 tRNA fragments. The chloroplast genome is a circular molecule of 205 Kb, and each chloroplast contains about 80 copies organized into protein-DNA structures called nucleoids (Salomé and Merchant, 2019). Beneath the flagellar basal bodies, 12 microtubules extend asymmetrically across the cytoplasm composing the cytoskeleton. Associated with the most acetylated microtubule (D4), the eyespot is a sandwich-like structure composed of layers of carotenoid-rich lipid granules intermediated by layers of thylakoid membranes. At the eyespot site, the chloroplast envelope is appressed to an area of plasma membrane reach in light-activated cation channels "channelrhodopsins" (ChR1 and ChR2). The carotenoid-rich layers function as a light amplifiers, reflecting light toward or away from the channelrhodopsins and triggering transient Ca^{2+} fluxes that regulate the movement of the cilia, thus controlling phototaxis (Mittelmeier et al., 2011; Ueki et al., 2016). The presence of the eyespot is just one of the peculiarities distinguishing *C. reinhardtii* chloroplast from the one of land plants. The rather recent development of cryo-electron tomography combined to cryo-focused ion beam milling enabled the detailed visualization and description of the chloroplast ultrastructure in this species (Engel et al., 2015). *C. reinhardtii* thylakoids do not differentiate into grana stacks and stroma-lamellae, but rather into continuous stacks of variable length and uniform spacing. The number of layers can range from 2 to 15 thylakoids, with an average of 3 layers per stack. While plant plastoglobules are constitutively attached to thylakoids through half lipid-bilayer (Austin et al., 2006), *C. reinhardtii* ones are independent from the thylakoids and generally found in proximity of flat thylakoid stacks (Engel et al., 2015). One of the main differences between plants and green algae is the localization of the enzyme RuBisCO, that in flowering plants is dissolved within the stroma matrix. In green algae instead, RuBisCO is found in the pyrenoid: the core of the carbon-concentrating mechanism (CCM). This structure is composed of a thick starch-sheet enveloping the RuBisCO molecules, packed together into a spheric complex. The stability of the complex is maintained by the presence of the molecular linker Essential Pyrenoid Component 1 (EPYC1) (Mackinder et al., 2016). Thylakoid stacks approaching the

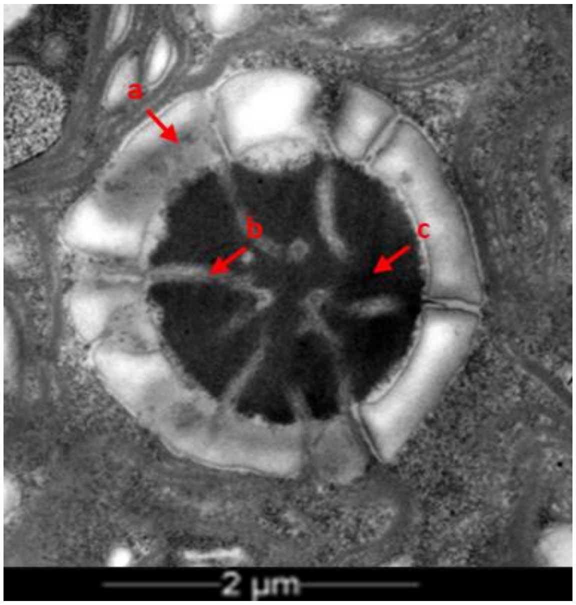

Figure 1. 6: Electron micrograph of *C. reinhardtii* pyrenoid. (a) The external starch sheath, (b) the pyrenoid microtubules, (c) the dense mass of RuBisCO. (Personal data).

pyrenoid collapse and merge into narrow tubular structures (pyrenoid tubules) that penetrate the starch-sheet, forking and twisting until they reach the center of the structure. The internal volume of the pyrenoid tubules is in part occupied by the thylakoid lumen, and in part by 2-to-8 smaller tubules (microtubules) found to be continuous with the stroma from the inter-thylakoid space (Engel et al., 2015). The finality and functioning of the pyrenoid will be better discussed in the section dedicated to the CCM.

C. reinhardtii can divide through sexual or asexual reproduction, the latter being the most common upon optimal environmental conditions. The vegetative cycle is based on the multiple fission of a mother cell into a variable number of daughter cells that will be all clones. Experimental cultures' synchronization can be achieved through temperature, light-quality or light-intensity cycles. The most common synchronization protocol is the 12:12 hours light-dark cycle at constant temperature (optimum of growth: 25 °C). The vegetative cycle starts with a long (10-to-14 hours) growth phase (G1), upon which the mother cell can increase its cell volume up to 10-folds. This phase is light-dependent, and it starts at the onset of the illumination. The increase in volume determines the number of "commitments" (multiple binary divisions) that the cell undertakes within the G1 phase. During the dark phase, the mother cell enters subsequent rounds of DNA duplication (S)/chromosomes segregation (M) phases, each cycle lasting for 30-45 minutes. No gap (G2 phase) is observed within each S/M cycle in this species. At the end of a multiple fissions' round, a variable number of zoospores of similar size will hatch from the mother cell wall and re-enter the G1 phase for a new round (Cross and Umen, 2015). In fully inorganic growth media, *C. reinhardtii* doubles 1-2 times every 24h, but the presence of an organic carbon source, acetate being the favorite, induces the G1 phase also in the dark leading to 2-3 doublings/day (Sager and Granick, 1953). Acetate is incorporated into acetyl-CoA and metabolized through the glyoxylate cycle, or "modified tricarboxylic acid (TCA) cycle" as it shares with the latter 3 out of 5 enzymes (citrate synthase, aconitate hydratase and malate dehydrogenase) (Kornberg and Krebs, 1957). The key enzyme of the glyoxylate cycle is the isocitrate lyase (ICL), which catalyzes the cleavage of isocitrate molecules (C_6) into glyoxylate (C_2) + succinate (C_4). The Glyoxylate cycle provides the C_4 skeletons for the biosynthesis of soluble carbohydrates and amino acids, but it is also considered a TCA cycle's anaplerotic pathway as it replenishes it with carbon intermediates taken away by the cataplerotic reactions (e.g., gluconeogenesis, aspartate, glutamate, and alanine biosynthesis). When *C. reinhardtii* is grown in presence of both light and acetate (mixotrophy), the cell adjusts its metabolic fluxes by differentially-regulating many nuclear-encoded chloroplast proteins involved in light harvesting and inorganic carbon fixation (Wienkoop et al., 2010). The acetate-dependent regulation of photosynthesis is conserved in other green algae (Kroymann et al., 1995). In parallel, an induction of the isocitrate lyase is observed, together with an increase in the respiration rate. Biomass partitioning studies by stable isotope ratio mass spectrometry demonstrated that in presence of acetate, roughly 50% of the cell biomass comes from acetate-derived C_i (Heifetz et al., 2000).

When vegetative cells are transferred into nitrogen-depleted media in the presence of light, gametogenesis is induced, marking the beginning of the sexual phase. *C. reinhardtii* is a heterothallic species, and sexuality is genetically determined by the mating-type (MT) locus of which two alleles (mt$^+$ and mt$^-$) represent the opposite sexes. Gametes are smaller than their vegetative counterpart, more tapered and particularly active swimmers. Each MT synthetizes different hydroxyproline-rich glycoproteins called agglutinins that are essential for cell-cell recognition and fusion. The agglutinins are localized in the cilia, that the cells use to sense the presence of the other MT by physical interaction. When two gametes of opposite MT collide, their cilia clump (agglutination) trigger the release of autolysin that digests the cell wall of the couple. Mating structures specific for each MT initiate the gametic fusion into a tetra-ciliate zygote that quickly synthetizes a new cell wall that confers resistance to hydric stress. The two nuclei fuse earlier than the chloroplasts, while the organelles' genomes do not fuse, and the plastid genome of the mt$^-$ is degraded leading to the uniparental transfer of the mt$^+$ DNA. The opposite happens for the mitochondrial genome that comes from the mt$^-$. In a limited number of cases, fragments of chloroplastic DNA from the mt$^-$ can recombine with the mt$^+$ chloroplastic genome generating genetic diversity within the progenies (Gillham, 1969; Boynton et al., 1987; Salomé and Merchant, 2019). Zygotes mature into pigment-rich zygospores that can be easily manipulated and stored in N-depleted agar plates for laboratory purposes. The initiation of the germination process is activated by their transfer to a nutrient-rich environment. Both blue (phototropins) and red (animal-like cryptochrome) photoreceptors are involved in the regulation of gametogenesis and germination (Zou et al., 2017; Salomé and Merchant, 2019). During the meiotic process, the parental genomes are shuffled by a series of recombination events that lead to the formation of 4 unique genotypes. The four daughter cells (tetrad) hatch from the zygospore starting a new vegetative cycle.

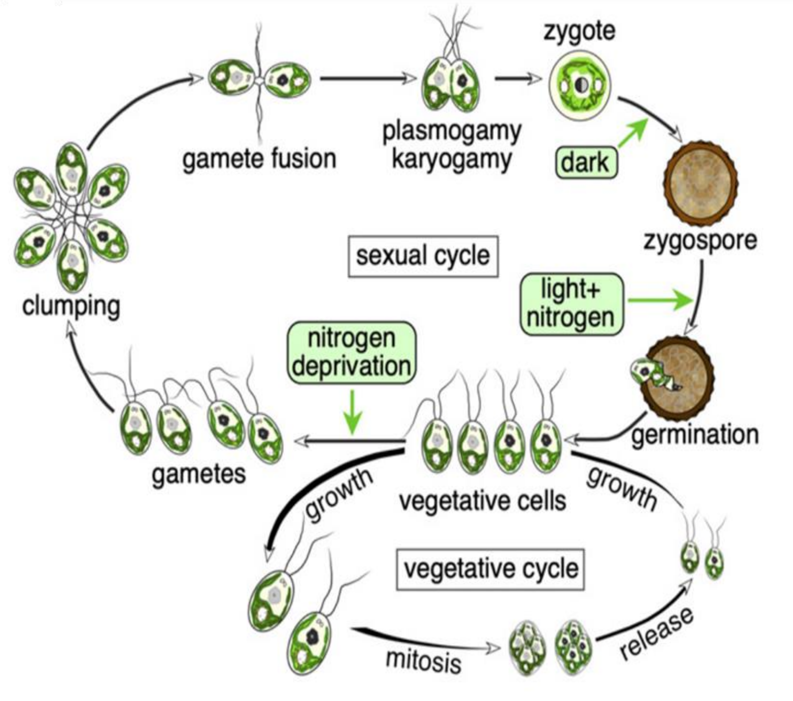

Figure 1. 7: The sexual and vegetative cycles of C. reinhardtii. Figure from (Salomé and Merchant, 2019).

1.1.8 Intraspecific diversity within *C. reinhardtii*

Most of the research on *C. reinhardtii* to date is carried out on a limited number of interrelated strains considered as the standard of the species. The standard laboratory strains were proposed to descend from the meiotic products of a single zygospore isolated by Gilbert M. Smith in 1945 in Massachusetts (Harris, 2008). Smith was among the first to isolate *C. reinhardtii* zygospores from soil samples obtaining mating pairs that he used to investigate the physiological basis of sexuality. In the following years, other scientists used Smith's strains to perform crossings and isolated new progeny with interesting phenotypes (Sager, 1955; Ebersold, 1956), of which MT pairs would be later deposited into common repositories and shared with the rest of the community (Pröschold et al., 2005). The genealogy of the laboratory strains is poorly documented, and they were initially grouped into three sub-lineages: Cambridge line, Sager line and Ebersold-Levin line. Each line would include strains with peculiar phenotypes, such as the 21gr strain (fast-growth in the dark) and 4*y* strain (yellow-in-the-dark) from Sanger line (Sager, 1955), and UTEX 2247 together with all the strains belonging to the Ebersold-Levine line, incapable of using nitrate as nitrogen source (Pröschold et al., 2005). Other strains were selected for strong negative phototaxis, high transformation efficiency (Pazour et al., 1995) and other morphological differences. Early phylogenetics studies were mainly based on the comparison of Restriction Fragment-Length Polymorphisms (RFLP) and sequences of small loci such the mRNA untranslated regions (UTRs) or the ribosomal-DNA cistron's internal transcribed spacers (ITSs). The outcome of such studies highlighted the presence of multiple polymorphisms among the group of laboratory strains, challenging the hypothesis of the recent common ancestry (Kubo et al., 2002; Pröschold et al., 2005). The publication of the first draft genome of a laboratory strain (Merchant et al., 2007) and the development of cheaper and faster next-generation sequencing (NGS) technologies provided the tools to look at the subject from a brand-new prospective. In Gallaher et al. (2015), whole-genome sequencing (WGS) data from 39 standard laboratory strains, representative from all three lineages and of both MTs, were aligned to the reference genome and scanned for polymorphisms. A total of 607,117 variants were detected among the strains, including single nucleotide polymorphisms (SNPs), short insertions or deletions (InDels) and structural variants. The authors reported that 98.2% of the observed genetic diversity is organized in a complex pattern that supports the hypothesis of the strains' common ancestry, proposing that they all derive from the crossing of two strains with 2% relative divergence. Each genome presents a specific recombination pattern allowing for an accurate sorting of the strains into 5 groups. The new 5-lineages model was proposed as an update to the old 3-lineages model. The study also highlighted the presence of wide intraspecific diversity in cell size and growth rate among the strains under optimal and Fe-limited growth conditions.

Before the 21st century, little was known about the natural diversity present within *C. reinhardtii*. Beside the highly studied standard laboratory strains, new interfertile strains (hereafter named "field-isolated strains") were isolated from natural samples from eastern North America (Harris, 2008) and Japan (Nakada et al., 2009), but poorly characterized until 2015 when a comprehensive study of comparative genomics led to the resequencing and analysis of the whole genome of most of them (Flowers et al., 2015). The study included a total of 12 field-isolated strains from different North American locations, and 8 among the most used laboratory strains. Genomes were sequenced to a sequencing depth of 50x to 90x, achieving a reference genome's coverage spanning from 92% to 97% for the field-isolates, and above 99% for the laboratory strains. A genomic analysis revealed the presence of remarkably high levels of polymorphism among field-isolated strains, including about 6.4 million biallelic SNPs and numerous InDels, structural variants, transposable elements and genes copy number polymorphisms. About 1.65 million SNPs are spread across ~38.5Mb of gene-containing regions, with the 9.5% of the mutations

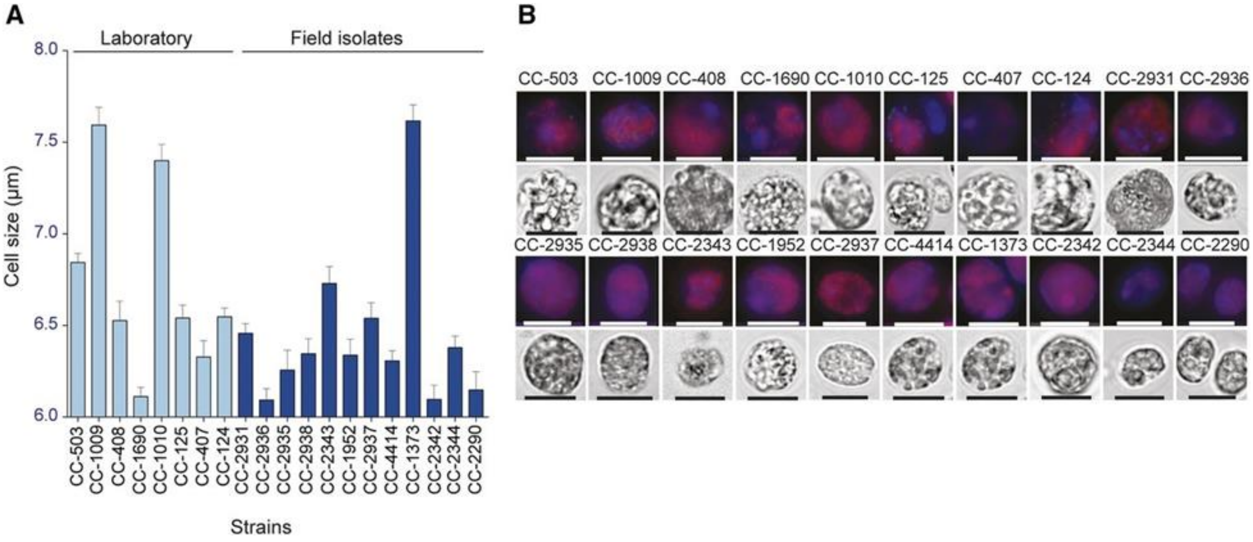

Figure 1. 8: Phenotypic variation in (A) cell size and (B) fluorescent and bright-field micrographs among laboratory and field-isolated strains of *C. reinhardtii*. Figure from (Flowers et al., 2015).

being nonsynonymous, 16.3% being synonymous, and 18.7% being intronic. Hundreds of genes belonging to all functional categories (e.g. photosynthesis, kinase activity, mitochondrion) of the primary metabolism were predicted to harbor many loss-of-function (LOF) mutations. Moreover, de novo assembly of reads that did not map on the reference genome revealed the presence of novel genes, on an average of 32 per strain, with respect to the reference strain CC-503. Extensive variation at the phenotypic level was observed when comparing the strains' cell size and growth rate, suggesting that the high levels of polymorphism translate into tangible morphological and physiological differences. The authors estimated an average nucleotide diversity (π) of 0.028 (3% divergence) across the genome of field-isolated strains, confirming that *C. reinhardtii* is among the most diverse eukaryotic species studied so far. Even so, this extraordinary level of intraspecific diversity is certainly not due to an unusually high mutation rate in the species. Two independent studies estimated a base-substitution mutation-rate (μ) spanning from 6.76×10^{-11} (Sung et al., 2012) to 3.23×10^{-10} (Ness et al., 2012). The authors reported such values to be among the lowest spontaneous base-substitution rates known among eukaryotes. The neutral theory of molecular evolution enounces that in a finite population, genetic diversity levels at neutral sites reflect a balance between mutational input and the random loss of genetic variation (genetic drift), and that the latter is inversely proportional to the effective population size (N_e) of the species (Leffler et al., 2012). Therefore, the important genetic divergence among *C. reinhardtii* field-isolates, despite the low rate of mutation, could be simply explained by a large N_e size resulting in low rates of genetic drift, thus maintenance of higher neutral genetic diversity. Thanks to the availability of the discussed μ and π direct estimates, an approximation of N_e can be calculated as $Ne= \pi/2\mu$ resulting in a number in the order of 10^8 (Flowers et al., 2015), among the highest known population sizes in eukaryotes (Charlesworth, 2009).

1.2 Aim of the thesis

A peculiarity of scientific research is that each discovery leads to the opening of new questions, pushing humans to come up with new strategies to fulfill their craving for knowledge. The discovery of such genetic diversity among *C. reinahrdtii* strains provides new food for thought and, as usual, leads to new scientific questions. *C. reinhardtii* has been used for over half a century as model organism to study the genetics, biochemistry, and biophysics of photosynthesis, and yet, nobody has ever assessed the extent of intraspecific photosynthetic diversity within the species, nor tried to make use of such natural resource. **The first objective** of this thesis was to provide some insights about the degree of natural phenotypic variation occurring among different field-isolated and laboratory strains of *C. reinhardtii*, with a focus on photosynthesis. While doing so, a new culturing condition suitable to perform photosynthetic mass-phenotyping was established as a preparatory step to the development of the second objective. The general characterization of a large panel of strains is presented and discussed, pinpointing the most variable and interesting photosynthetic traits and their fluctuation under several physiological conditions. An example of phenotypic diversity between a laboratory and a field-isolated strain was used to investigate the dynamics of proton-motive force regulation. In this respect, a new role of the CCM is proposed. **The second objective** was the development of a quantitative-genetic study to dissect the genetic bases of photosynthetic traits, identifying genomic regions associated with photosynthesis and photoprotection. The study is in collaboration with the group of Quantitative Genetics and Genomics (at the Unit of Animal Genomics) headed by Dr Tom Druet, and the one of functional genomics and plants molecular imaging, headed by Prof Marc Hanikenne. In the frame of this project, a restricted number of founder strains from the initial panel was selected and used to develop a Multiparent Advanced Generation InterCross (MAGIC) design that led to the creation of a recombinant population composed of 768 terminal lines. Each line was sequenced with high-throughput technologies and phenotyped for many traits related to photosynthesis and metal homeostasis. Quantitative trait loci (QTLs) associated with the traits were mapped, and candidate genes were searched within the corresponding confidence intervals. My contribution to this project concerned: the selection of the founder strains, the establishment of the crossing protocol, the realization of part of the crossing scheme, the development of the photosynthetic mass-phenotyping method and conditions, the study and selection of photosynthetic traits, the analysis and interpretation of the photosynthetic data set (phenotypic data), and the interpretation of the genomic analyses' output. The bioinformatics and QTL-mapping work was carried out by group of Tom Druet.

Chapter 2

2.1 Preface

This chapter is dedicated to the phenotypic characterization of twenty-five *C. reinhardtii* wild-type strains of which the majority was included in Flowers et al. (2015). Thus, whole-genome sequencing (WGS) data was already available, together with their detailed genomic characterization. Most of the work presented in this chapter was preparatory with respect to the mass-phenotyping of the MAGIC population. The first aim was the establishment of a new growth condition that could be suitable for the cultivation of 768 strains and that could enhance, rather than conceal, phenotypic differences detectable by chlorophyll *a* variable fluorescence analysis. The second aim was to provide a general photosynthetic characterization of the twenty-five wild-type strains, and take this information into account during the selection of the eight strains that would become the founders of the MAGIC design. A third aim was to phenotype the selected founder strains using a more conventional experimental design and investigate more in depth some of the observed intraspecific differences. To accomplish this last goal, the phenotyping of the founders was followed by a, in-depth multimethodological comparison between a laboratory and a field-isolate strain, providing a wide overview about their physiological state in response to photo-oxidative stress.

As summarized during the previous chapter, the photosynthetic metabolism is equipped with many pathways that work in synchrony to confer the process a high degree of plasticity and adaptability to the ever-changing environmental conditions. As I compared individuals from the same species, I assumed that the core components of the photosynthetic apparatus would be well conserved among the strains and hypothesized that phenotypic differences would be better highlighted if cells were grown under some form of environmental stress rather than their optimal growth condition. *C. reinhardtii* can be easily exposed to different stressing factors under experimental condition. Abiotic stress could be related to suboptimal growth temperature, nutrients excess/limitation, salt stress and photo-oxidative stress. Moreover, *C. reinhardtii* can uptake acetate which induces the remodeling of cell's metabolism (Puzanskiy et al., 2021), altering the response to some abiotic stresses such as the photo-oxidative stress response (Fischer et al., 2006). To learn more about the acetate-induced photosynthetic behavior, phenotyping was carried out under both photo-autotrophic and mixotrophic growth conditions. The growth condition chosen for the mass-phenotyping and the characterization of the 25 initial strains will be described in the section "Materials and Methods".

The results presented in section 2.2.3 will be part of a manuscript in collaboration with the group of "Sensing and Signaling in Microalgae" (Laboratory of Cell & Plant Physiology, CEA-Grenoble, Grenoble, France), led by Dimitris Petroutsos. Figure 2.19 and 2.21 (mRNA and proteins' extraction and analysis) were carried by Yizhong Yuan on biological samples produced by me in Liege.

2.1.1 Chlorophyll *a* variable fluorescence as a tool of mass-phenotyping

The technique chosen for the photosynthetic characterization of the MAGIC population was the time-resolved chlorophyll *a* fluorescence (ChlF) emission detection: a tool used for almost half of a century as a simple and reliable way to study the activity and dynamics of the photosynthetic apparatus (Bradbury and Baker, 1981; Ögren and Baker, 1985; Seaton and Walker, 1990).

When chlorophylls are excited by light the excitation energy is quickly transferred to the open RCs and used to perform photochemistry. If the excitation energy exceeds the demand of photochemistry and cannot be transferred to another energy quencher, as it happens during qE, then it is re-emitted by pigments as photons with longer wavelength: that is fluorescence. A well-established relationship exists between fluorescence emission, photochemical and non-photochemical ChlF quenching, as the three mechanisms are linked to the same energy source. Exposure of a sample to different light intensities yields different levels of fluorescence, and the difference between the highest fluorescence emission pick and the basal level of fluorescence is called variable fluorescence (F_v). Approximatively 90% of ChlF emission at room temperature originates from PSII, while PSI fluorescence emission is observable only at 77 °K (Papageorgiou and Govingjee, 2004). Therefore, room-temperature fluorescence yield depends on the redox state of PSII and can be used to calculate its photochemical efficiency (ϕ_{PSII}) at a specific light intensity. To do so, four reference values are used to define the system: *i*) the basal level of fluorescence (F_o) is the fluorescence signal emitted by dark-adapted cells (when all RCs are open), *ii*) the maximal fluorescence is the fluorescence signal emitted by dark-adapted (F_m) or light-adapted (F_m^t) cells exposed to a saturating light (all RCs are closed), *iii*) and the steady-state fluorescence (F_s^t) is the signal emitted by cells exposed to an actinic light (AL) (Eberhard et al., 2008). The maximum quantum efficiency of PSII (Fv/Fm) is defined by the equation:

$$(\Phi_{II})_{max} = \frac{Fv}{Fm} = \frac{Fm - Fo}{Fm}$$

Similarly, the effective quantum efficiency at a given light-intensity is derived from the equation:

$$\Phi_{II} = \frac{\mathrm{Fm^t} - \mathrm{Fs^t}}{\mathrm{Fm^t}}$$

The latter value can be multiplied for the light-intensity to obtain a rough estimation of the electron-transport rate (rETR) expressed as: μmoles of photons · m^{-2} · s^{-1}. Finally, the NPQ activity is described as follows:

$$NPQ = \frac{Fm - Fm^t}{Fm^t}$$

In the decades following the discovery of the Kautsky effect (Kautsky and Hirsch, 1931), the application of ChlF emission was limited to biophysically oriented basic research, serving as a tool in the study of the primary photosynthetic reactions. The diffusion of this technique to other research fields was slowly achieved with the progress of technology and the development of more simple and sensitive instruments. The first fluorometric measurements embraced the methodology of the dark-light induction curve of PSII, providing useful information about the dynamics of electron transport along the photosynthetic ETC. With the introduction of pulse-amplitude modulation (PAM) fluorimetry, the possibility to perform more sophisticated measurements attracted the interest of many other research-branches like: plant-stress physiology, ecophysiology and phytopathology (Schreiber, 2004).

The main features of a PAM fluorimeter are: *i*) a weak and short-lasting (µs) pulsing light used to probe the fluorescence emission intensity without altering it (detection light), *ii*) an actinic light used to induce photosynthesis, *iii*) a saturating (>3000 μmoles of photons · m^{-2} · s^{-1}) pulsing light used to close all the RCs, *iv*) a sensitive and fast-responding photodiode equipped with an optical filter to confer wavelength-selectivity on the recorded signal.

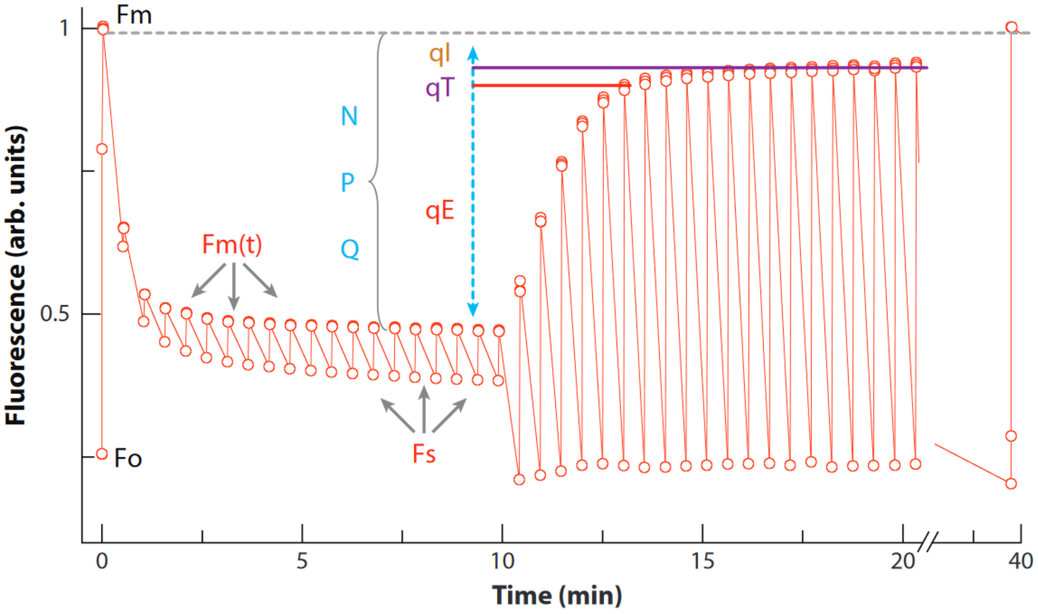

Figure 2. 1: Example of fluorescence yield fluctuation in a leaf subjected to continuous illumination (~500 µmol of photons · m^{-2} · s^{-1}, of red light), measured using a Joliot-type fluorometer. The decrease in Fm^t observed upon illumination is due to the activation of NPQ following the *pmf* formation. After 10 minutes of illumination, the actinic light is turned off and the relaxation of the NPQ components (qE, qT and qI) takes places in parallel to the dissipation of the *pmf*. Figure from (Eberhard et al., 2008)

In the last decades, fluorescence-derived parameters have been used to compare different species (Seaton and Walker, 1990; Beer and Björk, 2000; Juneau and Harrison, 2005), to perform high-throughput phenotyping of mutant populations and identify mutants impaired in photosynthesis and metabolism

(Eberhard et al., 2008; Wakao et al., 2021), and to map quantitative-trait loci (QTLs) involved in photosynthesis and stress-response (Yin et al., 2010; Tsai et al., 2019; Fernández-Calleja et al., 2020; Sedlar et al., 2020; Goto et al., 2021). Despite of its recognized potential (Rungrat et al., 2016), the latter application was only partially exploited on few crop-plants and never attempted on a unicellular haploid photoautotrophic species.

2.1.2 Algal CCM, NPQ and *pmf* regulation in *C. reinhardtii*

When the environmental light intensity is too high, CO_2 availability becomes the limiting factor for photosynthesis and the survival of cells depends on their ability to adapt to such condition and minimize the photo-oxidative damage. *C. reinhardtii*, as most of the aquatic photoautotrophs, is particularly responsive to light stress due to the 10,000-fold slower diffusion of CO_2 into water with respect to air. Moreover, the continuous evolution of oxygen coming from water-photolysis further penalizes carboxylation over oxygenation leading to the multiple consequences summarized within the introduction (Chapter 1 – Carbon reactions and photorespiration). As a result, when grown under photoautotrophic conditions (TMP growth medium), *C. reinhardtii* feels easily threatened by light and low-CO_2, responding with wide adjustments in gene expression (Fang et al., 2012). Among the up-regulated genes, *LHCSR1, PSBS1, PSBS2, LHCSR3.1,* and *LHCSR3.2* are involved in photoprotection. The last two are paralogs and translate for the pigment-binding Light-harvesting Complex Stress-Related 3 (LHCSR3) protein (Peers et al., 2009), the main effector of NPQ (specifically of qE) in this species. Differently than in plants, qE is not present in *C. reinhardtii* cells grown under LL, thus ChlF detection is a very powerful tool to determine the physiological state of this species with respect to low-CO_2 stress.

Another essential group of low-CO_2 inducible genes are the ones codifying for the components of the biophysical carbon concentrating mechanism (CCM), a central stress-response mechanism evolved by *C. reinhardtii* to cope with the HL-induced CO_2 limitation. The CCM consists in a battery of active transporters located across all cellular compartments, which import exogenous bicarbonate into the cell and concentrate it into the chloroplast. From the alkaline stroma, bicarbonate ions (HCO_3^-) enter the acidic lumen through bestrophin-like transporters (Mukherjee et al., 2019), and eventually reach the pyrenoid, where the carbonic anhydrase 3 (CAH3) (Karlsson et al., 1998) converts them into H_2O and CO_2. The thick starch sheath surrounding the pyrenoid is believed to limit the diffusion of the otherwise fast-escaping CO_2 molecules, so creating a CO_2-rich environment around the RuBisCO and increasing the rate of carboxylation reactions (Raven et al., 2008). Besides the transport of exogenous bicarbonate, another important CCM function is to limit losses of endogenously derived CO_2 due to passive diffusion through the lipid bilayers. For instance, the CO_2 leaking through the pyrenoid is re-converted into bicarbonate ions within the stroma, where the alkaline pH and the LCIB/LCIC complex (Miura et al., 2004; Yamano et al., 2010) catalyze the reaction. So far, 15 carbonic anhydrases (CAHs) have been discovered in *C. reinhardtii* (Aspatwar et al., 2018) and found to be localized in many subcellular compartments (Moroney et al., 2011). It is believed that the trapping of metabolism-derived CO_2 (e.g., oxidative decarboxylation reactions), its conversion into bicarbonate and transport into the chloroplast is essential to offset the energetic costs of the CCM (Raven, 2001; Fei et al., 2022). Moreover, the mitochondrial CAH4 has been proposed to be involved in the buffering of the mitochondrial matrix's pH (Eriksson et al., 1996).

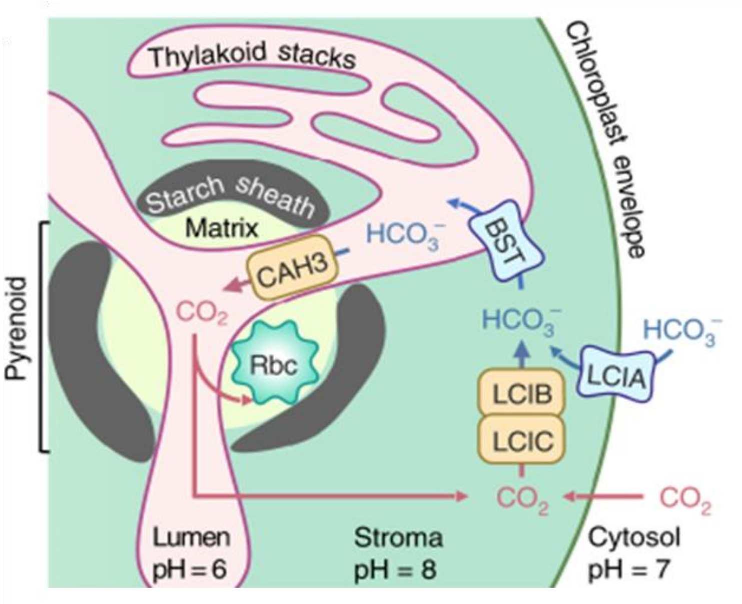

Figure 2. 2: Cartoon of a Chlamydomonas chloroplast with known CCM components. Figure from (Fei et al., 2022)

One complex, thus fascinating, aspect of *C. reinhardtii* physiology is the multilevel-regulation of the low-CO_2 inducible metabolism. All low-CO_2 inducible genes are under the control of the low-CO_2 activated zinc-finger type transcription factor CIA5 (also known as CCM1)(Moroney et al., 1989; Fukuzawa et al., 2001; Fang et al., 2012). The upstream regulatory network has not yet been elucidated, but it was recently shown to be light-independent (Redekop et al., 2022; Águila Ruiz-Sola et al., 2023). Moreover, a retrograde Ca^{2+} signaling (from the pyrenoid to the nucleus) was found to be essential for the regulation of both CCM (Wang et al., 2016) and NPQ (Petroutsos et al., 2011) genes, suggesting that the low-CO_2 stress sensing takes places in the proximity of the pyrenoid. For what concerns the regulation of the *q*E genes, another transcriptional regulatory mechanism dependent on the control of the UV-B (Allorent et al., 2016) and blue-light photoreceptors (Petroutsos et al., 2016) on the CONSTANS/NF-YB/NF-YC transcriptional module was well elucidated (Gnesutta et al., 2017; Gabilly et al., 2019; Tokutsu et al., 2019). Nonetheless, several evidences point to the existence of other mechanisms of transcriptional and post-transcriptional (for LHCSR3.1, LHCSR3.2 and PSBS) regulation not yet identified (Gabilly et al., 2019). A light-dependent regulation mechanism was observed also for the majority of CCM genes, even if CAH3, CAH6 and LCIB transcripts were found to be upregulated even in dark, but translated only in presence of light (Rawat and Moroney, 1995; Tirumani et al., 2014). So far, many transcription factors involved in low-CO_2 response were identified (Arias et al., 2020), but the dynamics of the regulatory mechanism is still far from being elucidated. As mentioned during the introduction, the *pmf* is partitioned into two distinct components: the electric potential gradient ($\Delta\Psi$) and the H^+-concentration gradient (ΔpH), and both components are accepted to be thermodynamically equivalent at driving ATP synthesis (Gräber and Witt, 1976; Leiser and Gromet-Elhanan, 1977; Hangarter and Good, 1982). From a physiological perspective, the alkalinization of the stroma and acidification of the lumen occupy an important regulatory role during the activation of photosynthesis and its adaptation to fluctuating light and CO_2 conditions. For instance, several enzymes of the Calvin-Benson-Bassham (CBB) cycle are pH-sensitive and fully active only upon high stromal pH values (Tikhonov, 2015), while the turnover of Cyt b_6f decreases with the acidification of the lumen (Tikhonov et al., 1981). The same holds for the activation of qE and CCM, both under the control of the ΔpH. The light-driven lumen acidification causes LHCSR3's protonation triggering the activation of qE, thus the acidification kinetics can be conveniently followed *in vivo* by measuring ChlF. (Ballottari et al., 2016; Tian et al., 2019). As for the CCM, an acidic lumen (~ pH 5) is essential to rapidly convert HCO_3^- to CO_2, and mutants with reduced ΔpH display lower NPQ and CCM activity (Moroney and Ynalvez, 2007; Burlacot et al., 2022). As high ΔΨ leads to increased rate of charge recombination and PSII photoinhibition (Satoh and Katoh, 1983; Davis et al., 2016), and the water-splitting-complex is damaged by pH values lower than 5 (Kramer et al., 2003), the *pmf* extent and partitioning must be governed by a highly responsive regulation mechanism.

In *Arabidopsis thaliana*, the *pmf* is mainly regulated by the activity of four ion-channels: AtTPK3, AtKEA1-3, AtVCCN1, and AtCLCe. The first and the second act on the partitioning between ΔΨ and ΔpH by regulation of the trans-membrane $\Delta K^+/\Delta H^+$ ratio (Carraretto et al., 2013; Armbruster et al., 2014; Kunz et al., 2014). Nonetheless, the localization and role of AtTPK3 is still under debate as the channel was localized by several groups in the contractile vacuoles rather than the chloroplasts, and no effect on photosynthesis was reported by the authors (Höhner et al., 2019; Jaślan et al., 2019; Tang et al., 2020). AtKEA1-3 instead, is directly involved in the fast dissipation of the ΔpH during the transition from HL to LL or dark, down-regulating the activity of qE. The chloride channels (AtCLC) family includes several slow transport-rate H^+/Cl^- antiporters, but the evidences presented so far suggest only a minor role of this class in *pmf* regulation, and a more relevant role in nitrate uptake (Teardo et al., 2005; Marmagne et al., 2007; Herdean et al., 2016a). The latter (AtVCCN1) counterbalances the light-driven pumping of H^+ toward the lumen by voltage-dependent import of negative (Cl^-) ions, thus collapsing the ΔΨ, and promoting lumen acidification and fast qE induction (Herdean et al., 2016b; Dukic et al., 2019; Hagino et al., 2022). Interestingly, AtVCCN1 is a bestrophin channel, very similar to the bestrophin-like channels BST1-3 (Fang et al., 2012; Mukherjee et al., 2019) found in *C. reinhardtii*. Interestingly, this class of channels was previously shown to be highly permeable to both Cl^- and HCO_3^- ions (Qu and Hartzell,

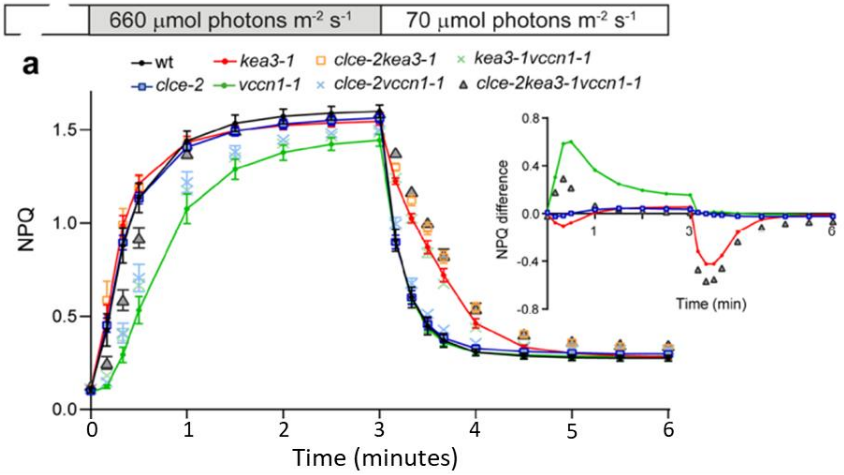

Figure 2. 3: NPQ induction and relaxation kinetics in *Arabidopsis* mutants impaired in K^+ and Cl^- trans-thylakoid ion transporting. Figure adapted from (Dukic et al. 2019)

2008).

Little is known about the regulation of the *pmf* in *C. reinhardtii*. Putative AtKEA1-3 homologs (Cre04.g220200.t1.1 ; Cre16.g687450.t1.1 ; Cre12.g493000.t1.1) were identified, but they have never been characterized, so their involvement in *pmf* regulation is still to be confirmed (Chanroj et al., 2012). Moreover, no TPK homologs are found in this species, where the osmoregulatory activity of the contractile vacuoles is mediated by the K^+ channel KCN11 (Xu et al., 2016). Six homologs from the CLC family were predicted and found to lack the nitrate selectivity filter motif (present only in AtCLCa), suggesting that they are low-selectivity anion-transporters (Calatrava et al., 2017). *C. reinhardtii s*' bestrophin-like transporters were demonstrated to import HCO_3^- into the acidic luminal compartment while consuming ΔpH (Burlacot et al., 2022), but their involvement in Cl^- transport was never investigated. Whether Cl^- is the main H^+-counterion in *C. reinhardtii* remains still unknown. Bicarbonate biochemistry is also known to be central for pH-buffering in eukaryotic cells of mammals (for a review: Cordat and Casey, 2008) and invertebrates (Russell and Boron, 1976; Thomas, 1977; Boron, 1978; Hu et al., 2018). Evidences were found in both plants (Koroidov et al., 2014) and green algae (Shutova et al., 2008) that HCO_3^- enhances oxygen-evolution by buffering protons coming from the OEC. Nonetheless, the CCM capacity to concentrate CO_2 up to 40-folds higher than the external level (Badger et al., 1980) comports a much higher bicarbonate influx into the lumen of green algae, suggesting that in *C. reinhardtii* the bicarbonate buffering-effect might be much more relevant than in plants.

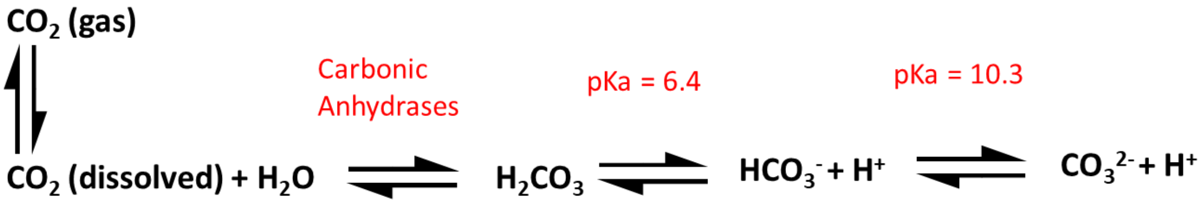

Figure 2. 4: Chemical reactions describing the equilibrium between different forms of inorganic carbon.

2.2 Results and Discussion

2.2.1 Photosynthetic diversity within *C. reinhardtii*

To investigate the degree of photosynthetic intraspecific diversity within *C. reinhardtii*, twenty-five wild type strains from different backgrounds (Table 1) were grown into deep-well microplates in a total volume of 0.8 mL (see also the figure “Methods 1”), in presence/absence of 17.4 mM acetate, under 100 µmol of photons · m^{-2} · s$^{-1.}$ After two days, 200µL of culture were transferred into white flat-bottom 96-wells microplates and let dark-adapt for 20 minutes. Following, the photosynthetic phenotype was characterized by time-resolved chlorophyll *a* variable fluorescence detection, using the protocol described in Figure 2.5.

Table 1: Initial panel of *Chlamydomonas reinhardtii* strains. “Lab” stands for “Laboratory”. Strains coming from North America are divided into three lineages based on their geographical origin: Northeast (NE), Southeast (SE), West (W).

CC strain ID	SAG strain ID	Common name	Region of isolation	Origin
CC-5325	—	Jonikas wt	—	Lab
CC-503	—	cw92	—	Lab
CC-3348	73.72	C-8	—	Lab
CC-1690	—	21gr	—	Lab
CC-125	34.89	137c +	—	Lab
CC-124	33.89	137c -	—	Lab
CC-1010	11-32b	UTEX 90	—	Lab
CC-1009	11-32a	UTEX 89	—	Lab
	83.81	cw15	—	Lab
CC-4414	—	DN2	—	Lab*
CC-410	11-32c	—	—	Lab*
CC-1418	18.79	—	—	Lab*
CC-1374	77.81	—	—	Lab*
—	11-31	—	—	Lab*
CC-2938	—	—	Quebec, Canada (NE)	Nature
CC-2937	—	—	Quebec, Canada (NE)	Nature
CC-2936	—	—	Quebec, Canada (NE)	Nature
CC-2935	—	—	Quebec, Canada (NE)	Nature
CC-2931	—	—	Durham, NC, USA (SE)	Nature
CC-2344	—	Jarvik #356	Ralston, PA, USA (SE)	Nature
CC-2343	—	Jarvik #224	Melbourne, FL, USA (SE)	Nature
CC-2342	—	Jarvik #6	Pittsburgh, PA, USA (SE)	Nature
CC-2290	32.89	S1 D2	Minnesota, USA (W)	Nature
CC-1952	—	S1 C5	Minnesota, USA (W)	Nature
CC-1373	54.72	—	South Deerfield, MA, USA (NE)	Nature

** Strains initially reported to be new isolates from the wild and later discovered to be genetically like laboratory isolates.*

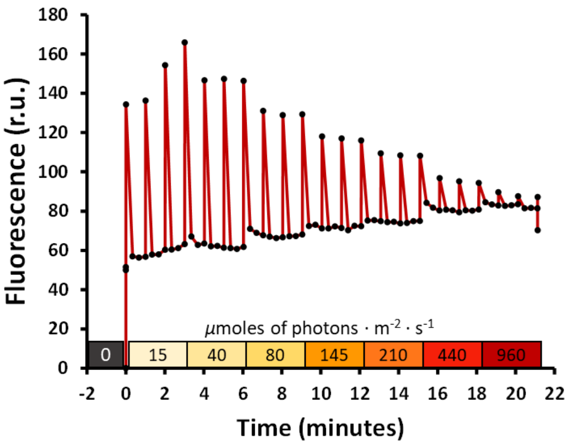

Figure 2. 5: Cells were let in the dark for 20 minutes before the measurement. PSII variable fluorescence was monitored through a saturation-curve including 7 light-steps of 3 minutes each (one saturating pulse per minute). Fv/Fm was calculated on the first pulse, while rETR and NPQ were calculated on the last two pulses of each light-step as reported in the preface. The two values at each light intensity were averaged to obtain a single rETR and NPQ value for each light-step.

It was reported in Flowers et al. (2015) that *C. reinhardtii's* population structure matched the geographical distribution, as strains isolated in the same area present more similar genotypes. My analysis highlights the presence of wide intraspecific diversity among all the strains in both photoautotrophic and mixotrophic conditions. In our experimental setup, the observed phenotypic variation seems not to be related to the geographic origin of the strains, and wide phenotypic variability exists among strains from the same area.

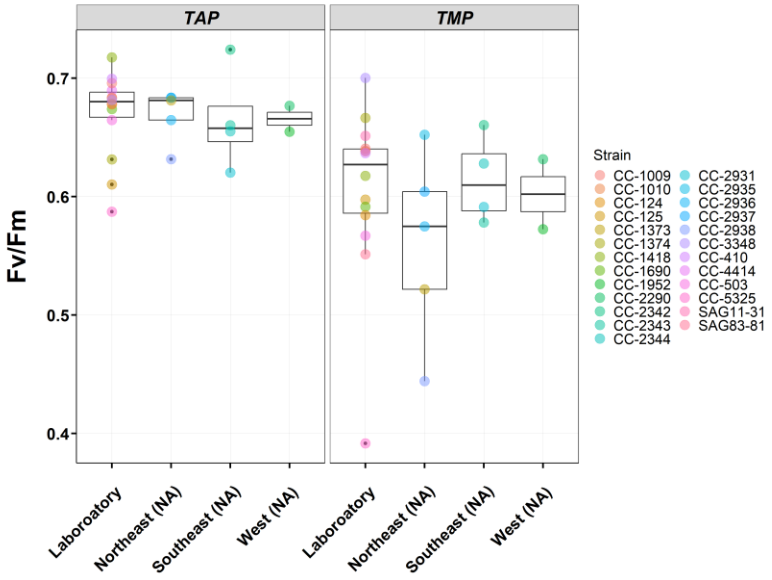

Figure 2. 6: Variability in the Fv/Fm within *C. reinhardtii* wild-types strains grown in TAP and TMP. Each box includes strains sharing similar geographical origin. Each point is the average of 6 (TMP) or 9 (TAP) biological replicates.

Upon optimal growth conditions, *C. reinhardtii* presents a maximum PSII quantum yield (Fv/Fm) of 0.65-0.75 (Santabarbara et al., 2019). In our experimental setup, *C. reinhardtii* cultures grown into shaking flasks under low-light (30 µmol of photons · m^{-2} · s^{-1}) display a Fv/Fm of ~0.75 in both autotrophic and mixotrophic condition (see Fig. 2.11), and no differences are visible among the strains. On the other hand, cells cultured into deep-wells show higher phenotypic diversity for this trait, suggesting that the tested growth condition is sub-optimal for some of the strains. It was previously shown that the decrease of Fv/Fm is due to irreversible damage to the D1 core-subunit of PSII (Ohad et al., 1990) and that the availability of acetate during growth makes cultures less susceptible to photoinhibition when subjected to photo-oxidative stress (Roach et al., 2013).

The same pattern is observable in our data, where the absence of acetate results in a higher number of strains with a lower Fv/Fm. A clear acetate-dependent physiological shift is visible in our dataset (Sup. Figure 2-A), and the mixotrophic cultures show higher photosynthetic efficiency (rETR) and lower photoprotective capacity (Sup. Figure 2-B). On the other hand, low rETR and high NPQ values are observable in photoautotrophic cultures, suggesting the existence of a negative correlation between rETR and NPQ. Looking at the Pearson's correlation (Figure 2.7), the relationship between photosynthesis and photoprotection seems more significant in presence of acetate. Moreover, a stronger negative correlation is observed for both physiological conditions during the first light-steps of the saturation curve suggesting that, when photosynthesis is limited by light, photoprotection might compete with photochemistry for the excitation energy.

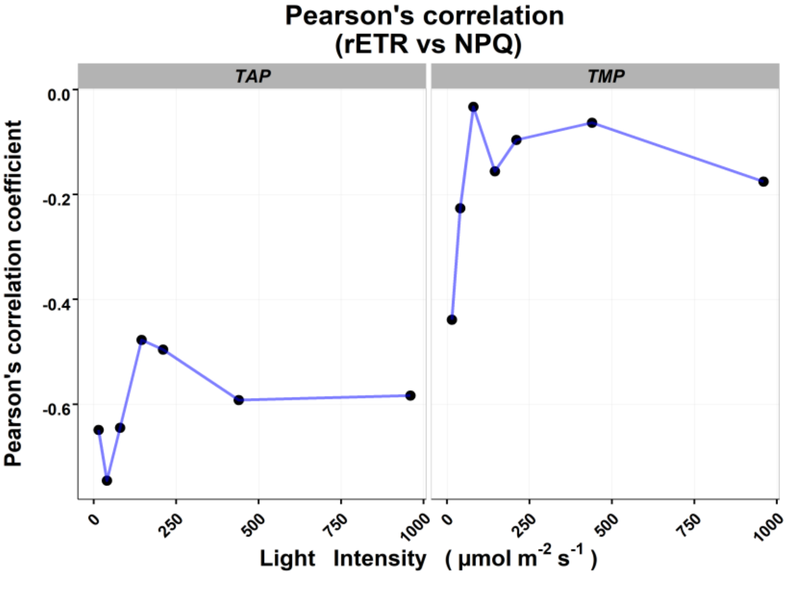

Figure 2. 7: Correlation between rETR and NPQ upon mixotrophy and photoautotrophy as function of the light intensity.

No relationship between photosynthetic response and geographical origin was detected, even when looking at the ETR and NPQ data (Sup. Figure 1). Therefore, given the common ancestry of laboratory strains and considering that they have been maintained for more than half of a century under unnaturally easing conditions with respect to the field-isolated strains, I decided to compare the photosynthetic phenotype between the two groups.

Despite the similar Fv/Fm, our results show significant phenotypic divergence among the two groups with respect to their photosynthetic behavior (Figure 2.8). Under mixotrophic conditions, the group of laboratory strains displayed higher rETR (1.7-fold-change at the last light-step) and lower NPQ. On the other hand, less consistent differences in rETR and only little differences in the NPQ-induction were observed among photoautotrophic cultures, suggesting that the variation between the two groups is related to acetate metabolism and its effect on chloroplast's physiology.

Under photo-autotrophic conditions, some strains presented negative rETR values during the last light-step of the saturation-curve (see Figure 2.8 and Sup. Figure 1). This is clearly an artifact that took place under saturating light, and it could be linked to a technical limitation of the fluorescence detector. Such negative numbers originate when the distance between the Fm' and Fs' (pulse amplitude) is so small that it falls below the sensibility threshold of the detector. Upon this condition, the Fs' point might be higher than the Fm', yielding a negative phi-PSII, thus a negative rETR.

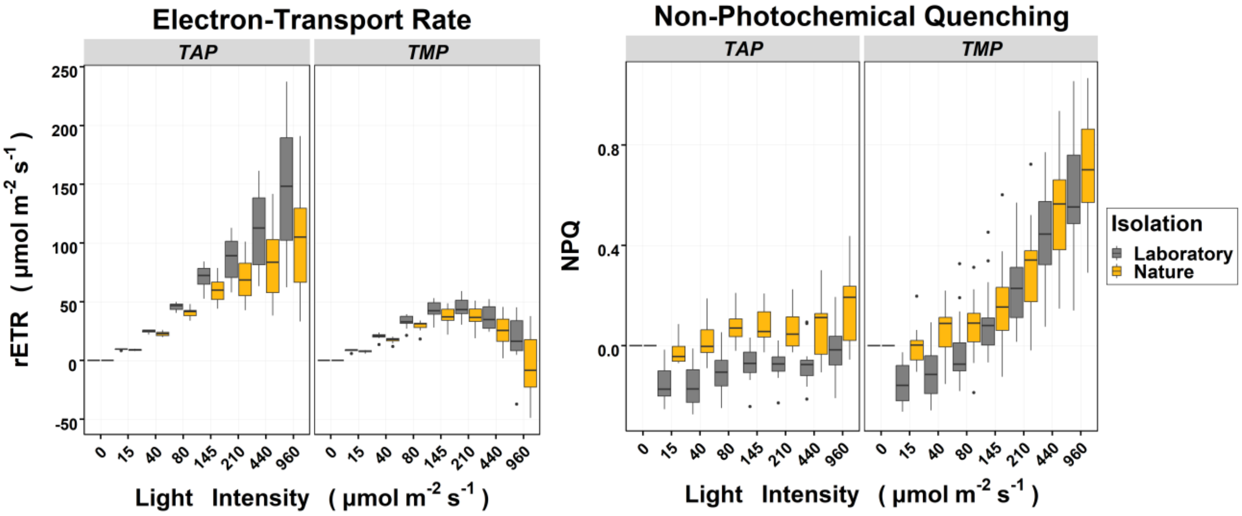

Figure 2. 8: Diversity between laboratory and field-isolated strains. The relative Electron-Transport Rate (rETR) and Non-Photochemical Quenching (NPQ) are presented as function of the light intensity. Two boxes correspond to each light intensity; the grey represents the variation among the 9 laboratory strains, while the yellow represents the variation among the 16 field-isolates.

Negative NPQ values originate when some form of NPQ is active in the dark and relaxes in the light, so Fm^t is higher than Fm. This well-established phenomenon is linked to the activity of NDH2 in the dark, partially reducing the PQ-pool and promoting the STT7-dependent state-transition (qT) toward state 2. Exposure of dark-adapted samples to non-saturating light causes a fast PQH_2-oxidation, resulting in the relaxation of qT and raise of the overall fluorescence signal (Allorent et al., 2013; Roach, 2022). Under mixotrophy, NPQ remains closer to 0 in the field-isolated strains suggesting that, when dark-adapted, they develop less qT than the laboratory strains. The same pattern is visible under photoautotrophic conditions, during the first two light-steps of the saturation curve (see Table 2 for statistics).

Table 2: Statistical significance of the difference between laboratory and natural strain. P-values calculated by Welch’s Two Sample t-test. For values highlighted in light-yellow: p-value < 0.01.

Light Intensity (μmol m^{-2} s^{-1})	**TAP**			**TMP**		
	Fv/Fm	**rETR**	**NPQ**	**Fv/Fm**	**rETR**	**NPQ**
0	8.30E-01	—	—	5.15E-01	—	—
15	—	2.13E-02	3.00E-05	—	1.62E-02	1.51E-04
40	—	4.42E-03	2.09E-05	—	2.40E-03	1.35E-03
80	—	3.67E-03	2.53E-06	—	5.23E-02	1.11E-01
145	—	1.87E-02	3.74E-05	—	1.14E-01	3.85E-01
210	—	3.38E-02	1.69E-04	—	8.58E-02	3.43E-01
440	—	4.27E-02	5.91E-03	—	3.30E-02	2.85E-01
960	—	4.35E-02	1.19E-02	—	4.76E-02	2.76E-01
P-value (Laboratory vs Nature)						

2.2.2 The MAGIC founders

The preliminary phenotyping of 25 *C. reinhardtii* wild-type strains uncovered the presence of wide intraspecific diversity (Sup. Figure 3), with the group of laboratory strains being more similar to each-other than to the group of natural isolates. Deep-wells culturing seemed adequate to support growth for all strains, yielding reproducible phenotypic traits that can easily be parameterized by ChlF detection. The next step of this project was the selection of 8 WT strains to use for the development of the Multiparent Advanced Generation Inter-Cross (MAGIC) design. As an initial screening criterium, the 25 strains were assessed for their mating efficiency (mating protocol described in "Materials and methods"). Most of the strains were found to be inter-compatible with the others, excepted for CC-2938, CC-4414, CC-1374, CC-124, and CC-2343, presenting a low or moderate mating efficiency (Figure 2.9). Nonetheless, no further attempts to cross them were carried out, thus the low mating efficiency could be related to the mating conditions being suboptimal for some of the strains. Since the five strains belonged to geographical groups including more than one representative, they were filtered out from the initial panel.

The final selection of the eight founders was based on two main criteria: the genotype (or geographical origin) and the phenotype. Among the North American isolates, CC-1952 was selected from the West region, CC-2936 and CC-2937 from the Quebec region, CC-2931 and CC-2344 from the South-East region, and CC-1010 was picked among the laboratory strains due to its outstanding photosynthetic efficiency in TAP (Sup. Figure 3). Based on their peculiar origin, we finally picked two strains for which no whole-genome sequencing data was available before this project: CC-1418 (SAG18.79), listed by the Sammlung von Algenkulturen (SAG) as "USA, Florida, red tide", and CC-410 (SAG11-32c), listed by SAG as "Caroline Islands, South Pacific, soil from Jaluit". However, some pre-existent reports indicated that the two strains were similar to lab strains in terms of chloroplasts DNA (Pröschold et al., 2005) and Gulliver retrotransposon pattern (Ferris, 1989). Our genomic analysis will confirm those previous reports, demonstrating that CC-410 and CC-1418 were not endemic from the reported areas, but rather mislabeled

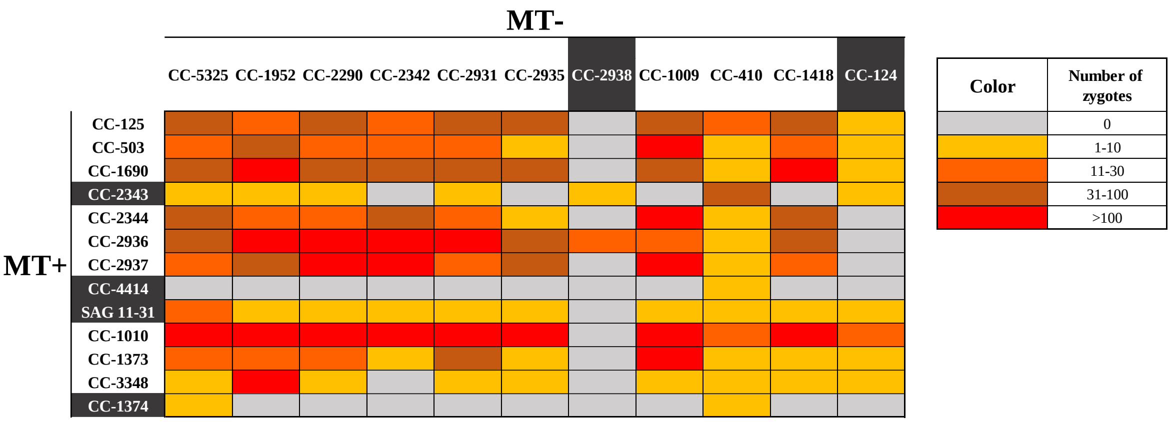

	MT-										
MT+	CC-5325	CC-1952	CC-2290	CC-2342	CC-2931	CC-2935	CC-2938	CC-1009	CC-410	CC-1418	CC-124
CC-125	🟫	🟧	🟫	🟧	🟫	🟫	⬜	🟫	🟧	🟫	🟨
CC-503	🟧	🟫	🟧	🟧	🟧	🟨	⬜	🟥	🟨	🟧	🟨
CC-1690	🟫	🟥	🟫	🟫	🟫	🟫	⬜	🟫	🟨	🟥	🟨
CC-2343	🟨	🟨	🟨	⬜	🟨	⬜	🟨	⬜	🟫	⬜	🟨
CC-2344	🟫	🟧	🟧	🟫	🟧	🟨	⬜	🟥	🟨	🟫	⬜
CC-2936	🟫	🟥	🟥	🟥	🟥	🟫	🟧	🟧	🟨	🟫	⬜
CC-2937	🟧	🟫	🟥	🟥	🟧	🟫	⬜	🟥	🟨	🟧	⬜
CC-4414	⬜	⬜	⬜	⬜	⬜	⬜	⬜	⬜	🟨	⬜	⬜
SAG 11-31	🟧	🟨	🟨	🟨	🟨	🟨	⬜	🟨	🟨	🟨	🟨
CC-1010	🟥	🟥	🟥	🟥	🟥	🟥	⬜	🟥	🟧	🟥	🟧
CC-1373	🟧	🟧	🟧	🟨	🟫	🟨	⬜	🟥	🟨	🟨	🟨
CC-3348	🟨	🟥	🟨	⬜	🟨	🟨	⬜	🟨	🟨	🟨	🟨
CC-1374	🟨	⬜	⬜	⬜	⬜	⬜	⬜	⬜	🟨	⬜	⬜

Color	Number of zygotes
⬜	0
🟨	1-10
🟧	11-30
🟫	31-100
🟥	>100

Figure 2. 9: Mating efficiency among different wild-types *Chlamydomonas* strains. The mating efficiency of the strains is expressed as the number of zygotes observed per surface-unit and represented by color code as described in the legend. The strains highlighted in black are the ones presenting the lowest mating efficiency.

laboratory strain subclones. The development of the MAGIC design began shortly after the selection of the eight founders, and it will be better described in Chapter 3.

To learn more about the molecular bases of photosynthetic diversity, a more detailed characterization of the eight founders was carried out as follows. Mixotrophic precultures in middle log-phase were harvested and assessed for their chlorophyll content. The required volume was centrifuged at 1500 g for 5 minutes and resuspended into fresh medium, at the concentration of 2µg (mixotrophic cultures: TMP + 20mM acetate. Hereafter referred to as TAP) or 5µg (autotrophic cultures: TMP) of Chl/mL. Cultures were let shaking for ~20 hours under 30µmol m^{-2} s^{-2} of continuous light. The following day, LL-samples were harvested and their Chl content, Chl *a*/*b* ratio and ChlF yield measured (see Figure 2.10). Afterwards, the experimental light was increased to 300µmol m^{-2} s^{-2} and new measurements were repeated after 4 hours (HL samples). Besides the three selected laboratory strains, CC-5325 (Jonikas' strain), the CLiP library recipient strain (Li et al., 2016), was included in the analysis as fourth representative of the lineage.

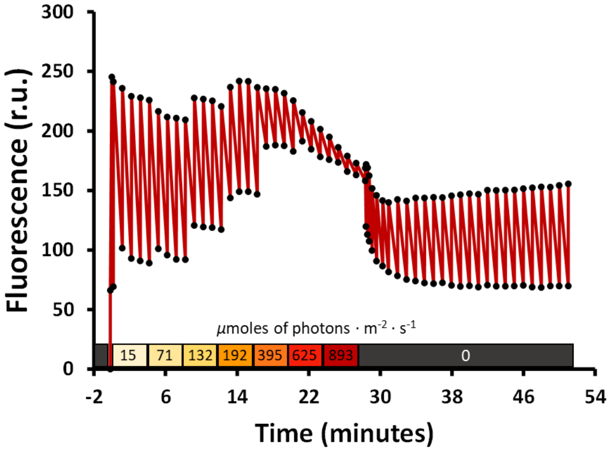

Figure 2. 10: Modified version of the initial ChlF detection protocol (Fig. 2. 5). To obtains more resolution upon saturating light-exposure, a LL-step was replaced with a HL-step and the span of all light-steps was increased to 4 minutes. A dark interval of 23 minutes was added at the end of the saturation curve to monitor the relaxation of the fast-relaxing NPQ components (qE and qT) and the recovery of the Fv/Fm.

LL-samples presented an average Chl *a*/*b* ratio of 1.96 ± 0.02 (SE) in TAP and 2.01 ± 0.02 (SE) in TMP ($p>0.09$). Few significant ($p < 0.05$) differences were observed (Sup. Figure 4) among mixotrophic cells: CC-2931 showed a significantly lower ratio than CC-410 and CC-1418, while CC-1418 had a significantly higher ratio than CC-1952. In autotrophy, CC-1010 showed a significantly higher Chl *a/b* ratio than all the others, and CC-1418 was significantly different from CC-410 and CC-2936. On the other hand, a significantly different trend in Chl *a*/*b* was observed between TAP and TMP after the HL treatment. The data shows an average ratio of 1.92 ± 0.02 (SE) for TAP-grown and of 2.1 ± 0.02 (SE) for TMP-grown cells ($p<0.0002$). Moreover, the treatment seemed to lessen the variability among the strains under both growth conditions. In TAP, significant ($p < 0.05$) differences were observed between CC-1418 and other 2 strains (CC-1952 and CC-CC-410), while in TMP, CC-1010 was significantly ($p < 0.05$) different from CC-1952, CC-2931, and CC-410.

In addition to Fv/Fm, rETR, and NPQ (at all light intensities), the new ChlF detection protocol was used to monitor the amount of NPQ relaxed upon 10 minutes of darkness (Fast-relaxing NPQ), and the Fv/Fm recovery after the saturation curve (calculated on the last pulse of the sequence). LL-samples (Figure

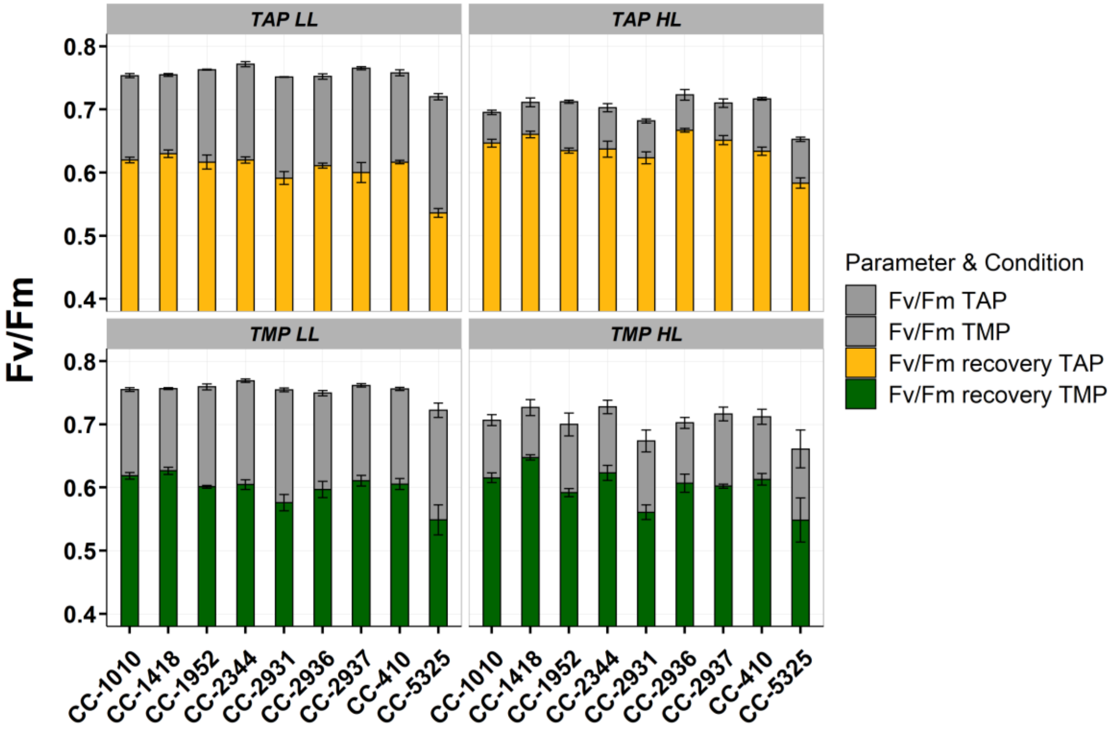

Figure 2. 11: Maximum quantum yield of PSII (Fv/Fm) in all conditions, before and after (Fv/Fm recovery) the exposure of the sample to the actinic lights used to measurement of the PSII-saturation curve. All samples where dark-adapted for 20 minutes before the measurements. Values ± SE, n=3.

2.11) presented an average Fv/Fm of 0.75 ± 0.005 (SE) in TAP and 0.75 ± 0.004 (SE) in TMP ($p>0.\ 9$). Under mixotrophic conditions, CC-5325 and CC-2344 presented a significantly ($p < 0.05$) different Fv/Fm than the rest, while in TMP, CC-2344 was the only one to be significantly different from the others ($p < 0.05$). The 4-hours HL treatment resulted in a small, but significant decrease in Fv/Fm for both TAP (0.70 ± 0.007 SE ; $p<0.0001$) and TMP (0.70 ± 0.007 SE ; $p<0.0001$). After the treatment, no significant difference was detected among TMP cultures, while in TAP, CC-5325 maintained a lower Fv/Fm than all the others, followed by CC-2931 which showed significant differences with 6 out of the 8 other strains ($p>0.05$).

To investigate the impact of the actinic light within the saturation curve measurement, a second Fv/Fm was taken 23 minutes after the last light-step (Fv/Fm recovery). The result shows a significant decrease in Fv/Fm under all conditions ($p<0.0003$), with an identical average value of 0.60 ± 0.01 (SE) for both LL-TAP and LL-TMP ($p>0.6$), and a significantly higher ($p<0.02$) average value for HL-TAP (0.64 ± 0.008 SE) with respect to HL-TMP (0.60 ± 0.010 SE). This result is in line with the precedent reports attributing to acetate a direct or indirect photoprotective effect on PSII (Roach et al., 2013). Under mixotrophic conditions, CC-5325 remains the most different strain ($p<0.05$) in both LL and HL, followed by CC-2936 which after HL treatment displays significant differences in Fv/Fm recovery compared to four other strains (CC-2931, CC-410, CC-5325, CC-1952 ; $p<0.05$). Among LL-TMP samples, only CC-1418 shows significant differences with two other strains (CC-1952, CC-2931 ; $p<0.05$). CC-1418 remains the most different even after the light treatment, displaying significant differences with five other strains (CC-2931, CC-1952, CC-2937, CC-1010, CC-410 ; $p<0.05$).

To assess the photosynthetic and photoprotective efficiency as a function of the light intensity, rETR and NPQ were calculated for each light-step of the saturation curve (Sup. Fig. 5). When comparing TAP and TMP average values (Sup. Fig. 5), significant differences were observed for both parameters under almost all light intensities ($p<0.005$). The only exception was observed on LL-samples, where no differences in NPQ was found between growth-media upon the second light-step of the saturation curve. Within each condition, the highest light intensity (893µmol m^{-2} s^{-2}) was used to compare rETR and NPQ among the

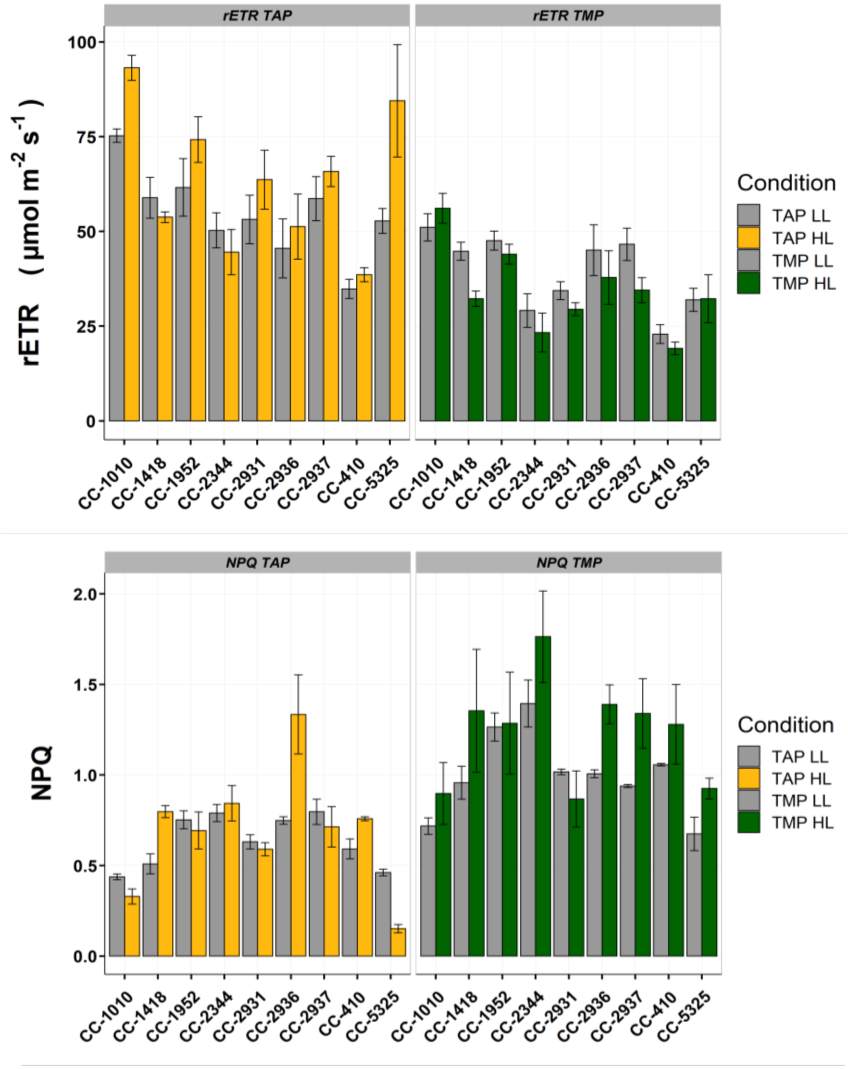

Figure 2. 12: Characterization of 9 Chlamydomonas wild-type strains by chlorophyll *a* variable fluorescence. Strains were grown for ~20 hours under 30µmol m^{-2} s^{-2} of continuous light (LL) and exposed for 4 hours to 300µmol m^{-2} s^{-2} (HL). (A) Relative electron-transport rate and (B) non-photochemical quenching upon exposure to 893 µmol of photons m^{-2} s^{-2}. Values ±SE, n=3.

strains (Fig. 2.12). In all conditions, CC-1010 displayed the highest rETR, being always significantly higher than CC-410 and CC-2344, which displayed always the lowest ($p<0.05$). Moreover, CC-410 consistently showed differences with CC-1418 and CC-2937. Under TAP-LL, CC-5325 was found to be different from CC-1010 and CC-410, and no additional difference was detected among the strains. More differences were detected under TMP-LL, where CC-5325 was different from other 3 strains (CC-1010, CC-1952, and CC-1418), CC-410 was different from CC-1952, CC-1010 was different from CC-2931, and CC-2344 was different from CC-2937.

The strains responded to the HL treatment with a variable trend. Among TAP samples, CC-1010 was the only one which presented significant variation in its rETR ($p<0.02$). CC-1010 was found to be different from all other strains, except CC-5325, which due to its high standard error (replicate a= 62.3 ; replicate b= 78.4 ; replicate c= 112.6) presents no differences with any other strain. Among TMP samples, significant variation in the rETR after HL was observed only for CC-1418 ($p<0.02$).

When the average NPQ in TAP (LL = 0.64 ± 0.04 SE ; HL = 0.69 ± 0.1 SE) was compared to the average value in TMP (LL = 1.0 ± 0.07 SE ; HL = 1.23 ± 0.09 SE), significant differences were observed both before ($p<0.002$) and after ($p=0.002$) HL (Sup. Figure 5). Within TAP samples, a differential response between LL and HL cultures was detected only during the first two light-steps of the saturation curve. A stronger response to the treatment was observed under autotrophic condition, with a significant increase in NPQ starting from the third light-step of the saturation curve. Interestingly, no significant difference was detected between TMP-LL and TMP-HL samples for the last light-step of the curve (893 µmol of photons m^{-2} s^{-2}), probably due to the high relative standard deviation (46%) within the 9 strains. Even if the HL treatment seemed not to affect the maximal NPQ capacity (Figure 2.12 - B), a HL-dependent change in fast-relaxing NPQ was observed for most of the strains (Figure 2.13). As previously observed in deep-well cultures, the laboratory strains (CC-1010 and CC-5325) presented a lower NPQ than most of the field isolates when cultured in presence of acetate. The results show that the difference is mainly linked to a differential regulation of the NPQ fast-relaxing components (qT and qE) under TAP-HL. Under this condition, CC-2936 was found significantly different only from CC-1010, CC-5325 and CC-1952, probably due to the high standard error between independent replicates (replicate a= 0.94 ; replicate b= 0.74 ; replicate c= 0.50).

The fast-relaxing NPQ was generally positive (except for CC-5325) in TMP-LL samples, pointing to a lower amount of qT in the dark, and to the presence of some qE even before the HL treatment. Variability among the strains was higher after HL, and only few of them showed significant similarities in terms of fast-relaxing NPQ (e.g., CC-2936 and CC-1952, or CC-410 and CC-1418). In this experimental setup, CC-2931 developed more fast-relaxing NPQ under mixotrophy than under autotrophy ($p<0.002$).

Overall, our dataset shows that significant phenotypic differences in response to light exist among *C. reinhardtii* wild-types, under both TAP and TMP conditions. Almost all strains were found to have a similar Fv/Fm, with exception of CC-5325 (Jonikas' wild-type) displaying a constitutively lower Fv/Fm when grown in presence of acetate. Main differences were observed at the level of the ETR and NPQ as function of the light intensity, suggesting that intraspecific differences may involve a differential regulation of the molecular players involved in linear and alternative electron-transport, as well as energy partitioning and dissipation.

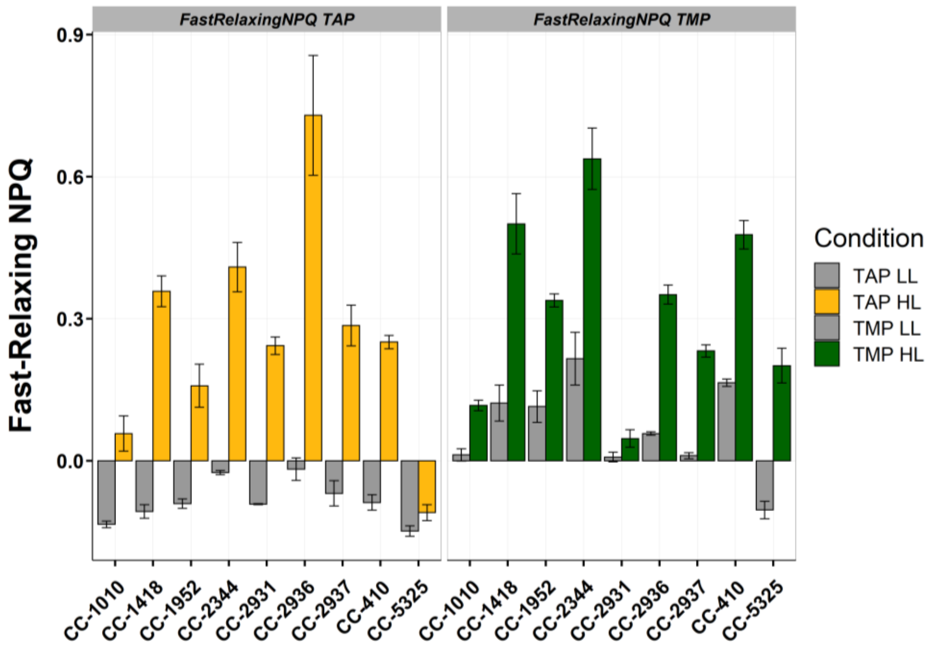

Figure 2. 13: Amount of NPQ relaxed after 10 minutes of dark. The last Fm measured under 893 µmol of photons m^{-2} s^{-2} was used as "Fm^t ", while the Fm value after 10 minutes of dark was used as "Fm". The fast-relaxing NPQ was calculated using the NPQ formula: $(Fm-Fm^t)/Fm^t$. Values ±SE, n=3.

2.2.3 Learning from intraspecific diversity: The wild-type strain CC-2936 as a model to study the interaction between low-CO_2 inducible pathways, ionic proton-motive force regulation and photosynthesis.

Differential pmf regulation between CC-2936 and CC-1010

The results produced so far suggest that different *C. reinhardtii* wild-types differ in the way they photosynthesize and photoprotect. The differences were particularly evident when comparing the laboratory strains to the field isolated strains under both growth conditions, after the HL treatment. The first question arising is: What is the nature of the observed differences? Acetate metabolism was previously observed (Fett and Coleman, 1994; Eriksson et al., 1998), and recently proved to boost the intracellular CO_2 levels, so inhibiting photoprotection- and CCM-related genes (Águila Ruiz-Sola et al., 2023). Instead under photoautotrophy, high-rates of photosynthesis create an intracellular CO_2 limitation that upregulates the low-CO_2 inducible genes. So, differences in NPQ and rETR between strains could be partially due to a differential regulation of their low-CO_2 inducible loci. Moreover, the activation of NPQ and CCM components, and the ETC redox-poising are all under the control of the proton-motive force. Therefore, a differential *pmf* regulation could also be involved in the phenotypic variation. To investigate the nature of the observed differences, the field isolated strain CC-2936 was chosen for a direct comparison with the laboratory strain CC-1010. CC-2936 was chosen among the other field isolates because: *i*) Its genome was found to be enriched in uncharacterized genes, absent in the laboratory lineage as well as other field isolates (Flowers et al., 2015). *ii*) CC-2936 presents an unusually high transposable elements copy-number (Sack et al., 1994; Flowers et al., 2015), *iii*) The strain displayed significant differences with respect to CC-1010, like the high NPQ and low rETR in presence of acetate. To obtain more information about the strains, a new experimental design was carried out. Precultured cells were diluted to the concentration of 8µg of Chl/mL into sterile flasks containing fresh TMP medium. Experimental cultures were kept in agitation under 470 µmol of photons m^{-2} s^{-1} (vHL) to stimulate the photo-oxidative stress response and the accumulation of the endogenous pH-sensing fluorescence-quenching LHCSR proteins. A control was kept in agitation under 30 µmol of photons m^{-2} s^{-1} (LL). Samples were harvested after 24 hours of vHL; a more stressing treatment if compared to the precedent experimental design. The same saturation curve was used to investigate the light-dependency of the electron-transport rate (rETR) and the kinetics of NPQ induction and relaxation (Figure 2.14-A). While no difference in rETR and NPQ was observed among LL samples (data not shown), significant phenotypic variation was observed on vHL-treated cells. Despite the similar Fv/Fm (data not shown), a 2-fold-change difference was observed when comparing the maximal rETR capacity of the two strains (Figure 2.14-E), suggesting that in CC-2936, the linear electron transport is subjected to some sort of limitation that results in the saturation of the ETC already at low-light intensities. In CC-1010, NPQ was poorly active under low-light, reaching only 10% of the maximal NPQ capacity (0.18 ± 0.05) by the end of the second light-step (50 µmol of p. m^{-2} s^{-1}) (Figure 2.14-B). A much higher NPQ value was observed for CC-2936, reaching 43% of its maximum NPQ (0.85 ± 0.08) ($p<0.00001$). A smaller difference ($p=0.03$) was observed during the last light-step (600 µmol of p. m^{-2} s^{-1}), where the maximum NPQ was higher in CC-2936 (2.07 ± 0.11) than CC-1010 (1.78 ± 0.07). Significant differences between the two strains were observed also in the speed of NPQ deactivation (Figure 2.14-C). Within the first 5 seconds of dark, CC-1010 relaxed 70% of its maximum NPQ, whereas the same relaxation extent was observed in CC-2936 after 2 minutes, resulting in the presence of higher NPQ in the dark. A similar slow NPQ relaxation was recently observed in *Arabidopsis thaliana* (Dukic et al., 2019) and *Phaeodactylum tricornutum* (Seydoux et al., 2022) mutants impaired in the chloroplastic H^+/K^+ antiporter KEA3; a regulator of the trans-thylakoid ΔpH. During the fluorescence measurement, aliquots of samples were harvested at minute 26 (last light-step) and minute 33 (after 5 minutes of dark) and plunged into liquid nitrogen. Their 77°K emission spectra were used to investigate the involvement of state transition (qT) in the slow-relaxing NPQ phenotype of CC-2936 (Figure 2.14-D). Samples exposed to 600 µmol of p. m^{-2} s^{-1} were closer to state 1 (majority of LHCIIs bound to PSII), and a small, but significant difference in the 685nm/715nm ratio was found between the strains ($p<0.05$; CC-1010 = 0.80±0.02 ; CC-2936 = 0.89±0.02). After 5 minutes of dark, an increase in the 685nm/715nm ratio was observed for both strains ($p<0.001$), suggesting a general trend of state transition toward state 2 (majority of LHCIIs bound to PSI). Nonetheless, a significantly higher ratio ($p=0.0001$) was observed for CC-1010 (1.29 ± 0.03) when compared to CC-2936 (1.01 ± 0.02).

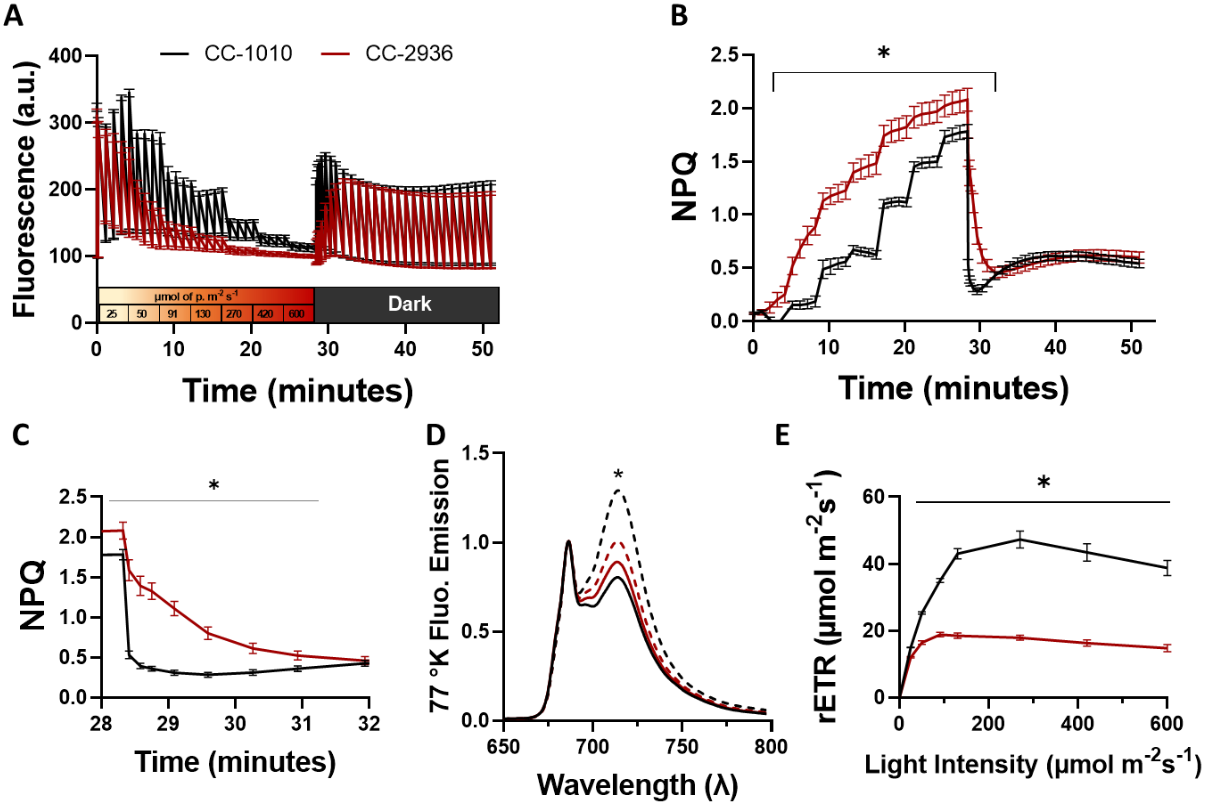

Figure 2. 14: Diversity between CC-1010 (black line) and CC-2936 (red line) wild-types. Fresh LL-growing cells were transferred under 470µM of photons m^{-2} s^{-1} in photoautotrophic condition for 24h, then assessed for their photosynthetic phenotype. **(A)** Changes in the in-vivo time-resolved chlorophyll *a* fluorescence emission were detected under fluctuating light-intensities and during vHL-to-dark transition. The strains show differences in their Fm dynamics during both phases of the measurement. **(B)** These differences are caused by a different kinetics of NPQ activation and deactivation. At the beginning of the dark phase, CC-2936 presents a slower Fm-relaxation, **(C)** due to the presence of dark NPQ. **(D)** 77°K fluorescence emission spectrum during the vHL (solid lines)-to-dark (dashed lines) transition. **(E)** Photosynthetic-induction curves describe differences in PSII relative Electron-Transport Rate (rETR) among the strains. rETR=(Fm-Fs/Fm)*light intensity. NPQ=(Fm-Fm'/Fm'). Error bars indicate SE ($n \geq 5$). * = $p < 0.05$.

The nigericin-resistant trans-thylakoid ΔpH phenotype of CC-2936

To get more insights about the slow NPQ relaxation detected in CC-2936, 24h-vHL grown cells were treated with the H^+/K^+ antiporter nigericin to the final concentration of 2.5µM, right before measuring PSII-fluorescence. Nigericin is a lipophilic molecule that quickly diffuses within lipid double layers. In the presence of a transmembrane K^+- and H^+-chemical gradient, the antiporter transports the ions through the membrane, and the ion transported downward its gradient drives the motion of the other against its gradient, until equilibrium is reached. Nigericin is commonly used in plants and green algae to dissipate the trans-thylakoid ΔpH component of the *pmf* upon illumination. A linear correlation between NPQ development and acidification of the chloroplast lumen was previously demonstrated (Briantais et al., 1980; Kanazawa and Kramer, 2002). Therefore, the impact of nigericin on the luminal pH can be followed through the measurement of NPQ. In CC-1010, the effect of nigericin was consistent with what observed on other *C. reinhardtii* laboratory strains in previous reports (Allorent et al., 2016). During the saturation curve, nigericin-treated samples presented higher levels of Fm^t (Figure 2.15-A/B) due to the deactivation of the pH-triggered NPQ component (qE) (Figure 2.15-C/H). Moreover, the treatment led to a significant decrease in rETR (Figure 2.15-E), mainly attributable to a shortage of ATP to support high-rates of carbon fixation. The absence of qE resulted in the oversaturation of the electron-transport chain and PSII-photodamage during the last light-steps of the curve (Figure 2.15-G). A different response to the treatment was observed in CC-2936, where nigericin was unable to prevent the formation of the light-driven ΔpH, resulting in the regular quenching of the Fm (Figure 2.15-A/B) due to the presence of qE (Figure 2.15-C/H). Despite the ineffectiveness of nigericin on CC-2936's qE, a significant increase in the speed of NPQ relaxation was observed. At the end of the saturation curve, treated CC-2936 samples relaxed 84% of the maximum NPQ in just 10 seconds. This evidence suggests that nigericin was able to diffuse within CC-2936's cells and contribute to the dissipation of the ΔpH only in the dark. The treatment did not induce changes in CC-2936's rETR (Figure 2.15-E), suggesting that in this strain, LEF is not limited by the intracellular levels of ATP, and that the activation of the NPQ in presence of nigericin is efficiently preventing CC-2936 from PSII photodamage (Figure 2.15-G). The 77°K fluorescence emission spectrum was measured as already explained above (Figure 2.15-I). Samples exposed to 600 µmol of p. m^{-2} s^{-1} displayed a predominant emission pick from PSII, indicating that the majority of the LHCIIs was bound to the PSII-reaction centers (state 1) in both strains. The presence of nigericin caused a significant ($p<0.05$) decrease in the 715nm/685nm ratio, suggesting that the treatment promoted state 1. Despite the differences observed on light-exposed samples, the presence of nigericin did not alter CC-2936's qT in the dark.

To retrieve direct information about the light-driven thylakoid-membrane electric potential (ΔΨ) formation and decay, samples were diluted to the concentration of 8µg of Chl/mL in a solution of TMP + 10% ficoll and changes in their electrochromic shift (ECS) signal were detected as explained in the section "materials and methods". No difference in their steady-state ECS was detected under control conditions (Figure 2.15-E), whereas nigericin addition caused a significant ECS drop in CC-1010 under high-light ($p<0.01$). An opposite trend was observed in CC-2936 where the nigericin treatment induced higher ECS at low light intensities ($p<0.05$) while no change was detected under high-light. The ATPase conductivity to protons (gH+) was estimated for each light intensity by fitting the ECS relaxation during the first 300ms of dark with an exponential decay. While nigericin treatment caused a significant reduction of this parameter in cells grown under LL (data not shown), no significant differences in gH+ were observed in both control and nigericin-treated vHL-samples (Figure 2.15-F).

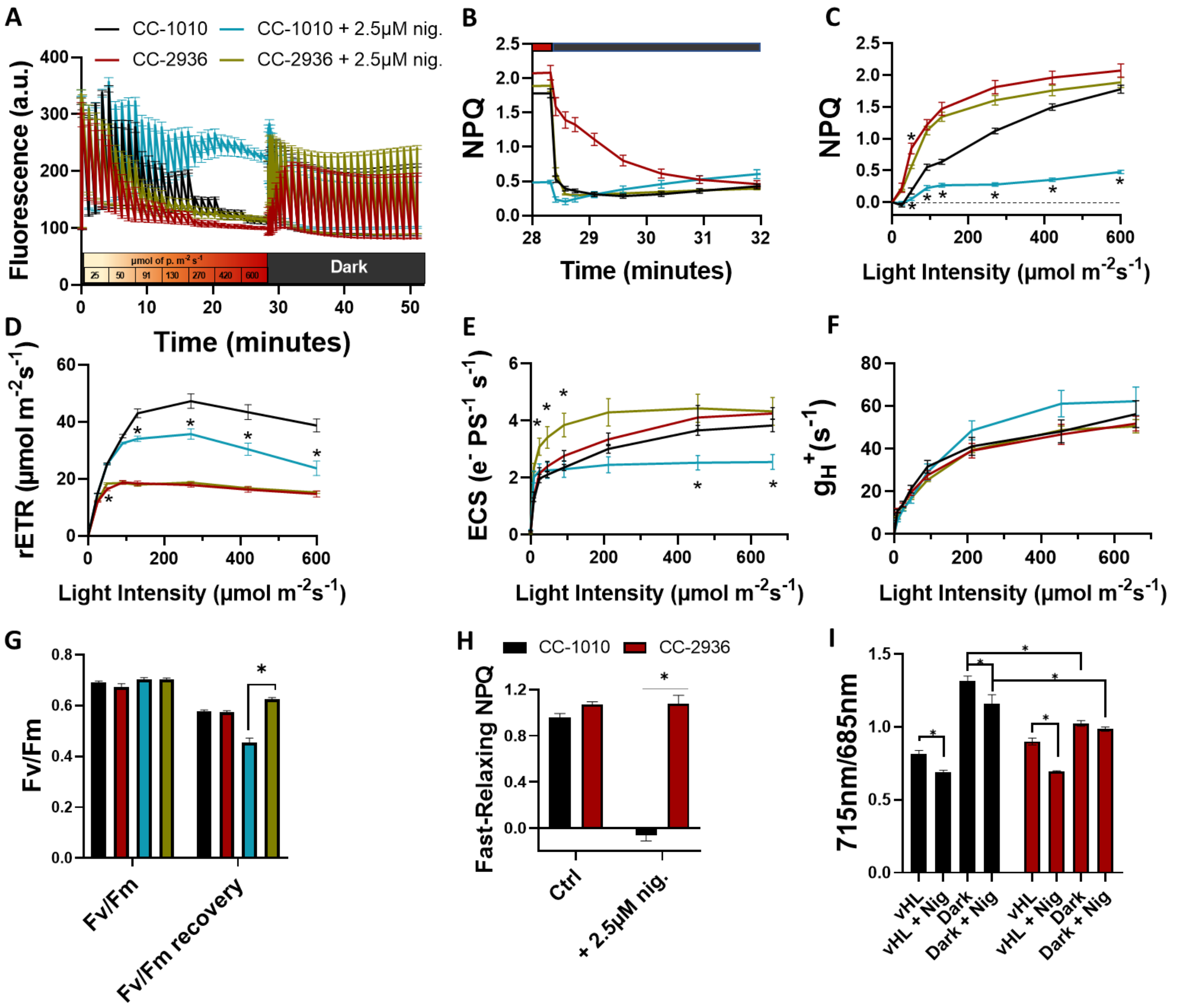

Figure 2. 15: Effect of nigericin on CC-1010 and CC-2936. Short prior to fluorescence detection, samples were treated with nigericin (nig) to the final concentration of 2.5 µM. **(A)** The protocol used to monitor changes in PSII-variable fluorescence was composed of 7 light-steps of 4 minutes each, plus 23 minutes of dark. **(B)** Significant differences were observed in the NPQ relaxation kinetics and **(C)** its induction as function of the light intensity. In the presence of the uncoupler, **(D)** CC-1010's rETR is significantly reduced, while CC-2936's remains stable. **(E)** The steady-state ECS was detected after 3 seconds of illumination at each light-intensity. The treatment induced significant differences in both strains, with a different trend. **(F)** No difference was detected in the conductivity of the ATPase. **(G)** Fv/Fm before and after the saturation curve. **(H)** Amount of NPQ relaxed within the first 10 minutes of dark. **(I)** Ratio of the 77°K fluorescence emission bands from PSI (715nm) and PSII (685nm). Error bars indicate SE ($n \geq 3$). * = $p < 0.05$.

It is reported in literature that the combination of an electrical K^+-uniporter and nigericin induces a net uniport for H^+, whereas K^+ cycles across the membrane (Nicholls and Ferguson, 1992). To improve our understanding about the nigericin-related CC-2936's phenotype, we combined nigericin with the two K^+-uniporters: nonactin and valinomycin. Moreover, following the recent discovery of bestrophin-like transporters importing bicarbonate into the thylakoids lumen (Mukherjee et al., 2019) while consuming *pmf* (Burlacot et al., 2022),we decided to include the condition "bicarbonate + nigericin" to check if the entry of the negative bicarbonate ions into the lumen could neutralize the ΔpH and lead to NPQ inhibition in CC-2936. However, combining nigericin with saturating concentrations of nonactin or valinomycin had no effect on NPQ(Figure 2.16-A). The data highlights a different trend for bicarbonate supplementation, that caused a significant reduction in CC-2936's fast-relaxing NPQ and an increase in its rETR (Figure 2.16-B) as compared to CC-1010.

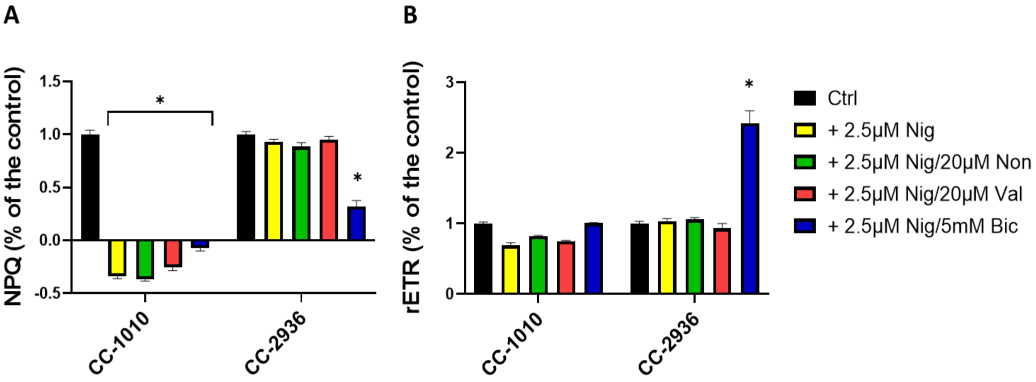

Figure 2. 16: Effect of nigericin (nig) and other K^+ ionophores or bicarbonate on NPQ and rETR. To better understand CC-2936's nigericin-insensitive lumen acidification, 24h-vHL-acclimated samples were treated with nigericin in combination with two other electrical K+ uniporters (nonactin = non ; valinomycin = val) or with bicarbonate (bic). (A) Impact of the treatments on the fast-relaxing NPQ (relaxed in the first 10 minutes of dark). Only bicarbonate-supplemented samples displayed a significant NPQ inhibition in CC-2936. (B) Moreover, a two-foldchange increase in rETR was observed under the same condition. Values were normalized on the Ctrl's average for each strain. * = $p < 0.05$ (n=4, except Val = 2).

Impaired Carbon-Concentrating Mechanism and link between CCM, pmf and nigericin-resistance in CC-2936

For a better interpretation of our previous results, we assessed the impact of different concentrations of bicarbonate on photosynthesis and photoprotection. Cells were grown under TMP-vHL for 24h and treated with sodium-bicarbonate right before measuring PSII-variable fluorescence. The strains responded to the treatment with a similar trend, as higher concentrations of exogenous bicarbonate ($\geq$1mM) increased rETR in all samples, with CC-1010 reaching a 1.3 FC increase ($p<0.05$) and CC-2936 reaching a 3.1 FC increase ($p<0.02$) as compared to their controls (Figure 2.17-A/B). Lower concentrations of bicarbonate (<1mM) significantly boosted rETR in both strains during the first three light-steps of the PI curve ($p<0.05$). Despite this initial increase, a down-regulation in CC-1010's electron-transport rate was observed before the end of the saturation curve, reaching 0.7 FC of the control at the last light-step in presence of 0.25mM bicarbonate ($p<0.001$). No negative effects were detected in CC-2936, where the smallest concentration of bicarbonate significantly increased its rETR at every light-step ($0.01<p<0.03$) except for the last two light-intensities ($p=0.07$; $p=0.6$).

As for the rETR, the effect of bicarbonate on NPQ was dependent on its concentration (Figure 2.17-C/D). Low concentrations of bicarbonate (<1mM) had no impact on the maximum NPQ, as confirmed by the estimation of the portion of fast-relaxing NPQ (Figure 2.17-E), but a significant decrease in NPQ was observed on both strains during the first light-steps of the saturation curve. On the other hand, 1mM bicarbonate significantly decreased the maximum NPQ in CC-1010 (0.8 FC ; $p<0.005$) whereas CC-2936 was unaffected ($p>0.1$), and 10mM bicarbonate negatively impacted NPQ in both CC-1010 (0.48 FC ; $p=0.001$) and CC-2936 (0.73 FC ; $P<0.01$), with the latter being significantly less impacted ($p<0.03$) (Figure 2.17-E).

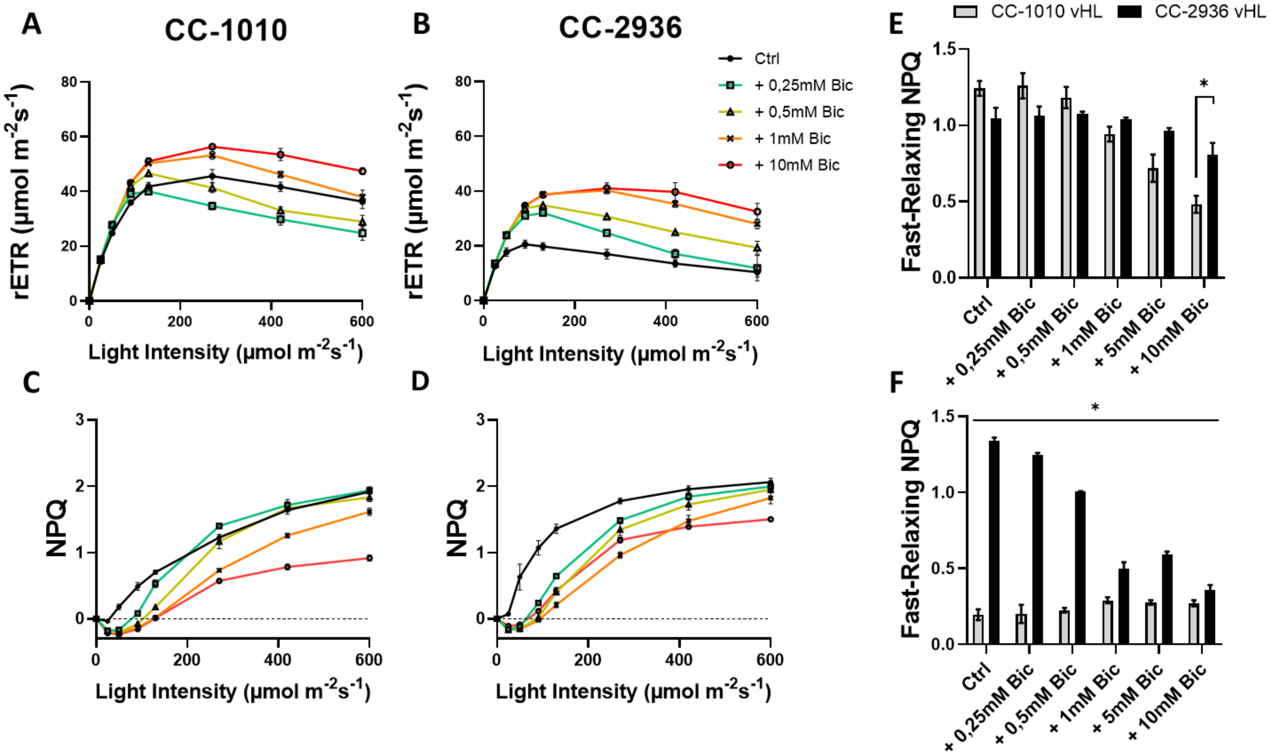

Figure 2. 17: Impact of different concentrations of sodium-bicarbonate on **(A-B)** the relative electron transport rate (rETR), **(C-D)** non-photochemical quenching (NPQ), and fast relaxing NPQ. The latter, in **(E)** absence or **(F)** presence of 2.5µM nigericin. Values ± SE. * = $p<0.05$ (n=3, except figure F where n = 2)

During the experiment presented in Figure 2.16, the combined effect of nigericin and bicarbonate induced a 60% decrease in CC-2936's fast-relaxing NPQ. To investigate the possible synergic effect of the two compounds, we included an additional set of samples treated with 2.5µM nigericin and supplemented with several concentrations of sodium-bicarbonate (Figure 2.17-F). In line with our previous observations, nigericin-treated CC-1010 displayed a significant reduction in fast-relaxing NPQ ($p<0.02$), and no statistical difference in this parameter was found between samples treated with 10mM bicarbonate, 2.5µM nigericin, or the combination of the two. On the other hand, a synergic effect of the two treatments was observed in CC-2936, as samples treated with nigericin or 1mM bicarbonate did not present any significant NPQ inhibition, whereas the combination of the two treatments yielded a 54% decrease in CC-2936's fast relaxing NPQ. An impact of bicarbonate supplementation was observable also on CC-1010's NPQ-relaxation kinetics for which speed was significantly decreased ($p \leq 0.03$) during the first minute of dark (Figure 2.18). Such effect was visible for every of the tested bicarbonate concentrations, and it was not observed on nigericin-treated samples.

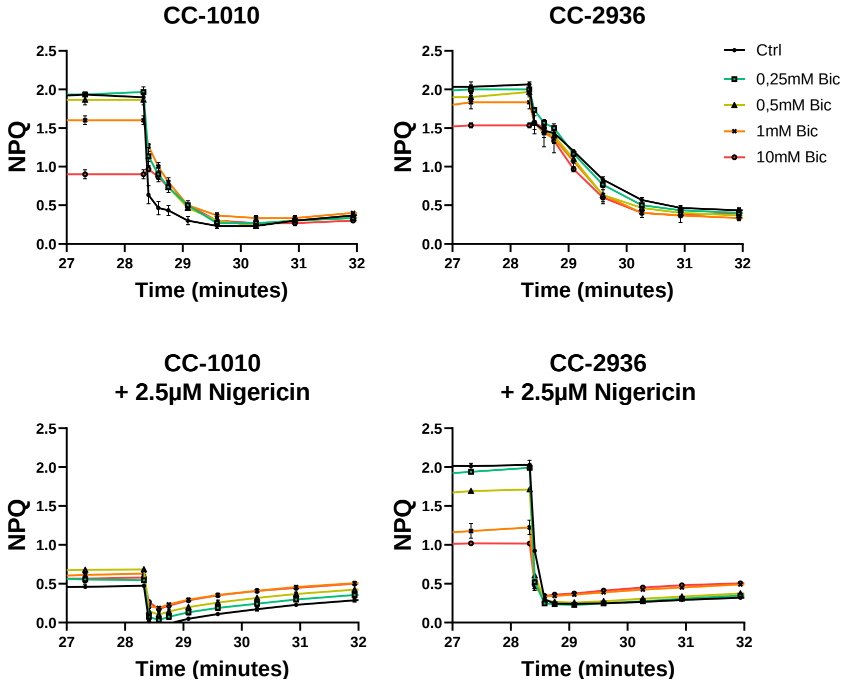

Figure 2. 18: Impact of different concentrations of sodium-bicarbonate (Bic) on the non-photochemical quenching (NPQ) relaxation kinetics in absence or presence of 2.5µM nigericin. Values ± SE. (n=3)

Differential regulation of low-CO_2-inducible transcripts and proteins between the strains

The previous results suggest that, while CC-1010's photosynthetic activity is mainly limited by other factors than CO_2, in our standard growing conditions, CC-2936 is starving of inorganic C_i. As introduced before, *C. reinhardtii* relies on the carbon-concentrating mechanism's activity to optimize its C_i-management. The results demonstrate that CC-2936 can take up exogenous bicarbonate from the growth medium, transport it from the plasma-membrane to the pyrenoid, and convert it into CO_2 boosting the CBB cycle. Nonetheless, once there is no more dissolved C_i, the strain seems unable to optimize the use of metabolism-derived CO_2, recycling it into endogenous bicarbonate. To gain insights into the regulation of the low-CO_2-inducible metabolism among the two strains, cells were grown on TMP-LL (30 µmol of p. m^{-2} s^{-1}) for 24h, and samples were harvested (LL samples) to assess the basal level of target low-CO_2-inducible transcripts and proteins. Following, cultures were exposed to 470 µmol of photons m^{-2} s^{-1}(vHL) for 1 hour, and new samples were harvested after 1h (for transcripts analysis) and 4h (for protein analysis). The analysis revealed the presence of low-CO_2 inducible mRNAs even in LL-samples, suggesting that TMP cultures were already lightly stressed by the absence of any organic or inorganic C_i supplementation. Under TMP-LL condition, significant differences between strains were detected only for Low-CO_2-Inducible A (LCIA) and Carbonic Anhydrase 1 (CAH1), both components of the CCM (Figure 2.19-A). After exposure to vHL, a stronger transcriptional induction was observed in CC-2936 for all the assessed genes, except LCI1. The same pattern was observed at the protein level (Figure 2.19-B) for the NPQ effectors, as the densitometric analysis revealed significant differences in the accumulation of LHCSR3, (p=0.02), LHCSR1 (p<0.0005), and PSBS (p<0.0001). No difference was observed for the mitochondrial carbonic anhydrases (CAH4/5). CC-2936 shows a higher amount of several low-CO_2 inducible transcripts and proteins, confirming that the strain is experiencing a stronger CO_2 limitation

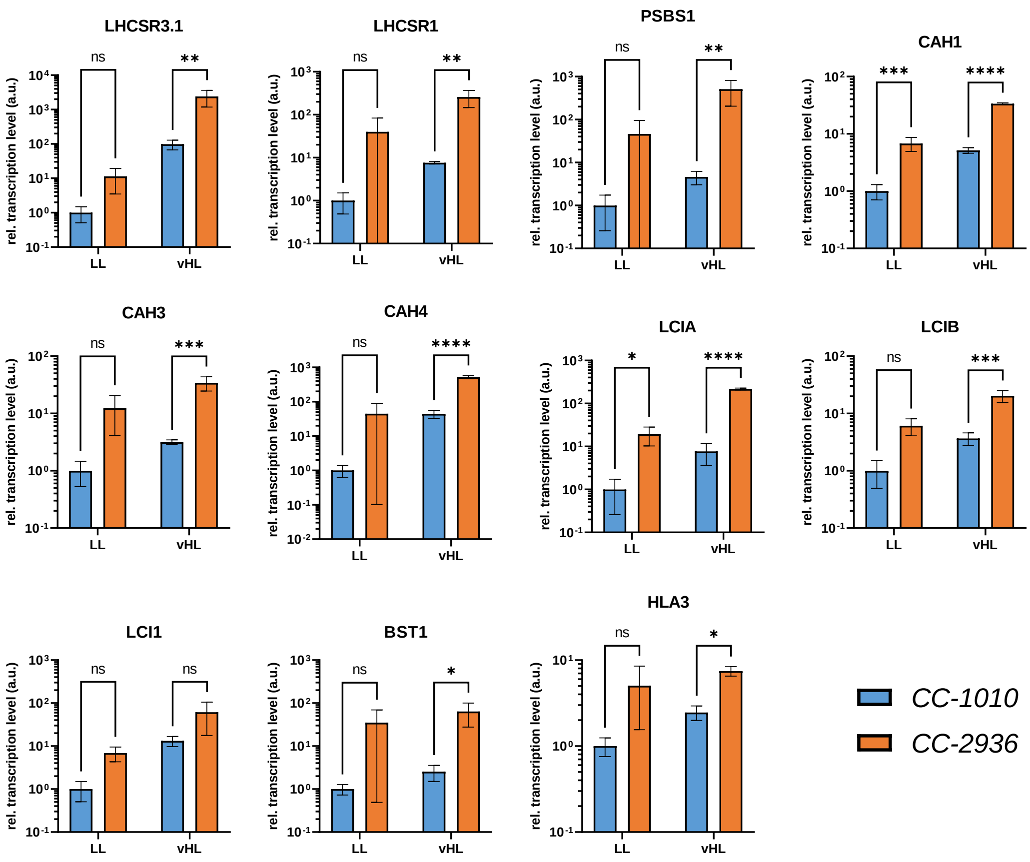

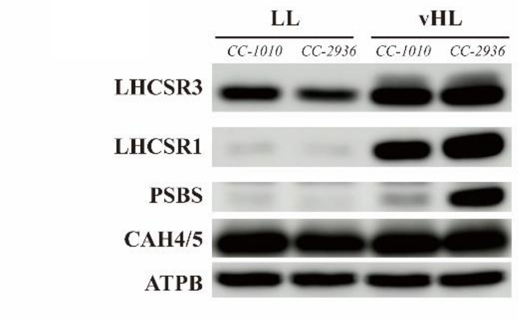

Figure 2. 19: Accumulation of low-CO2 inducible transcripts and proteins. Cells were cultured under TMP-LL for 24h, thus exposed to vHL for 4h. Samples were taken before the vHL treatment, after 1h (figure A) and after 4h (figure B) of vHL. (A) mRNA levels of several low-CO_2 responsive genes (NPQ and CCM) assessed by RT-qPCR.

Statistical significance was computed through ANOVA Dunnett's multiple comparisons test (*, $p < 0.05$, **, $p < 0.01$; ***, $p < 0.001$; ****, $p < 0.0001$; ns, not significant), n = 3, mean ± SD. (B) Immunoblot analysis of LHCSR3, LHCSR1, PSBS and ATPB (loading control). Analysis performed by Yizhong Yuan (CEA-than CC-1010. Such CO_2 shortage could be easily explained by the low-capacity of CC-2936 to produce endogenous bicarbonate, resulting in the passive diffusion of metabolic CO_2 outside of the cell. Nonetheless, the biological reason for the bicarbonate shortage remains unclear and other hypothesis cannot be excluded. It is important to remember that CC-2936 is not a product of artificial mutagenesis, the strain is a field isolate from Quebec, and its metabolism has evolved to cope with whatever limitation imposed by the natural environment. Laboratory strains artificially impaired in CCM activity have been reported to poorly grow under low-CO_2 (Karlsson et al., 1998; Yamano et al., 2010; Machingura et al., 2017; Rai et al., 2021). To investigate the presence of differences between CC-2936 and CC-1010, their growth on TMP was monitored under LL (50 µmol of photons m^{-2} s^{-1}), vHL (600 µmol of photons m^{-2} s^{-1}), and vHL-0.15% CO_2 (low-CO_2) for several days. No difference in the overall population's stationary phase density was detected between the strains under any of the conditions when grown on minimal medium (Figure 2.20). Nonetheless under TMP-LL, CC-1010 reached ½ of its stationary phase density 1.16 times faster than CC-2936 ($p=0.014$), while in TMP-vHL, CC-2936 reached ½ of its stationary phase density 1.24 times faster than CC-1010 ($p=0.027$). When we reproduced the same experiment in presence of 20mM acetate (Sup. Figure 7), differences between the strains were observed under both LL and vHL condition. Despite of the similar stationary phase density among TAP-LL samples, CC-1010 reached ½ of it 1.14 times faster than CC-2936 ($p=0.025$). Moreover, a drastic decrease in CC-2936's stationary phase density was observed in cultures exposed to TAP-vHL ($p<0.0001$).

In CC-2936, a link was observed between bicarbonate limitation, different NPQ-activation kinetics, and nigericin-resistant ΔpH. Despite its penetration into the cell, the incapacity of nigericin to dissipate CC-2936's trans-thylakoid ΔpH indicates that some physico-chemical proprieties of the system disfavor nigericin's H^+/K^+ antiporting activity. Upon light exposure, both CC-1010 and CC-2936 develop a trans-thylakoid H^+-gradient, from the stroma to the lumen, linked to their photosynthetic activity. Thus, we hypothesize that the limiting factor for nigericin to work in CC-2936 is a different distribution of K^+ ions across the thylakoid membranes. A piece of evidence supporting this hypothesis comes from the slow NPQ relaxation kinetics observed in this strain. As explained before, a similar phenotype was observed in *A. thaliana* (Dukic et al., 2019) and *P. tricornutum* (Seydoux et al., 2022) mutants impaired in the pmf-regulating H^+/K^+-antiporter KEA3. As a matter of fact, treating the samples with the H^+/K^+-antiporter nigericin substantially increased the NPQ-relaxation kinetics in CC-2936. Protein phylogenetic analyses showed that all plants, from unicellular algae to flowering plants, have three types of KEAs classified as clades Ia, Ib, and II. Green algae, like *C. reinhardtii* and *V. carteri*, contain only one gene in each group (Chanroj et al., 2012). AtKEA3 belongs to the subtype Ib, and the *C. reinhardtii* homologous

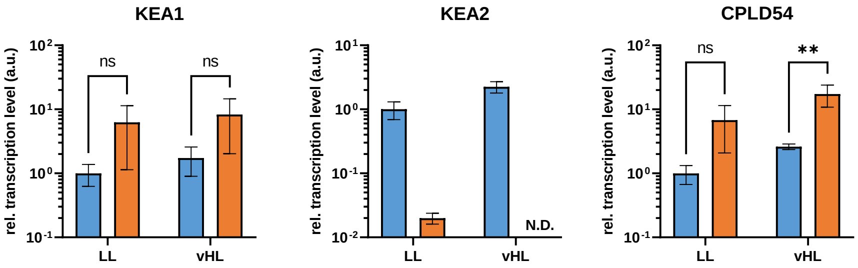

Figure 2. 20: mRNA levels of the KEAs genes before and after 1h of vHL (470 µmol of p. m^{-2} s^{-1}) treatment in CC-1010 (blue bars) and CC-2936 (red bars). Statistical significance was computed through 2-way ANOVA Dunnett's multiple comparisons test (*, $p < 0.05$, **, $p < 0.01$; ***, $p < 0.001$; ****, $p < 0.0001$; ns, not significant; N.D., not detected), $n = 3$, mean ± SD. Analysis performed by Yizhong Yuan (CEA-Grenoble).

Cre16.g687450 (or CPLD54) was found to localize in the thylakoid membranes. In the pioneering work of (Mackinder et al., 2017), CPLD54 was found to interact with the bestrophin-like transporters (BST1-3), previously named low-CO_2 inducible 11 (LCI11) in (Fang et al., 2012). Interestingly, BSTs were found to interact also with the LCIB/LCIC complex, responsible for the conversion of CO_2 into bicarbonate within the stroma (Mackinder et al., 2017). The interaction between KEA3 and a bestrophin-like transporter fits our hypothesis as a simple explanation to the co-operative effect observed between the exogenous bicarbonate supplementation and the nigericin treatment on CC-2936's ΔpH. AtKEA1 and AtKEA2 were identified as chloroplast inner envelop proteins and showed to be essential for chloroplasts osmoregulation in plants (Kunz et al., 2014). Since the function of KEAs in the regulation of the *pmf* is conserved across algae and plants, we compared the mRNA levels of the three KEA genes in CC-1010 and CC-2936, looking for candidates that could explain a different K^+ diffusion across chloroplastic compartments between the strains. Under TMP-vHL condition, significant differences were found between strains for two out of three genes (Figure 2.21), with KEA2 being undetected on all CC-2936's biological replicates, and CPLD54 (KEA3) being significantly more transcribed than in CC-1010 ($p<0.01$).

Proteome-wide changes between CC-2936 and CC-1010

Despite the wide phenotypic diversity between the lab strain CC-1010 and the natural isolate CC-2936, their similar growth capacity under minimal (TMP) condition is one of the intriguing findings of this work. Even if CC-2936's rETR was observed to drastically increase upon bicarbonate supplementation, the strain still thrives under control condition, fulfilling the metabolic requirements imposed by a WT-like growth rate. To gain a broader understanding of the physiological differences occurring between CC-1010 and CC-2936, fresh LL-TMP acclimated cells were exposed to HL (300µmol of photons m^{-2} s^{-1}) for 24h. The harvested pellets were frozen in liquid nitrogen and sent to a proteomic platform to be analyzed by *label-free* shotgun proteomics.

The analysis identified a total of 2034 protein groups across all samples (3 biological replicates), of which 26 were marked as "reverse" or "contaminant" and therefore excluded from further bioinformatic analyses. The protein sequences of the remaining proteins were blasted against the protein database created based on the proteome of the most recent *C. reinhardtii* genome release (Craig et al., 2022).

Hits with coverage and identity > 50% and e-value < 10E-5 were retained for differential expression analysis with the use of DEqMS (Zhu et al., 2020) and DEP (Zhang et al., 2018) packages from Bioconductor. The former package takes into account the variance in the number of peptides detected for each protein group and requires samples with less than two replicates to be excluded from the analysis (Figure 2.22). On the other hand, DEP does not take the variance in peptides number into account and uses imputation to estimate the putative intensity of missing replicates, inferring significance for those proteins detected only in 1 out of 3 biological replicates. The two packages together identified a total of 418 differentially expressed proteins (~20% of the dataset) of which 60 were uniquely identified by DEP, 298 were uniquely identified by DEqMS, and 65 were commonly identified by both analyses (Sup. Table 1).

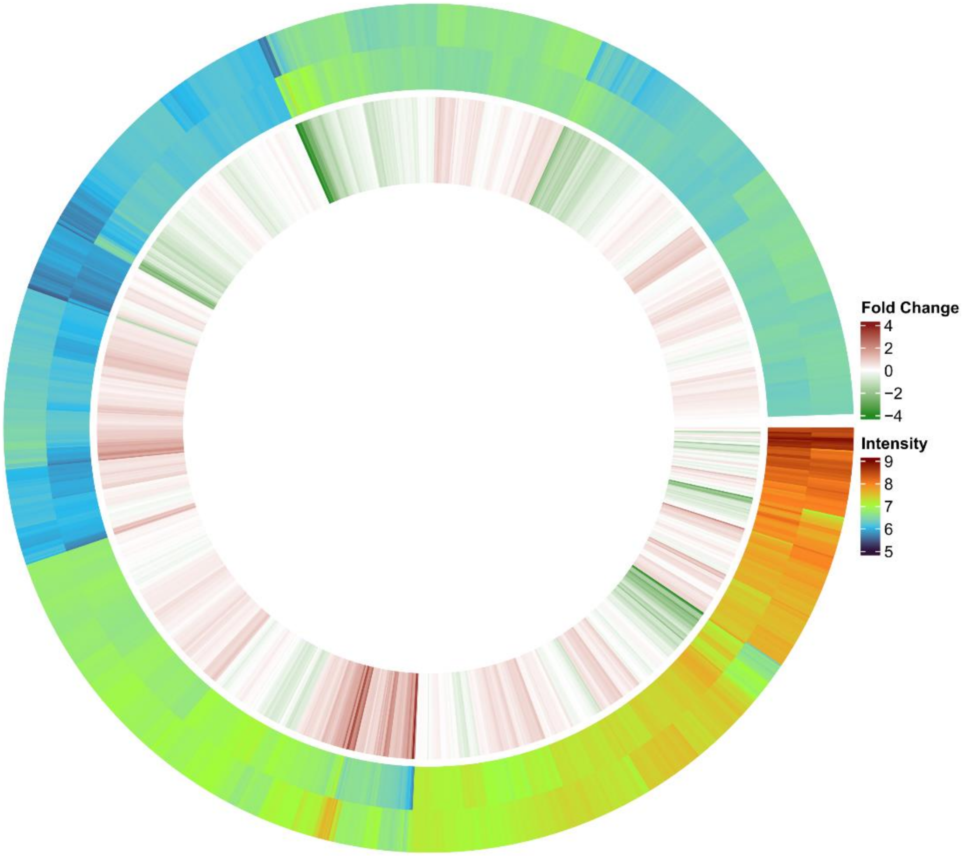

Figure 2. 21: Visualization of the *label-free* shotgun proteomics dataset. Proteins with less than 2 values for each group were filtered out resulting in a remaining total of 1494 protein-intensities. From the outer to the inner ring: *i*) log10 average intensities from CC-1010, *ii*) log10 average intensities from CC-2936, *iii*) log10 fold-change calculated as CC-1010/CC-2936.

A rough overview of DE-proteins localization was obtained using the PredAlgo annotations (Tardif et al., 2012) released with the new *C. reinhardtii* genome assembly (v.6). Considering all proteins found to be significantly more abundant in one strain over the other, we split the DE dataset into two subsets and sorted them based on PredAlgo localization predictions. High diversity was observed between the two subsets (Figure 2.23), with CC-2936 presenting a higher fraction of chloroplast-predicted overexpressed proteins (~54%) than CC-1010 (~27%), while the latter showed a higher density of mitochondrion-predicted proteins as well as proteins from other compartments.

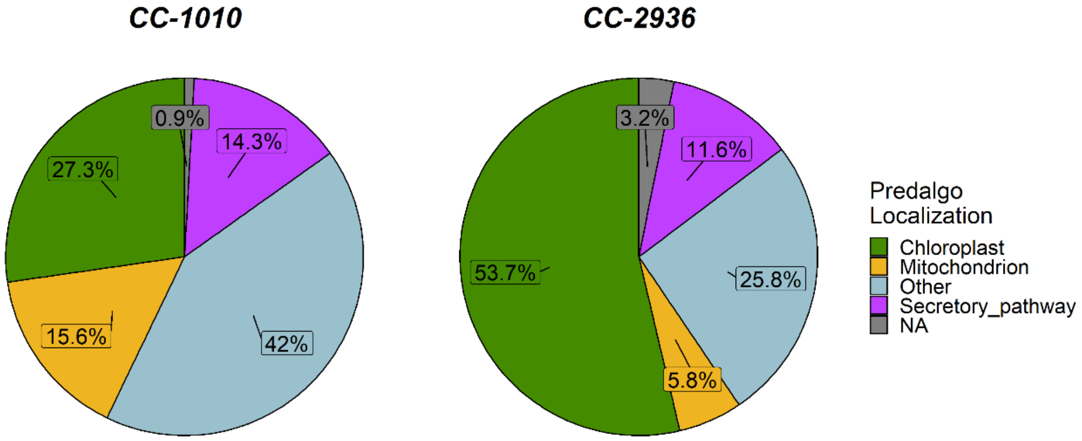

Figure 2. 22: PredAlgo prediction of significantly DE-proteins' intracellular localization, 231 proteins for CC-1010 and 190 proteins for CC-2936. The "NA" fraction includes DE proteins lacking a PredAlgo annotation.

To define what metabolic pathways were significantly represented within the two DE-protein subsets, we use the Gene Ontology (GO) terms (The Gene Ontology Consortium, 2008) associated with DEqMS-identified proteins to perform a pathway-enrichment analysis using GeneMerge software (Castillo-Davis and Hartl, 2003). Significant proteins were selected based on p-value corrected by Benjamini-Hochberg method (False Discover Rate = 5%) and with a fold change ≥ 2. Among 363 DE-proteins, 114 presented no association with any GO term and were therefore no further analyzed. The results revealed a variety of overrepresented processes for both strains (Table 3). CC-1010's DE protein-fraction included several GO terms associated with response to stress (look at GO:0045454 ; GO:0006979 ; GO:0006950 ; GO:0006457), carbohydrates metabolism (GO:0006520 ; GO:0005975), and primary heterotrophic metabolism (GO:0008152 ; GO:0006099). On the other hand, CC-2936's DE protein-fraction was found to be enriched in photosynthetic proteins (GO:0015979 ; GO:0009765 ; GO:0033014), fatty acids (FAs) biosynthetic enzymes (GO:0006633), and chaperones (GO:0006457 ; GO:0000413).

Table 3: List of significantly (FDR ≤ 5%) overrepresented biological processes within CC-1010 (light blue) and CC-2936 (light

Strain	GO Term	Description	Contributing Genes
🟦	GO:0006520	amino acid metabolic process	Cre12.g489700; Cre09.g387726;
	GO:0009058	biosynthetic process	Cre03.g175250; Cre09.g387726; Cre10.g451950;
	GO:0005975	carbohydrate metabolic process	Cre11.g476650; Cre03.g185550; Cre01.g032650; Cre16.g677450;
	GO:0045454	cell redox homeostasis	Cre09.g391900; Cre06.g271200; Cre02.g142351; Cre01.g033550; Cre07.g328150; Cre12.g517150; Cre02.g088200; Cre12.g496700;
	GO:0006094	gluconeogenesis	Cre07.g338451; Cre02.g141400;
	GO:0008152	metabolic process	Cre17.g699000; Cre12.g507400; Cre06.g295450; Cre02.g088600; Cre01.g071662; Cre07.g343700; Cre12.g537200; Cre09.g396650; Cre16.g675650; Cre12.g517150; Cre07.g353450;
	GO:0006796	phosphate-containing compound metabolic process	Cre09.g387875; Cre10.g424100;
	GO:0006457	protein folding	Cre01.g038400; Cre02.g080650; Cre03.g178450;
	GO:0006508	proteolysis	Cre04.g226850; Cre17.g734900; Cre17.g746597; Cre06.g279400; Cre09.g407700; Cre01.g007700; Cre05.g241650; Cre08.g358522;
	GO:0006979	response to oxidative stress	Cre09.g417150; Cre02.g087700;
	GO:0006950	response to stress	Cre12.g542350; Cre02.g080650;
	GO:0006412	translation	Cre14.g621450; Cre12.g504200; Cre06.g308250; Cre17.g701200; Cre13.g573351; Cre09.g388200; Cre06.g290950; Cre06.g289550; Cre06.g272800; Cre10.g459250; Cre02.g106600; Cre05.g234637; Cre02.g091100; Cre10.g432800; Cre08.g358556;
	GO:0006099	tricarboxylic acid cycle	Cre03.g171950; Cre12.g537200;
🟩	GO:0006633	fatty acid biosynthetic process	Cre04.g216950; Cre12.g519100;
	GO:0015979	photosynthesis	CreCp.g802312; Cre12.g510050; Cre03.g198850; Cre09.g396213; Cre06.g261000; Cre08.g372450; Cre02.g082500;

	GO:0009765	photosynthesis, light harvesting	Cre01.g066917; Cre08.g365900; Cre17.g720250;
	GO:0006457	protein folding	Cre08.g358562; Cre12.g505850;
	GO:0000413	protein peptidyl-prolyl isomerization	Cre12.g561000; Cre01.g002300;
	GO:0033014	tetrapyrrole biosynthetic process	Cre09.g409100; Cre16.g663900;
	GO:0006414	translational elongation	CreCp.g802267; Cre12.g519180;

During the analysis we observed that, due to incomplete GO term annotation, some relevant IDs were not recognized as contributing elements to their main pathway. For instance, the enzyme isocitrate dehydrogenase 3 (IDH3 ; PNW83946.1 ; Cre04.g214500), significantly more accumulated in CC-1010, is not associated with the term GO:0006099 (TCA cycle) (Phytozome, *C. reinhardtii* CC-4532 v6.1). As a result, the protein contributed to the enrichment of GO:0016616 and GO:0055114 (see Sup. Table 2), but not to its main pathway. Therefore, a complemented view of the overrepresented pathways was obtained using KEGG (Kyoto Encyclopedia of Gene and Genomes) Orthology (KO) terms (Kanehisa et al., 2016) associated with DE proteins. Also in this case, only 216 out of 363 DE proteins included a KO annotation, thus many DE proteins were lost during the analysis. Nonetheless, through this approach we observed that almost all key enzymes of TCA cycle are more accumulated in CC-1010 (Figure 2. 24). Despite the absence of exogenous acetate in the medium, phosphate acetyltransferase 1 and 2 (PAT1-2) were also found to be 1.5- and 4.5-fold-change more abundant in CC-1010. Other upregulated enzymes involved in acetate and pyruvate metabolism were found to be DE in CC-1010. Some examples are: acetyl-CoA synthetase/ligase 1 (7-fold-change) and 3 (8-fold-change), the family 6 aldehyde dehydrogenase (3.5-fold-change), pyruvate decarboxylase 3 (3.2-fold-change), malate dehydrogenase 1 (2.7-fold-change), and fumarate hydratase 1 (1.5-fold-change). Interestingly, these proteins belong to the fermentative network of *C. reinhardtii* and are generally up-regulated under hypoxic and anoxic stress (Gfeller and Gibbs, 1984; Banti et al., 2013; Yang et al., 2014).

Moreover, the glyoxylate cycle's enzymes (Plancke et al., 2014) isocitrate lyase (ICL1, 9.4-fold-change),

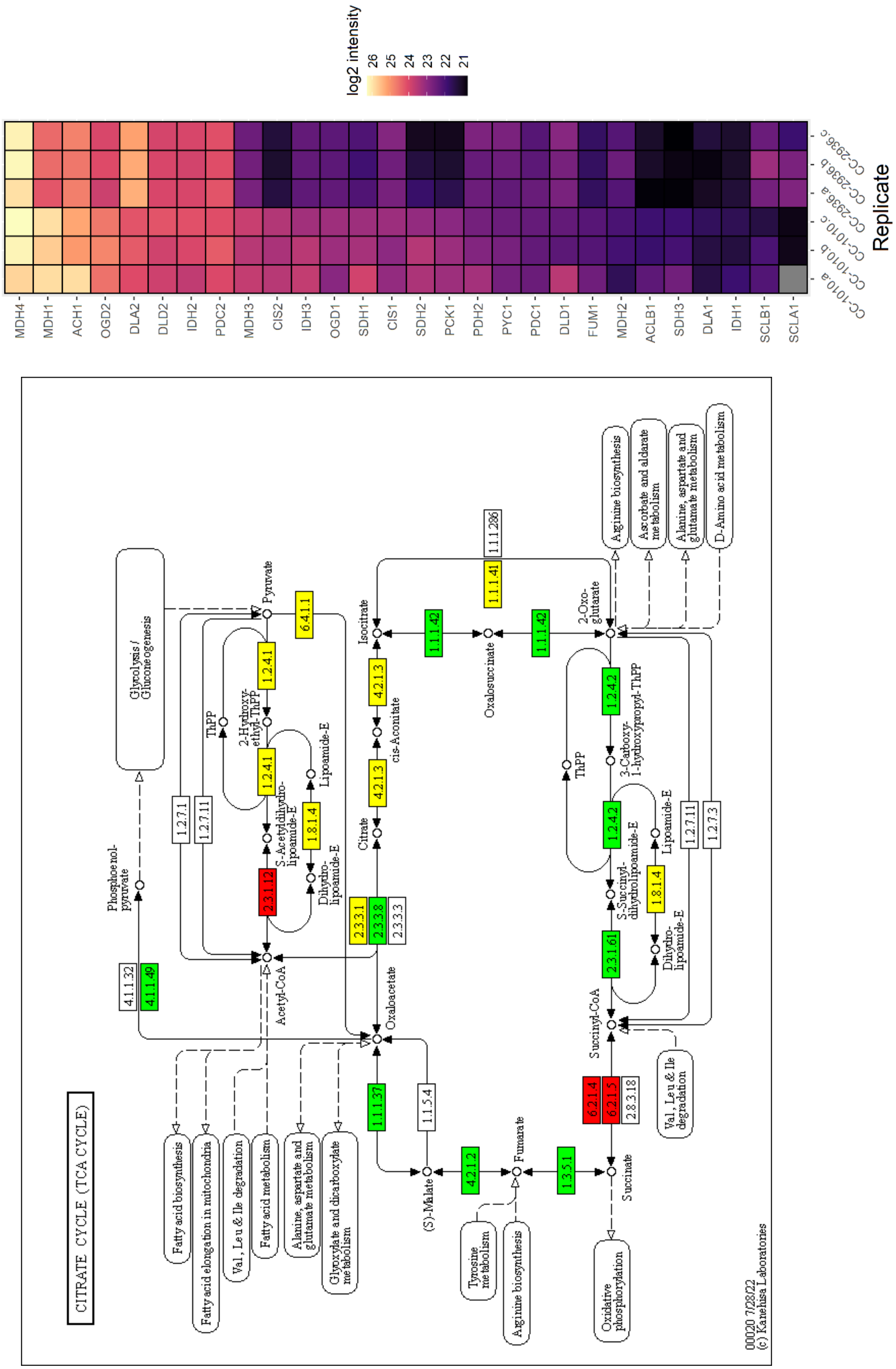

Figure 2. 23: (Right) Kegg map00020 - Citrate cycle (TCA cycle). Colored boxes represent proteins detected by label-free shotgun proteomics. Green (CC-1010) and red (CC-2936) boxes highlight DEqMS-selected DE proteins. (Left) Heatmap reporting the log2-intensities of DE-proteins involved in TCA-cycle.

malate-synthase (MAS1, 6.5-fold-change), and two NAD-dependent malate dehydrogenases (MDH1, 2.7-fold-change ; MDH3, 2-fold-change) were found to be more accumulated in CC-1010 (Sup. Figure 13). In agreement with these findings, several subunits of the mitochondrial complex I and II, and the mitochondrial cytochrome *c* were found to be significantly increased in CC-1010 (Sup. Figure 13).

Among the TCA-cycle enzymes, a different pattern was observed for the succinyl-CoA synthetase (SCL), for which both *α*- and *β*-chain are DE in CC-2936. This mitochondrial enzyme catalyzes the reaction: succinyl-CoA + H_2O + guanosine diphosphate (GDP) → succinate + guanosine triphosphate (GTP). The GO term-overrepresentation analysis revealed that in both strains, GTP-binding- (GO:0005525) and GTPase-activity- (GO:0003924) associated protein fractions are significantly enriched (Sup. Table 2). CC-1010's DE-fraction includes three RAB-Like GTP binding proteins (Cre06.g311900, Cre03.g189250, Cre09.g390763), known to regulate membrane trafficking (HUTAGALUNG and NOVICK, 2011) and cilia assembly (Yan and Shen, 2021). CC-2936's DE fraction includes several elongation factors (CreCp.g802267, Cre06.g284750, Cre03.g165000), *β*-tubulin (Cre12.g549550) and another flagellar element not yet characterized (Cre04.g218250). Also dihydrolipoamide acetyltransferase (DLA2), the core component (E2) of the chloroplastic pyruvate-dehydrogenase complex (cpPDC) (Mooney et al., 1999), was found to over accumulated in CC-2936. The cpPDC catalyzes the oxidative decarboxylation of pyruvate to acetyl-CoA, the initial reaction in chloroplast fatty acid biosynthesis (Camp and Randall, 1985). When we investigated other enzymes involved in fatty acid biosynthesis (Figure 2.25), we observed that also several subunits of the plastidial acetyl-CoA carboxylase (ACCase) complex (Thelen and Ohlrogge, 2002), and a putative 3-ketoacyl-ACP-synthase (KAS3, Cre04.g216950) (Li-Beisson et al., 2015) were over-accumulated in CC-2936. The ACCase complex occupies a central role in FAs biosynthesis, catalyzing the first committed step in the pathway from acetyl-CoA to long-chain fatty acids (Mekhedov et al., 2000). Interestingly, the first half-reaction, carried out by biotin carboxylase 1 (BC1), involves the ATP-dependent carboxylation of biotin using bicarbonate as C-substrate (Lee et al., 2008). The carboxyl-group is then transferred from biotin to acetyl-CoA to produce malonyl-CoA, the C-building block used by ketoacyl-ACP-synthase (KAS) for FAs elongation. Thus, a direct link exists between FAs biosynthesis initiation/elongation and bicarbonate metabolism. It was recently shown that, in *C. reinahrdtii* cells adapted to high CO_2 levels (1000ppm) for several days, a negative transcriptional response was observed for genes codifying for cpPDC, ACCase complex, KASIII, and

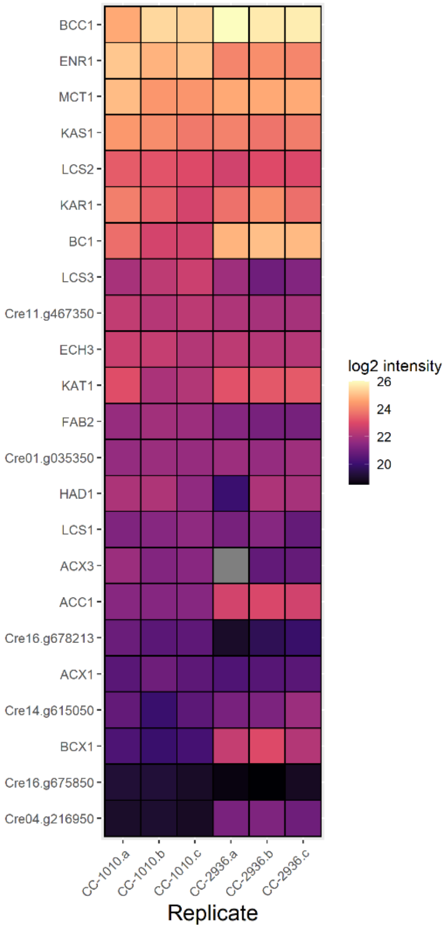

Figure 2. 24: Heatmap reporting the log2-intensities of DE-proteins involved in fatty acids biosynthesis. Grey cells represent undetected peptides.

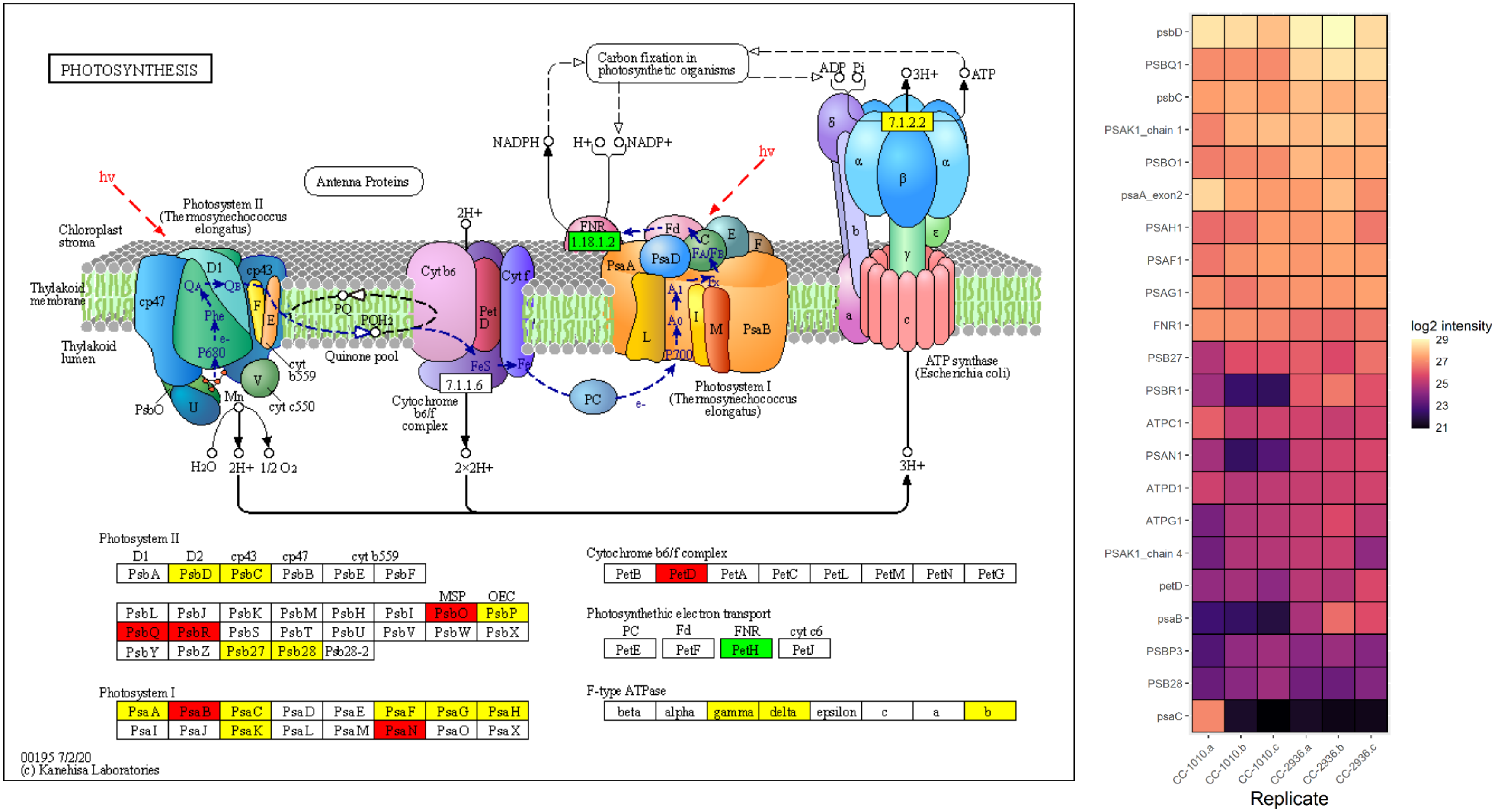

Figure 2. 25: (Right) Kegg map 00195 – Photosynthesis. Colored boxes represent proteins detected by label-free shotgun proteomics. Green (CC-1010) and red (CC-2936) boxes highlight DEqMS-selected DE proteins. (Left) Heatmap reporting the log2-intensities of DE-proteins involved in photosynthesis.

photosynthesis, while TCA cycle's enzymes were strongly upregulated (Zhang et al., 2021). A possible co-regulatory activity between some low-CO_2 inducible CCM's components and some chloroplastic FAs biosynthetic enzymes cannot be excluded. The cpPDC is located in the chloroplast's stromal compartment and known to be regulated by ions, NADH and acetyl-CoA availability (Tovar-Méndez et al., 2003). A carbon- and DLA2-dependent regulatory mechanism was recently discovered in *C. reinhardtii*, where DLA2 was shown to bind *psbA* mRNAs controlling the *de novo* synthesis of PSII-RC's subunit D1 (Bohne et al., 2013), taking place in the T-zone surrounding the pyrenoid (Uniacke and Zerges, 2007). DLA2's moonlight activity was recently proposed to be triggered by lysine-acetylation and subsequent disassembly of the cpPDC (Neusius et al., 2022).

Besides FAs biosynthesis, several photosynthetic components belonging to LHCII-PSII supercomplex, Cyt b*6*f, and PSI complexes were found to be DE in CC-2936 (Figure 2.26, Sup. Figure 13). The oxygen evolving complex's subunits PsbQ, PsbR, and PsbO were found to be more abundant in CC-2936, with a fold-change of 2.6, 6.8, and 1.7 respectively. It was previously demonstrated that, in *Chlamydomonas*, PsbR is involved in forming the recognition site for the binding of LHCSR3 to PSII-LHCII supercomplex, and that NPQ capacity decreases in strains showing low PsbR levels (Xue et al., 2015). PsbQ and PsbO were shown to be essential for the stabilization of the OEC, and to accumulate also as extrinsic proteins creating a barrier to prevent Ca^{2+} losses (see Yocum, 2022). Wide differences between the strains were observed at the level of the LHCII (Sup. Figure 13). In agreement with our previous mRNA and protein analysis (Figure 2.19), LHCSR1 was found to be 3-fold-change more abundant in CC-2936, and the same pattern was observed for LHCBM1 (2-fold-change). Both proteins were previously shown to play a role in PSII photoprotection under highlight conditions (Elrad et al., 2002; Dinc et al., 2016). Moreover, it was recently demonstrated that a mutant lacking LHCBM1 (*npq5*) accumulates very low levels of LHCSR1 (Liu et al., 2022), suggesting that LHCBM1 could promote LHCSR1 synthesis. Nonetheless, LHCBM1 is not a pH-sensor, and the way it contributes to NPQ or to other NPQ proteins' regulation remains still uncharacterized (Liu et al., 2022). Oppositely to what we observed in our previous experiment (Figure 2.19), LHCSR3 was found to be 1-fold higher in CC-1010. This discrepancy suggests that the difference in the intensity of the HL-treatment between the two experiments (vHL vs HL) may have triggered a different response in the strains. Nonetheless, consistent results were observed for three other low-CO2 inducible proteins CAH4 (2.7-FC) and LCI9 (2.8-FC) and Essential Pyrenoid Component 1 (4.4-FC) confirming a stronger induction of the low-CO2 inducible metabolism in CC-2936. Also the minor antenna protein LHCB4 (CP29), linking the LHCBM trimers to PSII-RC (Semchonok et al., 2017), was found to be more accumulated in CC-2936 (fold-change 1.8, Sup. Figure 13). It was recently observed that the light-driven N-terminal phosphorylation of LHCSR3 modulates the phosphorylation of LHCB4, but the implications of such mechanism are still unknown (Scholz et al., 2019). In agreement with the overaccumulation of photosynthetic proteins, CC-2936 showed the overaccumulation of the key enzymes involved in heme and chlorophyll biosynthesis (Sup. Figure 13). The proteomic data are consistent with the measurements performed *in vitro* (Figure 2.27 B) and *in vivo* (Figure 2.27 C) on TMP-grown samples, before and after exposing them to vHL for 24h. In *Chlamydomonas*, it was previously observed that both chlorophyll a/b ratio and chlorophyll/cell tend to decrease upon HL exposure (Bonente et al., 2012).

In agreement with our data, no variation in the antennae size was observed by the authors of the study, following the HL-treatment (Bonente et al., 2012). Furthermore, CC-2936 presented a lower PSI/PSII ratio than CC-1010. It is well established that both plants (Bailey et al., 2001; Ballottari et al., 2007) and *C. reinhardtii* (Bonente et al., 2012) respond to light-stress by down-modulating PSI against PSII. In CC-2936, the constitutively lower PSI/PSII ratio, the higher induction of some low-CO_2 inducible proteins, and the presence of a *pmf* favoring the fast NPQ activation (and slow relaxation), suggest that the strain may have evolved under the selective pressure of a sun-drenched environment.

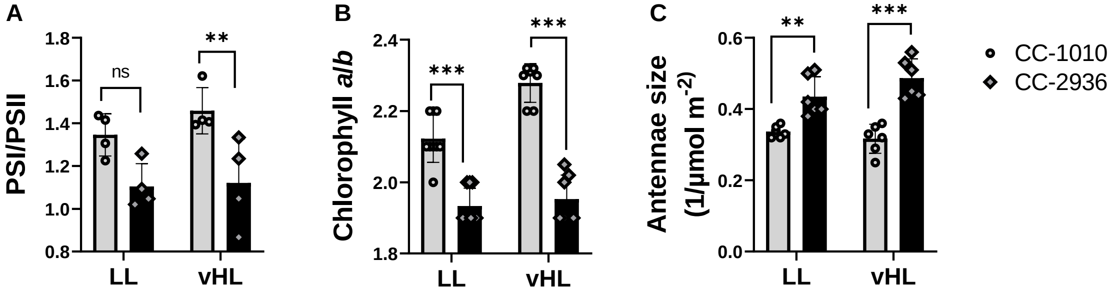

Figure 2. 26: Effect of 24h-vHL treatment on the photosynthetic machinery. (A) PSI/PSII ratio estimated by absorption spectroscopy using a single-turnover flash in presence/absence of DCMU and hydroxylamine (see materials and methods). (B) Chlorophyl a/b ratio estimated by spectrophotometry on cellular methanol extracts. (C) Antennae size estimated by time-resolved fluorescence in presence of DCMU (see materials and methods). $P<0.01$=**, $P<0.001$=*** (Two-ways ANOVA).

The mRNA level of BST1 was previously found to be significantly higher in 24h-vHL-exposed CC-2936's cells (Figure 2.19). Despite BST1 transporter not being detected by our proteomic analysis, the paralogue BST3 was found to be about 2-fold-change more abundant in CC-1010. Nonetheless, a complementary analysis will be needed to confirm the presence of a differential regulation between BST paralogues in the two strains.

Several glycolytic enzymes were detected by our analysis, and only three were found to be DE. In CC-1010, an increased level of two phosphoglycerate mutases (Cre06.g272050, 1.6-fold-change ; Cre06.g293150, 1.4-fold-change) was observed. Phosphoglycerate mutases (PGMs) are cytoplasmic enzymes catalyzing the reversible interconversion of 3-phosphoglycerate (3-PGA) to 2-phosphoglycerate (2-PGA) in glycolysis. It was recently demonstrated that PGMs are important regulatory nodes for carbon partitioning in cyanobacteria under nitrogen limitation (Orthwein et al., 2021), but no information is present about *C. reinhardtii*. On the other hand, CC-2936 presented an upregulation of the chloroplastic phosphoglycerate kinase (Cre11.g467770, 3.3-fold-change) with respect to CC-1010. This enzyme catalyzes the reversible transfer of phosphate from 1,3-bisphosphoglycerate (1,3BPG) to ADP in the first NADPH- and ATP-generating step of the glycolytic pathway. The directionality of this reaction is defined by the concentration of ATP and NAD(P)H within the compartment. It is believed that phosphoglycerate kinase (PGK) directionality coupled to the activity of the triose-phosphate transport system is a key process for the import/export of ATP and NADH between the chloroplast and all other compartments (Johnson and Alric, 2013). PGK plays also an important role in CBB-cycle, catalyzing the phosphorylation of 3-PG, producing 1,3-BPG and ADP, as part of the reactions that regenerate ribulose-1,5-bisphosphate while consuming ATP (Johnson and Alric, 2013). When exposed to HL under minimal condition, CC-2936 exhibited low ETR and a nigericin-resistant qE resulting from the over-acidification of the chloroplast lumen even under mild light intensities. Under such circumstances, photophosphorylation should not be limited by *pmf*, and the stroma should be rich in ATP, probably exceeding the 2 NADPH/3 ATP stoichiometric requirement of CBB-cycle. In CC-2936, a faster acidification of the lumen is further supported by the up-regulation of the two flavodiiron proteins A (1.6-fold-change) and B (1.8-fold-change) (Figure 2.28), previously shown to control the speed of lumen acidification, thus bicarbonate import (Burlacot et al., 2022) and qE activation (Chaux et al., 2017) in *Chlamydomonas*. *Vice versa*, a much higher ETR was observed for CC-1010 grown under the same conditions. Four up-regulated photosynthetic enzymes were identified in this strain: *i*) the ferredoxin-NADPH reductase (FNR, 1.5-fold-change), mediating the transfer of photosynthetic electrons to NADP$^+$, *ii*) PGRL1 and PGR5 (1.7- and 2-fold-change), the two effectors of CEF (Figure 2.28), *iii*) and the sedoheptulose-1,7-bisphosphatase (SBP1, 1.4-fold-change), converting sedoheptulose 1,7-bisphosphate to sedoheptulose 7-phosphate + P$_i$.

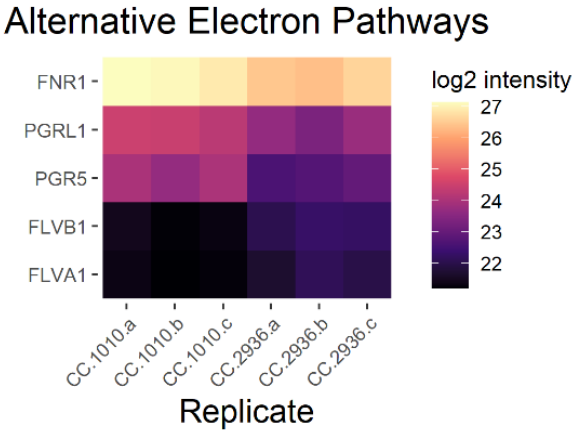

Figure 2. 27: Heatmap reporting the log2-intensities of DE-proteins involved in the electron-transfer from PSI to NADP$^+$ (FNR1), cyclic electron flow around PSI (PGRL1, PGR5), and water-water cycle (FLVA and FLVB).

2.3 Conclusions

In this chapter, I described the establishment of a new culturing condition that could be suitable for the cultivation of a high number of strains under both autotrophic and mixotrophic growth conditions. The culturing condition was designed to gently stimulate the low-CO_2 stress response while using a relatively low light intensity (150 *µmol* of photons · $m^{-2} \cdot s^{-1}$), with the advantage of avoiding overheating and evaporation of the culture's liquid fraction. Under this condition, I provided a comprehensive fluorescence-based phenotypic description of twenty-five wild-type strains partitioned into 9 laboratory isolates and 16 field-isolates. The analysis of the retrieved photosynthetic parameters revealed the existence of extensive phenotypic diversity among the strains, regardless on the area of isolation. Common photosynthetic trends within *C. reinhardtii* were pinpointed, showing that acetate supplementation boosts photosynthesis and represses NPQ during high-light stress. A remarkable phenotypic divergence between populations of laboratory and natural strains was observed under mixotrophy, demonstrating that the group of laboratory strains displays a lower NPQ and higher rETR in response to HL stress. A clear negative correlation of non-photochemical quenching over photochemical quenching capacity was observed under mixotrophic condition, suggesting that the acetate-driven inhibition of NPQ genes may have evolved to maximize the funnelling of excitation energy to photochemistry. Under mixotrophy, the higher rate of respiration induced by acetate metabolism could offset photosynthetic O_2 production (Morsy, 2011) while providing metabolic CO_2 to the reductive pentose phosphate pathway. In agreement, mixotrophic cells showed no significant change in chlorophyll *a/b* ratio in response to HL, displaying lower values than photoautotrophic cells. This result suggests that photoautotrophic cultures were more stressed by the HL treatment, downmodulating their antennae-size to alleviate the pressure on PSII while developing higher NPQ capacity.

A multimethodological comparison between the laboratory-isolate CC-1010 and the field-isolate CC-2936 revealed the presence of wide intraspecific diversity in the response to HL stress, shedding new light on the dynamics of proton-motive force regulation. By monitoring the NPQ induction/relaxation dynamics, I observed that, in CC-2936, the acidification of the lumen takes place at lower light intensity and relaxes at a slower speed in the dark. Moreover, the strain displays a reduced rETR, pointing to the presence of a bottleneck in its photosynthetic electron-transport chain. Using 77 °K fluorescence emission on HL exposed cells, I observed a more marked state transition capacity in CC-1010, suggesting that the higher rETR in this strain may result in a higher reducing state of the thylakoids' stroma. Following the hypothesis of a differential *pmf* regulation between CC-1010 and CC-2936, I used time-resolved fluorescence and electrochromic shift to study the effect of the K^+/H^+ antiporter nigericin on the trans-thylakoids ΔpH and ΔΨ. The results indicate that nigericin efficiently diffuses into CC-2936's chloroplasts, altering the speed of NPQ induction/ relaxation and promoting a more efficient charge separation under non-saturating light intensities. In contrast with what observed for CC-1010, in CC-2936, nigericin caused no significant inhibition of the fast-relaxing NPQ or decrease of the rETR or charge separations (ECS signal) under saturating light. For HL-exposed CC-2936, nigericin-treated cells displayed less qT upon the last step of the saturation curve and reached the same amount of qT than the control after 5 minutes of dark. This result implies that the observed fast-relaxing NPQ is mainly qE, thus that nigericin does not dissipate the trans-thylakoid ΔpH upon light exposure. Consequently, HL-exposed nigericin-treated CC-1010 displayed a clear reduction in Fv/Fm whereas CC-2936 displayed no sign of photodamage under the same condition. No synergic action was observed between nigericin and the electrical K^+ uniporters valinomycin and nonactin, making the nature of nigericin resistance still controversial. On the other hand, I demonstrated that supplementation with 1mM exogenous bicarbonate enables nigericin to dissipate a significant amount of ΔpH, resulting in the inhibition of more than 50% of CC-2936's qE. Our dataset provides first clear evidence that the endogenous bicarbonate influx induces changes in K+ distribution across the thylakoid membranes, elevating the biophysical CCM to the role of *pmf*-regulator, not only by facilitating the carboxylase activity of RuBisCO, but also through the control of the chloroplast's ionic strength. The analysis of CrKEA1-3 transcripts revealed an important differential regulation of KEA2 and KEA3 (CPLD54) between CC-1010 and CC-2936, making them interesting targets for future analyses. Interestingly, supplementation of CC-1010's HL-exposed cells with low doses of bicarbonate (0.25-0.5 mM) caused a visible rETR increase upon-non-saturating light intensities, followed by a significant decrease under saturating light-intensities when compared to the control condition. On the other hand, higher rates of rETR are maintained upon higher concentration of exogenous bicarbonate. My interpretation of this phenomenon is that bicarbonate influx (or CCM activity) results in the alteration of some other ions' distribution across chloroplastic compartments, and that once this adjustment takes place, its reversion may take several minutes. Therefore, small concentrations of exogenous bicarbonate would induce some ionic adjustments, and its sudden depletion by the CCM would cause photosynthesis to operate under non optimal ionic conditions. On the other hand, CC-2936 seems to be locked into a state that is optimal for bicarbonate utilization. CC-2936's rETR is highly increased by bicarbonate supplementation, even upon supplementation with small doses. The transcripts analysis of targeted NPQ and CCM elements strongly suggests that CC-2936 is experiencing a CO_2-limitation inducing an up-regulation of many low-CO_2 inducible transcripts. On the other hand, no difference in growth speed was visible when CC-1010 and CC-2936 were compared under TMP-LL and TMP-HL, even under 0.15%-CO_2 condition. These results suggest that CC-2936 cannot be considered an impaired strain as it is fully able of growing under HL and low CO_2 conditions. On the other hand, a real growth impairment was observed on CC-2936's HL-grown cultures upon mixotrophy, reaching a short stationary phase at a significantly lower OD, and quickly entering death-phase. The reasons of such response remain still unknown and further experiments will be needed to interpret the phenomenon.

A full-cell shotgun-proteomic approach was used on HL-exposed photoautotrophic cells to acquire an overview of the physiological state in both strains. The results showed differential representation of contraposing pathways among CC-1010 and CC-2936. While a clear over-representation of proteins involved in heterotrophic metabolism was observed in CC-1010, many chloroplastic protein were observed to over-accumulate in CC-2936. The most represented pathways observed in CC-1010 were the acetate fermentation/assimilation, TCA-cycle and glyoxylate cycle, some components of the mitochondrial ETC, the malate-aspartate shunt, and pyruvate metabolism. Moreover, some key glycolytic (phosphoglycerate mutase; Cre06.g272050 and Cre06.g293150) and gluconeogenesis (phosphoenolpyruvate carboxykinase; Cre02.g141400) cytoplasmic enzymes were found to be more accumulated in CC-1010.

Our data suggest that the capacity of CC-1010 to maintain a high rETR during HL exposure could highly rely on the activity of mitochondria. The higher rETR, qT capacity and accumulation of FNR1, PGRL1, and PGR5 suggest the presence of a high $NADPH/NADP^+$ ratio creating a reducing environment around CC-1010's thylakoids. In agreement with this hypothesis, I observed a higher accumulation of the chloroplastic enzymes Fe-superoxide dismutase (Cre10.g436050, 1.5-FC) and ascorbate peroxidase 1 (Cre02.g087700, 2.4-FC), the mitochondrial mono-functional catalase 1 (Cre09.g417150, 1.7-FC), and a glutathione S-transferase (Cre17.g742450, 2.8-FC). Under those circumstances, the mitochondria could play a key role in providing ATP to the chloroplast while altering the intracellular O_2/CO_2 ratio. The over-accumulation of enzymes involved in acetate-assimilation was observed, suggesting that in CC-1010, the glyoxylate cycle may occupy a role in the response to HL, possibly by the poising of the redox potential between mitochondria, cytoplasm, and chloroplast. Nonetheless, this phenomenon would imply the existence of an acetate-producing pathway in presence of O_2, that by the current knowledge represents a very remote possibility.

Our physiological data and proteomic analysis revealed that, in CC-2936, the HL stress-response strategy relies more on photoprotection and preservation of the chloroplastic ETC. The fast acidification of the thylakoids lumen results in the activation of NPQ already upon exposure to mild light intensities, and the qE remains active for short periods also in the dark. In agreement, the low electron-transport rate observed in this strain is probably due to the photosynthetic control operated by the ΔpH on Cyt b*6*f, creating a bottleneck for the electrons coming from PSII. The stabilization of PSII-OEC is also an important feature of CC-2936's HL-response, and the overaccumulation of PSBO, PSBQ, PSBR and PSBS may be needed to cope with a more acidic luminal pH. Under this condition, chloroplast ATPase activity should be limited only by the rate of ATP consumption, while CBB-cycle should be rather limited by NADPH availability. The proteomic analysis revealed also an overaccumulation of enzymes involved in fatty acids biosynthesis. Further analysis will be needed to elucidate their role in CC-2936's HL response. Equally unsolved remains the mystery of the nigericin-resistant ΔpH and the high affinity of this strain for exogenous bicarbonate. Our collaborators Dimitris Petroutsos and Yizhon Yuan from the CEA of Grenoble successfully isolated some CC-2936's KEA2-overexpressing mutants that will be characterized over the next months to clarify the involvement of this antiporter in bicarbonate metabolism and qE-relaxation kinetics. CC-2936 represents a very good model to study these phenomena due to his peculiar nigericin-resistant *pmf*, and its inclusion into typical experimental setups, beside a standard laboratory strain, will enrich our understanding of cell physiology, adaptation, and intraspecific variation in stress-response.

Chapter 3

3.1 Preface

This chapter is dedicated to the creation of a Multiparent Advanced-Generation InterCross (MAGIC) design in *Chlamydomonas reinhardtii* and its exploitation to identify loci involved in photosynthesis and photoprotection. The "Green MAGIC" is a multidisciplinary project, fruit of collaboration between three laboratories (Figure 3.1) from the University of Liege (Belgium). The people involved in the project are:

- **Tom Druet** and Agnieszka Misztak (Unit of Animal Genomics – GIGA-R & Faculty of Veterinary Medicine).
- **Pierre Cardol**, Fabrizio Iacono and Rebecca Houet (Genetics and Physiology of Microalgae – InBioS/PhytoSystems, Faculty of Sciences).
- **Prof. Marc Hanikenne**, Sara M. Esteves, and Alice Jadoul (Functional Genomics and Plant Molecular Imaging – InBioS/PhytoSystems, Faculty of Sciences).

My involvement in the project was previously discussed in Chapter 1, within the section "*Aim of the thesis*", and the obtained results will be presented and discussed across the current chapter. Despite of their distance from my field of expertise, some technical aspects of the genomic and quantitative genetics analyses carried out by Tom Druet and Agnieszka Misztak will be reported in this chapter as a necessary step for the understanding and discussion the project outcome.

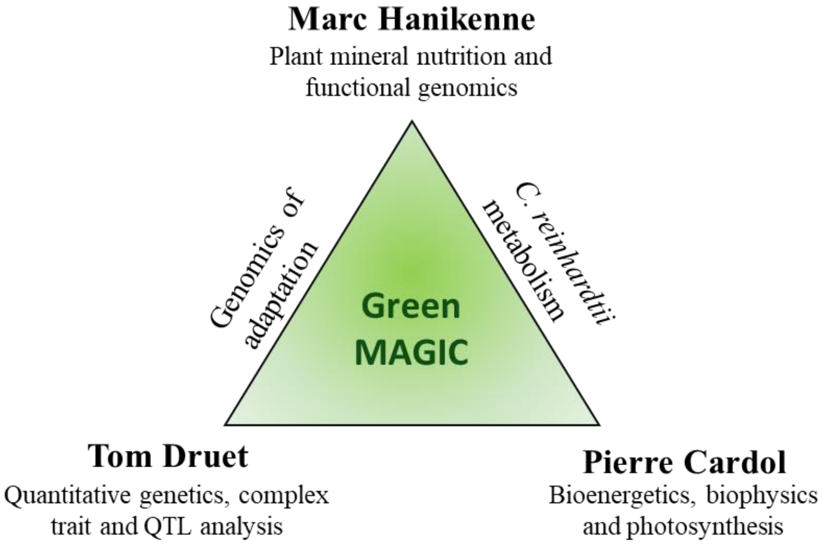

Figure 3. 1: The Green MAGIC consortium and expertise.

3.1.1 Multiparent Advanced Generation Inter-Cross (MAGIC) populations as tools for quantitative genetics studies

Differences between individuals of the same species depend on their qualitative and quantitative genetic traits. The former traits are described by discrete distribution and cause promptly visible phenotypic differences. Some examples of such traits include flower color in *Pisum sativum* (purple or white), response of an organism to a disease (resistant or susceptible), and the muscular hypertrophy in cattle (regular or double-muscled). Qualitative traits are often controlled by a single gene and their inheritance follows the mathematical principles of segregation and independent assortment originally proposed by Gregor Mendel. Many qualitative traits are under the control of a single gene, present within the population as two or more alleles. On the other hand, quantitative traits do not segregate in accordance with Mendel’s laws, and they are described by continuous distributions. Exceptions exist in nature, and some traits presenting a continuous distribution can be under the control of a single gene (Xu, 2022). Nonetheless, quantitative traits are often assumed to be controlled by multiple loci and their interaction with the environment. A good example of such traits is human skin color, affected by the genetics of the individuals and its interaction with the environmental levels of solar radiation. Due to the polygenic nature of quantitative traits, more advanced statistical tools are required to study the simultaneous segregation of all loci associated with the studied trait (quantitative trait loci, QTLs). Biometrical (or quantitative) genetics is a branch of genetics that, using advanced statistics, investigates the inheritance and genetic basis of quantitative traits. The study of quantitative traits’ genetics can be based on several approaches. One approach focuses on genetic linkage, defined as the tendency of neighboring loci on a chromosome to be inherited together during sexual reproduction. Meanwhile, physically distant loci have higher likelihood to segregate independently during the meiotic chromosomal crossover. Genetic linkage is measured in centimorgans (cM) or map units (m.u.), and it is used to describe the distance existing between two loci (or markers) on the same chromosome. Nonetheless, the linkage distance between two markers is not a physical measure, but rather a relative estimation of the expected rate of chromosomal crossovers between them. Two markers are 1cM away when they have 1% chance of crossover per generation. For 1 cM, the equivalent physical distance in base pairs (bp) changes from species to species, between sexes of the same species, and even between different chromosomes of the same individual (Hasan and Ness, 2020). In *C. reinhardtii*, the average recombination frequency was estimated as 10cM/Mb. In other words, for every 100,000 bp there is one in a hundred chances of crossover per generation (Merchant et al., 2007; Tulin and Cross, 2014).

A second quantitative genetics approach relies on the structure of linkage disequilibrium (LD), defined as the non-random association of alleles of different loci in a population. Therefore, LD describes the statistical relationship between two loci in the genome, even for loci located on different chromosomes. This statistical relationship is controlled by natural selection and other evolutionary forces (e.g. genetic drift, changes in population size, inbreeding, etcetera), and help to understand the history of a population. In genome-wide association studies (GWAS), the LD between markers and causative variants associated with a given phenotype is leveraged to detect these associations (see Slatkin, 2008; Xu, 2022).

One of the first steps for the development of a quantitative genetics study is the definition of the experimental mapping population, constituted of natural isolates (diversity panel), or created artificially through a controlled crossing design. The ideal population should be phenotypically divergent and harbor a good level of polymorphisms. Different kinds of segregating populations can be employed depending on the objective, spanning from naturally occurring inbred lines to synthetic populations. An example of synthetic mapping-resource commonly employed in plant breeding is the recombinant inbred line (RIL) population. To create a RIL population, two pre-selected parental inbred lines showing contrasting phenotypes are crossed for 2 generations yielding a recombinant F2. Each F2 line undergoes several rounds of self-fertilization (selfing), resulting in a final population of RILs for which genomes are mosaics of the parents (Rifkin, 2012; Theeuwen et al., 2022) (Figure 3. 2). Biparental F2-RILs do not present any defined structure, thus allowing the use of simpler mapping models and limiting the risk of discovering false-positive QTLs. On the other hand, chances of recombination between closely linked loci are very low as they undergo only few recombination events, and the confidence interval of the mapped QTLs generally include several hundreds of candidate genes (Kover et al., 2009). To solve this problem, more sophisticated mating designs were put in place, increasing the number of generations up to F12, followed by several generations of selfing, or “siblings mating” (inbreeding step). The increasing amount of recombination events results in shorter confidence intervals / higher mapping resolution. Therefore, advanced intercross lines (AILs) provide a higher mapping resolution improving the power of QTL detection techniques (Teuscher et al., 2005).

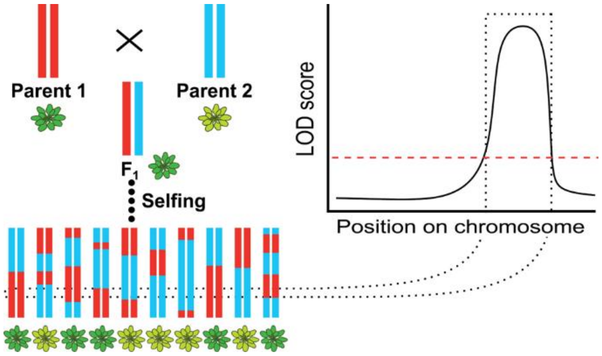

Figure 3. 2: Concept of QTL mapping on RILs population. The likelihood of the association is given as logarithm of odds (LOD) score, where higher values point to stronger associations. The regions on the genome, a locus, with a LOD score above the multiple-testing-corrected threshold is termed a QTL. Figure from Theeuwen et al. (2022).

A general challenge for the dissection of more complex traits is that the individual contribution from each locus is often small, and the causing variants may fall within noncoding regions. Detection of small-effect variants was achieved in mice by complementing the advanced intercross approach with an extension of the parental pool from two to several parents (Churchill et al., 2004; Yalcin et al., 2005). Similar mapping resources were developed in *Arabidopsis* (Kover et al., 2009) and several of the most diffused crop species (Huang et al., 2015). In a multiparent advanced-generation intercross (MAGIC) design (Cavanagh et al., 2008; Kover et al., 2009; Huang et al., 2015), the F1 lines from different parental origin are intercrossed for several generations and eventually inbred by selfing or sibs-mating. While advanced generations reduce the length of inherited parental segments, the multi-parental approach enlarges the genetic pool of the final population and increases its molecular markers density.

Despite of the relevance of *C. reinhardtii* in many fields of research and its suitability to be crossed and phenotyped under highly controlled conditions, no mapping population was ever generated in this species with the aim to map QTLs associated with interesting phenotypes. However, *C. reinhardtii* meets all the conditions needed for the development of projects of such kind:

1. *C. reinhardtii* is haploid, thus no self-fertilization is needed as the offspring from every crossing is already isogenic and can be easily multiplied asexually.
2. A well annotated genome assembly is available for the community (Merchant et al., 2007; Blaby et al., 2014; Craig et al., 2022).
3. Many divergent stocks have been already isolated, whole-genome sequenced, and can be easily acquired from several algae collections (Flowers et al., 2015; Gallaher et al., 2015).

The last decades have seen a raise of interest toward microalgae cultivation and biomanufacturing (de Souza et al., 2019; Sproles et al., 2021; Veerabadhran et al., 2021), but the current limit of the market lies in the high costs of production and biomass processing. The development of quantitative genetics tools on model microalgal species could play a central role for the expansion of the market, boosting the genetic improvement of microalgal strains with better fitness and higher yield of target bio-compounds.

3.2 Results and Discussion

3.2.1 The construction of a MAGIC population in *C. reinhardtii*

Genetic diversity among the 8 founders

Whole-genome sequencing (WGS) data was already available for most of the 24 initial wild-type strains, with exception of CC-3348, CC-1374, CC-410, and CC-1418. The four strains were previously reported to be a laboratory isolate identical to CC-407 (Ferris, 1989; Harris, 2008) Thus, CC-410 and CC-1418 were selected for their divergent phenotype to be part of the founder panel and their genome was sequenced at high coverage.

To investigate the genotype of the 22 wild-type strains, WGS data were mapped to the version 6 of the *C. reinhardtii* reference genome (Craig et al., 2022) and genomic variants were identified through variant-calling. The analysis identified a total of 8,313,680 variants (SNPs and small indels) within 17 linkage groups, of which 5,673,680 were selected, based on a set of quality-filtering criteria, for further analysis. Genetic distances between strains were calculated as the proportion of distinct genotypes $d_{ii'}$ among pairs of lines *i* and *i'* and ranged from 0.0002 to 0.4522. Our analysis confirms the previous knowledge that CC-410 and CC-1418 are close to each other (distance = 2e-4) and to the laboratory strain CC-1009 (distance = 1.6e-3) (Figure 3.3). Nonetheless, CC-410 displayed consistent differences in rETR with respect to CC-1418 during the phenotyping of the founders (section 2.2.2.). The MAGIC design was already in an advanced state when we learned about this information, so we had no choice but to accept the presence of the three closely related laboratory strains among the 8 founders. Nevertheless, the rest of the founders (CC-1952, CC-2344, CC-2931, CC-2936 and CC-2937) well captured the genetic diversity

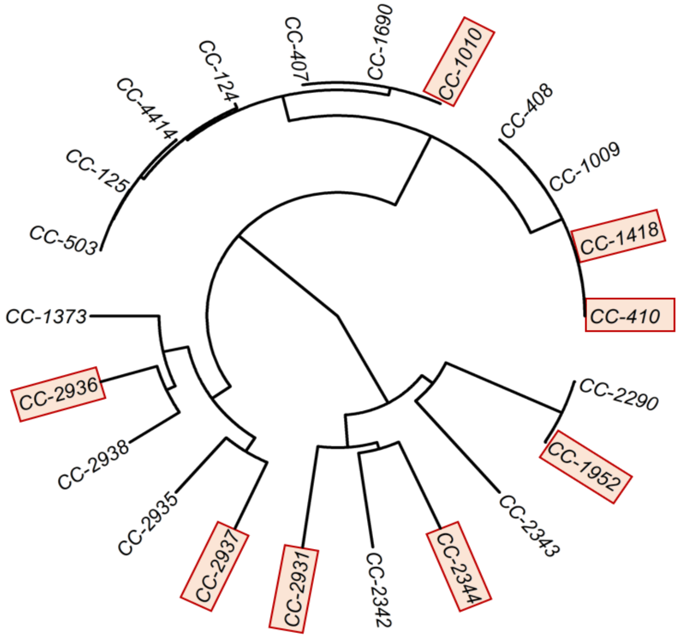

Figure 3. 3: Neighbor-joining tree representing the relationship among 22 Chlamydomonas reinhardtii reference strains. The red boxes indicate the 8 founders of the MAGIC design.

present within the group of wild-types (Figure 3.3).

The genetic relatedness was further characterized by the detection of identical-by-descendant (IBD) segments shared among the founders. It was previously reported that, despite of their distance, laboratory strains and some field isolated strains share relatively long IBD segments (Craig et al., 2019). Our analysis revealed that entire chromosomes are shared among laboratory strains, and even few segments longer than 1Mb are shared between laboratory strains and field isolates. Moreover, long IBD segments are shared also among field isolates such as 104 kb between CC-1952 and CC-2936, 181 kb between CC-1952 and CC-2344, 832 kb between CC-2936 and CC-2937 or 282 kb between CC-2937 and CC-2931. Presence of such IBD segments will result in higher levels of relatedness among the F8 lines, and in fewer apparent recombination events. In addition, founders sharing IBD segments have higher probability to carry the same alleles at these sites and transmit identical QTL effects to their descendants.

Description of the crossing design and genomic characterization of the MAGIC population

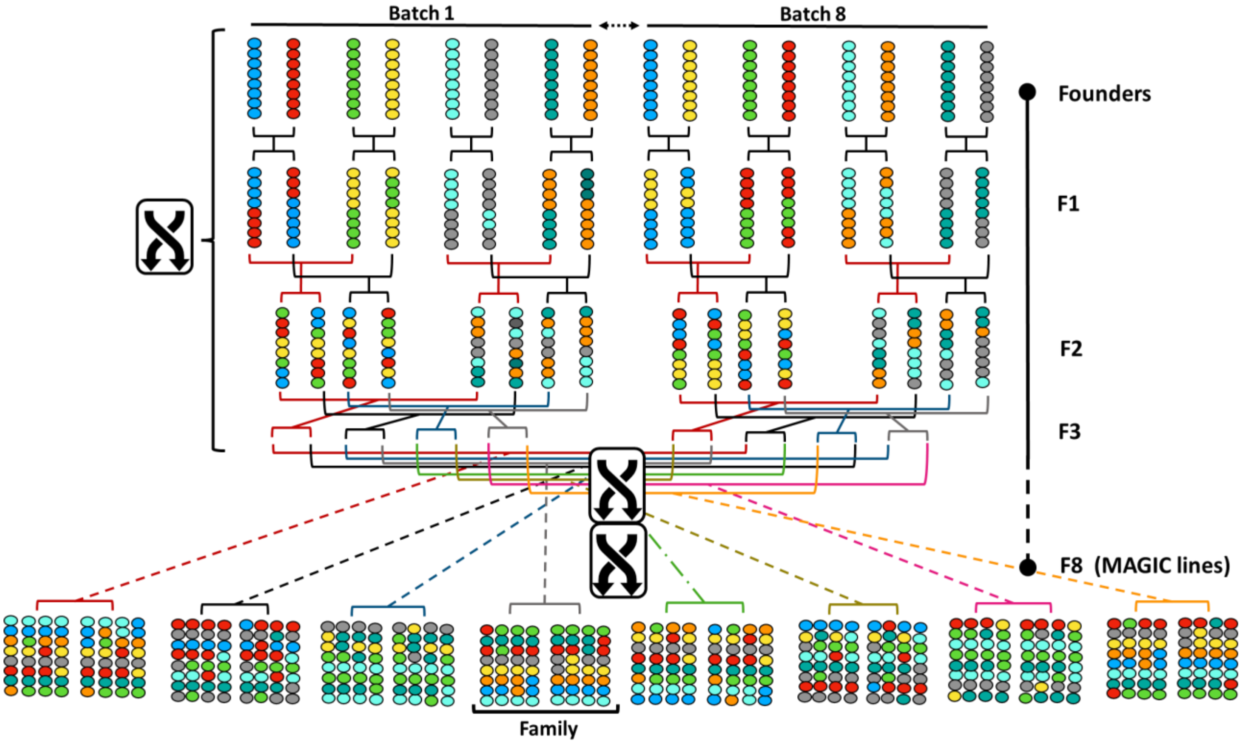

Figure 3. 4: Simplified representation of the Multiparent Advanced Generation InterCross (MAGIC) design developed in *Chlamydomonas reinhardtii*. Eight divergent founders were crossed to the opposite mating-type (mt) in all combinations for 2 times (32 crosses divided into 8 batches), and two siblings of opposite mt were isolated for each cross (64 F1 lines). Within each batch, the F1 was intercrossed for 2 more generations as shown above, yielding 64 F3 lines for which genome was a mosaic of the 8 founders. The crossing scheme used for each batch during the first 3 generations represents a crossing block (white boxes with black crossed arrows). At the beginning of the next crossing block, new batches were created in a way that the eight new batch-founders did not share any ancestor up the original 8 founders. The shuffling into new batches was repeated also for the F6 lines, ensuring that the new batch-founders did not share any ancestor up to the F3. The last crossing block consisted in only two generations, and during the isolation of the F8, the population was expanded to 256 MAGIC lines by isolating 8 siblings (4 mt^+ and 4 mt^-) per cross for a total of 32 families. Dashed lines indicate the steps of the MAGIC design that were omitted/oversimplified in this representation. Boxes with crossed arrows represent the random shuffling of the strains into new batches of 8 (4 mt^+ and 4 mt^-) and repetition of the 3-generations crossing scheme. The entire scheme was repeated 3 independent times leading to a total of 768 MAGIC lines.

The magic design was initiated by intercrossing every mt$^+$ with every mt$^-$ founder two independent times and isolating from each crossing one mt$^+$ and mt$^-$ for a total of 64 F1 progenies, sorted into 8 batches. The crossing scheme was structured in three 3-generations crossing blocks, the first block going from the founders to the F3 as shown in figure 3.4. At the end of each block, the 64 strains were shuffled into 8 new batches including 8 lines of opposite mating-type. The eight new F3 batch-founders were picked from eight different earlier batches, resulting in a F6 sharing no common ancestor up to the eight initial MAGIC founders. The same process of reshuffling took place at the F6 generation. The last crossing block included only 2 generations (F7 and F8) ending with the isolation of 4 mt$^+$ and 4 mt$^-$ per cross, thus resulting in a 4-FC expansion of the population and the constitution of the final 256 MAGIC lines. The expansion of the population created a substructure of 32 families composed by 8 siblings. The parents of each family did not share any common ancestor up to the F3. The entire design was repeated in 3 independent replicates resulting in a MAGIC population of 768 recombinant lines. The MAGIC lines were sequenced at the average depth of 9.2x (from 4.2x to 19.4x) and 3,121,994 variants were selected to infer the mosaic structure and estimate the founders' contribution to the population. The mosaic pattern was obtained for each line by inferring the chromosomal segments inherited from each of the initial 8 founders. Such segments, or "tracts", are defined as the continuous sections of a chromosome starting at the first position inherited from one founder and ending where the inheritance shifts to another founder. Our analysis revealed that every F8 individual chromosome is made of segments of various lengths, inherited from different founders. Some F8 lines displayed unexpected mosaic patterns for a variable number of chromosomic regions, variable in size, and presenting a very high density of short tracts ("*admixture patterns*"). For some strains, admixture was observed only in limited genomic regions, whereas 29 F8 lines presented such pattern in their entire genome. Whole-genome admixture patterns might have originated from the simultaneous sequencing of two or more colonies, therefore the 29 strains were excluded from further analyses. Moreover, 16.8% (124 out of 739) of the MAGIC population presented one to few admixed segments within a limited chromosomal region, and in several cases, the admixed region was observed to segregate among several siblings of the same family. The inheritance of a small chromosomal region from both parents by the same progeny, as a heterogeneous pair of copies, could explain the presence of such patterns. Nonetheless, the phenomenon remains uncharacterized and was not further investigated within this study.

The mosaic structure of the population was inferred on the 615 lines found to be exempt of admixture patterns (see materials and methods). The ancestry deconvolution analysis identified an average number of tracts per F8 line equal to 76.4 (median 76, range 46-112), and an average tract-length of 1457 kb (median 1020 kb). Tract-lengths are generally assumed to be independently and identically distributed exponential random variables, with a rate directly related to the recombination rate and the number of generations of crossing (Liang and Nielsen, 2014). Considering a recombination rate of 10 cM/Mb, the MAGIC lines presented a tract-length distribution corresponding approximately to 6-7 generations of crossing. The average contribution of the founders to the F8 population (Figure 3.5-A) was close to the expected 12.5%. The field isolated founders presented average contributions ranging from 10.9% to 14.6%, while individual contribution from the laboratory strains (CC-1010, CC-410 and CC-1418) was more variable (7.6%, 15.6% and 17.1% respectively). Nonetheless, the latter three cannot be easily distinguished due to their close genetic background, and their individual contribution estimates may be impacted by their similarity. Despite all, the sum of their average contributions to the F8 is 40.4%, which is close to the expected contribution of 37.5%.

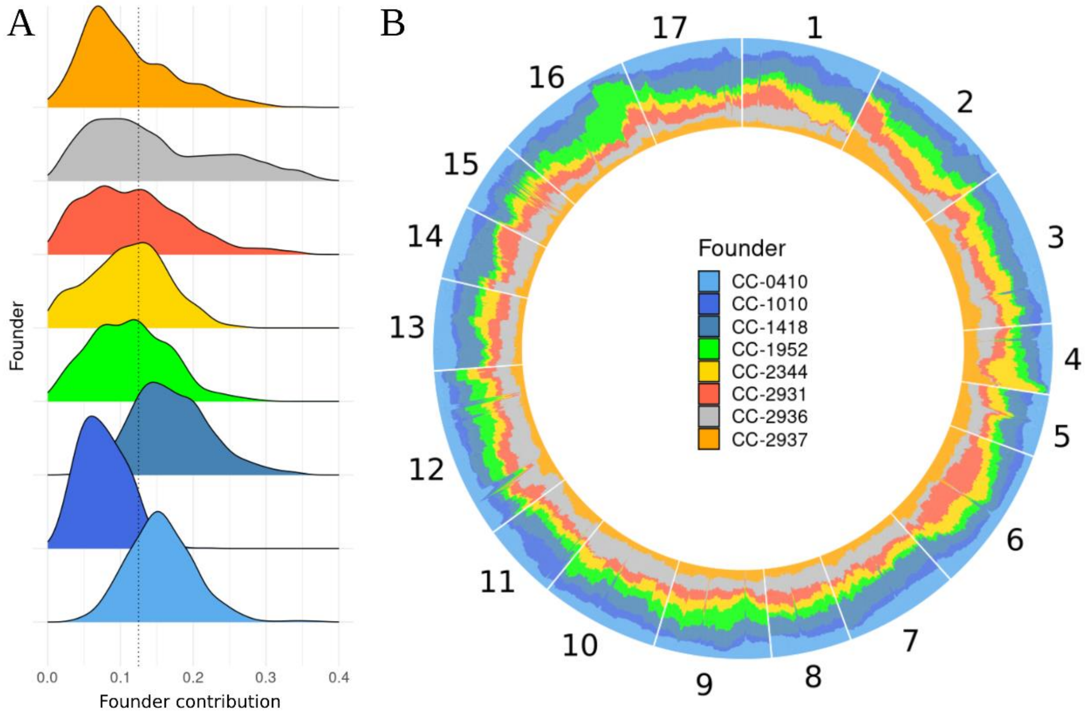

Figure 3. 5: Founder's genetic contribution to the MAGIC population. (A) Overall view of the founder's contribution on 615 MLs. (B) Local founder's contribution across the 17 chromosomes composing the genome of 768 MLs.

The variation along the genome of the contribution of the eight founders to the population was also studied. To that end, the founder probabilities were averaged in 10 kb windows for each F8 line. These values were then used to estimate the contribution of each founder in each window at the population level. The analysis of the local founder's haplotype probability distribution for each chromosome revealed an overall homogeneous pattern of contribution across the genome (Fig.3.5-B). On the other hand, some genomic regions displayed higher contributions from one or a few founders. An example can be observed on chromosome 16, where CC-1952's haplotype frequency was found to be much higher than the frequency of other founders. A similar example can be observed at the end of chromosome 4, where the haplotype of CC-2344 was much more present in the population.

To further investigate the population's structure, 2,712,214 biallelic variants were selected to perform a principal component analysis (PCA). The first two principal components together explain 6.7% of the variation among the MAGIC lines (MLs) and allow to discern the three independent replicates of the MAGIC design (Sup. Figure 8). Other components seem unrelated to the substructure, and it takes 235 principal components to capture 90% of the genetic diversity among the MLs. This result suggests that our crossing design yielded a homogeneous F8, minimizing the presence of substructure within the population.

Similarity among the F8 lines was estimated based on the distribution of proportion of identical-by-state (IBS) genotypes $SI_{ii'}$ among each pair of F8 lines. These similarity indices ranged from 0.563 to 0.999 % of IBS genotypes with an average of 0.680 and a median of 0.675 (Sup. Figure 9). We observed that 92 pairs of lines had a similarity index above 0.95 (less than 5% different genotypes) indicating that these were not siblings, but identical colonies. A total of 126 F8 lines had at least one ‘clone’, and the largest group of clones involved five lines (two other groups contained four clones). The levels of pairwise relatedness $g_{ii'}$ ranged from 0.023 to 0.893 and were equal to 0.159 on average, slightly higher than the expected 0.125. Overall, the results confirm that the eight generations of crossing resulted in a relatively uniform level of relatedness among F8 lines, as planned. Several levels of structure were observed within the population (Sup. Figure 10), of which the first level was the higher genetic relatedness within the independent replicates of the design (three main blocks). In addition, a clear family-effect is observable. Indeed, families of eight individuals deriving from the same F7 parents are expected to have a genetic relatedness of 0.5. Neighboring families also display higher relatedness as they share the same grandparents. When relatedness was estimated for pair of F8 lines from the same or from different families, the average relatedness was equal to 0.491 (range 0.115-0.891) and 0.155 (range 0.023-0.625) respectively, in agreement with our expectations (Figure 3.6).

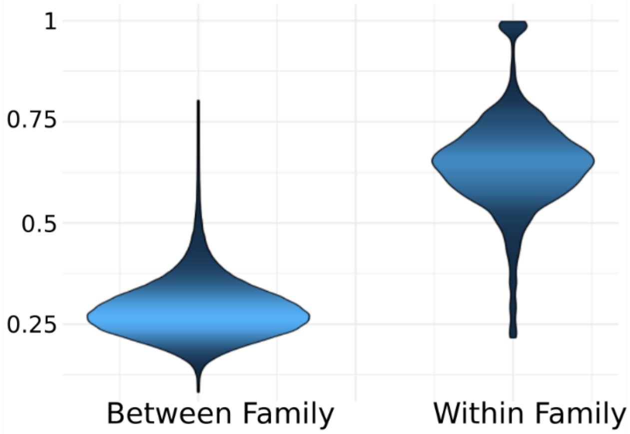

Figure 3. 6: Distribution of estimated relatedness among F8 lines, between and within families.

The between-family relatedness was found to be above 0.125, probably due to the remaining cryptic structure (e.g., relatedness between neighboring families) present among the genetic lines. Our estimation of relatedness assumes that founders are unrelated, however, they share several IBD segments that result in a higher relatedness within the MAGIC population. Accordingly, we re-estimated relatedness considering the IBD segments shared by the founders. We observed that, by taking into account that information, the average relatedness was higher, with an average of 0.648 within family (range 0.219-0.996) and 0.286 between family (range 0.084-0.801).

3.2.2 Phenotypic and genotypic characterization of the MAGIC population

The light protocols

As the tests performed on the 25 wild-types yielded only NPQ values lower than 1 and most of the strains presented high Fv/Fm values even in TMP (see Figure 2.7 and 2.8), I decided to increase the light-intensity of the growth chamber from 100 to 150 μmol of photons · m^{-2} · s^{-1}. As 96 samples were measured simultaneously, a great effort was made in finding the most accurate set up and reducing the variability caused by the technical error. An experiment was conducted to assess the uniformity of the measurement within the surface of a white flat-bottom 96-wells microplate, observing no variation within 96 technical replicates (Sup. Figure 11). The phenotyping of the MAGIC population was carried out over a period of 8 weeks, growing 96 MLs per week in double biological replicate under mixotrophy (TAP) or autotrophy (TMP). The previously presented ChlF modulation protocol (see figure 2.10 and 3.7-A) was used to monitor Fv/Fm, rETR, total and fast-relaxing NPQ. Given the previous observations about different kinetics of NPQ relaxation between CC-2936 and CC-1010 (see figure 2.14), I assessed different ways to capture NPQ diversity among the MAGIC lines. One way of doing so was to calculate, within the first 15 minutes of dark following the saturation curve, the number of minutes needed to reach the maximum Fm ("NPQ-relaxation time"). A second method was to calculate the amount of NPQ relaxed within the first 5 seconds of dark ("NPQ fast loss"). Due to the level of diversity among the samples in

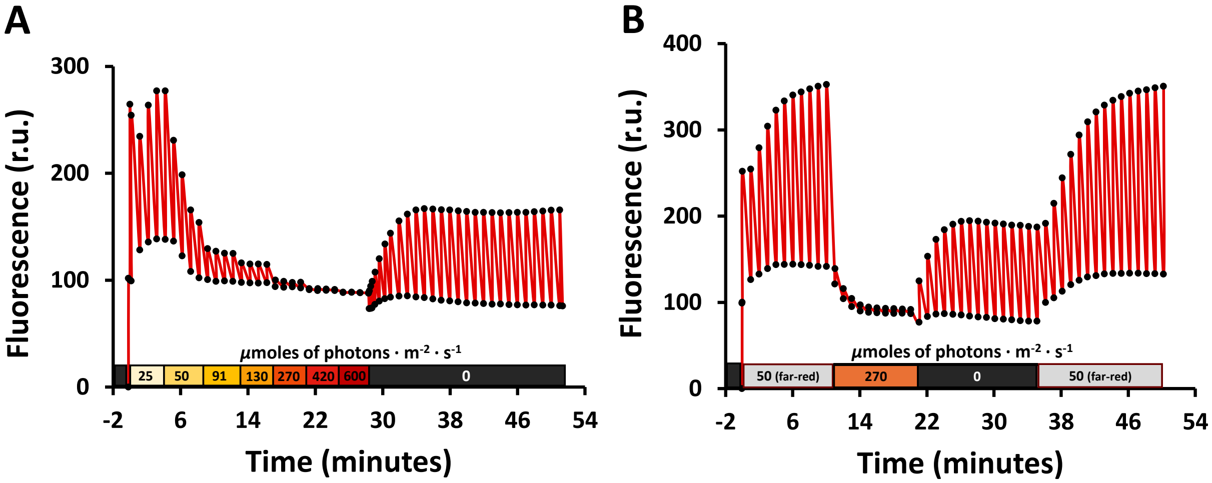

Figure 3. 7: The time-resolved chlorophyll fluorescence detection protocols used to phenotype the MAGIC population. (A) Saturation curve equal to the one presented in figure 2.10. The decrease in light-intensity with respect to figure 2.10 is due to the positioning of the samples at a different distance from the light source. (B) New protocol designed to estimate the state transition capacity upon dark (qT). The sequence starts with 10 minutes of far-red light (730-750 nm) to set all samples to "state 1", following, a mild high-light stress is applied for 10 minutes. After the stress, 15 minutes of dark allow the relaxation of NPQ's pH-dependent components and development of dark qT. The protocol ends with 15 minutes of far-red light to bring the samples back to state 1. The amount of dark state transition was estimated as Fm-Fm'/Fm' where Fm was the average of the last three Fm points of the sequence (far-red steady state fluorescence after dark) and Fm' was the average of the last three Fm points upon dark. The NPQ formula was also used to assess differences in chlorophyll a steady state fluorescence between the first and the second far-red treatment. In this case, Fm was the average of the last three Fm points upon the first far-red exposure (state 1 fluorescence emission before HL treatment) and Fm' was the average of the last three Fm points of the second far-red treatment (state 1 fluorescence emission after HL). The relative loss of fluorescence was defined as "photoinhibition" or qI.

response to the measurement and the impossibility to check all raw fluorescence curves one by one (3200 measurements in total), both NPQ and fast-relaxing NPQ were calculated during the dark phase using several timepoints as Fm' or Fm (after 1 minute, 11 minutes, or 22 minutes of dark, etc.) as an attempt to spot any unusual NPQ behavior among the MLs.

Beside the previous ChlF modulation protocol, I created a second protocol that could be used to parameterize state transition (qT) (Figure 3.7-B). The protocol consisted of 10 minutes of far-red light (730-750nm) to obtain the Fm of samples in full state 1 (Roach, 2022), followed by 10 minutes of HL aimed to refurbish the cellular NADPH supply, whereupon samples were left in the dark for 15 minutes, letting them develop physiological qT. Finally, 15 minutes of far-red light were applied to induce transition to full state 1, and qT was estimated as the difference between maximum fluorescence upon state 1 (Fm) minus the maximum fluorescence upon dark (Fm') divided Fm'. Moreover, I used the maximum fluorescence recorded on far-red adapted samples before (Fm) and after (Fm') the HL step to estimate the NPQ component that did not relax upon 15 minutes of dark + 15 minutes of far-red. I defined this component as photoinhibition (qI). To confirm that the fluorescence increase upon far-red illumination was linked to qT, the sequence was tested on the STT7-lacking mutant, *stt7,* after culturing it in TMP-LL (Sup. Figure 12-A) or TMP-vHL (Sup. Figure 12-B) for 24h. No Fm-relaxation was observed in *stt7* upon far-red, indicating that the wild-type fluorescence increase is clearly caused by transition from state "x", variable from strain to strain, to state 1. The sequence was also tested on CC-1010 and CC-2936, confirming the previous observation that the two strains present significant differences in their qT capacity in the dark (Sup. Figure 12-C). Small aliquots of the samples were harvested during the fluorescence measurement, at minute 35 (end of the dark step) and minute 50 (end of the second far-red step) and quickly plunged into liquid nitrogen to assess their 77°K fluorescence emission spectra. Due to the different nature of the two techniques (the former is *in vivo*, the latter is not), results were difficult to compare, and the different qT capacity observed *in vivo* on TMP-LL samples was not captured by the ratio of the 715nm/685nm 77°K emission bands (Sup. Figure 12-D). Instead, the difference (see section 2.2.3) between the two strains was well captured by both techniques when cells were grown under TMP-vHL.

Phenotypic diversity among the MLs

Pictures of the plates were taken every week across the phenotyping process, and 28 strains were observed to not grow under the experimental conditions. Thus, I decided to filter them out from the dataset. Moreover, datapoints found to be 4-standard-deviations away from the mean were considered as "missing value" for each trait. Under both TMP and TAP conditions, the analyzed traits presented a unimodal distribution with a variable level of skewness (Sup. Figure 14). A multimodal distribution was observed only for the parameter "NPQ Relaxation Time".

To retrieve information about the extent of phenotypic diversity present within MLs, the rETR and NPQ (Figure 3.8) of the 8 founders were compared to those of the entire population. No significant differences were observed between the two groups, indicating that the majority of the MLs presented a phenotype that significantly resembled the one of the 8 founders.

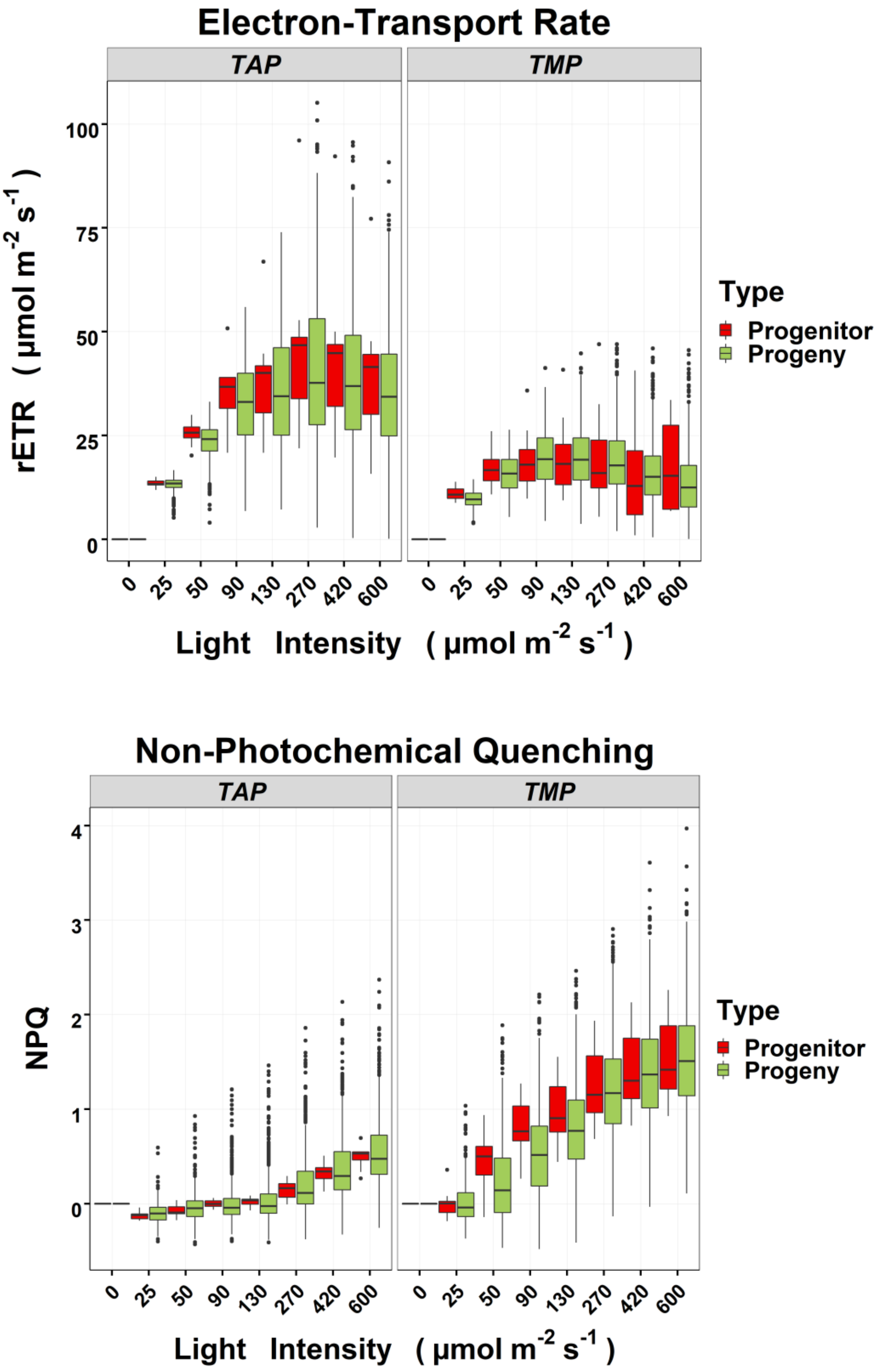

Figure 3. 8: Photosynthetic diversity within the MAGIC population. The rETR (above) and NPQ (below) phenotype of the 8 founders (red boxes) and of the 768 MLs (green boxes) was monitored on samples grown under mixotrophic (TAP) and photoautotrophic (TMP) condition. rETR values below 0 (36 entries) were filtered out.

However, for NPQ, several MLs presented extreme phenotypes that did not appear within the founders. The same pattern was also observed for other traits connected to NPQ such as the fast-relaxing NPQ (NPQ relaxed after 1 or 11 minutes of dark), the dark NPQ (NPQ present after 1 minute or 22 minutes of dark), the Fv/Fm (influenced by the qI developed during growth), the qT and qI. As the majority of MLs experienced a decrease in rETR upon light intensities above 270 μmoles of photons m^{-2} s^{-1} (Figure 3.8), we decided to use this light-step (from here referred to as “maximum ETR”) for the aim of QTL-mapping. On the other hand, maximal NPQ levels were always reached upon 600 μmoles of photons m^{-2} s^{-1} (Figure 3.8), thus we used the NPQ values recorded upon the last light-step (from here referred to as “maximum NPQ”) to map related QTLs. It is important to mention that, for both TMP and TAP samples, rETR at 270 μmoles of photons m^{-2} s^{-1} showed a correlation of 0.9 ($p<0.001$) to rETR values at 600 μmoles of photons m^{-2} s^{-1}, and even higher correlation was observed for NPQ (Sup. Figure 15). Therefore, data from the three light intensities could be used interchangeably for the aim of QTL-mapping, yielding similar results. As observed in my previous experiments, a negative correlation between NPQ and rETR was observed also within the MAGIC population. In TMP samples, *r* was below -0.4 only during the initial steps of the saturation curve (*r* = -0.45, $p<0.001$), while TAP samples displayed the same negative correlation coefficient (*r* = -0.45, $p<0.001$) throughout all light-steps (Sup. Figure 15, Figure 3.9).

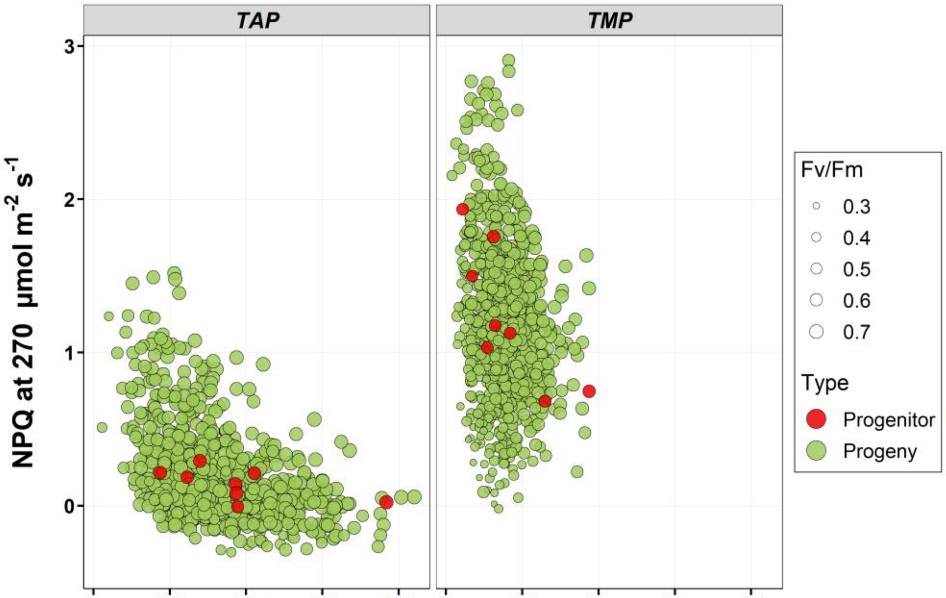

Figure 3. 9: Relationship between rETR and NPQ measured on the MAGIC population at 270 μmoles of photons m^{-2} s^{-1} (third-last step of the saturation curve). The Pearson’s coefficient (*r*) was -0.45 for TAP and -0.21 for TMP samples. The size of the dots represents the Fv/Fm value.

Under mixotrophic condition, a weak but significant positive correlation was observed between the initial Fv/Fm and the maximum rETR of the population (*r* = 0.2, $p<0.001$), while no correlation was observed between Fv/Fm and NPQ under the same condition. On samples grown photo-autotrophically, Fv/Fm was highly correlated to both maximum rETR and NPQ (r = 0.46 and 0.52 respectively, $p<0.001$), suggesting that under this condition both pathways contribute to the preservation of PSII-quantum efficiency without competing for the excitation energy. To evaluate the level of redundancy among all NPQ-related parameters candidate to QTL-mapping, their correlation to each-other and to the photosynthetic efficiency (Fv/Fm and maximum rETR) was computed (Sup. Figure 16). For the photoautotrophic condition, we observed a positive correlation between Fv/Fm and most of the assessed NPQ parameters. Exceptions were the state-transition capacity in the dark (qT), for which no correlation to Fv/Fm and maximum rETR was observed, and the NPQ-relaxation time (time in minutes corresponding to the highest Fm value recorded within the first 15 minutes of dark after the saturation curve), which was negatively correlated to both Fv/Fm and maximum rETR. Interestingly, a significant correlation was observed between rETR and all parameters related to the NPQ after 1 minute of dark. Particularly, the amount of fast-relaxing NPQ quantified after 1 minute of dark positively correlated to the Fv/Fm (*r* = 0.46, $p\leq0.001$) and maximum ETR capacity (*r* = 0.43, $p\leq0.001$), while a less significant correlation to the Fv/Fm (*r* = 0.33, $p\leq0.001$) and no correlation to the maximum rETR was observed for the same parameter calculated after 11 minutes of dark. An even higher positive correlation was observed between the maximum rETR and the amount of NPQ relaxed within 5 seconds of dark ("NPQ-fast loss") (*r* = 0.52, $p\leq0.001$). Accordingly, a negative correlation was observed between the maximum rETR and the amount of NPQ that did not relax after 1 minute of dark ("NPQdark_1m") (*r* = -0.43, $p\leq0.001$) and the NPQ-relaxation time (*r* = -0.22, $p\leq0.001$), suggesting that strains with higher rETR are more likely to relax a higher portion of NPQ within the first minutes of dark. This result recalls the precedent results obtained during the comparison of CC-1010 (high-ETR and fast-relaxing NPQ) and CC-2936 (low-ETR and slow-relaxing NPQ), suggesting that a higher buffering capacity of the lumen could improve electron-transport upon high-light while resulting in a fast NPQ-relaxation in the dark. No correlation was found between the maximum NPQ ("NPQ600") and "NPQ-fast loss", "NPQ-relaxation time" or qT. The latter showed positive correlation only with "NPQdark_1m" (*r* = 0.1, $p\leq0.01$) and "NPQdark_22m" (*r* = 0.28, $p\leq0.001$). This is not surprising as it is well known that state-transition accounts for an important portion of dark NPQ in *C. reinhardtii* (Allorent et al., 2013; Nawrocki et al., 2016; Steen et al., 2022). A negative correlation with qT was observed for qI (*r* = -0.26, $p\leq0.001$), NPQ-relaxation time (*r* = -0.17, $p\leq0.001$) and fast-relaxing NPQ after 11 minutes of dark (FmDR_11m) (*r* = -0.11, $p\leq0.01$). A switch in several parameters' correlation was observed when looking at the dataset of strains grown in presence of acetate (TAP). Under this condition, a significant negative correlation was found between the maximum rETR and most of the NPQ parameters. A positive correlation was found only with qT (*r* = 0.44, $p\leq0.001$), suggesting that, under mixotrophic condition, the amount of dark state-transition strongly relies on the rate of LEF, while no dependency was observed in absence of acetate (see Figure 3.10). A positive correlation was found between Fv/Fm and the NPQdark_22m, the latter being not correlated to qT and highly correlated to qI (*r* = 0.54, $p\leq0.001$). Therefore, it is tempting to conclude that the differences in Fv/Fm observed within the population are the result of a pre-existent qI differentially developed upon the experimental stress condition. Indeed, we found that strains that were more susceptible to qI were also less likely to present a high value of maximum rETR (*r* = -0.47, $p\leq0.001$). Under photoautotrophic conditions, higher correlation was observed between the maximum NPQ and most of the other NPQ-related parameters under this condition, confirming the trend observed for the founders.

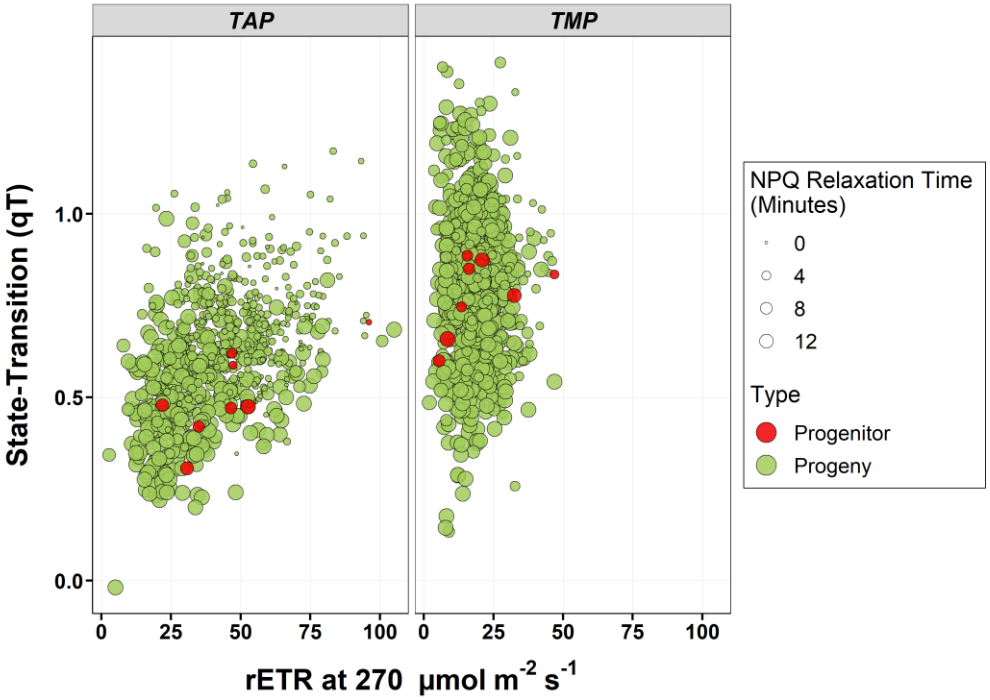

Figure 3. 10: Relationship between maximum rETR and qT measured on the MAGIC. The Pearson's coefficient (*r*) was -0.44 for TAP and 0.002 for TMP samples. The size of the dots represents the parameter "NPQ-Relaxation Time". For the latter, a correlation of -0.35 (TAP) and -0.22 (TMP) was observed with maximum rETR, while -0.47 (TAP) and -0.17 (TMP) was the correlation observed with qT.

Heritability and genetic correlation among photosynthetic traits

A single-trait linear mixed model was used for the estimation of heritability and repeatability (see Materials and Methods). All phenotypes were highly repeatable (measured as r^2 between biological replicates) suggesting that the experimental setup minimized the environmental error and that photosynthetic traits could be highly heritable. The repeatability ranged from 0.62 to 0.97 (out of 22 assessed traits, 20 and 10 traits had repeatability above 0.80 and 0.90 respectively). Our analysis of the heritability (h^2) confirmed that the observed phenotypic differences have strong genetic bases under both trophic conditions (Figure 3.11), ranging from 0.38 to 0.83 in TAP (mean = 0.63) and from 0.51 to 0.83 in TMP (mean = 0.67). Previous estimations of heritability for ΦPSII were attempted in *Arabidopsis* plants exposed to 200 and 550 µmol m_{-2} s_{-1}, yielding similarly high values (see Flood et al., 2016)

To improve our understanding of the genetic constraints existing between photosynthetic traits, genetic correlation was computed for each trait between phenotypes measured in different trophic conditions, and for each pair of traits recorded under the same condition. Phenotypes measured in TMP presented genetic correlations most often between 0.40 and 0.70 with their counterpart measured in TAP (0.54 on average; see Sup. Table 5). A much lower genetic correlation was observed for "NPQ_fast_loss" (0.26), suggesting a strong contribution of the environmental factors and/or the genetic contribution of many loci to this trait under different trophic conditions.

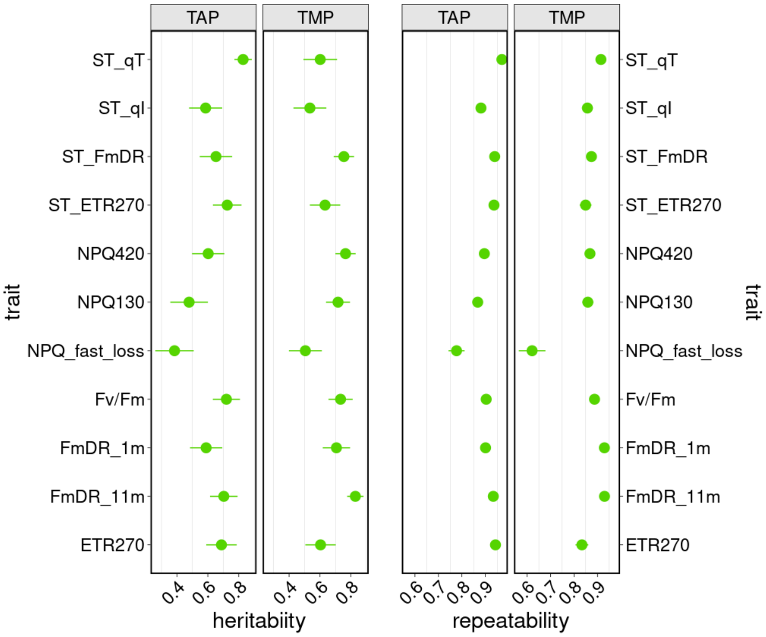

Figure 3. 11: (Left) Heritability and (right) repeatability of the different photosynthetic traits in TAP and TMP. The dots represent the averages and the lines the standard error.

As for the phenotypic correlation analysis discussed at the beginning of this paragraph, genetic correlations between pairs of different traits were also identified (Figure 3.12). Under mixotrophic condition, four main correlation clusters were identified. The first cluster includes the state-transition capacity in the dark ("qT") and the rETR measured under 270 μmoles of photons m^{-2} s^{-1} ("ETR270"), both showing a strong genetic correlation (0.6) with each-other and a negative correlation with the rest of NPQ-related parameters. The second cluster includes the NPQ capacity under mild ("NPQ130" ; 130 μmoles of photons m^{-2} s^{-1}) or very high-light intensity ("NPQ420" ; 420 μmoles of photons m^{-2} s^{-1}), and the amount of NPQ relaxed after 1 minute ("FmDR_1m") or 11 minutes ("FmDR_11m") of dark. This cluster of traits showed very high positive correlation with each other and a weaker positive correlation with the amount of NPQ lost within the first 5 seconds of dark ("NPQ_fast_loss"), while they negatively correlated to the first cluster. A third cluster including the maximum quantum yield of dark-adapted PSII ("Fv/Fm") and "NPQ_fast_loss" showed no correlation, or week negative correlation, with cluster one and weak positive correlation with cluster two. Finally, "qI" formed a cluster on its own being negatively correlated to cluster one and cluster two and showing a weak positive correlation to cluster three. Under photoautotrophic condition, we observed a shift in the genetic correlation matrix's structure, suggesting that different sets of loci contributed to the phenotypes in TMP. A major change was observed for "qT", for which genetic correlation with the maximum ETR dropped dramatically (from 0.6 to -0.09) in absence of acetate, while remaining negatively correlated to "qI". The latter resulted more (positively) correlated to "NPQ130". While weak- or no correlation was observed for "Fv/Fm" in TAP, a strong positive correlation was observed with all other traits (except "qT") under photoautotrophic conditions. Finally, we observed a weakening of the negative correlation between “ETR270” and NPQ-related parameters, with “NPQ130” showing the strongest correlation.

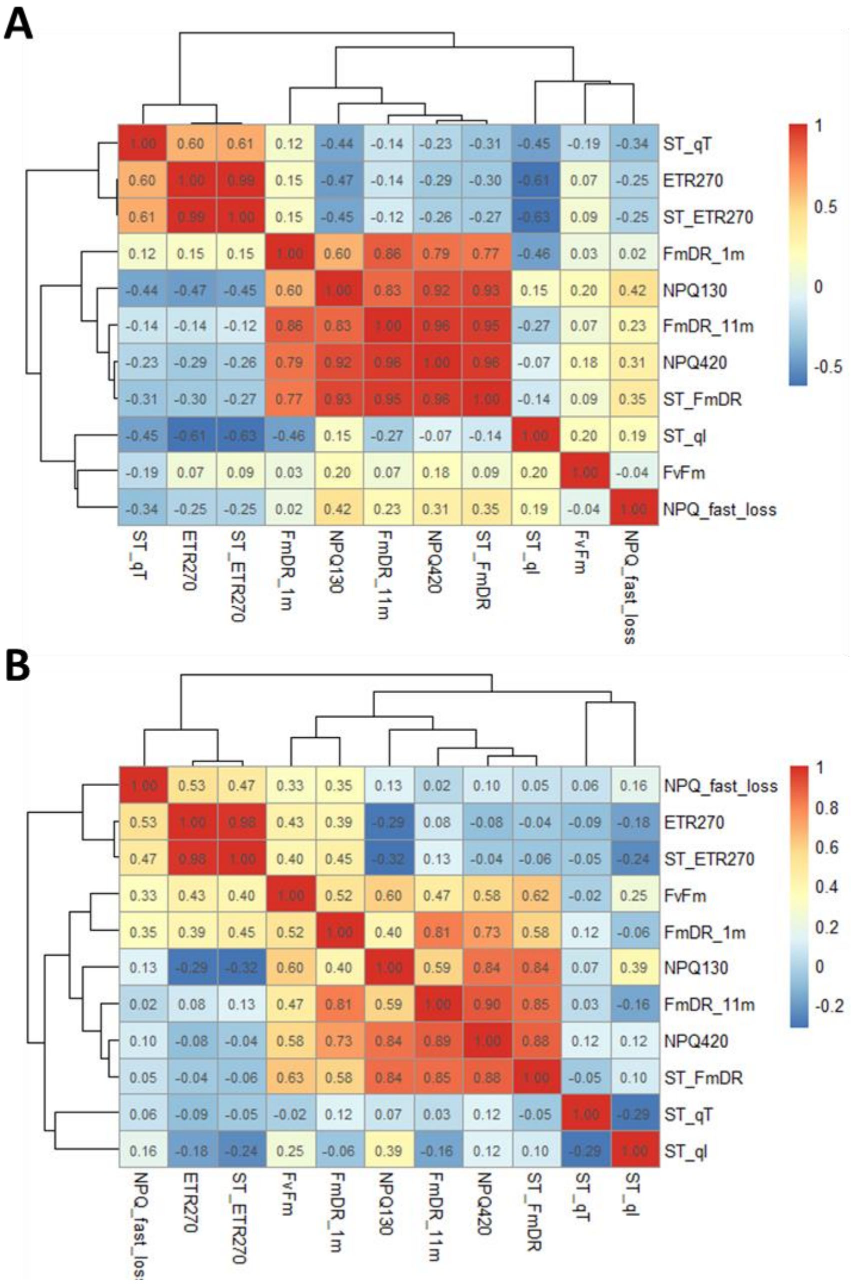

	ST_qT	ETR270	ST_ETR270	FmDR_1m	NPQ130	FmDR_11m	NPQ420	ST_FmDR	ST_qI	FvFm	NPQ_fast_loss
ST_qT	1.00	0.60	0.61	0.12	-0.44	-0.14	-0.23	-0.31	-0.45	-0.19	-0.34
ETR270	0.60	1.00	0.99	0.15	-0.47	-0.14	-0.29	-0.30	-0.61	0.07	-0.25
ST_ETR270	0.61	0.99	1.00	0.15	-0.45	-0.12	-0.26	-0.27	-0.63	0.09	-0.25
FmDR_1m	0.12	0.15	0.15	1.00	0.60	0.86	0.79	0.77	-0.46	0.03	0.02
NPQ130	-0.44	-0.47	-0.45	0.60	1.00	0.83	0.92	0.93	0.15	0.20	0.42
FmDR_11m	-0.14	-0.14	-0.12	0.86	0.83	1.00	0.96	0.95	-0.27	0.07	0.23
NPQ420	-0.23	-0.29	-0.26	0.79	0.92	0.96	1.00	0.96	-0.07	0.18	0.31
ST_FmDR	-0.31	-0.30	-0.27	0.77	0.93	0.95	0.96	1.00	-0.14	0.09	0.35
ST_qI	-0.45	-0.61	-0.63	-0.46	0.15	-0.27	-0.07	-0.14	1.00	0.20	0.19
FvFm	-0.19	0.07	0.09	0.03	0.20	0.07	0.18	0.09	0.20	1.00	-0.04
NPQ_fast_loss	-0.34	-0.25	-0.25	0.02	0.42	0.23	0.31	0.35	0.19	-0.04	1.00

	NPQ_fast_los	ETR270	ST_ETR270	FvFm	FmDR_1m	NPQ130	FmDR_11m	NPQ420	ST_FmDR	ST_qT	ST_qI
NPQ_fast_loss	1.00	0.53	0.47	0.33	0.35	0.13	0.02	0.10	0.05	0.06	0.16
ETR270	0.53	1.00	0.98	0.43	0.39	-0.29	0.08	-0.08	-0.04	-0.09	-0.18
ST_ETR270	0.47	0.98	1.00	0.40	0.45	-0.32	0.13	-0.04	-0.06	-0.05	-0.24
FvFm	0.33	0.43	0.40	1.00	0.52	0.60	0.47	0.58	0.62	-0.02	0.25
FmDR_1m	0.35	0.39	0.45	0.52	1.00	0.40	0.81	0.73	0.58	0.12	-0.06
NPQ130	0.13	-0.29	-0.32	0.60	0.40	1.00	0.59	0.84	0.84	0.07	0.39
FmDR_11m	0.02	0.08	0.13	0.47	0.81	0.59	1.00	0.90	0.85	0.03	-0.16
NPQ420	0.10	-0.08	-0.04	0.58	0.73	0.84	0.89	1.00	0.88	0.12	0.12
ST_FmDR	0.05	-0.04	-0.06	0.63	0.58	0.84	0.85	0.88	1.00	-0.05	0.10
ST_qT	0.06	-0.09	-0.05	-0.02	0.12	0.07	0.03	0.12	-0.05	1.00	-0.29
ST_qI	0.16	-0.18	-0.24	0.25	-0.06	0.39	-0.16	0.12	0.10	-0.29	1.00

Figure 3. 12: Genetic correlations between photosynthetic phenotypes measured in (**A**) TAP and (**B**) TMP.

3.2.3 Quantitative trait loci (QTLs) mapping

In the frame of our collaborative project, QTL mapping was performed on 116 phenotypic traits, analyzed all at once using the same bioinformatic pipeline. Hereby, I describe the overall outcome of the mapping analysis performed on all phenotypic traits but focusing my attention only on the results that strictly concern the phenotypes discussed within this manuscript. The rest of the results are discussed in Cardoso Esteves (2023). A visual summary of spatial distribution of photosynthetic QTLs is provided in figure 3.13.

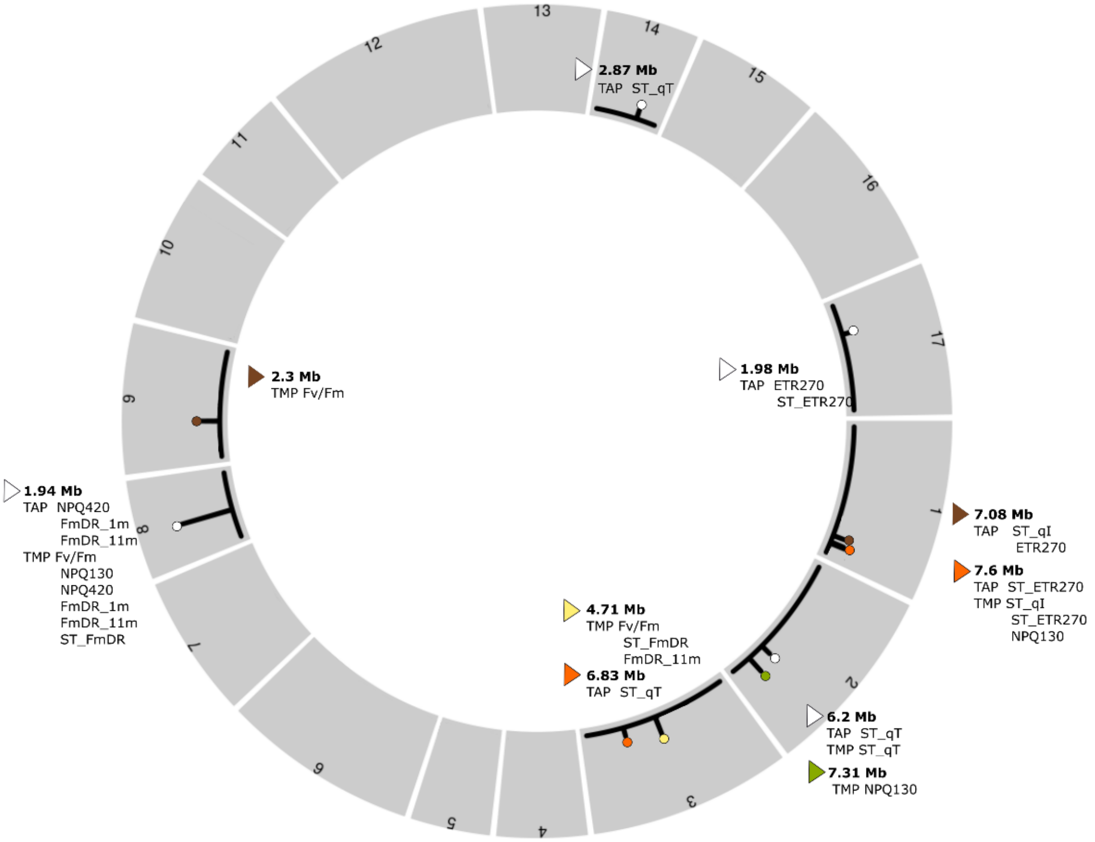

Figure 3. 13: Visual summary of QTL groups related the photosynthetic traits relevant to this dissertation. The grey block composing the circos represent the 17 chromosomes of *C. reinhardtii*. Full chromosomes are marked in black when they harbor at least one QTL, with the lollipops marking the position of the QTL peak (position with highest significance) for each group. The height of the lollipop bar reflects the QTL's significance level on a -log10 scale.

The analysis of eleven photosynthetic traits measured under two trophic conditions (TAP and TMP) led to the identification of 26 significant QTLs (from 0 to 3 QTLs per trait). The average confidence intervals of the mapped QTLs were 584 kb in length (median 395 kb), with the shortest being 150 kb long and including 22 genes, and the biggest being 1790 kb long and including 294 genes. The most significant QTL (p-value = 4.47E-52) was mapped on chromosome 8 for the trait "FmDR_11m" under photoautotrophic condition, accounting for 37% of between-line genetic variance. No QTLs were found for "NPQ_fast_loss". This result is consistent with the low heritability values observed for this trait. In most cases, two or more QTLs associated with different traits were mapped on the same chromosomal region. Based on overlapping confidence intervals (CIs), we summarized the 93 QTLs, including those reported in Cardoso Esteves (2023), into 30 QTL regions (or "QTL groups"; Table 4). For photosynthetic traits, the only QTL regions associated with a single trait were found to be associated with qT. The rest was either grouped with other photosynthetic QTLs, or with traits related to metal homeostasis (not discussed within this thesis, see Cardoso Esteves, 2023).

Table 4: Summary of QTLs mapped during the Green MAGIC project. QTLs associated with the photosynthetic traits described within this PhD dissertation are highlighted in bold.

QTL Group	Condition	Trait	Chr	Start (Mb)	Stop (Mb)	Genes (no.)	Log10(P-val.)	Size (kb)	Explained Variance
1	Cu	K.nmol	09	7.20	7.62	64	7.64	420	0.12
1	Cu	ODvar	09	7.21	7.73	84	10.48	520	0.33
1	Mn	K.nmol	09	7.20	7.69	79	8.31	490	0.13
1	Fe	PhiPSII	09	7.20	7.74	88	10.43	540	0.21
1	S	K.nmol	09	7.20	7.58	60	11.62	380	0.16
1	S	ODvar	09	7.21	7.35	22	12.37	140	0.15
1	S	Fv/Fm	09	7.21	7.63	66	12.13	420	0.13
1	S	PhiPSII	09	7.21	7.59	61	17.21	380	0.26
1	**TMP_photo**	**NPQ130**	**09**	**7.20**	**7.62**	**64**	**7.88**	**420**	**0.12**
1	TAP	K.nmol	09	7.21	7.58	59	13.94	370	0.13
1	TAP	Na.nmol	09	7.21	7.59	61	8.41	380	0.17
1	TAP	ODvar	09	7.21	7.74	87	7.97	530	0.14
1	Ca	K.nmol	09	7.18	7.33	26	6.85	150	0.17
2	Ca	Zn.nmol	10	5.63	5.71	15	43.36	80	0.51
2	Mn	Zn.nmol	10	5.63	5.71	15	87.8	80	0.46
3	Ca	Fv/Fm	09	2.01	2.33	47	17.2	320	0.17
3	Cu	Fv/Fm	09	2.01	2.34	49	7.12	330	0.09
3	Fe	Fv/Fm	09	2.01	2.34	49	11.32	330	0.06
3	TAP	Fv/Fm	09	2.02	2.33	46	17.68	310	0.16
3	**TMP_photo**	**Fv/Fm**	**09**	**2.02**	**2.42**	**60**	**6.73**	**400**	**0.08**
4	Cu	NPQ	16	7.45	7.99	94	7.36	540	0.09
4	TAP	NPQ	16	7.45	7.86	71	9.2	410	0.07
5	Ca	Fe.nmol	01	7.20	8.21	138	7.29	1010	0.22
5	Mn	K.nmol	01	7.10	7.87	100	10.32	770	0.17
5	Mn	Fe.nmol	01	7.34	7.85	74	15.39	510	0.24
5	Fe	K.nmol	01	7.39	7.83	64	8.56	440	0.10
5	S	K.nmol	01	6.91	8.09	163	7.92	1180	0.06

5	**TAP_photo**	**ST_ETR270**	**01**	**7.06**	**7.83**	**96**	**10.91**	**770**	**0.12**
5	**TMP_photo**	**ST_qI**	**01**	**7.46**	**7.82**	**48**	**11.2**	**360**	**0.13**
5	**TMP_photo**	**ST_ETR270**	**01**	**7.19**	**7.35**	**5**	**7.22**	**160**	**0.05**
5	TAP	K.nmol	01	7.21	7.92	94	8.74	710	0.08
5	TAP	Mn.nmol	01	7.51	7.82	46	9.12	310	0.08
5	Mn	PhiPSII	01	7.46	7.92	70	7.38	460	0.07
5	**TMP_photo**	**NPQ130**	**01**	**7.35**	**7.82**	**67**	**6.96**	**470**	**0.03**
6	Cu	Mn.nmol	03	2.49	2.71	36	17.43	220	0.16
6	Fe	Mn.nmol	03	2.59	2.94	56	10.04	350	0.07
6	TAP	Mn.nmol	03	2.49	2.71	36	17.69	220	0.12
7	Cu	Mn.nmol	10	2.21	2.50	43	9.68	290	0.07
7	TAP	Mg.nmol	10	2.21	2.73	86	7.73	520	0.07
7	TAP	Mn.nmol	10	2.21	2.51	44	9.09	300	0.07
8	Cu	Fe.nmol	01	4.63	6.41	286	8.11	1780	0.15
8	Cu	Zn.nmol	01	5.49	6.15	106	6.71	660	0.13
9	Cu	Ca.nmol	07	1.42	2.13	118	7.7	710	0.08
9	Mn	P.nmol	07	1.58	2.76	186	7.84	1180	0.06
9	Mn	Ca.nmol	07	1.58	2.34	117	11.16	760	0.10
9	TAP	Ca.nmol	07	1.58	2.73	183	8.12	1150	0.08
10	Mn	Mg.nmol	16	6.32	6.45	18	17.61	130	0.26
10	Mn	P.nmol	16	6.32	6.60	44	12.34	280	0.20
10	Mn	Ca.nmol	16	6.32	6.83	80	8.2	510	0.08
10	TAP	Mg.nmol	16	6.32	6.56	38	13.42	240	0.16
10	TAP	P.nmol	16	6.22	6.57	57	8.91	350	0.07
11	Mn	Fv/Fm	03	4.55	4.90	59	18.79	350	0.15
11	S	Fv/Fm	03	4.31	6.26	371	7.4	1950	0.06
11	**TMP_photo**	**Fv/Fm**	**03**	**4.44**	**5.68**	**244**	**9.09**	**1240**	**0.14**
11	**TMP_photo**	**ST_FmDR**	**03**	**4.31**	**5.49**	**227**	**8.59**	**1180**	**0.07**
11	**TMP_photo**	**FmDR_11m**	**03**	**4.73**	**4.95**	**42**	**6.97**	**220**	**0.05**
12	Mn	Fv/Fm	09	0.44	0.59	24	7.41	150	0.05
13	Fe	Mn.nmol	09	3.46	3.69	31	16.74	230	0.12
14	Fe	Mn.nmol	16	5.13	5.77	108	20.22	640	0.15
15	Fe	Ca.nmol	16	4.82	5.15	48	9.39	330	0.13
16	**TAP_photo**	**ST_qT**	**02**	**6.08**	**6.45**	**63**	**10.71**	**370**	**0.09**
16	**TMP_photo**	**ST_qT**	**02**	**6.20**	**6.35**	**22**	**6.61**	**150**	**0.09**
17	**TAP_photo**	**ST_qT**	**03**	**5.74**	**7.53**	**294**	**8.63**	**1790**	**0.04**
18	**TAP_photo**	**ST_qT**	**14**	**2.62**	**2.95**	**47**	**9.72**	**330**	**0.08**
19	**TAP_photo**	**ST_qI**	**01**	**6.53**	**7.77**	**171**	**11.73**	**1240**	**0.20**
19	**TAP_photo**	**ETR270**	**01**	**6.73**	**7.84**	**149**	**7.98**	**1110**	**0.10**
20	**TAP_photo**	**NPQ420**	**08**	**1.84**	**2.61**	**126**	**7.34**	**770**	**0.10**
20	**TAP_photo**	**FmDR_1m**	**08**	**1.73**	**2.12**	**66**	**15.42**	**390**	**0.18**

20	**TAP_photo**	**FmDR_11m**	**08**	**1.84**	**2.22**	**64**	**11.48**	**380**	**0.13**
20	**TMP_photo**	**Fv/Fm**	**08**	**1.54**	**2.22**	**114**	**8**	**680**	**0.08**
20	**TMP_photo**	**NPQ130**	**08**	**1.84**	**2.11**	**46**	**17.43**	**270**	**0.16**
20	**TMP_photo**	**NPQ420**	**08**	**1.85**	**2.02**	**27**	**44.76**	**170**	**0.37**
20	**TMP_photo**	**FmDR_1m**	**08**	**1.85**	**2.11**	**45**	**33.76**	**260**	**0.31**
20	**TMP_photo**	**FmDR_11m**	**08**	**1.85**	**2.02**	**27**	**51.35**	**170**	**0.37**
20	**TMP_photo**	**ST_FmDR**	**08**	**1.84**	**2.11**	**46**	**26.86**	**270**	**0.22**
20	TAP	NPQ	08	1.49	2.57	180	9.46	1080	0.12
21	**TAP_photo**	**ST_ETR270**	**17**	**1.53**	**2.65**	**201**	**7.27**	**1120**	**0.11**
21	**TAP_photo**	**ETR270**	**17**	**1.71**	**2.20**	**83**	**6.86**	**490**	**0.10**
22	TAP	OD1T	10	2.48	4.08	245	8.12	1600	0.06
22	TAP	Fe.nmol	10	2.51	4.18	262	6.89	1670	0.08
23	Mn	ODvar	01	7.42	8.22	119	13.61	800	0.13
24	S	Mg.nmol	15	2.59	3.02	20	7.1	430	0.20
24	S	Fv/Fm	15	2.82	3.24	58	9.23	420	0.03
26	Fe	Fv/Fm	03	3.96	4.40	83	6.77	440	0.04
27	Mn	Ca.nmol	04	2.48	2.77	29	6.96	290	0.05
28	Cu	Zn.nmol	12	5.40	5.71	24	6.74	310	0.12
28	Fe	Zn.nmol	12	5.40	5.86	84	6.93	460	0.16
29	Mn	Zn.nmol	01	8.00	8.21	36	15.32	210	0.08
30	Ca	Fv/Fm	01	8.07	8.21	21	7.35	140	0.03
30	Ca	NPQ	01	8.08	8.20	18	11.31	120	0.03
30	Cu	Fv/Fm	01	8.06	8.21	25	7.42	150	0.05
30	Cu	NPQ	01	8.09	8.20	16	14.12	110	0.22
30	Mn	NPQ	01	8.05	8.20	27	16.54	150	0.16

For QTLs mapped to the same genomic region, likelihood ratio curves often presented similar patterns, and founder haplotype effects, estimated for each trait of the group, presented the same structure (e.g., the same founder haplotype had an outstanding effect; Figure 3.14). To determine whether overlapping CIs represented a single pleiotropic QTL or multiple neighboring QTLs, a multiple-trait LMM was used to estimate the genetic correlations among QTL effects for each genomic region. Large correlations were observed among QTL effects on different traits associated with the same region. For a large majority of cases, these correlations were > 0.90, indicating pleiotropy. Even if not every pair of traits within a QTL group showed such high QTL effects' correlation, a correlation > 0.90 was observed with at least one other trait in the group. A lower correlation was observed for QTL-group 16, where two overlapping QTLs affecting qT in TAP and TMP showed a correlation between QTL effects around 0.80, still high enough to consider this QTL as pleiotropic.

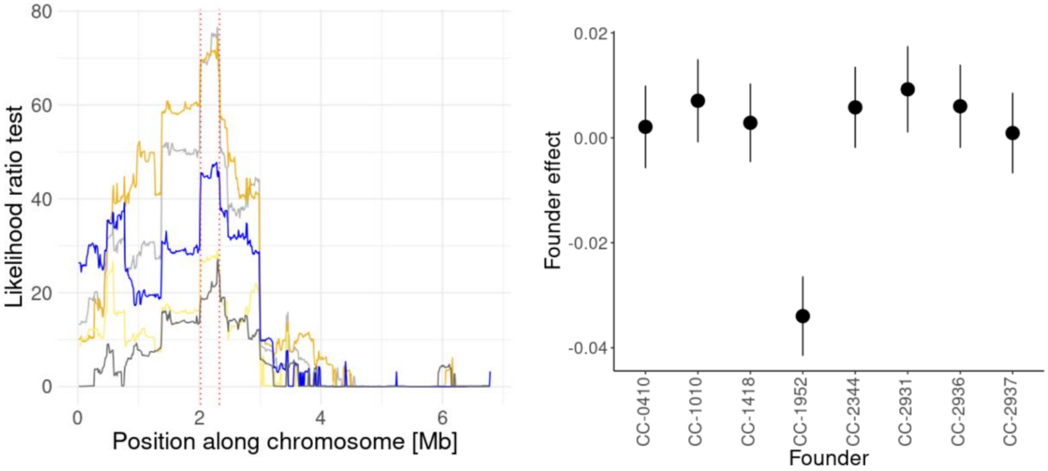

Figure 3. 14: Illustration of pleiotropic QTL affecting Fv/Fm in six different experimental conditions (QTL-group 3). The panel on the left shows the likelihood ratio curves of the 5 traits along chromosome 9. The panel on the right shows the 8 founder haplotype effects for the condition showing the highest significance within the QTL-group (grey line in the left panel).

Pleiotropy could involve the same phenotype measured under different nutrients deficiency conditions, as illustrated for QTL-group 3 affecting Fv/Fm in Figure 3.14. Pleotropic QTLs might also affect different phenotypes under the same condition (“condition-specific QTL”). Some examples of such QTLs can be observed for QTL-group 11, affecting the phenotype only under autotrophic condition, and for QTL-groups 16, 17, 19, and 21, found only under mixotrophy. Overall, many of the pleiotropic QTLs affect several phenotypes under multiple conditions. Two outstanding QTLs affecting many phenotype x condition combinations, related to photosynthesis, growth, and mineral concentration are: QTL on chromosome 1 (QTL-group 5; including 12 traits), and on chromosome 2 (QTL-group 1; including 13 traits). Another major pleotropic QTL is linked to QTL-group 20, on chromosome 8, and associated with 10 photosynthetic traits related to photoprotection, under autotrophic or mixotrophic conditions. In general, QTL effects were positively correlated: photosynthetic traits affected by pleiotropic QTLs were observed to follow similar trends. Similarly, QTL effects measured in one condition were positively correlated with the effects in another conditions, indicating genotype-by-environment interactions changing the magnitude of QTL effects without re-ranking founder haplotype effects or creating opposite effects.

3.2.4 QTL confidence intervals and fine-mapping

We used a multiple-trait QTL association mapping approach for each QTL group containing more than one trait, to take advantage of multiple correlated traits information and reduce the overall confidence interval of each group. As expected, this approach achieved systematically higher significance (measured by likelihood ratio test, or LRT) compared to the single-trait approach. The CIs were successfully reduced in 12 QTL groups and remained identical in 4 groups (1,2,3,20). However, a modest CI increase was obtained for 3 out of 19 QTL groups (4,7,11). The final confidence intervals ranged from 70 to 1480 kb (average = 466; median = 370), in agreement with the LD between 10 kb-windows. The number of genes within the CI ranged from 9 to 225 (average = 73; median = 59). To further characterize each QTL-group, we performed a sequence-based association study within each determined CI. This approach relied on genotype probabilities estimated for the F8 lines on all the variants selected at the sequence level (see material and methods). These genotype probabilities were obtained by combining the low-fold sequence information (the read observed in each F8), the founder probabilities (the probability to derive from one founder at one position) and the genotypes from the eight founders (determined with high-confidence thanks to their high sequencing coverage). Fine-mapping was performed for all QTL regions. Hereafter, we illustrate the approach for some of the regions of interest: the most significant QTL-region on chromosome 8 (QTL-group 20), associated with NPQ-related traits, the QTL-group 3, significant for Fv/Fm under five conditions, and the QTL-group 16, associated with qT. For each of these QTLs, a clear pattern was observed among the founder haplotype effects, and it was possible to determine which founders probably share identical QTL alleles. As visible from the Manhattan plot in figure 3.15-A, two QTLs were mapped for FmDR_11m, one on chromosome 3 and a second of much higher significance, on chromosome 8. The latter is a pleotropic QTL associated with several photoprotective traits showing similar likelihood ratio test curve profile, of which TMP_FmDR_11m showed the highest significance. The likelihood ratio curves of all QTL-group's members are also shown (Figure 3.15-B). At the maximum position of the QTL mapping, haplotype founder effects present three levels suggesting at the presence of three QTL alleles (Figure 3.15-C). CC-2931 carries an allele with an outstanding negative effect, whereas CC-1952 and CC-2344 seem to carry a different allele enhancing the phenotype (Figure 3.15-C). After performing the sequenced-based GWAS, the lead bi-allelic SNP (highest significance) correspond to an allele specific to CC-2931, presenting high linkage disequilibrium with 672 other bi-allelic SNPs. As Freebayes calls haplotypes (not only SNPs), approximately 12.4% of the used variants were multi-allelic (> 2 alleles). Among those, a tri-allelic variant fits the pattern observed among the haplotype effects and therefore achieves higher significance than the biallelic variants. Using this information, we could sort each variant within the CI (Figure 3.15-D) based on whether the alleles partially (variants colored in yellow) or fully (variants colored in green) fit the founder haplotype effects. For example, many biallelic variants captured only a part of the haplotype effects, e.g., being carried only by CC-2931, whereas CC-1952 and CC-2344 carry the same variant as the rest of the founders. Although tri-allelic variants present higher association, there is no guarantee that the causative polymorphism is a tri-allelic variant, and the QTL could be the result of two closely linked distinct mutations, one carried by CC-2931 and the other carried by CC-1952 and CC-2344.

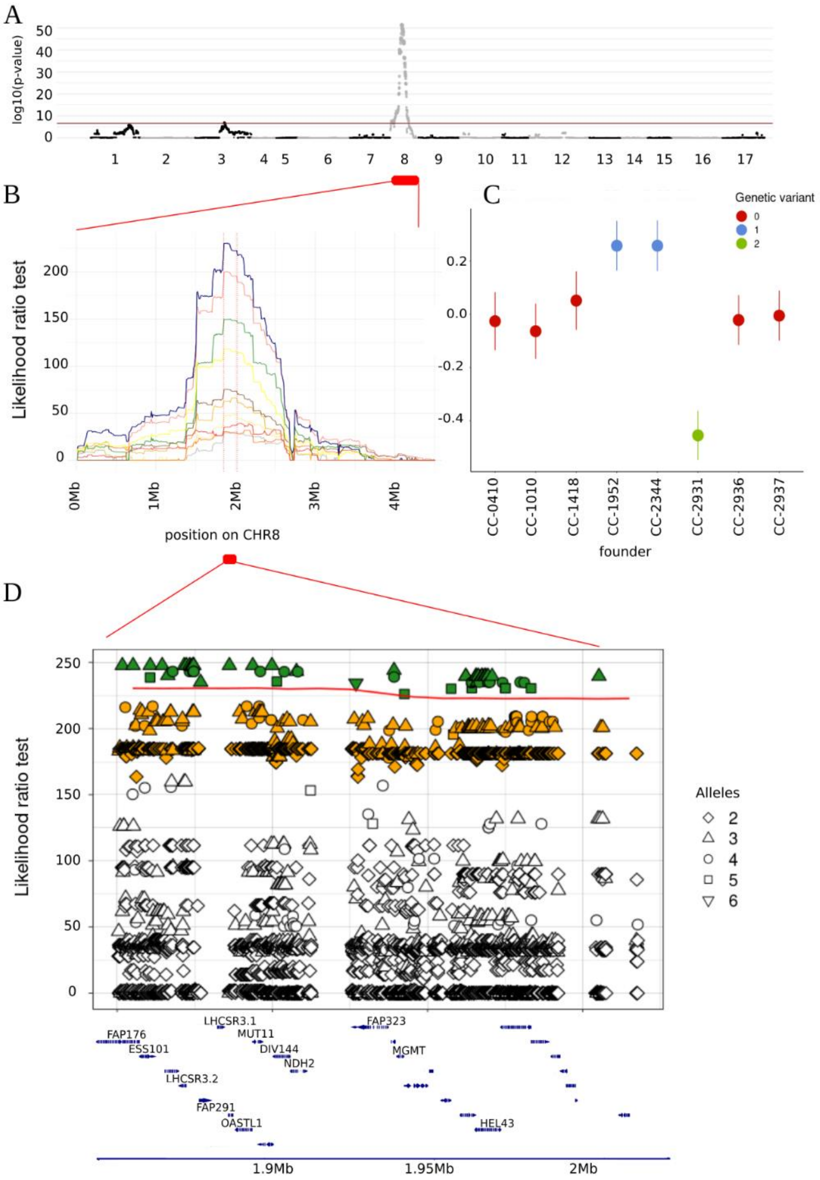

Figure 3. 15: Description of the QTL-group 20. (A) Manhattan plot showing the strength of association (-log10-P) of the analyzed variants (dots), distributed across the entire genome, with the variation for FmDR_11m. The red line represents the significance threshold, and the dots above the line indicate the localization of the significant associations mapped for that trait. (B) Magnification of the genomic region corresponding to the pleotropic QTL located on chromosome 8. The colored lines indicate the LR curves for the traits belonging to the QTL-group. The line colored in blue corresponds to FmDR_11m, showing the highest association. The two red-vertical lines indicate the corresponding QTL-confidence interval. (C) Founder haplotype effects for the trait FmDR_11m. The color code indicates the number of alleles (in this case three) of the variant showing highest association (pinpointed through the fine-mapping analysis), and their distribution among the founders. (D) Distribution and allele-number of the refined set of candidate variants after fine-mapping. The variants colored in green are those that fit the haplotype effect pattern, while those in yellow fit the pattern for CC-2931. The blue

So far, the analysis of the QTL on chromosome 8 allowed us to reduce the set of candidate variants from the initial number of 5166 to a final set of 816 candidates (yellow and green variants in figure 3.15-D). However, it was not possible to further refine this subset of variants based on statistical evidence, due to the lack of recombination in the region. We observed that variants unique to CC-2931 (colored in yellow) presented stronger association and were responsible for a large part of the signal. Therefore, a first approach could be to focus our search on all the significant variants, both bi- or multi-allelic, for which CC-2931 carries a unique allele. Doing so, we could further reduce the number of candidate variants to 750. Nonetheless, the overall number of genes harboring at least 1 candidate variant would remain the same (27 genes within the confidence interval).

For the QTL-group 3, on chromosome 9, results show a strong effect associated with CC-1952 (Figure 3.16). Similarly to what was observed for the QTL on chromosome 8, when we tagged variants with an allele specific to CC-1952, we found that they captured all the most significant variants, but also that the overall number of candidate variants remained high and widespread over the entire confidence interval. The number of such candidate variants is equal to 1182, distributed across 42 genes (Figure 3.16).

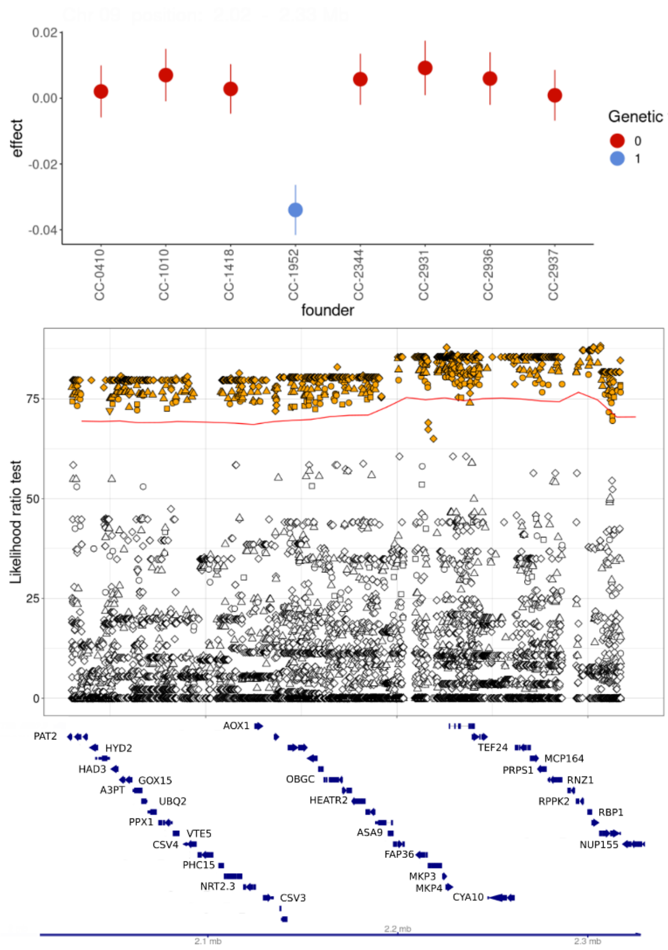

Figure 3. 16: Fine-mapping of QTL-group 3 on chromosome 9. The top-panel shows the founder haplotype effects for the trait Fv/Fm_-Mn (see Cardoso Esteves, 2023). The color code indicates the number of alleles (in this case two) of the variant showing highest association (pinpointed through fine-mapping analysis), and their distribution among the founders. The bottom-panel shows the distribution and allele-number (shape) of the refined set of candidate variants after fine-mapping. The variants colored in yellow are those that better fit the haplotype effect pattern (CC-1952 carries a unique allele). The blue tracks represent the genes found within the CI.

Finally, for the QTL-group 16 (chromosome 2), we observed that variants opposing laboratory strains to the field-isolated strains were among the most significant variants (256 variants in total, spread across 31 genes, Figure 3.17). Interestingly, a small part of the QTL region presented a higher LRT, probably due to recombination in the genomic region, resulting in an increase of signal. For this QTL, our approach based on the founder haplotype effects led to a reduction of the credible gene set from 57 to 9 final candidate genes.

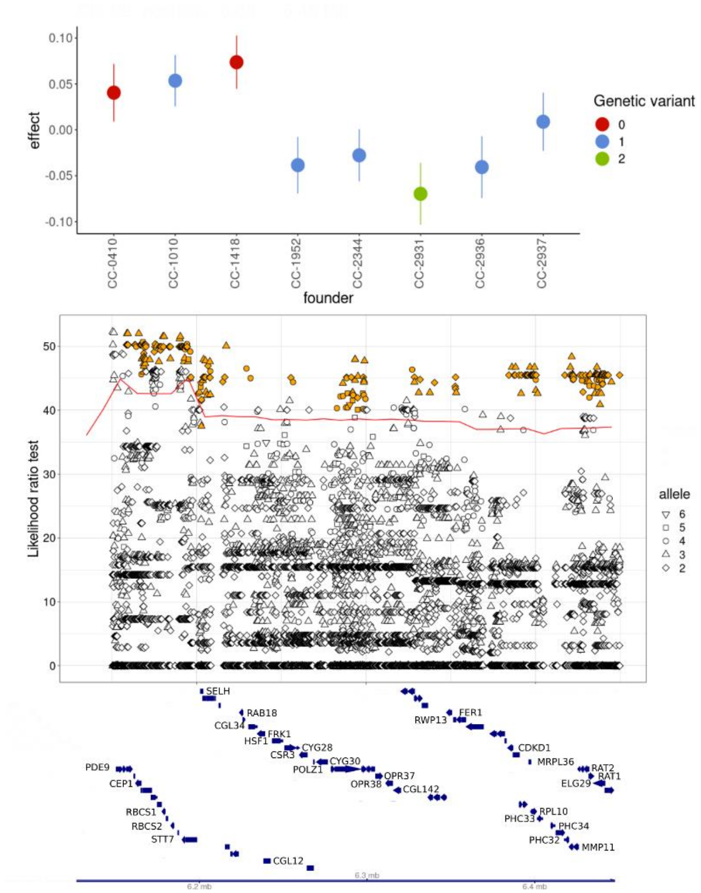

Figure 3. 17: Fine-mapping of QTL-group 16 on chromosome 2. The top-panel shows the founder haplotype effects for the trait qT_TAP. The color code indicates the number of alleles (in this case three) of the variant showing highest association (pinpointed through fine-mapping analysis), and their distribution among the founders. The bottom-panel shows the distribution and allele-number (shape) of the refined set of candidate variants after fine-mapping. The variants colored in yellow are those that better fit the haplotype effect pattern (the three laboratory strains carrying a different allele than the rest of the founders for those variants). The blue tracks represent the genes found within the CI.

The three QTL groups presented above include some strong candidate genes within their CI. For the QTL associated with photoprotection (chromosome 8), we found the presence of the two homolog genes coding for the main NPQ effector protein LHCSR3 (*LHCSR3.1* and *LHCSR3.2*). Nonetheless, none of the significant variants were predicted to result in moderate or high-impact mutations, and about 20 variants were considered as “modifier” by SnpEff (Cingolani et al., 2012), being localized within untranscribed regions. Our analysis cannot predict if such variants cause differences in the regulation of gene expression, so further analyses will be required before drawing any conclusion. Moreover, other 25 genes are present within the same confidence interval, many of which have not yet been characterized. Another very strong candidate gene was found within the CI of QTL group 16 (chromosome 2), associated with state transition under both autotrophic and mixotrophic conditions. The gene in question is *STT7*, the chloroplast protein kinase required for state transition in *C. reinhardtii* (Depège et al., 2003). In this case, SnpEff predicted 1 mutation with moderate effect and 20 variants classified as “modifier”. The gene is located within the CI portion presenting a higher LRT, close to other two strong candidate genes coding for RuBisCO’s small subunit 1 (*RBCS1*) and 2 (*RBCS2*). The latter two harbor only few “modifier” mutations, spread across the gene regions. Finally, for the QTL on chromosome 9, associated to Fv/Fm under 5 different conditions, the refined gene set includes *Protoporphyrinogen IX oxidase 1* (*PPX1*), participating to heme and chlorophyll biosynthesis in the chloroplast, and recently proposed to interact with the ETC by transferring electrons to the PQ-pool during the oxidation of protoporphyrinogen IX (Protogen) into protoporphyrin IX (Proto) (Brzezowski et al., 2019).One moderate-effect and 8 modifier variants were predicted on *PPX1*.

By combining founder haplotype effects with a sequenced-based association approach, we reduced the number of candidate variants and genes for most of the confidence intervals. However, as founder haplotypes were inherited in relatively large blocks, a high number of variants show equally high significance and match the founder haplotype effects pattern. Even for QTLs including strong candidate genes like the ones presented above, several other genes (often of unknown function) are found within the CIs (see Sup. Table 6). Therefore, additional experiments will be required to identify causative variants. Moreover, for some QTLs, it was not possible to identify a clear founder haplotype effect pattern (high heterogeneity among the founders). For QTLs showing such patterns, our current approach was ineffective at reducing the number of candidate variants. In addition, for some regions, we observed high variation among significance levels of variants presenting the same allele pattern in the founders. This suggests that, in those regions, the founder probabilities at two close loci are different, indicating fuzzy LD patterns in the region. This phenomenon may be due to the admixture pattern reported earlier on.

3.1 Conclusion

In this chapter, I described the creation and characterization of the first MAGIC population available in the species *C. reinhardtii*. For many decades, the *Chlamydomonas*' community conducted countless experiments on a handful of interrelated strains, assuming that the outcome would apply to the entire species. If this is true in most cases, some preliminary studies (Ferris, 1989; Flowers et al., 2015; Gallaher et al., 2015) revealed the presence of wide genetic and phenotypic intraspecific diversity among strains from different origins. Our study greatly complements the current knowledge, showing that the wide phenotypic diversity existing among different *C. reinhardtii* wild-type strains challenges the meaning of "standard" in this species. Under our experimental conditions, some strains showed poor mating capacity with others, pointing to the existence of intraspecific variation in the regulation of sexual reproduction. Our data suggest that wide intraspecific diversity in the management of metals homeostasis exists in *C. reinahrdtii* (see Cardoso Esteves, 2023). As gametogenesis is induced by nutrients deprivation, it would be reasonable to think that, under equal experimental conditions, some strains may need more time to perceive the same level of stress, thus producing less gametes. Indeed, sexual reproduction is a complex biological process, involving several crucial phases. Low compatibility might be caused by many other reasons. Some examples are: low mating affinity (recognition and agglutination), zygotes apoptosis, or zygospores' low germination energy. Thus, some targeted research will be needed to better understand the dynamics of sexual reproduction among the strains, under controlled or natural environments.

The MAGIC design was constructed by crossing 8 founders from different origins through 8 generations of crossing. The final MAGIC population is composed of 768 genetic lines sub-structured into 96 families of 8 siblings. Our genomic analysis on 2,712,214 bi-allelic variants revealed the mosaic structure of the population, showing the high-level of genetic diversity enclosed in this biological resource. The average level of pairwise relatedness among the population was close to our initial predictions, confirming the overall equal genetic contribution of the eight founders to the MAGIC lines. The MAGIC population was constructed to address biological questions using quantitative genetics, and we developed a quantitative genetic study to dissect the complex architecture of photosynthesis. The photosynthetic phenotyping of the MAGIC population was performed by time-resolved chlorophyll fluorescence, retrieving information about the quantum efficiency of PSII under increasing light intensities, and its recovery in the dark. In parallel, several NPQ-related parameters were measured, including the level of dark qT, for which wide and highly reproducible differences were observed among the population. The MLs exhibited transgressive trait variation (offspring extremes exceeded the parental extremes) for most of the measured parameters. However, no transgressive segregation was observed for the maximal electron-transport rate, highlighting the biophysical constrains of chloroplast's electron-transport. In agreement with our previous observations, a negative correlation between maximal rETR and maximal NPQ was observed in the MAGIC population, only upon mixotrophic growth. Our data demonstrates that the negative correlation is independent from the initial Fv/Fm, and strains with high Fv/Fm can display either high or low rETR as function of their NPQ capacity. Moreover, no correlation was observed between Fv/Fm and maximal NPQ under the same condition, suggesting that in presence of acetate, different physiological mechanisms ensure the stability of the ETC upon HL exposure. On the other hand, the correlation analysis of data retrieved on photoautotrophic cultures highlighted the importance of both photochemical and non-photochemical quenching in the protection of PSII maximum yield under minimal condition. Moreover, we observed a positive correlation between the amount of NPQ relaxed during the first minute of dark and the maximal rETR, similarly to the pattern observed on CC-1010 and CC-2936. According to the existing evidence and knowledge, I conclude that under low-CO_2 conditions, the ETC capacity could be set by the buffering capacity (or ionic strength) of the chloroplast subcompartments, regulated by the activity of the cellular transportome (i.e. all channels and membrane transporters that participate to efflux and influx of ions). The presented results provide the first evidence of an active role of the CCM in the regulation of K^+ fluxes *in vivo*. This novel finding opens the road to new research, potentially critical for the engineering of the CCM into plants.

Despite of its relevance, photosynthesis is the only major physiological trait not to have been directly bred for during the agricultural history (Flood et al., 2011; Flood et al., 2016). The dissection of the heritable structure of photosynthesis on a fine scale is an uncharted territory in many model species. In this study we provide the first estimation of heritability available in *C. reinhardtii* for the main photosynthetic parameters, measured in TAP and TMP. Overall, the photosynthetic parameters showed high heritability, suggesting the presence of a strong genetic base, suitable for strains improvement by artificial selection. The solid genetic bases of photosynthetic traits also highlight the potential for adaptation of *C. reinhardtii* in response to the environmental pressure. Interestingly, a switch in heritability was observed for some parameters depending on the trophic condition. In presence of acetate, the highest heritability value was observed for qT, followed by the maximum rETR, and Fv/Fm. On the other hand, the fast-relaxing NPQ (FmDR_11) and other NPQ-related parameters showed higher heritability under minimal conditions. These results suggest that, depending on the trophic conditions, the environmental factors may have a variable influence on the different photosynthetic traits.

The genetic correlation between photosynthetic traits was also computed. The results of our analysis suggest the presence of pleiotropic variants affecting the measured traits, and that the genetic relationship between traits is highly influenced by the trophic conditions. A clear example of such phenomenon was observed for the Fv/Fm, that showed high genetic correlation with NPQ-related parameters only under photoautotrophic conditions. Another interesting pattern was observed for qT, showing high correlation with the maximum rETR and a negative correlation with NPQ, only under mixotrophic conditions. Our quantitative genetic approach led to the mapping of 26 QTLs linked to photosynthesis, including 3 associated with rETR, >3 with NPQ-related parameters, 3 specifically with state transition, and 3 with Fv/Fm. In agreement with the genetic correlations estimated between photosynthetic traits, our analysis led to the mapping of several pleotropic QTLs affecting two or more traits. The photosynthetic QTL with the largest effect in terms of % of phenotypic variation was mapped on chromosome 8 (group 20), associated with NPQ, and its confidence interval encompassed the two main photoprotective genes *LHCSR3.1* and *LHCSR3.2*. The combination of founder haplotype effects with a sequenced-based association approach was used to refine the set of candidate variants within each confidence interval. This approach led to the reduction of the number of candidate variants for each confidence interval. Following the fine-mapping process, some of the credible gene sets were reduced to a number of genes as small as 9 (e.g., QTL group 16), thus some interesting candidate genes could be identified for most of the QTLs by glimpsing at the gene lists. Genes that are potentially involved in the associated phenotype, like *LHCSR3.1* and *LHCSR3.2* for NPQ and *STT7* for qT, are indeed very appealing candidates. Nonetheless, the candidate gene-sets also include many uncharacterized genes, sometimes accounting for over 50% of the total genes within the confidence interval. Thus, more work will be needed to pinpoint and validate the causative gene variants for each group. A strategy to gain more information about QTLs including evident candidates (e.g., *LHCSR3*, *STT7*, and *PPX1*) would be the selection of MLs presenting different haplotypes for the locus of interest. The selected lines could be used to assess the transcript-levels of the candidate genes as well as the protein levels, so to exclude/confirm the presence of differential regulation for those elements. Moreover, MLs carrying different alleles could be used as founders in new crossing schemes of smaller size, leading to further recombination events and consequent reduction of the CIs.

Chapter 4

4.1 Materials and methods

Strains and growth conditions

Strains used in this study were purchased through the Chlamydomonas Resource Center website (https://www.chlamycollection.org/) and maintained on Tris-Acetate-Phosphate (Gorman and Levine, 1965) (TAP)-1.5% agar plates under 22°C and 10 µmol m^{-2} s^{-1} (LL) of white continuous light.

For experiments into flasks: pre-cultures were routinely started from fresh agar plates into liquid TAP medium at very low cellular concentration. Pre-cultures were cultured in sterile Erlenmeyer flasks at 25 °C under 30 µmol m^{-2} s^{-1} (LL) of white continuous light until mid-log phase. Total chlorophylls content was estimated by methanol extraction and spectrophotometric analysis (Lambda 265 PDA UV-VIS Spectrophotometer, PerkinElmer) as explained in (Porra et al., 1989). Pre-cultured cells were harvested by centrifugation (1500 g for 5 minutes) and resuspended into sterile Tris-Minimal-Phosphate (TMP) medium with (mixotrophic growth) or without (photoautotrophic growth) the addition of glacial acetate to the final concentration of 20 mM. Experimental cultures were started at different concentrations of total chlorophylls/mL, ranging from 2 to 10, according to the experimental needs. In all experiments, temperature was maintained at 24±1°C and batch cultures were cultivated using a home-made device consisting of a computer interfaced to a rack equipped with white LEDs and propped on an orbital shaker. Experimental light was defined as low-light (LL ; 30 µmol m^{-2} s^{-1}), high-light (HL ; 300 µmol m^{-2} s^{-1}), and very high-light (vHL ; 470 µmol m^{-2} s^{-1}).

For the phenotyping of the MAGIC population: cells grown on TAP-1.5% agar plates were inoculated at very low cellular concentration into 2mL of sterile TAP and cultured into transparent flat-bottom 24-well microplates, agitating under 25 °C and 100 µmol m^{-2} s^{-1} of white light (“preculture-1”). After 48 hours, 50µL of preculture-1 were transferred to a sterile round-bottom 96-deep-well microplate filled with TAP to a final volume of 800µL and cultured without agitation under 25 °C and 50 µmol m^{-2} s^{-1} of white light (“preculture-2”). After 72 hours, 120µL (photoautotrophic experiments) or 50µL (mixotrophic experiments) of preculture-2 were transferred to a sterile round-bottom 96-deep-well microplate filled with TMP or TAP to a final volume of 800µL and cultured without agitation under 25 °C and 150 µmol m^{-2} s^{-1} of white light (“experimental cultures”). After 48h of growth under the experimental condition, pictures of the plates were taken from the bottom, then cells were harvested and phenotyped (section 3.2.2).

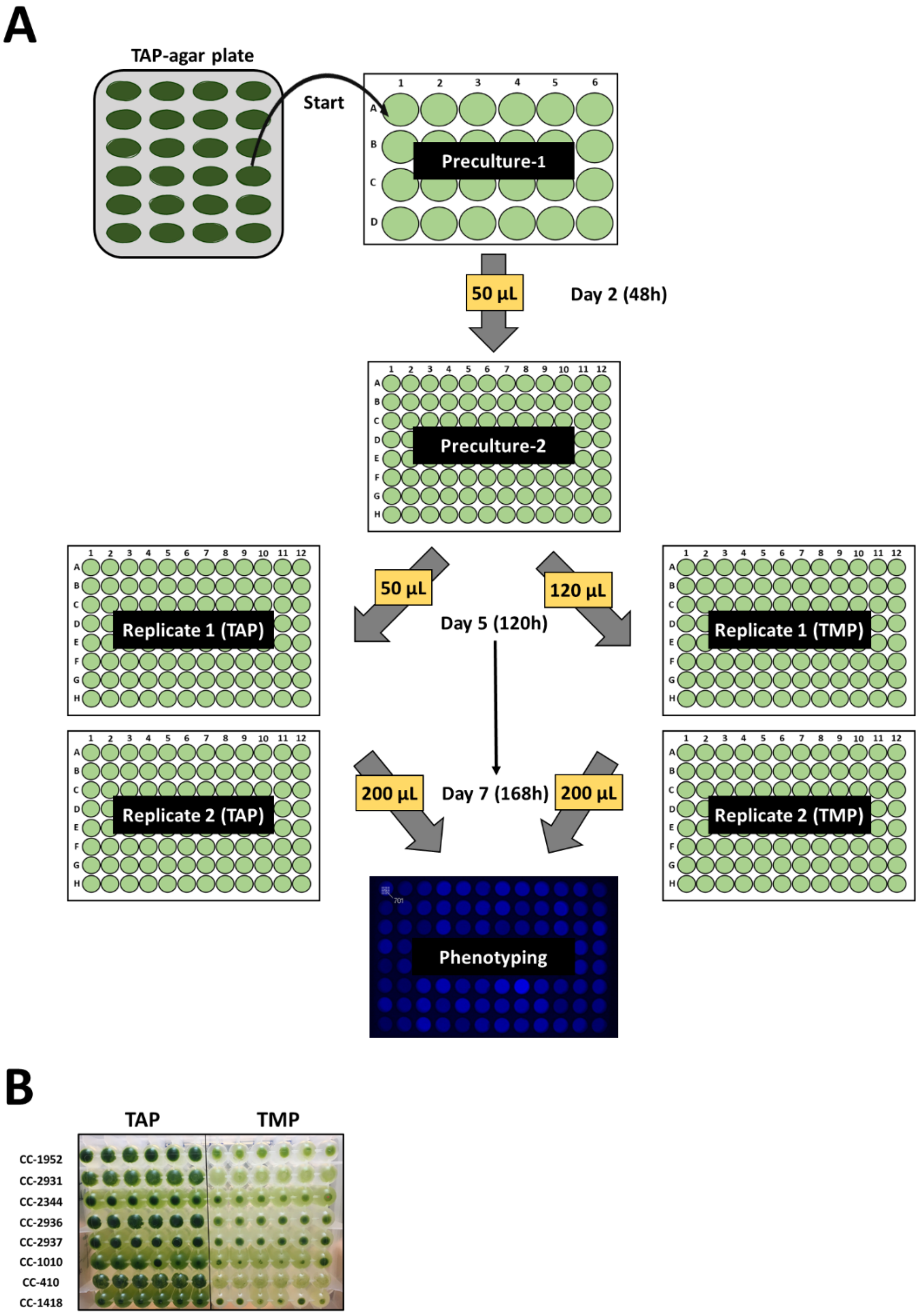

Methods 1: MAGIC population growth and phenotyping. (A) Graphic representation of the experimental procedure developed for the phenotyping of the MAGIC population. The light regime was continuous, and the light intensity was 100 µmol of photons m^{-2} s^{-1} (preculture-1), 50 µmol m^{-2} s^{-1} (preculture-2), and 150 µmol m^{-2} s^{-1} (experimental cultures). (B) A picture of a deep-well plate containing 12 replicates of each founder (6 in TAP and 6 in TMP).

Mating, progeny isolation and mating-type determination

TAP-1.5% agar-grown cells were transferred into transparent flat-bottom 24-well plates filled with 2 mL of N-deprived TMP medium and let differentiating overnight under 100µmol m^{-2} s^{-1} (25°C, no agitation). On the following day, two opposite mating-types were mixed (1mL of each) into a new plate and let under 100µmol m^{-2} s^{-1} (25°C, no agitation). After 1, 3 and 6 hours of mating, 50µl of the mating mix were spotted on different TAP-1/10 Nitrogen-3%-agar plates and kept under the same condition but covered by a thin layer of paper to reduce the light intensity to minimum levels. After 5 days, vegetative cells were scraped out using a sterile scalpel, and the presence of zygospores was assessed by using a stereoscope. Zygospores were harvested in bulk by cutting and transferring a stripe of agar containing between 50 and 100 zygospores to a new TAP-1.5% agar Petri dish. After the transfer, possible parental contaminations were removed by exposing the agar stripes to chloroform for 30 seconds. After 24 hours, 1 mL of sterile TMP was dropped on the agar stripe and the progeny was thoroughly spread with the help of a sterile L-shaped spreader. Agar plates were kept under 100µmol m^{-2} s^{-1} (25°C), and grown colonies appeared after 5-7 days.

From each crossing, 12 colonies were picked using sterile pipet-tips, and transferred to a new TAP-1.5% agar plate. In parallel, a small amount of colony biomass was suspended into 25µL of DNA extraction mix (15µL of sterile milliQ water, 100 µg of proteinase K, and 5µl of 5x Colourless GoTag reaction buffer) and incubated one hour at 58 °C and one hour at 96 °C. Mating-type determination was carried out by the amplification of the *fus1* (MT+ locus) and *mid* (MT- locus) (Ferris et al., 1996; Ferris and Goodenough, 1997) (Sup. Table 4 for primer sequences) using the PCR reaction mix listed below. The amplification protocol consisted of 35 cycles, each cycle being composed of: 30 seconds at 94°C (Denaturation), 45 seconds at 55 °C (Hybridization), and 60 seconds at 72 °C (Polymerization). The 35 cycles were preceded by 2 minutes at 94 °C and followed by 7 minutes at 72 °C. PCR products separated by electrophoresis on a 1%-agarose gel (5µl midori green/100ml of gel) for 30 minutes under 100V.

Reagents	PCR-reaction mix (25µL)
5x Green GoTaq Buffer	5,00µl
100% DMSO	1,25µl
dNTPs (10mM)	0,50µl
Primers (5µM)	1,25µl
	1,25µl
	1,25µl
	1,25µl
GoTaq DNA polymerase	0,13µl
Home-made GoTaq	0,37µl
H2O	10,25µl
DNA-extraction mix	2,50µl

Growth curves

Fresh cells were suspended into 60 mL of TMP at the concentration of 1.5µg of chlorophylls/mL and transferred into sterile glass-tubes. Mixotrophy was induced by supplementing the "TAP" cultures with sterile glacial acetate to the final concentration of 20mM. The optical density of the cultures was recorded every 30 minutes using a *MC1000-OD* multicultivator equipped with a cooling unit AC-710 (PSI®; Photon Systems Instruments®). Light regime was continuous and LL and vHL corresponded to 50 and 600 µmol m^{-2} s^{-1} respectively. Agitation of the cellular suspension was achieved by bubbling the cultures with regular air entering the system through a 0.2*µ*m sterilizing grade filter. The 0.15%-CO_2 condition was achieved by forcing the passage of regular air into a 1L bottle containing 50g of soda lime (Sigma-Aldrich®).

Time-resolved chlorophyll a variable fluorescence emission

Changes in chlorophyll *a* fluorescence emission were measured at room temperature using a SpeedZen II imaging system (JBeam Bio, France) (Johnson et al., 2009) equipped with blue (detection light) and red (actinic & saturating lights) LEDs. White flat-bottom 96-well microplates (Greiner®) were filled with 200µL of sample and left in the dark for 10 minutes (unless differently stated) before measuring. Nigericin, valinomycin, nonactin and DCMU were purchased from Sigma-Aldrich® and stocks were prepared dissolving the compounds into 100% methanol. The final solutions used for the treatment were prepared by diluting the stocks with distilled water.

Absorption spectroscopy

The electrochromic shift (ECS) is the phenomenon described as the shift in the absorption spectra of some photosynthetic pigments following the establishment of the electrochemical proton gradient (**Δ**µH+)(Baker et al., 2007; Bailleul et al., 2010). To measure ECS, experimental cultures were concentrated to 16µg of chlorophylls/mL and let recover under the experimental light intensity during 4h. Following, samples were diluted with a factor of 1:2 into a solution of TMP + ficoll 20% w/v. Samples' light-induced absorption changes were detected at 520nm (maximal ECS signal) and 546nm (background) using a Joliot-Type Spectrophotometer (JTS-10, BioLogic®) (Béal et al., 1999). ECS was measured on dark-adapted samples under continuous light (4 seconds illumination followed by 2.5 seconds of dark) at different light-intensities (see Figure 2.15). The ECS fast phase (*a*-phase) was measured on new dark-adapted samples upon excitation with a single-turnover pulse generated by a saturating laser flash. After subtraction of the background (520-546 nm), the total number of charge separations was estimated by dividing the corrected ECS signal measured under continuous light by the *a*-phase value recorded on each sample. ECS values shown in Figure 2.15 were calculated as the difference between the average ECS value recorded during the last 0.5 seconds of light (steady state ECS) and the lowest value recorded within the first 0.75 seconds of dark (fully relaxed ECS). The aggregate conductivity of the thylakoid membrane to protons (g_{H}^{+}) was estimated by fitting the ECS signal during the first 300ms of dark with a one-phase exponential decay. The rate constant (K) was multiplied by 1000 to transform the values from ms^{-1} to s^{-1}. PSII contribution was calculated as the loss of *a*-phase signal following the simultaneous addition of 20µM DCMU and 1mM hydroxylamine to inhibit any form of charge separation through PSII reaction centers. PSI/PSII ratio was therefore calculated as the inhibitors-insensitive portion of the *a*-phase signal divided by the sensitive one.

Low temperature (77°K) fluorescence emission

Cultures were adjusted to the final concentration of 5µg of chlorophylls/mL. Following acclimation (see section 2.2.3), 1 mL of sample was quickly transferred into 1.5 mL plastic cuvette and immersed into liquid nitrogen. Fluorescence emission was measured at the temperature of 77°K by a UV-VIS-NIR spectrometer (Ocean Insight©) adapted to a cuvette-holder and set to an integration time of 1000 ms. Optical fibers were plunged into liquid nitrogen together with samples. Raw data were normalized on the 685nm fluorescence emission band.

mRNA quantification

Total RNA was extracted using the RNeasy Mini Kit (Qiagen©) and treated with the RNase-Free DNase Set (Qiagen). 1 µg total RNA was reverse transcribed with oligo dT using Sensifast cDNA Synthesis kit (Meridian Bioscience©, USA). qPCR reactions were performed and quantitated in a Bio-Rad CFX96 system using SsoAdvanced Universal SYBR Green Supermix (BioRad©). The primers (0.3 µM) used for qPCR are listed in Sup. Table 3. Statistics were calculated using PRISM GraphPad. All mRNA quantification analyses and data processing were performed by Dr Yizhong Yuan and Dr Dimitris Petroutsos from the Cell & Plant Physiology Laboratory (LPCV) of the CEA of Grenoble (France).

Label-free shotgun proteomic analysis

Cell pellets were thawed and suspended in a 10-time pellet volume of lysis Buffer (Tris HCl 10 mM pH 7.4, 1% SDS, Protease Inhibitor Cocktail Complete EDTA-free, PhosStop). Samples were sonicated for 30 cycles of 30 seconds “ON” / 30 seconds “OFF” with Bioruptor from Diagenode© (Cat. No. UCD-200). The samples were centrifuged at 15,000 g for 10 min at room temperature. The supernatants were collected and quantified with RC-DC Protein Assay Kit® (Bio-Rad, Hercules, CA, USA) according to the manufacturer's instructions. For each sample, an aliquot corresponding to 15 µg of proteins according to the RC-DC quantitation were diluted with 50 mM ammonium bicarbonate aqueous solution to a protein concentration of 0.17 µg/mL. The protein samples were reduced using dithiothreitol (DTT) and alkylated with iodoacetamide before applying the 2D Clean-Up kit® (GE Healthcare Life Sciences) according to manufacturer’s recommendations, in order to eliminate impurities not compatible with mass spectrometry analysis. The protein pellets after the washing steps were further resolubilized in bicarbonate ammonium 50mM. The samples were digested in solution with trypsin (16 hours at 37°C ratio trypsin/total proteins (w/w) (1/50) then 3h at 37°C with ratio 1/100 (w/w) in 80% ACN). The digestion was stopped by the addition of trifluoroacetic acid (TFA) at 0.5% (V/V) final concentration. Finally, the samples were dried under vacuum using SpeedVac® (Thermo Scientific). After the digestion step, samples were resuspended in 0.1% TFA aqueous solution. For each sample, an aliquot corresponding to 3.5 µg of digested proteins was purified using C18 Tips (Thermo Scientific Pierce) according to the manufacturer’s recommendations. Then, samples were evaporated to dryness in a speed vacuum. Peptides were suspended in 0.1% TFA aqueous solution and spiked with a commercial mixture of protein digest standards originated from non-human biological material: the MassPREP™ Digestion Standards (Waters, Corp., Milford, USA), at 50 fmol of ADH per injection. This commercial standard consists of two standard mixtures (MPDS Mix 1 and MPDS Mix 2) containing protein digests of Yeast Alcohol Dehydrogenase (ADH), Rabbit Glycogen Phosphorylase b, Bovine Serum Albumin, and Yeast Enolase present at known protein ratio; allowing therefore to check for relative quantitation of the samples spiked. Sample injection order on the nanoUPLC- ESI-Q orbitrap was randomized and 9 µL, corresponding to 1 µg of protein digest were injected per sample.

The LC-MS/SM analyses were performed on an Acquity M-Class UPLC (Waters, Milford, USA) hyphenated to a Q Exactive Plus (Thermo Scientific, USA), in nanoelectrospray positive ion mode. The trap column is a Symmetry C18 5µm (180 µm x 20 mm) and analytical column is a HSS T3 C18 1.8 µm (75 µm x 250 mm) (Waters, Corp., Milford, USA). The samples were loaded at 20 µL/min on the trap column in 98% solvent A during 3 minutes (solvent A is 0.1% formic acid in water and solvent B is 0.1% formic acid in acetonitrile) and subsequently separated on the analytical column at a flow rate of 600 nL/min with the following linear gradient: initial conditions 2% B; 5 min 7% B; 135 min 30% B, 150 min 40% B; 154 min 90% B until 158 min then back in initial conditions at 162 min until 177min for reconditioning. The total running time was 180 min. The mass spectrometer method is a TopN-MSMS method where N was set to 12, meaning that the spectrometer acquires one Full MS spectrum, selects the 12 most intense peaks in this spectrum (singly charged and unassigned charge precursors excluded) and makes a Full MS2 spectrum of each of these 12 compounds. The parameters for MS spectrum acquisition are: Mass range from 400 to 1600 m/z; Resolution of 70,000; AGC target of 3e6 or Maximum injection time of 50 ms. The parameters for MS2 spectrum acquisition are: Isolation Window of 2.0 m/z; Normalized Collision energy (NCE) of 28; Resolution of 17,500; AGC target of 1e5 or Maximum injection time of 50 ms. The main nanoelectrospray source parameters were: spray voltage of 2.3 kV, capillary temperature of 270°C and S-Lens RF level of 50.

For label-free quantification (LFQ) application, MaxQuant version 1.6.17.0 was used for the analysis of raw files. MS/MS spectra were analyzed using the Andromeda search engine and the following settings: database “NCBI database restricted to *Chlamydomonas reinhardtii* taxonomy (38964 sequences, downloaded on 9th of July 2021)” for interrogation to which the sequences of the four proteins of the standard MPDSMix and the sequence of procine trypsin used for digestion were added. Oxidation of methionine and deamidation of asparagine and glutamine (N,Q) was set as variable modifications, carbamidomethylation of the cysteines as fixed modification. The maximum number of missed cleavages was set at two and the minimal peptide length for identification was set at 7 amino acids and at least two peptides per protein, including at least one unique peptide, were required for identification. Data normalization was performed using the LFQ algorithm (Cox et al., 2014). Match between run feature was set True (matching window of 2 min and alignment time window of 20 min). The minimum ratio count for LFQ was set at 2 and MS/MS was required for LFQ comparison. The main search tolerance was set at 4.5 ppm. Peptide spectrum match (PSM) and protein false discovery rates (FDR) were both set at 0.01. The annotation and statistical analysis of the proteomic dataset was conducted on R.Studio as described in section (2.2.3). After the differential expression analysis, the enrichment analysis was performed on DEqMS-detected proteins, selected based on p-value corrected by Benjamini-Hochberg method (False Discover Rate = 5%) and with a fold change ≥ 2.

Whole-genome sequencing and read mapping

Two founders (CC-410 and CC-1418) and 768 MAGIC F8 lines were sequenced at the GIGA genomic platform. For the two founders, sequencing libraries were prepared with the Illumina TruSeq DNA PCR-

Free kit, whereas the Sopachem PlexWell kit was used for the F8 lines. In both cases, the manufacturer protocol was followed. Libraries were then sequenced on an Illumina NovaSeq sequencer. For the six additional founders, the available sequencing data was downloaded from (Flowers et al., 2015). The data was subsequently mapped to the version 6 of the *Chlamydomonas* reference genome (Craig et al., 2022) to which the chloroplast and the mitochondria sequences available from Gallaher et al. (2018) were added. To that end, we followed the best practice workflow from the Broad Institute consisting first in generating unmapped BAM (uBAM) files from FASTQ files with the FastqToSam command, marking adapter sequences using the MarkIlluminaAdapters command, and converting the resulting SAM files to FASTQ with the SamToFastq command. After application of these three commands from Picard tools 1.141, the FASTQ files were mapped with BWA-MEM (bwa v0.7.17) and mapped BAM and unmapped BAM files were then merged with MergeBAMAlignment from Picard tools 1.141. Finally, we removed potential duplicates (MarkDuplicates) and sorted the BAM file (SortSam) with Picard tools 1.141. The depth of coverage for each sample was estimated using DepthOfCoverage with GATK (v3.2.2). A total of 21 lines with a cover below 4x were re-sequenced. For these lines, the two BAM files were merged when their initial cover was > 1x and when genotypes were identical in the two BAM files for more than 99% of the called variants (for nine out of 21 lines).

Variant calling

Variant calling was performed with Freebayes v1.2.0-17 (Garrison and Marth, 2012) in two steps. First, we called variants using the 20 strains sequenced in Flowers et al. (2015) and the two newly sequenced founders. Freebayes was run per chromosome, with ploidy set to 1 (-p 1) and with --min-alternate-count set to 5. To study the structure or relatedness among these 22 reference strains, we kept variants identified on the 17 chromosomes with QUAL > 50, with DP > 499 or < 2350 (corresponding to approximately 2.5% and 97.5% quantiles), and with AO ≥ 20. Regions with extreme total coverage (> 10,000) were flagged to exclude them in the next step that was applied to the eight founders and the 768 F8 lines jointly. For this calling, the genome was divided into small chunks around 500kb long and Freebayes was run for haploid organisms (-p 1), with --min-alternate-count set to 5, and with the "--use-best-n-alleles 8". To obtain a set of high-quality variants for modelling the mosaic structure of the F8 lines, we filtered out markers with QUAL ≤ 50, with DP < 2000 or > 10250 (corresponding to 2.5% and 97.5% quantiles), and with AO < 20. In addition, markers with identical genotypes among the eight founders were also removed as these are non-informative. We also restricted our selection to variants covered by at least 1 read in each founder, with a maximum of eight alleles and for which founders had only one allele each (one allele accounted for at least 95% of the allele depth (**AD**).

Genetic relatedness and identity-by-descent sharing among reference strains

As a measure of genetic distance, we counted the proportion of distinct genotypes d_{ij} among pairs of strains *i* and *j*. As in Flowers et al. (2015), a circular dendrogram was constructed based on these distances to visualize relationships among the lines and plotted with the circlize_dendrogram function in R. In addition, we also identified identity-by-descent (IBD) segments among the eight selected founders with the hidden Markov model (HMM) implemented in hmmIBD (Schaffner et al., 2018). We ran the program with default options on the filtered VCF files and using the 17 chromosomes.

Modeling the F8 lines as mosaic from the founders

A HMM describing F8 lines as mosaic from the eight founders was applied, similar to models applied in other MAGIC designs (e.g., Kover et al., 2009) using CHROMIBD (Druet and Farnir, 2011). In this model, we determine at each marker position the probability that the modeled F8 line inherited its chromosome segment from one of the founders. The eight founders represent thus eight hidden states from the model. The transition probabilities $\tau_{k,k'}$ between successive markers m and $m+1$ are inspired from Mott et al. (2000):

$$\tau_{k,k'} = \begin{cases} e^{-Gd_m} + \left(1 - e^{-Gd_m}\right)\frac{1}{K} & if\ k = k' \\ \left(1 - e^{-Gd_m}\right)\frac{1}{K} & if\ k \neq k' \end{cases}$$

Where G is the number of generations of crossing, equal to 8 in our design, d_m is the genetic distance between markers m and m+1 and K is the number of founders. We assumed 1 Mb corresponds to 10 cM in *Chlamydomonas reinhardtii*, close to the or 1.2 x 10^{-5} cM/bp estimated by Liu et al. (2018). The emission probabilities are obtained by comparing genotypes in the F8 line with those in the founders. However, as the F8 lines are not sequenced at high coverage, we modified the emission probabilities to account for the uncertainty in the genotype calling and therefore we rely on the genotype likelihoods (GL) estimated by Freebayes. The emission probability at marker m for founder k for the F8 line i can be computed as:

$$P(O_{im}|S_{im} = k) = \sum_{j=1}^{N_m} P(G_{im} = j)\, P(G_{km} = j)$$

Where O_{im} are the observations at marker m for F8 line i (its sequencing data, such as read counts), S_{im} is the state of F8 line i at marker m, N_m is the number of alleles at marker m, $P(G_{im} = j)$ is the probability that the genotype from line i at marker m corresponds to allele j and is obtained from the genotype likelihoods, $P(G_{km} = j)$ is the equivalent probability but for founder k. When the emission probability is lower than 0.0005, we set it equal to 0.0005 to accommodate for unaccounted genotype calling errors. The emission probabilities are set to 1.00 at marker positions not covered by any read. With such an HMM, the Viterbi algorithm provides the most likely mosaic (sequence of founder inheritance) for the modeled F8 line whereas the Forward-Backward algorithms provides at each marker position the founder probability corresponding to the probability that the modeled F8 line derives from one specific founder (the IBD probability that line i derives from founder k at marker m noted as $P(S_{im} = k)$). For relatedness measures and QTL mapping, these IBD probabilities were averaged in 10 kb windows and noted as $\bar{P}(S_{iw} = k)$ where w indicates the window number.

Estimation of population structure and genetic relatedness in the experimental population

We used PLINK to perform a PCA based on the genotype data from the design (eight founders and 768 F8 lines). The relatedness among F8 lines was first estimated either based on a similarity index defined as the proportion of IBS genotypes $SI_{ii'}$ among lines i and i', or from IBD relationship with founder lines in 10 kb windows, averaged over the entire genome:

$$g_{ii'} = \frac{1}{N_W}\sum_{w=1}^{N_W}\sum_{k=1}^{8}\bar{P}(S_{iw} = k)\bar{P}(S_{i'w} = k)$$

where $g_{iu'}$ is the genetic relatedness between lines i and i' computed over the N_W 10kb windows.

Estimation of genetic parameters associated with recorded phenotypes

For each trait t, defined as a phenotype by growth condition combination, we relied on the following single-trait linear mixed model to estimate the heritability and repeatability:

$$\boldsymbol{y}_\mathrm{t} = \boldsymbol{X}_\mathrm{t}\boldsymbol{\beta}_\mathrm{t} + \boldsymbol{Z}_\mathrm{ut}\boldsymbol{u}_\mathrm{t} + \boldsymbol{Z}_\mathrm{pt}\boldsymbol{p}_\mathrm{t} + \boldsymbol{e}_\mathrm{t}$$

where $\mathbf{y}_\mathrm{t}$ is the vector of recorded observations for trait t (two replications before filtering), $\boldsymbol{\beta}_\mathrm{t}$ is a vector of fixed effects (for trait t) including the design effect (3 levels) and the phenotyping batch (8 levels), $\mathbf{u}_\mathrm{t}$ is the vector of random polygenic effects for trait t of each F8 line, $\mathbf{p}_\mathrm{t}$ is the vector of random permanent environment effect of each F8 line, and $\mathbf{e}_\mathrm{t}$ is a vector with residual error terms associated with each record. The random polygenic effect represents the combined effect of all individual loci of one F8 line, and are assumed to be normally distributed $\boldsymbol{u}_\mathrm{t} \sim \mathrm{N}\left(\mathbf{0}, \mathbf{G}\sigma^2_{\mathrm{g,t}}\right)$, where **G** is the genomic relationship matrix (**GRM**) among F8 lines obtained from IBD probabilities and $\sigma^2_{\mathrm{g,t}}$ is the additive genetic variance associated with trait t. Note that F8 lines with a similarity > 0.95 where clustered, we considered that they had the same polygenic effect. The so-called random permanent environment effects correspond to random effects associated with a F8 line. These can be non-genetic effects but also genetic effects that are non-additive (not captured through the GRM). They are used to model the fact that two repeated measures on the same line are correlated, the effects were normally distributed with $\boldsymbol{p}_\mathrm{t} \sim \mathrm{N}\left(\mathbf{0}, \mathbf{I}\sigma^2_{\mathrm{p,t}}\right)$, where **I** is an identity matrix and $\sigma^2_{\mathrm{p,t}}$ is the variance associated with the random permanent environment effects.

Finally, the random residual error terms are also normally distributed $\boldsymbol{e}_{\mathrm{t}} \sim \mathrm{N}\left(\mathbf{0}, \mathbf{I}\sigma^2_{\mathrm{e,t}}\right)$, with $\sigma^2_{\mathrm{e,t}}$ being the residual variance. The heritability for trait *t* can be computed as:

$$h_t^2 = \frac{\sigma^2_{\mathrm{g,t}}}{\sigma^2_{\mathrm{g,t}} + \sigma^2_{\mathrm{p,t}} + \sigma^2_{\mathrm{e,t}}}$$

whereas the repeatability is obtained as:

$$r_t^2 = \frac{\sigma^2_{\mathrm{g,t}} + \sigma^2_{\mathrm{p,t}}}{\sigma^2_{\mathrm{g,t}} + \sigma^2_{\mathrm{p,t}} + \sigma^2_{\mathrm{e,t}}}$$

A multiple trait model traits was subsequently applied to estimate the genetic correlations among T traits:

$$\mathbf{y} = \mathbf{X\beta} + \mathbf{Z}_{\mathrm{u}}\mathbf{u} + \mathbf{Z}_{\mathrm{p}}\mathbf{p} + \mathbf{e}$$

Where **y** = ($\mathbf{y}_1$, $\mathbf{y}_2$, …, $\mathbf{y}_{\mathrm{T}}$) is the vector of all phenotypes, **β** = ($\boldsymbol{\beta}_1$, $\boldsymbol{\beta}_2$, …, $\boldsymbol{\beta}_{\mathrm{T}}$) is a vector with fixed effects for different traits. Similarly, **u**, **p** and **e** are vectors of corresponding random effects for all the traits. The incidence matrices are obtained from the combination of trait-specific incidence matrices. For instance:

$$\mathbf{Z}_u = \begin{bmatrix} \mathbf{Z}_{u1} & 0 & \cdots & 0 \\ 0 & \mathbf{Z}_{u2} & \cdots & 0 \\ \vdots & \vdots & \ddots & \vdots \\ 0 & 0 & \cdots & \mathbf{Z}_{uT} \end{bmatrix}$$

In our model, var(**u**) = **G** ⊗ $\mathbf{V}_{\mathbf{u}}$, where **G** is the genomic relationship matrix and $\mathbf{V}_{\mathrm{u}}$ is the matrix of genetic variances and covariances among traits. Similarly, var(**p**) = **I** ⊗ $\mathbf{V}_{\mathbf{p}}$ and var(**e**) = **I** ⊗ $\mathbf{V}_{\mathbf{e}}$, with $\mathbf{V}_{\mathbf{p}}$ and $\mathbf{V}_{\mathrm{e}}$ are the (co)variances matrices among random permanent and residual effects, respectively. For computational reasons, the (co)variances among traits were estimated by subgroup of traits. For the 14 phenotypes related to mineral nutrition and recorded in six different conditions, the correlations were first estimated within conditions and then by pairs of conditions. In addition, we also estimated the variance components for the same measure, recorded in the 6 conditions to assess the magnitude of genotype-by-environment interactions (14 six-traits models). For the 11 photosynthesis phenotypes measured in two different conditions (TMP and TAP), we fitted a multivariate model with 22 traits. Genetic parameters were estimated with the REML and AI-REML algorithm as implemented in REMLF90 and AIREMLF90 programs (Misztal et al., 2002). The standard deviations of heritabilities, repeatabilities and correlations were obtained by repeated sampling of parameters estimates from their asymptotic multivariate normal distribution (Meyer and Houle, 2013).

QTL mapping

We used a LMM approach to perform the association study (e.g., Runcie and Crawford, 2019; Odell et al., 2022). The QTL detection relied on a likelihood ratio test (LRT) comparing a model with QTL to a null model without QTL. The null model (H0) was identical to the model described above for the estimation of genetic parameters. The alternative model (H1) included an additional QTL effect. As successive positions are highly correlated, we reduced the computational cost by defining non-overlapping 10-kb windows and performing one test per window using the average IBD probability of all the SNPs in the window. Windows without any polymorphic sites in our final VCF were excluded. As a result, we reduced the number of tests from 3,121,994 polymorphic sites to 10,599 windows. The model including the QTL effect was defined as:

$$\mathbf{y}_t = \mathbf{X}_t\boldsymbol{\beta}_t + \mathbf{Z}_{ut}\mathbf{u}_t + \mathbf{Z}_{pt}\mathbf{p}_t + \mathbf{Z}_{qt}^{w}\mathbf{q}_{w,t} + \mathbf{e}_t$$

where $\mathbf{q}_{w,t}$ is the vector with the eight random founder haplotype effects (or QTL effects) for the tested window *w* for trait *t* that are assumed independently distributed with variance $\sigma^2_{q,t}$, and $\mathbf{Z}^{i}_{qt}$ is the incidence matrix relating the founder haplotype effects for window *w* to the F8 lines. This incidence matrix has one row for each F8 line and 8 columns (one per founder). The element $z^{w}_{qt}(i,k)$ from this matrix contains the probability that F8 line *i* derives from founder *k* in window *w*, based on the IBD probabilities estimated with the HMM (called founder probabilities). We applied a Leave-One-Chromosome-Out (LOCO) strategy (Lippert et al., 2011), meaning that in both models (H0 and H1) the GRM among polygenic effects were computed ignoring windows on the chromosome harboring the tested position *i*. To test for the presence of a QTL, the log-likelihoods of the two models are compared with an LRT (distributed as a χ^2 distribution with 1 df). The log-likelihood of both LMM were estimated with the REML algorithm and using the remlf90 program.

The number of independent tests was estimated by an approach described in (Druet et al., 2014). We performed a genome-wide scan with a simple linear model on a permuted phenotype (-Ca Zn.nmol.OD). We repeated this 10,000 times and saved the best genome-wide p-value for each permutation, providing the distribution of best p-values under H0 (absence of QTL). Corrected p-values for each p-value were then obtained as their rank among the sorted best p-values. We estimated the number of independent tests to be 3348, based on the Sidak formula and the sets of corrected and uncorrected p-values. The number of independent phenotypes was evaluated to be equal to 63 using the meff function (method = Galwey) from the poolR R package (Cinar and Viechtbauer, 2022). Thus, we performed a total of 210,924 independent tests and used the Bonferroni correction to set the significance thresholds to 0.05/210,924 = 2.37e-7. Confidence intervals (CI) were obtained using the LOD drop-off approach (Lander and Botstein, 1989). Here we used a conservative LOD drop-off value of 2 (see Lynch and Walsh, 1999). To estimate the variance associated with a QTL, we compared the estimated polygenic variance in model H0 and model H1. The polygenic variance reduction represents the variance explained by the QTL (Malosetti et al., 2008). For that approach, we used the GRM estimated by using all chromosomes. In addition, we estimated the variance among founder haplotype effects $\sigma^2_{q,t}$ (an approximation of the QTL variance if the founder alleles are homogeneously transmitted to F8 lines).

Multiple-trait QTL analysis

To determine whether QTLs mapping to the same location were pleiotropic, we performed multiple-trait QTL analysis within the CI from the overlapping QTL. We started by defining QTL groups by the union of all QTL from which the CI overlapped with at least the CI from another QTL in the group. The multiple-trait analysis relied on an LRT comparing the multiple-trait model without QTL that we previously defined (H0) to the same model including additional correlated QTL effects:

$$\mathbf{y} = \mathbf{X}\boldsymbol{\beta} + \mathbf{Z}_{\mathrm{u}}\mathbf{u} + \mathbf{Z}_{\mathrm{p}}\mathbf{p} + \mathbf{Z}_{\mathrm{q}}^{\mathbf{w}}\mathbf{q}_{\mathrm{w}} + \mathbf{e}$$

Where **q** is the vector of random founder effects for all T traits (containing 8 x T effects) and $\mathbf{Z}_{\mathrm{q}}^{\mathbf{w}}$ is the incidence matrices relating phenotypes with founder haplotype effects and obtained from the combination of trait-specific incidence matrices $\mathbf{Z}_{\mathrm{qt}}^{\mathbf{w}}$. In addition, var(**q**) = **I** $\otimes$ $\mathbf{V}_{\mathrm{q}}$, where **I** is an identity matrix (dimension 8) and $\mathbf{V}_{\mathrm{q}}$ is the T-by-T matrix of variances and covariances of founder haplotype effects among traits. High genetic correlations, obtained from $\mathbf{V}_{\mathrm{q}}$, among founder haplotype effects for two different traits indicate pleiotropy. The multiple trait approach also allowed us to combine information from several phenotypes to improve the CI.

Sequence-based QTL fine-mapping

Taking advantage of the availability of WGS data, we performed a sequence-based association study with QTL CI intervals. Since F8 lines were sequenced a relatively low coverage, we imputed their genotypes based on the founder genotypes and the IBD probabilities estimated with our HMM as:

$$P^I(G_{im} = j) = \frac{\sum_{k=1}^{8} P(S_{im} = k)P(G_{km} = j)}{\sum_{j'}^{N_m}\sum_{k=1}^{8} P(S_{im} = k)P(G_{km} = j')}$$

Where *i*, *j*, *k* and *m* refer to line, allele, founder, and marker numbers. As previously, *G* represents genotypes and $P(S_{im} = k)$ is the IBD probability. Note that for this imputation step, the genotype probability $P(G_{im} = j)$ obtained from the sequence data was ignored. These were subsequently combined with the imputed genotypes probabilities as:

$$P^C(G_{im} = j) = \frac{P(G_{im} = j)P^I(G_{im} = j)}{\sum_{j'}^{N_m} P(G_{im} = j')P^I(G_{im} = j')}$$

These final genotyping probabilities combined the two independent sources of information, the sequence data at marker *m*, and the genotype predicted from the IBD probabilities and genotype observed in the founders. The genotype probabilities were then used for performing an association study based on an LRT where the alternative model (H1) contained an additional variant effect:

$$\mathbf{y_t} = \mathbf{X_t}\boldsymbol{\beta}_\mathbf{t} + \mathbf{Z_{ut}u_t} + \mathbf{Z_{pt}p_t} + \mathbf{Z_{vt}^m v_{m,t}} + \mathbf{e_t}$$

where $\mathbf{v}_{m,t}$ is the vector of random effects for the different alleles at marker *m* for trait *t*. For QTL of interests, we identified the genetic variants for which the genotypes in the founders were compatible with the estimated founder haplotype effects. We subsequently verified whether this set of variants presented the highest significance levels. Variants matching these two conditions (highest significance levels and founder genotypes compatible with founder haplotype effects) were considered as potential candidate causative variants.

4.2 Supplementary figures

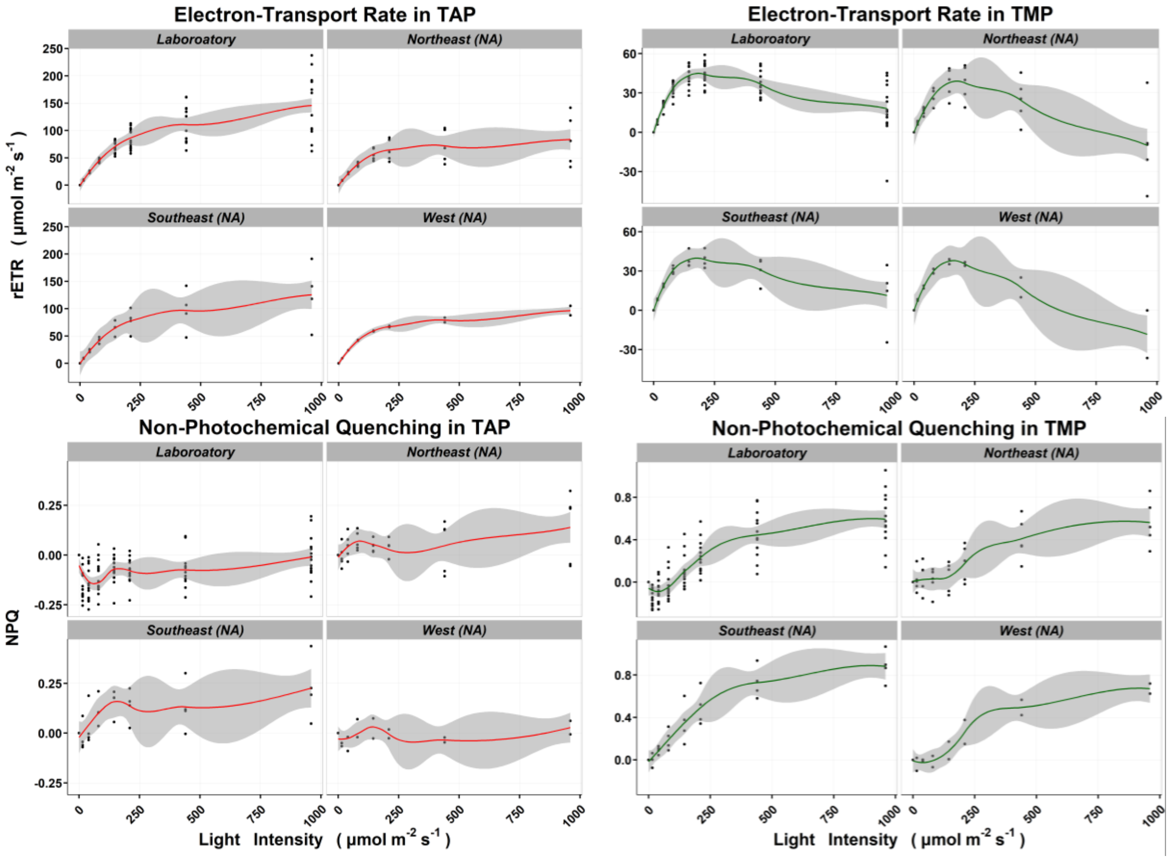

Sup. Figure 1: Photosynthetic characterization of the initial panel of wild-type strains divided based on their geographical origin. The red and green lines are smoothed lines, and the grey area delimits the 95% interval of confidence. Each point is the average of 6 (TMP) or 9 (TAP) biological replicates.

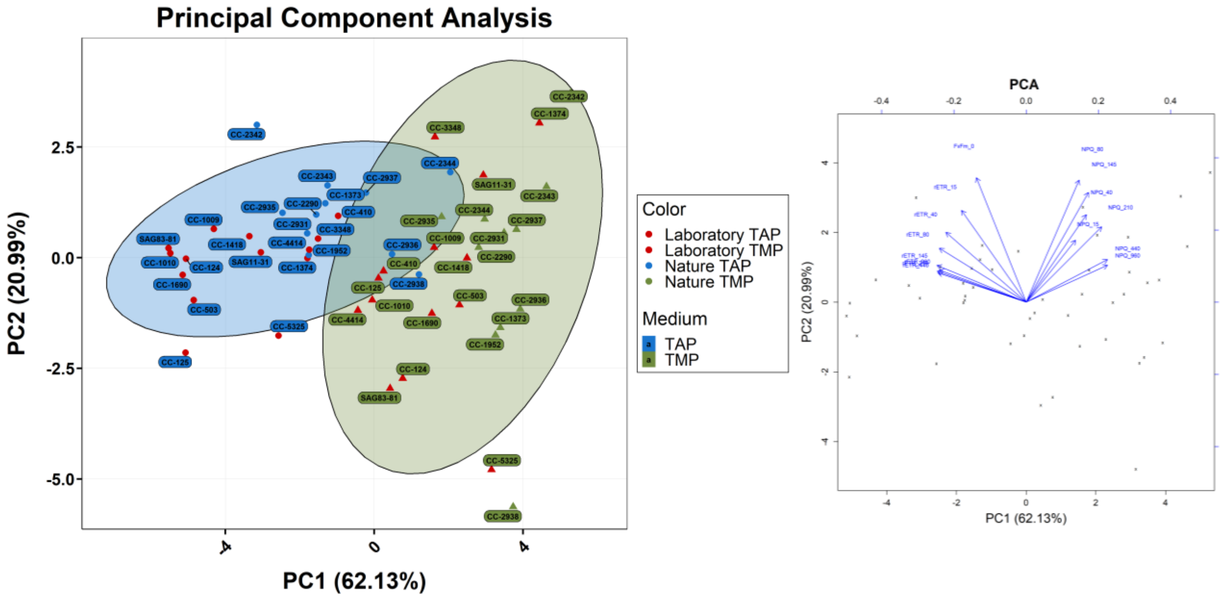

Sup. Figure 3: Phenotypic diversity within Chlamydomonas. (A) PCA of photosynthetic traits measured in mixotrophically (blue) and photoautotrophically (green) grown cells. Laboratory strains are highlighted in red. (B) Contribution of the photosynthetic traits to the principal components 1 and 2. The number following the "_" sign indicates the light-intensity.

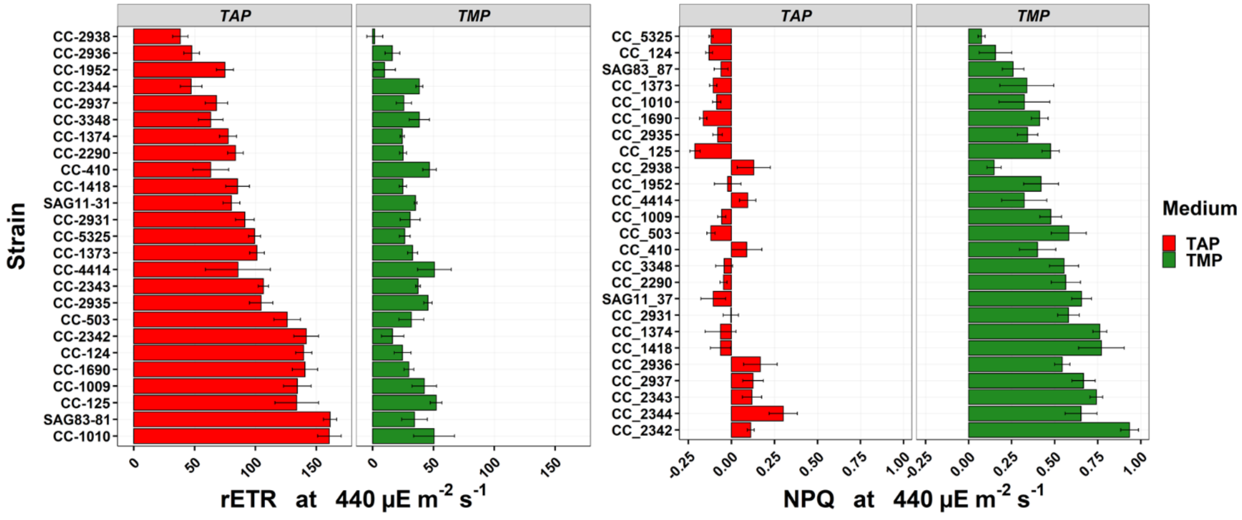

Sup. Figure 2: Photosynthetic (left panel) and photoprotective (right panel) efficiency among Chlamydomonas wild-types grown under mixotrophic and photoautotrophic condition. n = 9 (TAP) or 6 (TMP). Values ±SE.

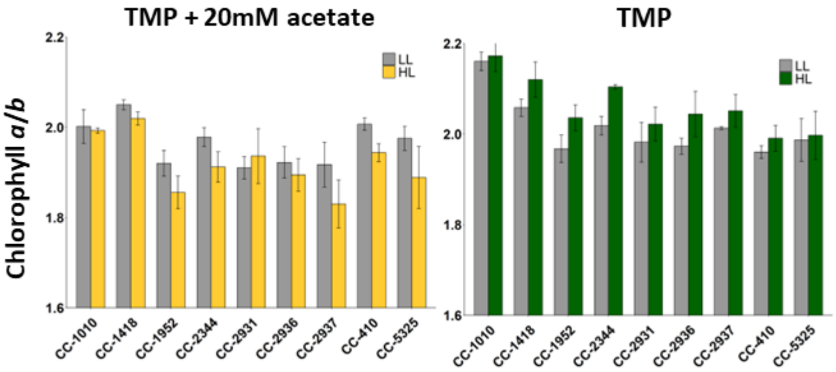

Sup. Figure 4: Comparison of the chlorophyll a/chlorophyll b ratio among 9 Chlamydomonas WT strains. Experimental cultures were cultured for ~20 hours under 30µmol m^{-2} s^{-1} of continuous light. The following day, LL-samples were harvested, and their methanol extracts used to calculate the Chl a/b ratio (see "Materials and Methods"). Afterwards, the experimental light was increased to 300µmol m^{-2} s^{-1} and new measurements were repeated after 4 hours (HL samples). Values ±SE, n=3.

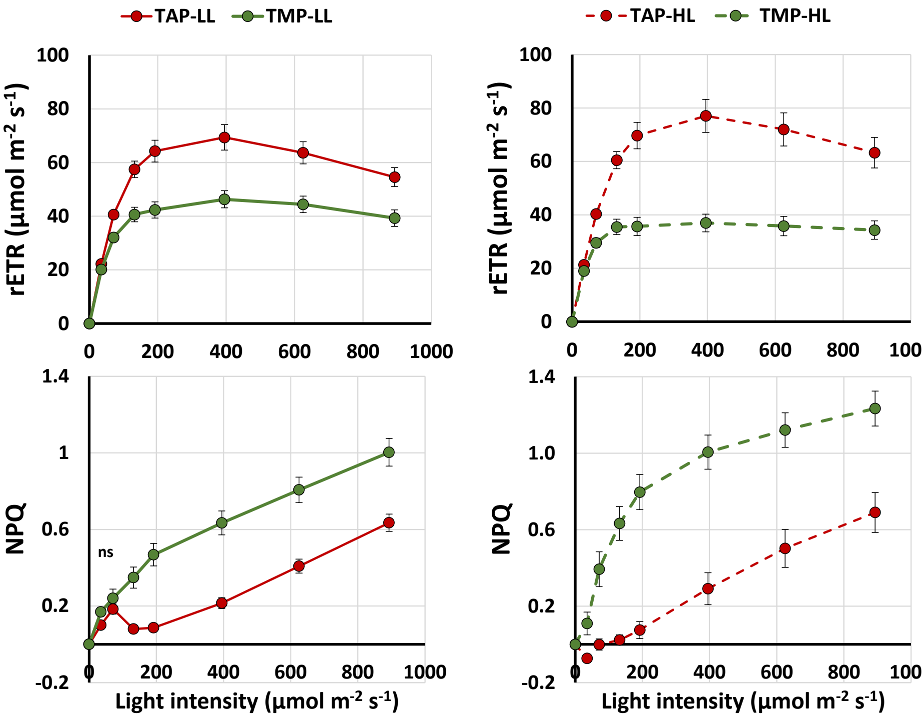

Sup. Figure 5: Overall impact of the growth condition on rETR and NPQ within *Chlamydomonas reinhardtii*. Each point is the average of 9 different *Chlamydomonas* WT strains (± SE). TAP samples (red) were compared to TMP samples (green) by Wench's t-test. Significant differences between conditions were found for all light intensities, except where indicated otherwise (p>0.05 = ns).

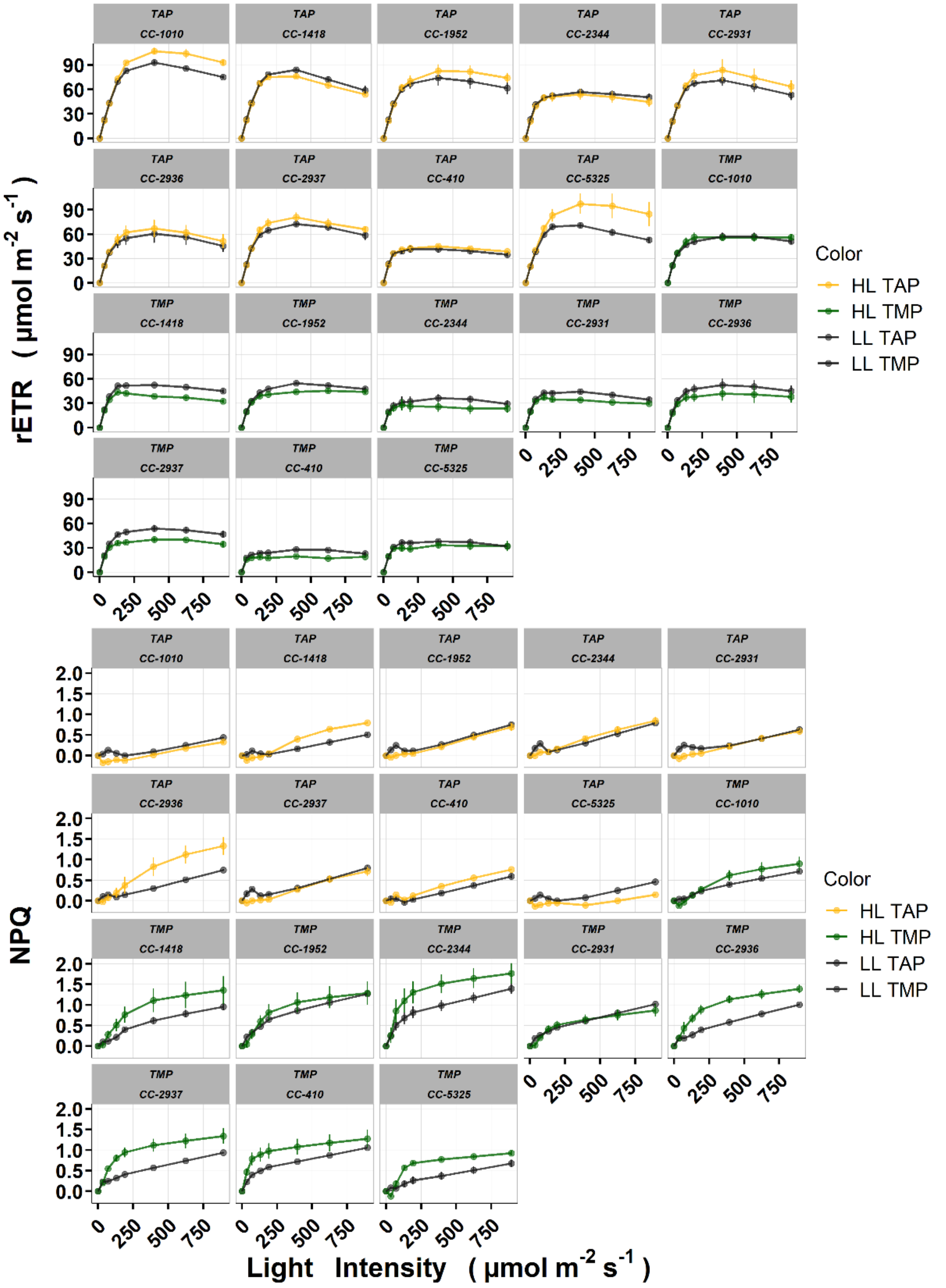

Sup. Figure 6: Characterization of 9 Chlamydomonas wild-type strains by chlorophyll a variable fluorescence. Strains were grown for ~20 hours under 30µmol m^{-2} s^{-2} of continuous light (LL) and exposed for 4 hours to 300µmol m^{-2} s^{-2} (HL). (A) Relative electron-transport rate and (B) non-photochemical quenching as function of the light intensity. Values ±SE, n=3.

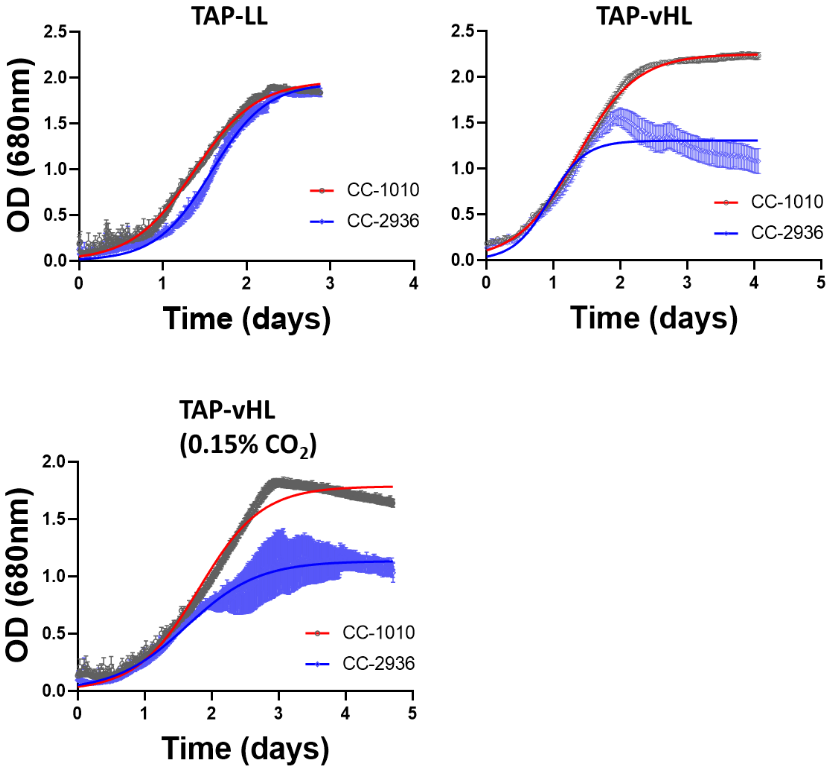

Sup. Figure 7: Acetate inhibits CC-2936's growth under vHL. Growth curves were performed using a Multi-Cultivator MC 1000 OD (Photon System Instruments ®), in a total volume of 60 mL. Precultures in log-phase were inoculated at the concentration of 2µg of chlorophyll/mL and cultured at the constant temperature of 24.5 °C, bubbling them with regular or 0.15%-CO_2 air under 50 (LL) or 600 (vHL) µmol of p. m^{-2} s^{-1}. The optical density at 680nm was monitored every 10 minutes for 3 days or more. The recordings (dots) were fitted with a logistic equation (least squares fit). n=4 (LL and vHL-0.15% CO_2) or 8 (vHL). Values ± SE.

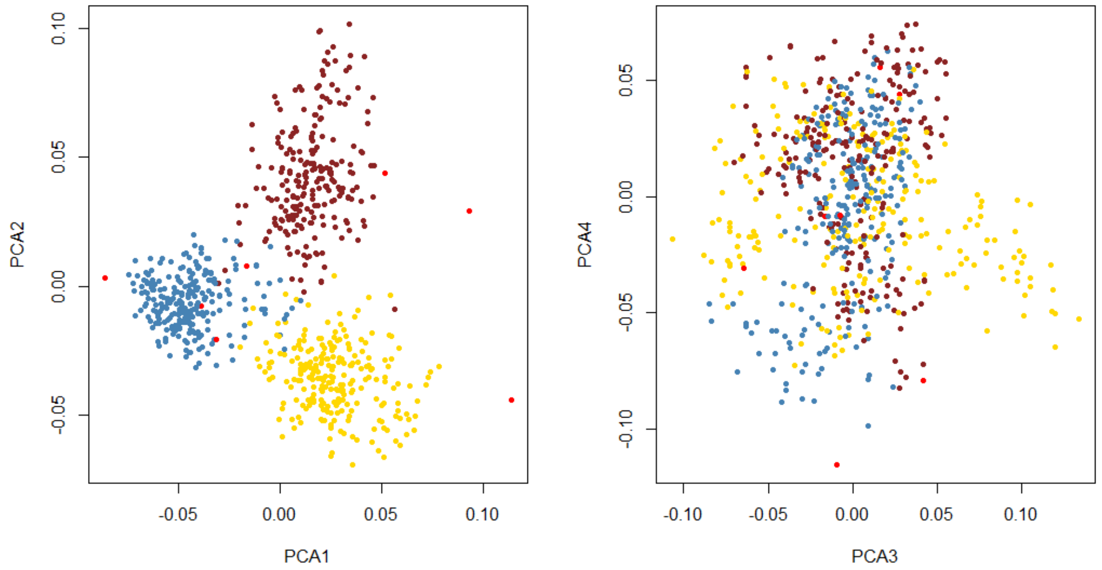

Sup. Figure 9: Principal component analysis (PCA) of the MAGIC population based on 2,712,214 bi-allelic variants. PC1 and PC2 (left panel) alone captured the population structure created by the three independent replicates of the MAGIC design (6.7% of the observed total variation).

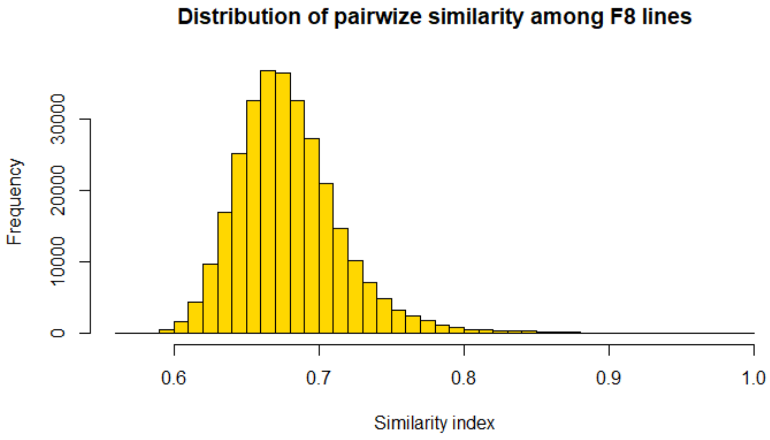

Sup. Figure 8: Distribution of pairwise similarity among the F8 lines, obtained as the proportion of IBS genotypes.

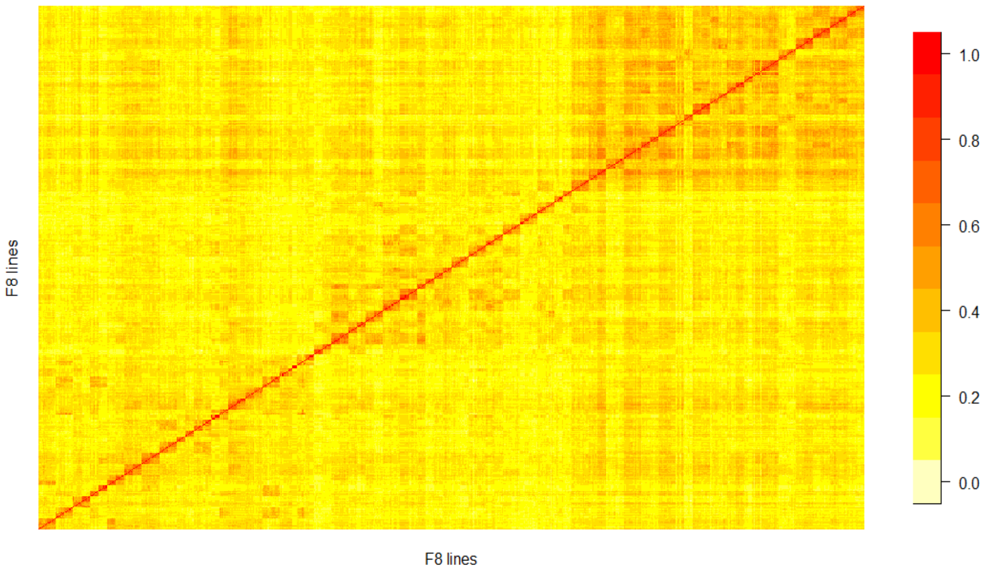

Sup. Figure 10: Estimated relatedness among F8 lines. The figure represents a heatmap of the relationship matrix. Each cell represents a pair of F8 lines. Lines are sorted by family and design. The intensity of the color indicates the level of relatedness.

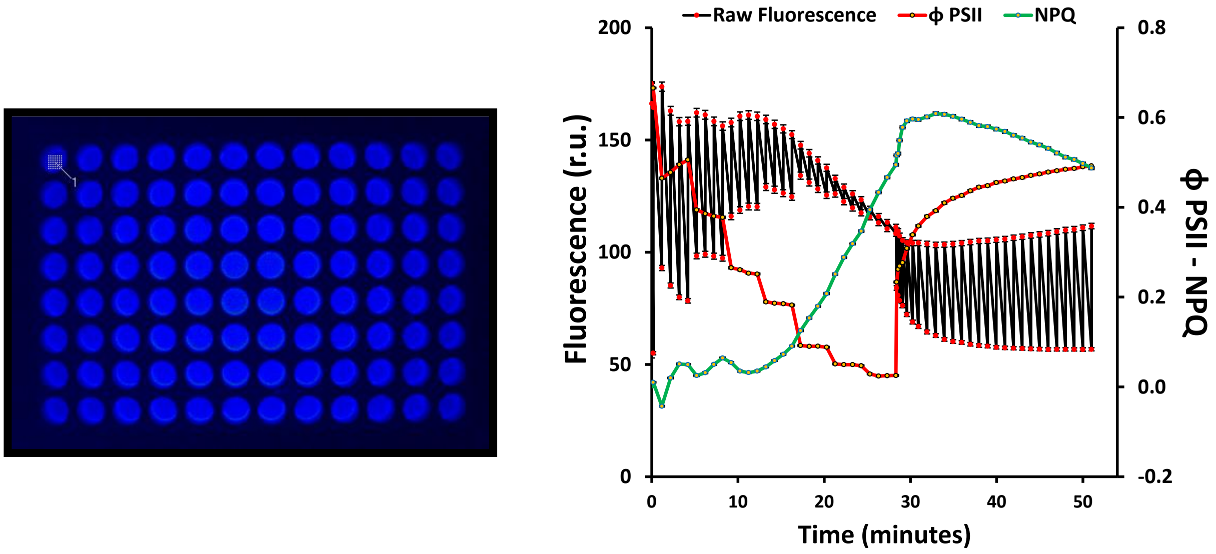

Sup. Figure 11: Evaluation of the level of background noise or technical error introduced by the simultaneous phenotyping of 96 strains. A white flat-bottom 96-wells microplate was filled at every position with 0.2 mL of the same culture. The plate was introduced into the fluorescence imaging device used for the phenotyping of the MAGIC population and measured with the same protocol. The figure on the left is a photograph of a plate's fluorescence signal (the blue color represents the fluorescence signal intensity), taken before the measurement. The right panel includes the average of all 96 technical replicates ± their standard error. Due to the small error values, error bars are not visible for NPQ and ϕ PSII.

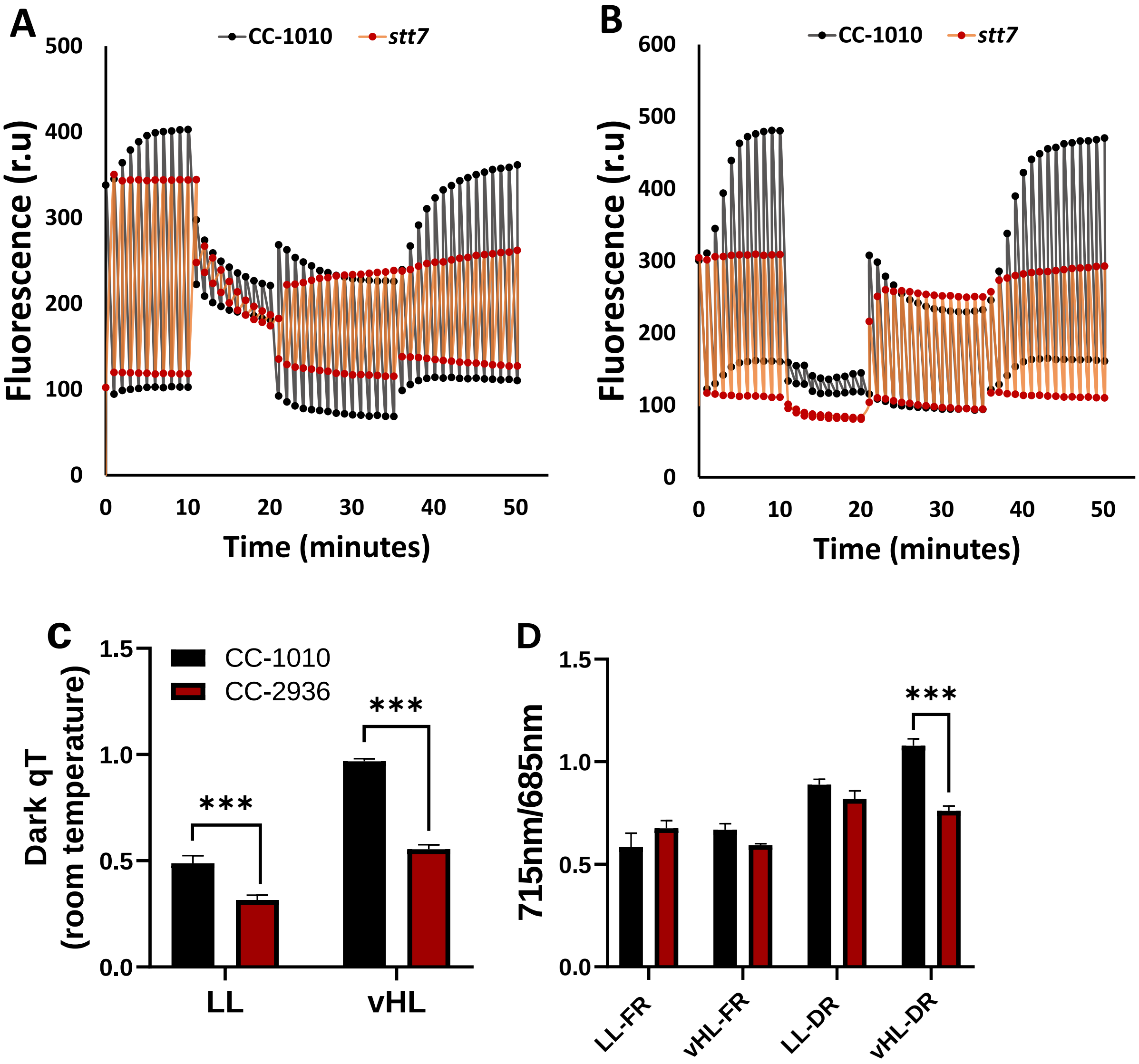

Sup. Figure 12: Time-resolved chlorophyll fluorescence detection protocol used to measure dark state transition. The two top panels show the comparison between CC-1010 and the mutant *stt7* (negative control), impaired in state transition, after 24h of acclimation to TMP-LL (A) or TMP-vHL (B). The bottom panels show the comparison between CC-1010 and CC-2936 grown in TMP for 24h under LL and vHL. The dark qT measured at room temperature (C) was significantly different between the strains for both LL- and vHL- exposed cells. Aliquots of the cultures were withdrawn during the room-temperature measurement, at the end of the dark-step (DR) and at the end of the second far-red step (FR) and plunged instantaneously into liquid nitrogen. The 77°K fluorescence emission spectra were used to calculate the 715 nm/685 nm ratio (D), finding significant differences between vHL samples' level of dark qT. The error bars represent the standard error calculated on 4 replicates. Significance was estimated through multiple t-tests ($p<0.0001$).

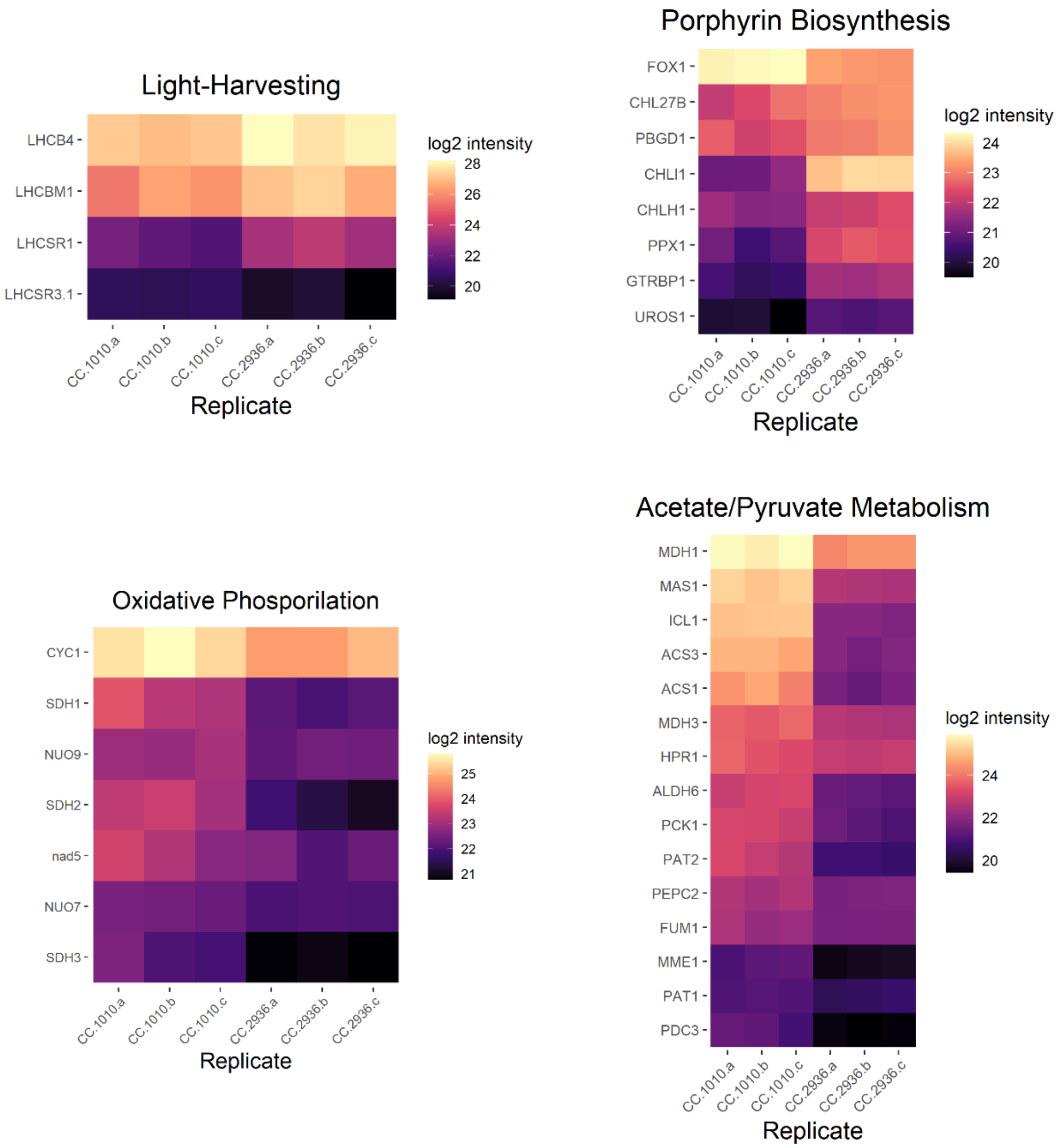

Sup. Figure 13: Differential regulation of light-harvesting (top-left), porphyrin biosynthesis (top-right), oxidative phosphorylation (bottom-left), and acetate/pyruvate metabolism (bottom-right) between CC-1010 and CC-2936. The heatmaps report the log2-intensities of DEqMS-filtered DE-proteins (*p*-value<0.05).

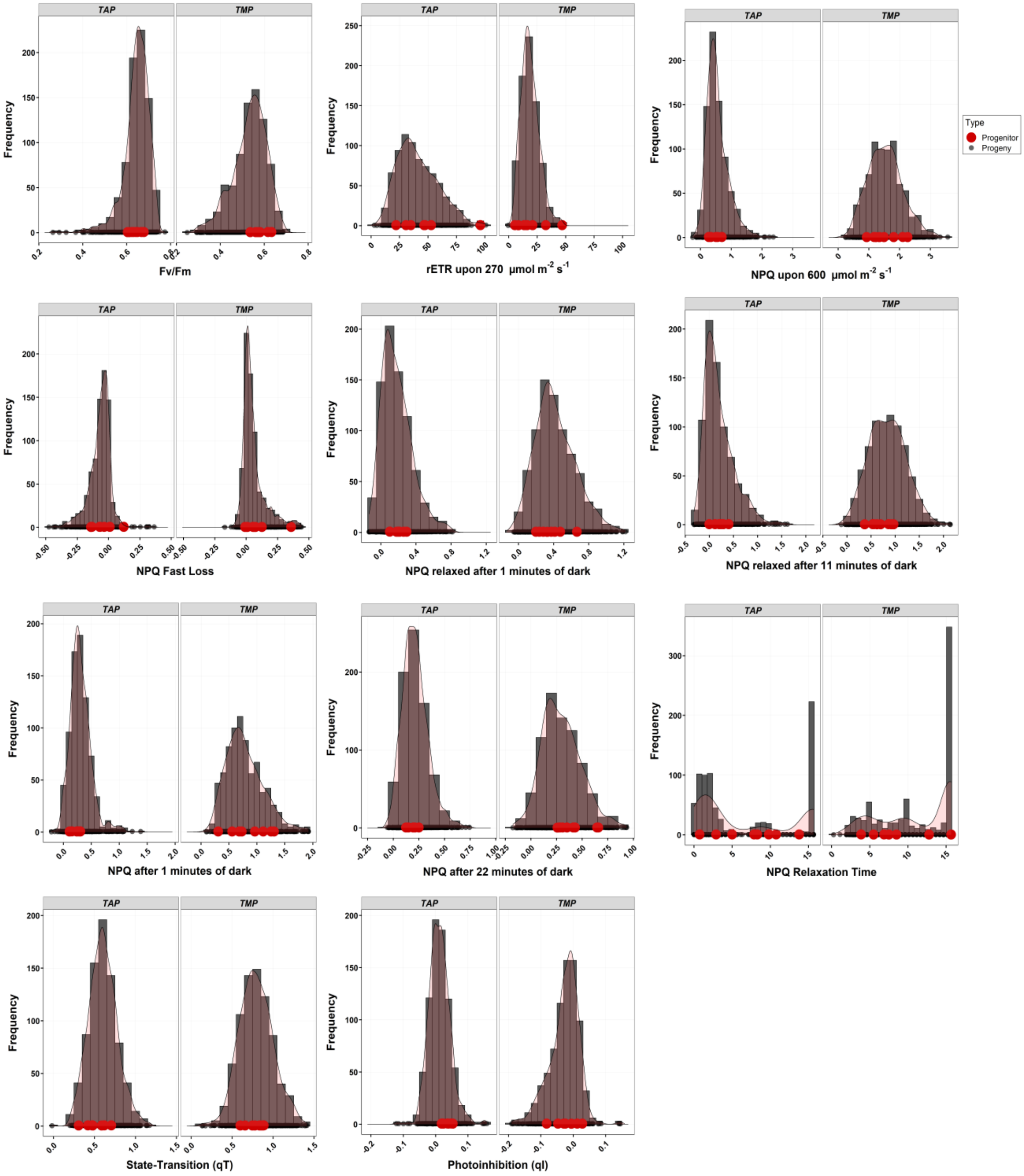

Sup. Figure 14: Probability distribution of photosynthetic traits. The red dots mark the distribution of the 8 founders among the MAGIC population (dark dots).

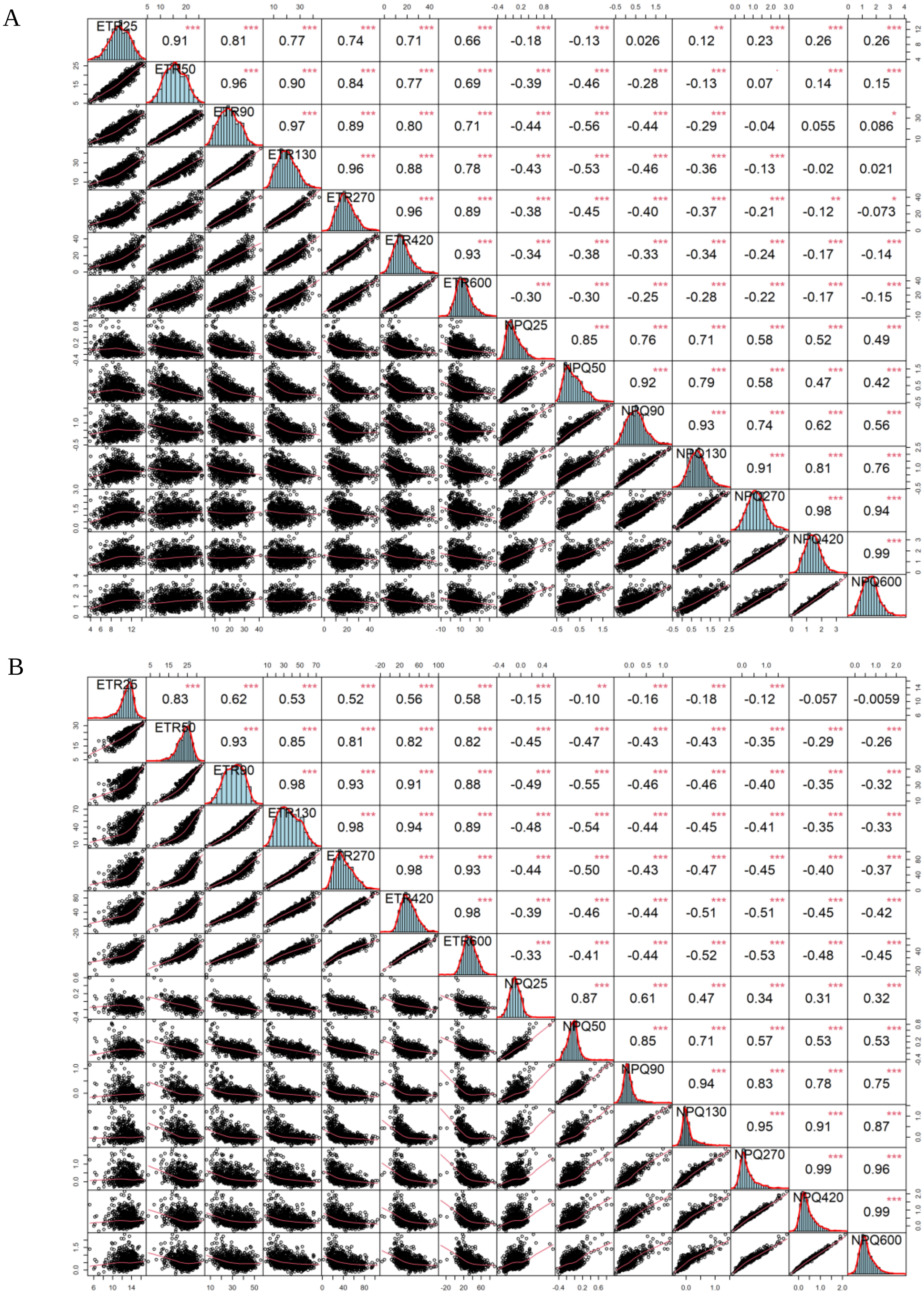

Sup. Figure 15: Distribution and Pearson correlation-coefficients of rETR and NPQ values calculated upon all light-steps of the saturation curve. Data is shown for both TMP (A) and TAP (B) conditions. Stars are equal to p-value ≤ 0.05 (*), or 0.01 (**), or 0.001 (***).

A

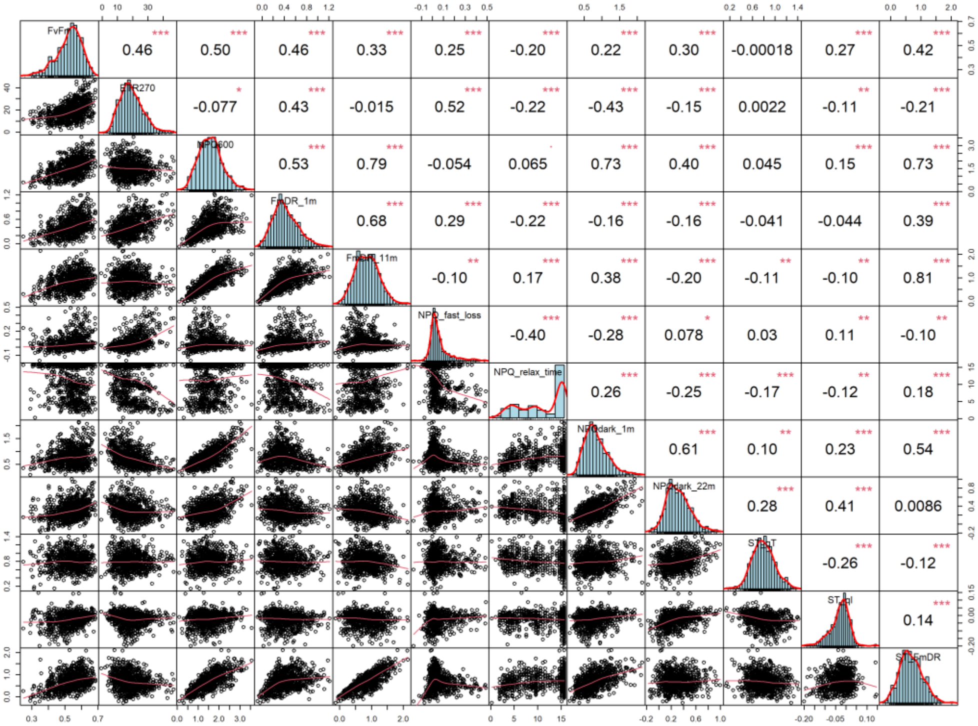

B

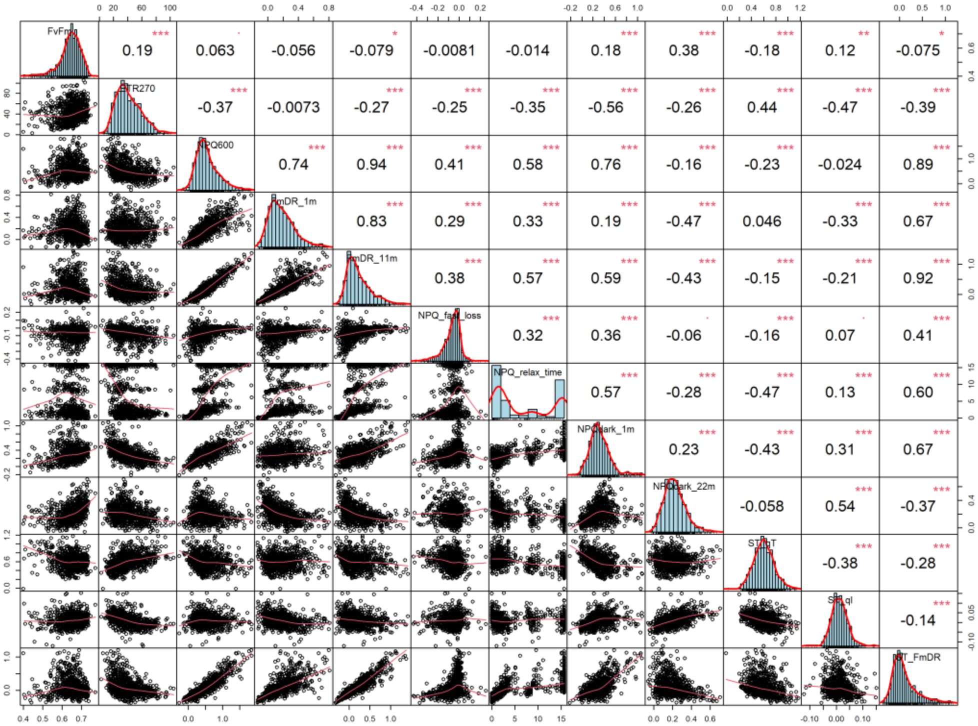

Sup. Figure 16: Correlation among all NPQ-related parameters in TMP (A) and TAP (B) samples. From left to right: Fv/Fm, maximum rETR, maximum NPQ, fast-relaxing NPQ relaxed after 1 minute or 11 minutes of dark (FmDR_1 and FmDR_11), NPQ lost within the first 5 seconds of darkness (NPQ-fast loss), time (minutes) corresponding to the highest Fm value registered within the first 15 minutes of dark (NPQ-relaxation time), NPQ present after 1 or 22 minutes of dark (NPQdark_1m and NPQdark_22m, dark state-transition capacity (ST_qT), photodamage developed during the measurement (ST_qI), NPQ relaxed after 11 minute of dark extracted from the same light protocol used to estimate qT (ST_FmDR). The prefix "ST_" before a parameter indicates that it was extracted from the "Strate-Transition" light protocol.

4.3 Supplementary tables

Sup. Table 1: List of differentially expressed proteins. Two independent DE analyses were conducted using the DEqMS and DEP packages from Bioconductor. Adjusted p-values (Adj. p-val.) are highlighted in yellow when < 0.05. Fold-change was calculated as the log2 of CC-1010/CC-2936. Rows are sorted from the lowest to the highest value of "Log10-FC (DEqMS)". Annotation was taken from the version 6 of the *Chlamydomonas* genome (CC-4532).

Accession	Locus ID	Gene Symbol	Description	Adj. p-val. (DEqMS)	Adj. p-val. (DEP)	Log2-FC (DEqMS)	Log2-FC (DEP)
XP_001697999.1	Cre06.g278195	—	Carboxyltransferase interactor	2.4E-05	4.0E-06	-4.4	-4.5
XP_001700856.1	Cre07.g321800	—	—	3.5E-05	3.6E-06	-4.2	-4.3
PNW69869.1	Cre18.g750047	FMG1A	Flagella Membrane Glycoprotein 1A	2.4E-06	4.2E-14	-4.2	-4.3
XP_001694493.1	Cre09.g395650	—	—	3.5E-05	2.8E-05	-3.6	-3.7
XP_001701853.1	Cre02.g077300	NOP1	Nucleolar protein, Component of C/D snoRNPs	2.4E-06	4.2E-14	-3.6	-3.7
pdb.6JO6.K	CreCp.g802312	psaB	photosystem I P700 apoprotein A2	2.4E-03	9.0E-01	-3.3	-1.2
XP_001694758.1	Cre09.g393765	—	Predicted protein with LysM domain	1.4E-05	3.0E-09	-3.3	-3.4
XP_001696588.1	Cre06.g261000	PSBR1	Photosystem II 10 kDa polypeptide	4.4E-03	3.2E-01	-3.1	-3.2
XP_001701993.1	Cre02.g093650	—	—	4.5E-03	3.1E-01	-2.8	-2.9
XP_001700222.1	Cre01.g054500	—	NADPH:NAD+ oxidoreductase	1.9E-04	1.8E-03	-2.7	-2.8
XP_001691232.1	Cre06.g306300	CHLI1	Magnesium chelatase subunit I, isoform 1	3.4E-05	1.3E-06	-2.7	-2.8
PNW72943.1	Cre14.g612633	—	—	4.4E-04	2.0E-02	-2.7	-2.8
XP_001699262.1	Cre16.g688550	GSTS1	Glutathione S-transferase	9.3E-05	1.7E-04	-2.6	-2.7
PNW85945.1	Cre03.g198850	—	Thylakoid llumen protein	1.4E-05	6.1E-10	-2.6	-2.7
PNW74438.1	Cre12.g484000	BCX1	Beta-carboxyltransferase (ACCase complex)	1.9E-04	2.0E-03	-2.4	-2.5
PNW83274.1	Cre05.g232600	—	—	2.8E-05	2.7E-09	-2.4	2.5
XP_001693782.1	Cre13.g577100	ACP2	Acyl-carrier protein 2	2.6E-03	2.4E-01	-2.4	-2.5
XP_001703377.1	Cre03.g164000	ANR1	Anaerobiosis-Related protein 1	5.2E-05	1.2E-06	-2.2	-2.3
XP_001701700.1	Cre02.g082500	PSAN1	Photosystem I reaction center subunit N	1.4E-02	5.4E-01	-2.2	-2.3
XP_001695920.1	Cre16.g673001	FAD4	Fatty acide desaturase 4	4.4E-04	4.6E-01	-2.1	-3.0
PNW70659.1	Cre17.g729150	—	—	7.1E-03	1.8E-01	-2.1	-2.5
PNW77439.1	Cre10.g436550	EPYC1	Essential pyrenoid	4.4E-04	8.4E-03	-2.1	-2.2

			component 1				
PNW83774.1	Cre04.g216950	–	Putative 3-ketoacyl-ACP-synthase (FAS complex)	5.2E-05	1.5E-05	-2.1	-2.2
XP_001690823.1	Cre12.g505850	CPN23	Chaperonin 23	8.9E-05	2.1E-05	-2.1	-2.2
PNW82543.1	Cre06.g283200	–	–	3.5E-05	4.8E-08	-2.1	-2.2
PNW74830.1	Cre12.g508000	–	Putative chloroplast envelope protein	2.7E-03	2.5E-01	-2.1	-2.2
PNW71205.1	Cre16.g693500	FAP40	Hydroxyproline-rich Flagellar Associated Protein 40	3.4E-03	2.1E-01	-2.0	-2.1
ACJ50095.1	CreCp.g802267	tufA	elongation factor 1-alpha	5.2E-05	1.1E-06	-1.9	-2.0
XP_001691962.1	Cre16.g688050	–	–	6.3E-03	3.9E-01	-1.9	-2.0
PNW78368.1	Cre09.g400050	–	–	4.4E-04	5.5E-04	-1.9	-2.2
PNW79595.1	Cre08.g359350	BC1	Biotin carboxylase (ACCase complex)	1.0E-03	2.7E-02	-1.9	-2.0
XP_001698633.1	Cre10.g465550	CLPD1	ClpD chaperone, Hsp100 family	1.6E-03	1.3E-01	-1.9	-2.0
XP_001693577.1	Cre13.g581650	PRPL7	Chloroplast ribosomal protein L7/L12	9.6E-03	5.1E-01	-1.8	-1.9
XP_001692244.1	Cre04.g229300	RCA1	RuBisCO activase 1, chloroplastic	4.2E-04	5.8E-03	-1.8	-1.9
XP_001699523.1	Cre11.g467770	PGK1	Phosphoglycerate kinase, chloroplastic	2.2E-03	1.0E-01	-1.8	-1.9
PNW70172.1	Cre17.g708750	NSG1	Nitrogen-starvation/gametogenesis expressed protein	4.2E-04	1.1E-02	-1.8	-1.9
XP_001702713.1	Cre10.g428200	–	–	6.9E-04	9.7E-03	-1.7	-1.8
XP_001694498.1	Cre09.g396300	PPX1	Protoporphyrinogen oxidase	5.3E-04	6.3E-03	-1.7	-1.8
XP_001696518.1	Cre06.g268600	NAB1	Nucleic acid binding protein	4.8E-03	7.1E-01	-1.7	-2.8
XP_001696125.1	Cre08.g365900	LHCSR1	Stress-related chlorophyll a/b binding protein 1	2.3E-03	1.3E-01	-1.6	-1.7
PNW79553.1	Cre08.g358562	CPN20	Chaperonin 20	3.9E-04	1.1E-03	-1.6	-1.7
XP_001701716.1	Cre02.g084000	–	–	4.6E-03	2.4E-01	-1.6	1.7
XP_001696769.1	Cre09.g408200	SRS4	Serine/arginine-rich pre-mRNA splicing factor	6.8E-04	2.3E-02	-1.6	-1.7
XP_001703442.1	Cre03.g176100	–	–	4.1E-02	7.3E-01	-1.5	-1.6
PNW70252.1	Cre17.g712100	MDAR1	Monodehydroascorbate reductase 1	4.4E-04	4.8E-03	-1.5	-1.6
PNW71576.1	Cre16.g659950	PRPS5	Chloroplast Ribosomal Protein S5	4.4E-04	7.6E-03	-1.5	-1.6
XP_001693109.1	Cre03.g193850	SCLA1	Succinyl-CoA ligase alpha chain	9.7E-03	5.9E-01	-1.5	-2.2
PNW83259.1	Cre05.g233305	–	–	1.5E-02	5.7E-01	-1.5	1.6
XP_001696200.1	Cre06.g273000	–	Protein Kinase C Binding Protein	1.3E-03	2.9E-02	-1.5	-1.6
XP_001702979.1	Cre12.g513950	SUFD1	Iron-sulfur cluster assembly protein	2.4E-03	9.8E-02	-1.5	-1.6

XP_001696827.1	Cre09.g415800	—	programmed cell death protein 4	4.2E-04	2.2E-03	-1.5	-1.6
XP_001694765.1	Cre09.g394473	LCI9	Low-CO2-inducible protein	3.7E-03	3.2E-01	-1.5	-1.6
XP_001695448.1	Cre06.g281800	—	—	7.4E-03	4.1E-01	-1.5	-1.4
XP_001696003.1	Cre05.g248400	CAH4	Mitochondrial carbonic anhydrase, beta type	1.6E-03	4.9E-02	-1.5	-1.6
PNW70873.1	Cre17.g737050	—	—	7.6E-04	2.8E-02	-1.5	-1.6
XP_001696945.1	Cre12.g519100	ACC1	Alpha-carboxyltransferase (ACCase complex)	2.9E-04	9.0E-04	-1.4	-1.5
PNW80662.1	Cre07.g325736	—	—	1.5E-03	9.5E-02	-1.4	-1.5
XP_001693371.1	Cre03.g200250	—	Putative isocitrate lyase/malate synthase	1.4E-03	2.9E-02	-1.4	-1.5
XP_001701331.1	Cre08.g372450	PSBQ1	Photosystem II Oxygen Evolution Enhancer protein 3	4.2E-04	1.9E-03	-1.4	-1.5
XP_001702816.1	Cre12.g558900	PETO1	Regulator of photosynthetic cyclic electron flow	4.4E-04	4.6E-03	-1.4	-1.5
PNW78531.1	Cre09.g393450	FAP233	Flagellar Associated Protein 233	1.1E-02	5.3E-01	-1.4	-1.5
XP_001699357.1	Cre16.g693600	FAP137	Hydroxyproline-rich Flagellar Associated Protein137	3.1E-02	6.7E-01	-1.4	-2.0
PNW76056.1	Cre12.g549350	—	—	1.7E-03	8.6E-02	-1.3	-1.4
PNW77802.1	Cre10.g452450	—	Chloroplast envelope protein	1.5E-02	4.9E-01	-1.3	-1.4
PNW84382.1	Cre03.g143887	TSR1	Arginyl-tRNA Synthetase	4.3E-03	2.1E-01	-1.3	-1.4
pdb.5DE3.A	Cre04.g218250	FAP313	Flagellar Associated Protein 313	2.1E-03	9.2E-02	-1.3	-1.4
XP_001696319.1	Cre06.g261450	—	High mobility group protein	1.5E-02	5.0E-01	-1.3	-1.4
XP_001693621.1	Cre13.g586916	SRS6	Serine/arginine-rich pre-mRNA splicing factor	2.2E-03	6.3E-02	-1.3	-1.4
PNW84736.1	Cre03.g156600	GTRBP1	Glutamyl-tRNA reductase binding protein 1	6.6E-04	3.6E-03	-1.3	-1.4
XP_001699897.1	Cre02.g800236	—	Histidine--tRNA ligase / Histidyl-tRNA synthetase	3.2E-02	5.5E-01	-1.3	-1.4
XP_001699266.1	Cre16.g682725	GSTS2	Glutathione S-transferase	1.1E-03	1.9E-02	-1.3	-1.4
PNW74097.1	Cre13.g585100	—	—	3.4E-02	6.8E-01	-1.2	-1.9
XP_001694756.1	Cre09.g393543	HCP2	Hybrid-cluster protein	2.1E-03	6.3E-02	-1.2	-1.3
XP_001702062.1	Cre07.g356350	DXS1	1-deoxy-D-xylulose 5-phosphate synthase, chloroplast precursor	2.4E-02	3.6E-01	-1.2	-1.3
XP_001703518.1	Cre03.g167250	—	—	2.9E-02	6.8E-01	-1.2	-1.3

XP_001701425.1	Cre11.g467535	—	Mitochondrial substrate carrier protein	1.2E-02	4.9E-01	-1.2	-1.3
PNW77089.1	Cre10.g421700	GPD4	Glycerol-3-phosphate dehydrogenase/dihydroxyacetone-3-phosphate reductase	2.2E-03	7.0E-02	-1.2	-1.3
XP_001693443.1	Cre13.g567450	HON1	Histone H1	7.9E-03	3.8E-01	-1.2	-1.3
XP_001698234.1	Cre16.g651550	MTT1	Mitochondrial transcription termination factor	7.6E-04	1.6E-02	-1.2	-1.3
PNW84481.1	Cre03.g145747	SHKH1	Chorismate synthase	6.2E-03	3.8E-01	-1.2	-1.3
PNW71784.1	Cre16.g683081	—	—	1.5E-02	4.7E-01	-1.2	-1.3
XP_001700039.1	Cre02.g097900	AST3	Aspartate aminotransferase	2.1E-02	5.5E-01	-1.1	-1.2
XP_001694951.1	Cre09.g391097	RPL24	Cytosolic 80S ribosomal protein L4	1.5E-02	4.8E-01	-1.1	-1.2
PNW72319.1	Cre16.g673100	—	—	1.7E-03	4.2E-02	-1.1	-1.2
PNW84792.1	Cre03.g158900	DLA2	Dihydrolipoamide acetyltransferase	1.2E-03	3.6E-02	-1.1	-1.2
BAF96750.2	Cre01.g049950	VLE1	Sporangin (Vegetative Lytic Enzyme 1)	3.2E-03	2.3E-01	-1.1	-1.2
PNW87756.1	Cre01.g000900	CPLD20	Conserved in the Plant Lineage and Diatoms	2.5E-03	8.1E-02	-1.1	-1.2
XP_001696943.1	Cre12.g519180	PSRP7	Chloroplast elongation factor Ts-like protein	2.8E-03	1.9E-01	-1.1	-1.2
XP_001690337.1	Cre10.g443250	CCT3	T-complex protein 1, gamma subunit	2.2E-03	5.3E-02	-1.1	-1.2
XP_001700985.1	Cre07.g315700	FKB16A	Peptidyl-prolyl cis-trans isomerase, FKBP-type	1.2E-02	6.0E-01	-1.0	-1.6
PNW75997.1	Cre12.g551800	—	—	1.5E-02	5.1E-01	-1.0	-1.1
XP_001697954.1	Cre16.g662702	—	—	7.0E-03	3.6E-01	-1.0	-1.1
PNW80854.1	Cre07.g332300	GWD2	Alpha-glucan water dikinase 2	9.6E-03	3.5E-01	-1.0	-1.1
PNW70258.1	Cre17.g712300	—	—	1.8E-03	3.2E-02	-1.0	-1.1
PNW86309.1	Cre02.g081250	—	—	2.5E-03	1.0E-01	-1.0	-1.1
PNW89085.1	Cre01.g066917	LHCBM1	Light-harvesting Chlorophyll a/b binding protein of LHCII	3.8E-02	7.1E-01	-9.9E-01	-1.1
XP_001697120.1	Cre17.g721700	CPLD44	conserved expressed thylakoid lumenal protein-like	2.4E-03	8.9E-02	-9.9E-01	-1.1
BAF46282.1	Cre06.g304500	ZYS4	Zygote-specific protein	3.3E-03	1.2E-01	-9.6E-01	-1.1
PNW77087.1	Cre10.g421600	TST2	Threonyl-tRNA synthetase	3.9E-02	6.9E-01	-9.6E-01	-1.1
PNW79282.1	Cre09.g409100	UROS1	Uroporphyrinogen-III synthase	5.1E-03	1.7E-01	-9.5E-01	-1.1

PNW72378.1	Cre16.g673953	FKB16G	Peptidyl-prolyl cis-trans isomerase, FKBP-type	1.1E-02	2.8E-01	-9.5E-01	-1.1
XP_001699001.1	Cre14.g615050	—	—	3.0E-02	5.9E-01	-9.4E-01	-1.0
XP_001691056.1	Cre12.g510850	CGL73	expressed protein Conserved in the Green Lineage	4.7E-02	5.2E-01	-9.4E-01	-1.3
XP_001700677.1	Cre05.g234639	CCT4	T-complex protein 1, delta subunit	2.9E-02	5.7E-01	-9.4E-01	-1.0
PNW81854.1	Cre06.g263250	—	—	3.4E-02	6.5E-01	-9.3E-01	-1.0
PNW87359.1	Cre02.g119550	NIP1	NaCl-inducible protein	3.9E-02	6.8E-01	-9.2E-01	-1.0
PNW80904.1	Cre07.g334600	CGL20	Conserved in the Green Lineage	3.4E-02	6.5E-01	-9.2E-01	-1.0
PNW74118.1	Cre13.g586050	—	—	4.3E-02	6.8E-01	-9.2E-01	-1.0
PNW82947.1	Cre06.g300700	—	Flavin reductase	2.8E-02	5.7E-01	-9.2E-01	-1.0
PNW84941.1	Cre03.g165000	EFG10	Translation elongation factor EFG/EF2, LepA-related	2.9E-02	6.2E-01	-9.1E-01	-8.9E-01
XP_001700372.1	Cre01.g002300	CYN19B	Cyclophilin 19-2	1.1E-02	3.9E-01	-9.0E-01	-1.0
PNW72074.1	Cre16.g683550	—	—	1.8E-02	4.1E-01	-8.9E-01	-1.2
XP_001691582.1	Cre17.g703700	SCLB1	Succinate-CoA ligase beta chain	3.9E-02	6.7E-01	-8.8E-01	-9.7E-01
XP_001699345.1	Cre16.g691800	FLVB1	Thylakoid flavodiiron protein	4.4E-03	9.7E-02	-8.7E-01	-9.7E-01
PNW82579.1	Cre06.g284750	EFG3	Translation elongation factor Tu family protein	3.5E-03	1.1E-01	-8.7E-01	-9.7E-01
XP_001696758.1	Cre09.g416850	POB32	Proteome of basal body 32	5.1E-03	2.0E-01	-8.6E-01	-9.5E-01
XP_001697193.1	Cre17.g720250	LHCB4	Light-harvesting minor chlorophyll a/b binding protein of photosystem II	1.1E-02	3.6E-01	-8.6E-01	-9.5E-01
PNW76826.1	Cre11.g477950	—	—	7.9E-03	3.2E-01	-8.5E-01	-9.4E-01
XP_001696050.1	Cre08.g366400	RAD23	UV excision repair protein	3.9E-03	8.1E-02	-8.4E-01	-9.4E-01
AAY23327.1	CreCp.g802264	petD	cytochrome b6/f complex subunit 4	3.8E-02	6.3E-01	-8.4E-01	-9.3E-01
PNW73147.1	Cre14.g620600	PHC2	Pherophorin-chlamydomonas homolog 2	2.9E-02	6.0E-01	-8.4E-01	-9.3E-01
XP_001689455.1	Cre01.g014350	PRX5	Peroxiredoxin, type II	8.2E-03	2.0E-01	-8.3E-01	-9.2E-01
XP_001701451.1	Cre16.g664550	SHMT1	Serine hydroxymethyltransferase	1.6E-02	4.0E-01	-8.0E-01	-9.0E-01
sp.Q8LPD9.1.PHOT_CHLRE	Cre03.g199000	PHOT1	Phototropin 1	3.4E-02	5.7E-01	-8.0E-01	-8.9E-01
XP_001694791.1	Cre09.g396772	—	Similar to Gametolysin and Autolysin	1.4E-02	1.5E-01	-7.9E-01	-8.8E-01
BAD98160.2	Cre17.g734612	MRP2	ABC transporter, multidrug resistance associated protein	2.8E-02	5.8E-01	-7.8E-01	-8.7E-01

XP_001694699.1	Cre09.g396213	PSBO1	Photosystem II Oxygen Evolution Enhancer protein 1	9.9E-03	3.8E-01	-7.7E-01	-8.7E-01
XP_001700895.1	Cre07.g325500	CHLH1	Magnesium chelatase subunit H	1.1E-02	2.2E-01	-7.7E-01	-8.6E-01
XP_001703461.1	Cre03.g173350	⊢	Predicted protein with ankyrin repeats	9.4E-03	2.1E-01	-7.6E-01	-8.5E-01
PNW88395.1	Cre01.g027550	⊢	⊢	9.9E-03	3.2E-01	-7.2E-01	-8.2E-01
XP_001702364.1	Cre12.g497300	CAS1	Rhodanese-like Ca-sensing receptor	1.3E-02	3.7E-01	-7.2E-01	-8.2E-01
PNW74783.1	Cre12.g510050	CHL27B	Copper target homolog 1, chloroplast precursor, functional variant	4.1E-02	6.7E-01	-7.2E-01	-8.2E-01
XP_001701464.1	Cre16.g666301	RPS30	Cytosolic 80S ribosomal protein S30	4.9E-02	7.0E-01	-7.0E-01	-8.0E-01
XP_001701593.1	Cre06.g293950	SHMT2	Serine hydroxymethyltransferase	3.7E-02	5.8E-01	-6.8E-01	-7.7E-01
PNW85233.1	Cre03.g177200	CRB3	RNA-binding protein C3, CELF family, subunit of CHLAMY1	2.0E-02	4.7E-01	-6.7E-01	-7.7E-01
PNW75567.1	Cre12.g531900	FLVA1	Thylakoid flavodiiron protein	2.3E-02	4.6E-01	-6.6E-01	-7.6E-01
XP_001699525.1	Cre11.g467773	⊢	⊢	4.0E-02	8.1E-01	-6.5E-01	-1.7
XP_001693248.1	Cre03.g192350	⊢	⊢	4.2E-02	6.3E-01	-6.5E-01	-7.4E-01
XP_001702917.1	Cre03.g182450	⊢	⊢	3.9E-02	5.8E-01	-6.5E-01	-7.4E-01
PNW83121.1	Cre06.g307450	⊢	SF3A1 splicing factor 3a, subunit 1	3.1E-02	6.2E-01	-6.4E-01	-7.4E-01
XP_001694098.1	Cre12.g546400	LC7B	Roadblock/LC7 Family Light Chain	2.6E-02	5.2E-01	-6.4E-01	-7.3E-01
PNW75777.1	Cre12.g561000	CYN28	Cyclophilin 28	2.1E-02	4.8E-01	-6.3E-01	-7.2E-01
XP_001697700.1	Cre05.g241000	⊢	⊢	1.5E-02	2.8E-01	-6.3E-01	-7.2E-01
XP_001702934.1	Cre03.g180750	METE1	Cobalamin-dependent methionine synthase	2.7E-02	5.5E-01	-6.2E-01	-7.2E-01
XP_001700042.1	Cre02.g097650	RPN6	26S proteasome regulatory subunit	4.0E-02	5.8E-01	-6.2E-01	-7.1E-01
XP_001701485.1	Cre16.g663900	PBGD1	Porphobilinogen deaminase	3.5E-02	5.2E-01	-6.1E-01	-7.0E-01
PNW75082.1	Cre12.g497350	PPR13	PentatricoPeptide Repeat protein 13	2.7E-02	5.0E-01	-5.9E-01	-6.9E-01
PNW85319.1	Cre03.g180800	⊢	Histone deacetylase complex protein	2.5E-02	4.3E-01	-5.9E-01	-6.8E-01
PNW77301.1	Cre10.g430501	⊢	⊢	3.7E-02	5.6E-01	-5.8E-01	-6.8E-01
PNW88341.1	Cre01.g025250	RFK2	Riboflavin kinase	4.2E-02	6.4E-01	-5.7E-01	-6.7E-01
PNW82126.1	Cre06.g275100	⊢	Nucleolin	2.6E-02	4.6E-01	-5.7E-01	-6.6E-01
XP_001703358.1	Cre03.g166050	SBD1	Selenium binding protein	4.3E-02	5.5E-01	-5.4E-01	-6.4E-01
pdb.6U42.B1	Cre12.g549550	TUB2	beta-2 tubulin	4.9E-02	⊢	-5.4E-01	⊢
CBL74084.1	Cre16.g685550	OASTL4	O-acetylserine (Thiol)-lyase/cysteine	3.3E-02	4.7E-01	-5.0E-01	-6.0E-01

			synthase 4				
XP_001693180.1	Cre03.g206550	CPLD2	conserved expressed protein with hydrolase motif	4.7E-02	7.7E-01	4.7E-01	3.7E-01
XP_001697607.1	Cre09.g405850	NUO7	NADH:ubiquinone oxidoreductase 49 kDa ND7 subunit	4.7E-02	7.7E-01	4.7E-01	3.7E-01
XP_001702649.1	Cre10.g434750	AAI1	Acetohydroxy acid isomeroreductase	4.4E-02	7.8E-01	4.7E-01	3.8E-01
XP_001692993.1	Cre12.g534800	GCSP1	Glycine cleavage system, P protein	4.9E-02	8.0E-01	4.8E-01	3.9E-01
XP_001703281.1	Cre03.g175200	TOC75	Translocon at the outer envelope membrane of chloroplasts, 75 kDa subunit	4.9E-02	7.7E-01	4.8E-01	3.9E-01
XP_001691218.1	Cre06.g308250	RPS4	Cytosolic 80S ribosomal protein S4	3.8E-02	7.4E-01	4.8E-01	3.9E-01
XP_001701977.1	Cre02.g091700	RIB72	Flagellar protofilament ribbon protein 72	4.3E-02	7.8E-01	4.8E-01	3.9E-01
XP_001690929.1	Cre12.g489700	OTC1	Ornithine carbamoyltransferase	3.9E-02	7.6E-01	4.9E-01	4.0E-01
PNW85419.1	Cre03.g185550	SBP1	Sedoheptulose-1,7-bisphosphatase, chloroplastic	4.8E-02	7.9E-01	5.0E-01	4.0E-01
PNW82765.1	Cre06.g293150	—	Phosphoglycerate mutase	4.2E-02	7.5E-01	5.0E-01	4.0E-01
XP_001691600.1	Cre17.g701200	RPL14	Cytosolic 80S ribosomal protein L14	4.9E-02	7.6E-01	5.0E-01	4.1E-01
XP_001697084.1	Cre12.g517150	APSR1	Adenylylphosphosulfate reductase	4.7E-02	7.5E-01	5.1E-01	4.1E-01
XP_001698101.1	Cre06.g278125	—	—	4.3E-02	7.8E-01	5.1E-01	4.1E-01
PNW75710.1	Cre12.g537800	RPL7	Cytosolic 80S ribosomal protein L7	3.7E-02	7.4E-01	5.1E-01	4.2E-01
XP_001701557.1	Cre06.g294650	AGT1	Alanine-glyoxylate transaminase	3.2E-02	7.2E-01	5.2E-01	4.2E-01
XP_001697145.1	Cre17.g724550	DIP13	Deflagellation Inducible Protein 13	3.8E-02	7.7E-01	5.2E-01	4.3E-01
sp.Q8LKI3.1.ALB32_CHLRE	Cre17.g729800	ALB3B	ALBINO3-like translocon protein	4.4E-02	7.9E-01	5.2E-01	4.3E-01
XP_001690591.1	Cre10.g436050	FSD1	Fe superoxide dismutase	4.9E-02	7.9E-01	5.3E-01	4.3E-01
sp.Q7PCJ6.1.RPOC2_CHLRE	CreCp.g802311	rpoC2	RNA polymerase beta" chain	4.7E-02	7.6E-01	5.3E-01	4.4E-01
XP_001699617.1	Cre17.g737250	EFG5	U5 small nuclear ribonucleoprotein	4.1E-02	7.4E-01	5.5E-01	4.6E-01
PNW69940.1	Cre17.g699000	PAT1	Phosphate acetyltransferase	2.9E-02	7.1E-01	5.5E-01	4.6E-01
XP_001697060.1	Cre12.g520500	RPLP0	Acidic ribosomal protein P0, Ribosomal protein	2.9E-02	6.9E-01	5.5E-01	4.6E-01

			L10				
XP_001699045.1	Cre14.g614300	–	–	2.3E-02	6.8E-01	5.5E-01	4.6E-01
pir||S78597	Cre01.g021251	ARG7	Argininosuccinate lyase	4.8E-02	7.8E-01	5.6E-01	4.6E-01
XP_001689450.1	Cre01.g013700	VDAC1	Voltage-dependent anion-selective channel protein	4.9E-02	7.9E-01	5.6E-01	4.7E-01
XP_001697352.1	Cre11.g476750	FNR1	Ferredoxin-NADP reductase, chloroplast	3.2E-02	7.1E-01	5.7E-01	4.7E-01
XP_001700898.1	Cre05.g241650	–	acylaminoacyl-peptidase	4.5E-02	7.2E-01	5.8E-01	4.5E-01
PNW76824.1	Cre11.g477850	TXC1	Transcriptional coactivator-like protein	4.7E-02	7.6E-01	5.8E-01	4.9E-01
XP_001698065.1	Cre06.g278222	RACK1	Receptor of activated protein kinase C	3.9E-02	7.8E-01	5.8E-01	4.9E-01
PNW75789.1	Cre12.g560450	–	–	2.4E-02	6.8E-01	5.9E-01	4.9E-01
XP_001702812.1	Cre12.g559250	POC14	Proteome of centriole protein 14	3.8E-02	7.4E-01	5.9E-01	4.9E-01
XP_001693235.1	Cre03.g199900	EIF4E	Eukaryotic translation initiation factor 4E	2.4E-02	7.1E-01	5.9E-01	5.0E-01
XP_001698518.1	Cre10.g451950	AAT1	Alanine aminotransferase	4.5E-02	7.7E-01	6.0E-01	5.0E-01
XP_001690123.1	Cre01.g038650	SRS2	Serine/arginine-rich pre-mRNA splicing factor	4.9E-02	7.8E-01	6.0E-01	5.0E-01
XP_001703470.1	Cre03.g172300	PHT3A	Mitochondrial phosphate carrier protein	4.9E-02	7.9E-01	6.0E-01	5.0E-01
XP_001691597.1	Cre17.g701700	FAB2	Plastid acyl-ACP desaturase	2.8E-02	7.4E-01	6.0E-01	5.0E-01
XP_001693339.1	Cre03.g204250	SAH1	S-Adenosyl homocysteine hydrolase	3.8E-02	7.7E-01	6.0E-01	5.1E-01
XP_001696634.1	Cre06.g254400	FUM1	Fumarate hydratase 1	2.8E-02	6.9E-01	6.0E-01	5.1E-01
XP_001702818.1	Cre12.g558600	–	–	2.5E-02	7.1E-01	6.1E-01	5.2E-01
XP_001691570.1	Cre17.g705000	FAP223	Flagellar Associated Protein 223	2.0E-02	6.2E-01	6.1E-01	5.2E-01
PNW87539.1	Cre02.g142351	–	–	2.0E-02	6.6E-01	6.2E-01	5.2E-01
PNW82816.1	Cre06.g295450	HPR1	Hydroxyl pyruvate reductase	3.1E-02	7.0E-01	6.2E-01	5.2E-01
PNW84727.1	Cre03.g156250	POC13	Proteome of centriole protein 13	4.3E-02	7.4E-01	6.2E-01	5.2E-01
XP_001690402.1	Cre10.g436350	SHKF1	Shikimate kinase	4.1E-02	7.8E-01	6.2E-01	5.3E-01
XP_001693266.1	Cre03.g194400	EIF3I	Eukaryotic translation initiation factor 3, subunit I	1.6E-02	6.2E-01	6.3E-01	5.4E-01
XP_001699654.1	Cre02.g115200	RPL27A	Cytosolic 80S ribosomal protein L27a	2.4E-02	6.7E-01	6.3E-01	5.4E-01
XP_001702485.1	Cre10.g432800	RPSA1	Cytosolic 80S ribosomal protein	1.9E-02	6.2E-01	6.3E-01	5.4E-01

			Sa				
XP_001701674.1	Cre02.g079600	TSF2	Phenylalanyl-tRNA synthetase	1.5E-02	5.7E-01	6.4E-01	5.4E-01
PNW80729.1	Cre07.g327400	NUO9	NADH:ubiquinone oxidoreductase ND9 subunit	1.8E-02	6.5E-01	6.4E-01	5.4E-01
PNW73565.1	Cre13.g564250	EIF3A	Eukaryotic translation initiation factor 3, subunit A	2.1E-02	6.7E-01	6.4E-01	5.5E-01
XP_001698656.1	Cre04.g215850	IPA1	Importin alpha	4.2E-02	7.5E-01	6.4E-01	5.5E-01
XP_001690850.1	Cre12.g508900	—	Mitogen-Activated Protein Kinase 6	3.9E-02	7.5E-01	6.4E-01	5.5E-01
PNW82205.1	Cre06.g278098	—	Methylcrotonoyl-CoA carboxylase alpha subunit	2.5E-02	7.3E-01	6.4E-01	5.5E-01
PNW75057.1	Cre12.g498500	DEG1C	Deg protease	3.2E-02	7.1E-01	6.4E-01	5.5E-01
PNW69669.1	Cre26.g756797	—	—	4.7E-02	7.8E-01	6.5E-01	5.5E-01
XP_001696183.1	Cre06.g275050	GGH2	Gamma-glutamyl hydrolase	1.8E-02	6.0E-01	6.5E-01	5.5E-01
XP_001698004.1	Cre06.g278185	UGD2	UDP-glucose dehydrogenase	3.9E-02	7.4E-01	6.6E-01	5.6E-01
PNW78814.1	Cre09.g391023	—	—	2.9E-02	7.0E-01	6.6E-01	5.6E-01
XP_001702026.1	Cre11.g476050	DHC15	Flagellar outer arm dynein heavy chain gamma	4.1E-02	7.6E-01	6.6E-01	5.7E-01
XP_001693495.1	Cre13.g573351	—	—	3.0E-02	7.1E-01	6.6E-01	5.7E-01
XP_001699746.1	Cre02.g106600	RPS19	Cytosolic 80S ribosomal protein S19	3.3E-02	7.5E-01	6.6E-01	5.7E-01
PNW82781.1	Cre06.g293850	CAG2	Gamma carbonic anhydrase 2	3.9E-02	7.6E-01	6.6E-01	5.7E-01
XP_001697877.1	Cre16.g662200	—	Putative adenylate cyclase	3.5E-02	7.7E-01	6.6E-01	9.4E-01
PNW79206.1	Cre09.g406200	PRORS1	Organellar class II (G, H, P and S) tRNA synthetase	4.6E-02	8.6E-01	6.8E-01	2.5
XP_001693107.1	Cre03.g193750	GCST1	Glycine cleavage system, T protein	3.7E-02	7.3E-01	6.8E-01	5.8E-01
XP_001689859.1	Cre14.g621450	RPL5	Cytosolic 80S ribosomal protein L5	2.4E-02	7.0E-01	6.8E-01	5.9E-01
CAE18153.1	Cre04.g226850	ASP1	Pepsin-type aspartyl protease	3.1E-02	7.6E-01	6.8E-01	5.9E-01
XP_001700656.1	Cre05.g234637	—	—	2.9E-02	7.2E-01	6.8E-01	5.9E-01
AVV65756.1	Cre07.g338451	FBP1	Fructose-1,6-bisphosphatase Type II	1.1E-02	5.8E-01	6.9E-01	5.9E-01
XP_001691408.1	Cre06.g303300	CYN37	Cyclophilin 37	4.5E-02	7.7E-01	6.9E-01	5.9E-01
XP_001696212.1	Cre06.g272050	GPM1	Phosphoglycerate mutase 1	9.9E-03	5.6E-01	6.9E-01	5.9E-01
XP_001696912.1	Cre12.g522600	CYC1	mitochondrial cytochrome c	2.5E-02	6.9E-01	6.9E-01	6.0E-01
XP_001700393.1	Cre17.g715300	PKD2	Polycystin-2	4.3E-02	7.7E-01	6.9E-01	6.0E-01
XP_001696749.1	Cre09.g416050	AGS1	Argininosuccinate synthase	1.4E-02	5.5E-01	6.9E-01	6.0E-01
BAC99309.1	Cre09.g393700	MMP3	Matrix	3.6E-02	7.4E-01	7.0E-01	6.1E-01

			metalloproteinase				
XP_001695517.1	Cre06.g289550	RPL32	Cytosolic 80S ribosomal protein L32	3.2E-02	7.4E-01	7.0E-01	6.1E-01
XP_001694468.1	Cre09.g393200	HSP70C	Heat shock protein 70C	1.4E-02	5.9E-01	7.1E-01	6.1E-01
XP_001702577.1	Cre10.g424100	–	Inorganic pyrophosphatase	2.3E-02	7.0E-01	7.1E-01	6.1E-01
XP_001703311.1	Cre03.g171350	SEC61A	SEC61-alpha subunit of ER-translocon	3.6E-02	7.3E-01	7.1E-01	6.2E-01
XP_001695303.1	Cre06.g279400	–	Serine carboxypeptidase	3.1E-02	7.0E-01	7.1E-01	6.2E-01
PNW83918.1	Cre04.g215600	–	THIOCYANATE METHYLTRANSFERASE 1-RELATED	3.4E-02	7.3E-01	7.1E-01	9.8E-01
XP_001696201.1	Cre06.g272800	RPS8	Cytosolic 80S ribosomal protein S8	3.1E-02	7.2E-01	7.2E-01	6.2E-01
XP_001692539.1	Cre07.g343700	OGD2	Dihydrolipoamide succinyltransferase, oxoglutarate dehydrogenase E2 component	1.3E-02	6.0E-01	7.2E-01	6.2E-01
PNW85184.1	Cre03.g175250	SQS1	Squalene synthase	1.4E-02	6.1E-01	7.3E-01	6.4E-01
XP_001702113.1	Cre01.g004300	ASN1	Asparagine synthase	1.1E-02	6.1E-01	7.4E-01	6.4E-01
XP_001696763.1	Cre09.g417150	CAT1	Mono-functional catalase	1.4E-02	6.2E-01	7.4E-01	6.4E-01
XP_001696420.1	Cre06.g250902	METH1	Cobalamin-independent methionine synthase	1.3E-02	5.7E-01	7.4E-01	6.5E-01
PNW81450.1	Cre07.g356600	–	–	1.6E-02	6.1E-01	7.5E-01	6.6E-01
XP_001695070.1	Cre09.g390763	FAP354	Rab-like GTP-Binding Flagellar Associated Protein 354	1.0E-02	5.6E-01	7.6E-01	6.6E-01
XP_001696428.1	Cre06.g250300	DHC16	Cytoplasmic Dynein 1b Heavy Chain	3.3E-02	7.5E-01	7.6E-01	6.6E-01
XP_001692654.1	Cre14.g631900	–	Similar to Putative Serine Protease	2.5E-02	6.9E-01	7.6E-01	6.7E-01
BAC57979.1	Cre12.g549750	FAP4	Flagellar Associated Protein 4	1.6E-02	5.8E-01	7.7E-01	6.8E-01
XP_001698582.1	Cre10.g459250	RPL35A	Cytosolic 80S ribosomal protein L35a	3.9E-02	7.4E-01	7.7E-01	6.8E-01
XP_001692870.1	Cre12.g537200	OGD1	2-oxoglutarate dehydrogenase, E1 subunit	7.9E-03	5.4E-01	7.8E-01	6.8E-01
PNW85106.1	Cre03.g171950	PEPC2	Phosphoenolpyruvate carboxylase 2	7.0E-03	4.1E-01	7.8E-01	6.9E-01
XP_001703259.1	Cre03.g178450	CPN10	Chaperonin 10	1.8E-02	6.3E-01	7.8E-01	6.9E-01
PNW71982.1	Cre16.g687350	ACX3	Acyl-CoA oxidase/dehydrogenase	2.9E-02	7.7E-01	7.8E-01	1.3
PNW79203.1	Cre09.g406050	PYR7	CTP synthase	9.3E-03	5.8E-01	7.9E-01	6.9E-01

PNW88904.1	Cre01.g050150	NFO1	NADH:flavin oxidoreductase/NADH oxidase	1.1E-02	5.5E-01	7.9E-01	6.9E-01
XP_001695400.1	Cre06.g290950	RPS5	Cytosolic 80S ribosomal protein S5	5.4E-03	4.2E-01	7.9E-01	6.9E-01
XP_001697622.1	Cre09.g407700	–	Cysteine endopeptidase	9.5E-03	5.3E-01	7.9E-01	7.0E-01
PNW70824.1	Cre17.g734900	–	–	1.6E-02	6.6E-01	7.9E-01	7.0E-01
XP_001692513.1	Cre07.g340200	PGRL1	Proton-gradient related-like	1.3E-02	5.7E-01	8.0E-01	7.0E-01
XP_001695223.1	Cre09.g402500	ATPVA2	Vacuolar ATP synthase subunit A	1.3E-02	6.4E-01	8.0E-01	7.1E-01
PNW69888.1	Cre17.g696850	POB16	Proteome of basal body 16	2.3E-02	6.5E-01	8.1E-01	7.2E-01
PNW75473.1	Cre12.g528000	FAP303	Flagellar Associated Protein 303	7.2E-03	5.3E-01	8.2E-01	7.3E-01
XP_001694428.1	Cre09.g388200	RPL10	Cytosolic 80S ribosomal protein L10	1.4E-02	5.6E-01	8.2E-01	7.3E-01
PNW71100.1	Cre17.g746597	–	–	9.6E-03	5.6E-01	8.3E-01	7.3E-01
XP_001690441.1	Cre07.g330200	RSP9	Radial Spoke Protein 9	1.4E-02	6.4E-01	8.3E-01	7.3E-01
XP_001690644.1	Cre07.g328900	CDPK3	Calcium/calmodulin-dependent protein kinase	3.3E-02	7.4E-01	8.3E-01	7.3E-01
XP_001689769.1	Cre01.g051000	–	Protein-/Histone-arginine N-methyltransferase	2.0E-02	9.1E-01	8.3E-01	1.3E-01
XP_001691181.1	Cre06.g311900	RAB7	RAB-Like GTP binding Protein	1.3E-02	5.5E-01	8.4E-01	7.4E-01
PNW78505.1	Cre09.g394550	RPPK2	ribose-phosphate pyrophosphokinase	3.4E-03	3.1E-01	8.4E-01	7.5E-01
XP_001695958.1	Cre16.g677450	–	–	2.0E-02	6.7E-01	8.5E-01	7.5E-01
PNW76340.1	Cre12.g549852	–	–	2.0E-02	6.7E-01	8.5E-01	7.6E-01
ADN96053.1	CreMt.g000500	nad5	NADH dehydrogenase subunit 5	4.2E-02	7.6E-01	8.5E-01	7.6E-01
PNW82583.1	Cre06.g284900	CYN20A	Cyclophilin 20-1	8.1E-03	5.5E-01	8.5E-01	7.6E-01
PNW73516.1	Cre13.g562150	–	–	3.0E-02	7.0E-01	8.5E-01	7.6E-01
XP_001698420.1	Cre10.g461900	–	Aldo/keto reductase	1.0E-02	5.5E-01	8.7E-01	7.7E-01
XP_001696415.1	Cre06.g251400	MME6	NADP-dependent malic enzyme 6	1.4E-02	5.6E-01	8.8E-01	7.8E-01
XP_001696661.1	Cre06.g250200	METM1	S-adenosylmethionine synthetase	4.7E-03	4.0E-01	8.8E-01	7.9E-01
PNW71657.1	Cre16.g663450	BST3	Bestrophin 3	7.2E-03	5.5E-01	8.9E-01	7.9E-01
XP_001693547.1	Cre13.g577850	FKB20	Peptidyl-prolyl cis-trans isomerase, FKBP-type	4.5E-02	7.6E-01	8.9E-01	8.0E-01
XP_001701995.1	Cre02.g093750	NRX2	Nucleoredoxin 2	9.5E-03	6.3E-01	9.0E-01	1.1
XP_001701027.1	Cre07.g320150	–	DnaJ-like protein, ER-targeted	1.8E-02	7.0E-01	9.0E-01	8.1E-01
XP_001701780.1	Cre02.g091100	RPL15	Cytosolic 80S ribosomal protein L15	6.3E-03	4.3E-01	9.0E-01	8.1E-01

PNW76658.1	Cre11.g467778	—	—	5.1E-03	3.1E-01	9.0E-01	8.1E-01
PNW84933.1	Cre03.g164700	—	—	4.3E-03	2.9E-01	9.0E-01	8.1E-01
XP_001690993.1	Cre12.g504200	RPS23	Cytosolic 80S ribosomal protein S23	2.3E-02	6.6E-01	9.1E-01	8.1E-01
XP_001696473.1	Cre06.g272900	—	Flavin-containing amine oxidase	6.3E-03	4.3E-01	9.1E-01	8.1E-01
XP_001701644.1	Cre02.g076900	FAP19	Flagellar Associated Protein 19	9.3E-03	5.4E-01	9.2E-01	8.2E-01
PNW76349.1	Cre12.g553678	—	—	3.3E-03	2.4E-01	9.3E-01	8.3E-01
PNW82805.1	Cre06.g294950	ENR1	Enoyl-ACP reductase	3.4E-03	2.9E-01	9.4E-01	8.4E-01
PNW77823.1	Cre10.g453350	—	—	2.3E-02	6.9E-01	9.4E-01	8.4E-01
CAA64619.1	Cre08.g367500	LHCSR3.1	Stress-related chlorophyll a/b binding protein 2	4.0E-02	9.1E-01	9.6E-01	2.7E-01
PNW81305.1	Cre07.g350500	TSV1	Valyl-tRNA synthetase	3.4E-02	7.4E-01	9.6E-01	8.7E-01
PNW78537.1	Cre09.g393150	FOX1	Multicopper ferroxidase	2.0E-03	2.1E-01	9.7E-01	8.8E-01
XP_001703228.1	Cre12.g515650	EIF3K	Eukaryotic translation initiation factor 3, subunit K	3.9E-03	2.9E-01	9.7E-01	8.8E-01
PNW73523.1	Cre13.g562450	—	Putative Importin beta, RAN-binding protein 7,8	3.1E-03	3.0E-01	9.8E-01	8.8E-01
PNW74853.1	Cre12.g507400	LCS3	Long-chain acyl-CoA synthetase	2.9E-02	7.4E-01	9.8E-01	8.9E-01
XP_001689618.1	Cre01.g033550	PDI2	Protein disulfide isomerase 2	6.3E-03	5.1E-01	9.8E-01	8.9E-01
PNW86489.1	Cre02.g088600	ACLB1	ATP citrate lyase, subunit B	7.2E-03	4.1E-01	9.8E-01	8.9E-01
pdb.1EP7.A	Cre09.g391900	TRXH1	Thioredoxin h1, cytosolic	2.6E-03	1.8E-01	9.9E-01	8.9E-01
XP_001691863.1	Cre03.g189250	RAB11	Small Rab-related GTPase	2.8E-03	2.6E-01	9.9E-01	9.0E-01
XP_001702941.1	Cre03.g181200	—	—	6.7E-03	4.2E-01	1.0	9.0E-01
XP_001697824.1	Cre16.g655750	TEK1	Tektin	1.8E-02	6.3E-01	1.0	9.1E-01
XP_001702395.1	Cre12.g496700	—	Thioredoxin-like protein	9.0E-03	4.5E-01	1.0	9.2E-01
XP_001693024.1	Cre12.g532100	CTAP3	Chloroplast translocon associated protein 3	1.8E-03	1.8E-01	1.0	9.2E-01
XP_001693922.1	Cre12.g542350	—	Universal Stress-Domain Containing Protein	3.3E-03	2.9E-01	1.0	9.3E-01
XP_001693861.1	Cre13.g586350	—	—	2.8E-03	2.0E-01	1.1	9.7E-01
CAC80841.1	Cre02.g145800	MDH3	NAD-dependent malate dehydrogenase 3	1.5E-03	1.4E-01	1.1	9.7E-01
PNW76799.1	Cre11.g476650	PUL1	Pullulanase-type starch debranching enzyme 1	2.0E-03	1.0E-01	1.1	9.7E-01
XP_001693870.1	Cre13.g587050	ERF1	Eukaryotic release factor	3.1E-02	7.2E-01	1.1	9.8E-01
XP_001698018.1	Cre06.g278148	—	—	2.5E-03	3.0E-01	1.1	9.9E-01

XP_001701755.1	Cre02.g088200	RB60	Protein disulfide isomerase 1	1.4E-03	7.9E-02	1.1	9.9E-01
XP_001695349.1	Cre06.g284650	—	Dual-specificity protein phosphatase	2.8E-02	—	1.1	—
XP_001701734.1	Cre02.g085900	IPP1	Inositol-phosphate phosphatase	2.1E-03	1.2E-01	1.1	1.0
ABA41403.1	Cre05.g238650	PHC5	Pherophorin-chlamydomonas homolog 5	3.7E-02	—	1.1	—
XP_001700905.1	Cre05.g242400	PGR5	Proton-gradient related	2.2E-03	1.4E-01	1.1	1.0
PNW83946.1	Cre04.g214500	IDH3	Isocitrate dehydrogenase, NADP-dependent	1.8E-03	1.1E-01	1.1	1.0
XP_001698944.1	Cre16.g678213	—	—	1.0E-02	5.1E-01	1.2	1.1
PNW80482.1	Cre07.g319300	GWD1	Alpha-glucan water dikinase 1	1.4E-03	1.5E-01	1.2	1.1
XP_001692276.1	Cre04.g221400	—	—	9.5E-03	7.9E-01	1.2	2.1
XP_001703723.1	Cre08.g358556	RPS29	Cytosolic 80S ribosomal protein S29	4.7E-02	7.7E-01	1.2	1.1
XP_001699660.1	Cre02.g114600	PRX2	2-cys Peroxiredoxin	2.5E-03	1.6E-01	1.2	1.1
XP_001695239.1	Cre09.g403900	FAP294	Coiled-Coil Flagellar Associated Protein 294	1.5E-03	1.2E-01	1.3	1.2
XP_001701947.1	Cre02.g087700	APX1	Ascorbate peroxidase 1	1.6E-03	1.3E-01	1.3	1.2
XP_001689506.1	Cre01.g020350	SDH3	Succinate dehydrogenase subunit b560	2.3E-03	1.8E-01	1.3	1.3
XP_001703717.1	Cre08.g358522	—	Cysteine endopeptidase	1.5E-03	8.8E-02	1.3	1.3
XP_001702022.1	Cre11.g474800	OTA1	Ornithine transaminase	3.4E-03	6.1E-01	1.3	1.8
XP_001689968.1	Cre01.g022650	—	—	8.2E-03	2.4E-01	1.4	1.3
PNW70340.1	Cre17.g715900	—	Similar to Dihydrofolate Reductase-Thymidylate	2.2E-03	2.2E-01	1.4	1.3
XP_001690543.1	Cre10.g439900	HSP70G	ER-located HSP110/SSE-like protein	3.0E-04	3.9E-03	1.4	1.3
XP_001689842.1	Cre14.g619133	SDH1	Succinate dehydrogenase flavoprotein subunit	2.1E-03	1.5E-01	1.4	1.3
PNW80273.1	Cre08.g384900	FAP356	Flagellar Associated Protein 356	2.6E-03	2.2E-01	1.4	1.3
XP_001694912.1	Cre09.g387875	—	Soluble inorganic pyrophosphatase	1.2E-03	6.1E-02	1.4	1.3
XP_001693118.1	Cre03.g194850	MDH1	NAD-dependent malate dehydrogenase 1, chloroplastic	4.3E-04	9.1E-03	1.4	1.4
PNW72538.1	Cre16.g689647	AGO3	Argonaute-like protein	7.2E-04	3.2E-02	1.5	1.4
XP_001696240.1	Cre06.g268750	MME1	Malate	4.4E-04	2.6E-02	1.5	1.4

			dehydrogenase 1, decarboxylating				
XP_001697990.1	Cre06.g278215	HIBCH1	3-hydroxyisobutyryl-CoA hydrolase	2.2E-02	7.1E-01	1.5	1.4
XP_001700521.1	Cre12.g495850	HBD1	3-hydroxybutyrate dehydrogenase	4.4E-04	1.3E-02	1.5	1.4
XP_001701095.1	Cre17.g742450	—	Similar to Glutathione S-Transferase	1.0E-03	6.7E-02	1.5	1.4
XP_001693633.1	Cre13.g588100	CYN19C	Cyclophilin 19-3	2.4E-04	2.4E-03	1.5	1.4
PNW78240.1	Cre09.g392867	FMG1B	Flagella Membrane Glycoprotein 1B	1.5E-03	1.1E-01	1.5	1.4
XP_001698522.1	Cre10.g452250	FAP41	Flagellar Associated Protein 41	2.3E-04	3.8E-03	1.5	1.5
PNW76132.1	Cre12.g546600	FEA2	Fe-assimilation protein	4.4E-04	1.5E-02	1.5	1.5
XP_001690070.1	Cre01.g032650	TAL1	Transaldolase	3.3E-03	5.9E-01	1.6	2.1
XP_001700276.1	Cre01.g007700		—	1.3E-03	6.6E-02	1.6	1.5
XP_001697678.1	Cre09.g406600	—	—	1.3E-03	3.3E-01	1.6	2.0
XP_001689661.1	Cre01.g038400	CRT2	Calreticulin 2, calcium-binding protein	2.9E-04	7.5E-03	1.7	1.6
XP_001703530.1	Cre03.g165700	PDC3	Pyruvate decarboxylase	1.7E-03	1.3E-01	1.7	1.9
XP_001695943.1	Cre16.g675650	ALDH6	Aldehyde dehydrogenase	1.4E-04	2.8E-03	1.8	1.7
PNW87557.1	Cre02.g141400	PCK1	Phosphoenolpyruvate carboxykinase	2.8E-04	1.1E-02	1.9	1.8
XP_001696290.1	Cre06.g264200	SDH2	Iron-sulfur subunit of mitochondrial succinate dehydrogenase	6.8E-04	7.1E-02	1.9	1.8
XP_001695040.1	Cre09.g387726	AST1	Aspartate aminotransferase	7.8E-04	3.6E-02	2.0	1.9
XP_001690462.1	Cre07.g328150	PDI4	Protein disulfide isomerase 4	8.8E-04	5.1E-02	2.0	1.9
PNW77079.1	Cre10.g421300	—	—	2.6E-02	5.6E-01	2.1	1.9
PNW84563.1	Cre03.g149100	CIS2	Citrate synthase, glyoxysomal/microbody form	3.5E-05	1.9E-06	2.1	2.1
XP_001694504.1	Cre09.g396650	PAT2	Phosphate acetyltransferase	9.4E-05	2.2E-04	2.2	2.1
XP_001701885.1	Cre02.g080650	HSP90B	Heat shock protein 90B	2.4E-04	2.9E-03	2.2	2.1
XP_001701685.1	Cre02.g080700	BIP1	Endoplasmic reticulum associated Hsp70 protein	2.4E-05	9.9E-08	2.2	2.1
PNW78473.1	Cre09.g396100	PHC15	Pherophorin-chlamydomonas homolog 15	1.5E-04	1.6E-03	2.2	2.1
XP_001695632.1	Cre03.g144807	MAS1	Malate synthase	1.4E-05	1.6E-09	2.7	2.6
PNW89098.1	Cre01.g071662	ACS1	Acetyl-CoA synthetase/ligase	3.6E-05	1.9E-05	2.8	2.7
XP_001702039.1	Cre07.g353450	ACS3	Acetyl-CoA synthetase/ligase	1.0E-05	3.9E-11	3.0	2.9

PNW82533.1	Cre06.g282800	ICL1	Isocitrate lyase	3.3E-06	4.2E-14	3.2	3.1
PNW82038.1	Cre06.g271200	—	Pyridine nucleotide-disulphide oxidoreductase	2.4E-06	4.2E-14	4.0	3.9
XP_001693011.1	Cre12.g533201	—	—	—	4.2E-14	—	-4.8
XP_001690252.1	Cre01.g051500	—	—	—	4.2E-14	—	-4.3
XP_001689723.1	Cre01.g045200	—	—	—	4.2E-06	—	-4.1
XP_001691214.1	Cre06.g308850	EIF3X	hypothetical eIF3-like protein	—	4.5E-10	—	-4.0
XP_001692997.1	Cre12.g534450	CGL86	forkhead-associated domain-containing protein	—	2.5E-07	—	-3.9
XP_001695311.1	Cre06.g280150	—	PsbP-like protein of thylakoid lumen	—	5.4E-05	—	-3.7
XP_001699339.1	Cre16.g691000	EFP1	Organellar elongation factor P	—	1.1E-03	—	-3.1
XP_001700902.1	Cre05.g242000	CHLD1	Magnesium chelatase subunit D, chloroplast precursor	—	3.5E-02	—	-3.1
XP_001690777.1	Cre12.g801389	—	—	—	2.3E-02	—	-3.0
XP_001694803.1	Cre09.g397660	—	—	—	2.9E-06	—	-3.0
XP_001701654.1	Cre02.g077750	FAP211	Flagellar Associated Protein 211	—	2.2E-05	—	-2.9
PNW76649.1	Cre11.g467769	—	—	—	5.6E-05	—	-2.8
XP_001694742.1	Cre09.g392467	ATX1	copper chaperone	—	2.0E-04	—	-2.8
PNW76244.1	Cre12.g542300	GLYK1	Glycerate kinase	—	2.6E-08	—	-2.6
XP_001691441.1	Cre06.g299650	CLPR6	inactive subunit of chloroplast ClpP complex	—	1.0E-05	—	-2.6
XP_001699923.1	Cre02.g111450	TEF4	Rhodanese-like protein	—	5.3E-04	—	-2.5
PNW76678.1	Cre11.g467400	—	—	—	5.5E-06	—	-2.5
PNW78171.1	Cre10.g466850	FKB18	Peptidyl-prolyl cis-trans isomerase, FKBP-type	—	1.2E-06	—	-2.4
XP_001689798.1	Cre01.g053000	GPD2	Glycerol-3-phosphate dehydrogenase/dihydroxyacetone-3-phosphate reductase	—	6.2E-03	—	-2.4
XP_001695509.1	Cre06.g288550	ECP76	76 kDa extracellular polypeptide	—	5.4E-05	—	-2.4
PNW85235.1	Cre03.g177250	—	Haloperoxidase-like protein	—	3.7E-02	—	-2.4
XP_001695913.1	Cre16.g672300	—	High mobility group protein	—	3.9E-03	—	-2.3
XP_001698908.1	Cre16.g689087	RTN1	related to reticulon	—	3.0E-03	—	-2.3
XP_001701107.1	Cre17.g740950	LHL4	LHC-like protein	—	1.1E-02	—	-2.2
XP_001703301.1	Cre03.g172850	OASTL3	O-acetylserine (Thiol)-lyase/cysteine synthase 3	—	3.9E-07	—	-2.2
XP_001698611.1	Cre10.g463350	—	Hydroxyproline-rich glycoprotein	—	9.7E-04	—	-2.2
PNW79602.1	Cre08.g359600	—	Predicted protein of	—	3.4E-03	—	-2.1

			CSE family				
XP_001692640.1	Cre14.g633550	SCP2	Sterol carrier/transfer protein	—	4.8E-03	—	-1.8
PNW87768.1	Cre01.g001550	CIF3	Chloroplast translation initiation factor 3	—	2.6E-03	—	-1.8
PNW89076.1	Cre01.g063997	—	—	—	1.2E-02	—	-1.8
XP_001701877.1	Cre02.g079700	PYR2	Aspartate carbamoyltransferase	—	7.4E-03	—	-1.7
PNW80539.1	Cre07.g321750	—	—	—	3.1E-02	—	-1.7
PNW74875.1	Cre12.g506650	—	—	—	1.2E-03	—	-1.7
XP_001696318.1	Cre06.g261500	CPLD58	Conserved in the Plant Lineage and Diatoms	—	2.2E-02	—	-1.5
XP_001693971.1	Cre12.g547100	CGL2	putative methyltransferase	—	2.1E-02	—	1.3
XP_001692444.1	Cre07.g347100	—	Putative sugar epimerase	—	3.2E-02	—	1.4
PNW70201.1	Cre17.g710100	—	—	—	2.3E-02	—	1.4
PNW73403.1	Cre14.g630859	HID1	3-hydroxyisobutyrate dehydrogenase	—	1.8E-02	—	1.5
PNW69930.1	Cre17.g698650	GGT1	Gamma-glutamyl transpeptidase	—	2.2E-02	—	1.8
XP_001699041.1	Cre14.g613800	—	—	—	6.0E-04	—	1.9
PNW81428.1	Cre07.g355600	NTR3	NADPH dependent thioredoxin reductase 3	—	1.8E-03	—	2.0
XP_001694832.1	Cre15.g801811	—	—	—	2.1E-04	—	2.1
XP_001700911.1	Cre05.g243550	—	—	—	8.2E-03	—	2.1
XP_001702381.1	Cre12.g498450	—	—	—	3.1E-03	—	2.2
XP_001694158.1	Cre12.g554850	TRXH2	Thioredoxin h2, cytosolic	—	1.8E-03	—	2.4
XP_001697531.1	Cre03.g155650	CLC1	Clathrin light chain	—	7.4E-04	—	2.7
XP_001697365.1	Cre11.g478100	—	—	—	1.4E-02	—	2.7
PNW87367.1	Cre02.g119900	—	Cysteine endopeptidase	—	1.1E-04	—	2.8
PNW87885.1	Cre01.g005850	FAP23	Cobalamin adenosyltransferase	—	1.1E-03	—	3.0
PNW87938.1	Cre01.g007774	—	—	—	5.4E-04	—	3.1
PNW81856.1	Cre06.g263300	—	—	—	8.1E-06	—	3.6
PNW86839.1	Cre02.g097800	HLA3	Bicarbonate ABC transporter	—	1.1E-04	—	3.8
XP_001701884.1	Cre02.g080700	BIP1	Endoplasmic reticulum associated Hsp70 protein	—	4.8E-04	—	4.2
PNW86626.1	Cre02.g094250	—	—	—	4.2E-14	—	5.0
XP_001694349.1	Cre08.g379800	—	—	—	4.2E-14	—	7.2

Sup. Table 2: List of significantly (FDR ≤ 5%) overrepresented molecular functions (MF), cellular components (CC), and biological processes (BP) within CC-1010 (light blue) and CC-2936 (light green). The analysis was conducted using the GO terms associated with 363 DEqMS-identified DE-proteins.

Strain	GO Term	Pop. Freq.	Pop. Frac.	Study Frac.	GO Category	Description	Contributing Genes
	GO:0016746	0.0010	18/17711	3/207	MF	acyltransferase activity	Cre17.g699000; Cre07.g343700; Cre09.g396650;
	GO:0046912	0.0002	3/17711	2/207	MF	acyltransferase activity, acyl groups converted into alkyl on transfer	Cre03.g149100; Cre02.g088600;
	GO:0004812	0.0017	30/17711	3/207	MF	aminoacyl-tRNA ligase activity	Cre09.g406200; Cre07.g350500; Cre02.g079600;
	GO:0003824	0.0094	166/17711	8/207	MF	catalytic activity	Cre12.g507400; Cre02.g088600; Cre01.g071662; Cre06.g272050; Cre12.g517150; Cre14.g614300; Cre07.g353450; Cre03.g165700;
	GO:0008234	0.0012	21/17711	2/207	MF	cysteine-type peptidase activity	Cre09.g407700; Cre08.g358522;
	GO:0005525	0.0065	115/17711	5/207	MF	GTP binding	Cre13.g562150; Cre06.g311900; Cre03.g189250; Cre09.g390763; Cre17.g737250;
	GO:0003924	0.0037	66/17711	4/207	MF	GTPase activity	Cre06.g311900; Cre03.g189250; Cre09.g390763; Cre17.g737250;
	GO:0004427	0.0002	4/17711	2/207	MF	inorganic diphosphate phosphatase activity	Cre09.g387875; Cre10.g424100;
	GO:0000287	0.0015	27/17711	3/207	MF	magnesium ion binding	Cre09.g387875; Cre10.g424100; Cre03.g165700;
	GO:0004471	0.0003	6/17711	2/207	MF	malate dehydrogenase (decarboxylating) (NAD+) activity	Cre06.g268750; Cre06.g251400;
	GO:0030145	0.0005	9/17711	2/207	MF	manganese ion binding	Cre06.g272050; Cre01.g007700;
	GO:0046872	0.0044	78/17711	4/207	MF	metal ion binding	Cre10.g453350; Cre10.g436050; Cre06.g272050; Cre06.g250902;

	GO:0051287	0.0018	32/17711	6/207	MF	NAD binding	Cre06.g295450; Cre06.g268750; Cre06.g251400; Cre09.g405850; Cre06.g278185; Cre06.g278148;
	GO:0008137	0.0005	8/17711	2/207	MF	NADH dehydrogenase (ubiquinone) activity	CreMt.g802339; Cre07.g327400;
	GO:0000166	0.0023	41/17711	3/207	MF	nucleotide binding	Cre09.g406200; Cre07.g350500; Cre02.g079600;
	GO:0016491	0.0123	217/17711	11/207	MF	oxidoreductase activity	Cre02.g145800; Cre09.g393150; Cre06.g271200; Cre01.g050150; Cre14.g619133; Cre03.g194850; Cre16.g675650; Cre06.g272900; Cre11.g476750; Cre02.g114600; Cre10.g434750;
	GO:0016627	0.0009	16/17711	2/207	MF	oxidoreductase activity, acting on the CH-CH group of donors	Cre16.g687350; Cre01.g020350;
	GO:0016616	0.0015	26/17711	5/207	MF	oxidoreductase activity, acting on the CH-OH group of donors, NAD or NADP as acceptor	Cre02.g145800; Cre06.g295450; Cre04.g214500; Cre03.g194850; Cre06.g278185;
	GO:0003755	0.0017	30/17711	3/207	MF	peptidyl-prolyl cis-trans isomerase activity	Cre06.g284900; Cre06.g303300; Cre13.g588100;
	GO:0030170	0.0020	35/17711	3/207	MF	pyridoxal phosphate binding	Cre09.g387726; Cre10.g451950; Cre11.g474800;
	GO:0004185	0.0004	7/17711	2/207	MF	serine-type carboxypeptidase activity	Cre17.g746597; Cre06.g279400;
	GO:0003735	0.0090	160/17711	14/207	MF	structural constituent of ribosome	Cre14.g621450; Cre12.g504200; Cre06.g308250; Cre17.g701200; Cre13.g573351; Cre09.g388200; Cre06.g289550; Cre06.g272800; Cre10.g459250; Cre02.g106600; Cre05.g234637; Cre02.g091100;

							Cre10.g432800; Cre08.g358556;
	GO:0030976	0.0003	6/17711	2/207	MF	thiamine pyrophosphate binding	Cre12.g537200; Cre03.g165700;
	GO:0008483	0.0006	11/17711	2/207	MF	transaminase activity	Cre09.g387726; Cre11.g474800;
	GO:0003743	0.0014	25/17711	3/207	MF	translation initiation factor activity	Cre03.g199900; Cre03.g194400; Cre12.g515650;
	GO:0051082	0.0011	19/17711	2/207	MF	unfolded protein binding	Cre01.g038400; Cre02.g080650;
	GO:0005737	0.0058	103/17711	14/207	CC	cytoplasm	Cre09.g406200; Cre07.g350500; Cre01.g032650; Cre03.g199900; Cre03.g194400; Cre13.g587050; Cre09.g387875; Cre06.g272050; Cre04.g215850; Cre01.g007700; Cre02.g079600; Cre10.g424100; Cre12.g515650; Cre03.g178450;
	GO:0030286	0.0010	18/17711	2/207	CC	dynein complex	Cre06.g250300; Cre11.g476050;
	GO:0005783	0.0007	12/17711	2/207	CC	endoplasmic reticulum	Cre01.g033550; Cre01.g038400;
	GO:0005852	0.0006	11/17711	2/207	CC	eukaryotic translation initiation factor 3 complex	Cre03.g194400; Cre12.g515650;
	GO:0005622	0.0073	129/17711	12/207	CC	intracellular anatomical structure	Cre14.g621450; Cre12.g504200; Cre06.g308250; Cre17.g701200; Cre09.g388200; Cre06.g289550; Cre06.g272800; Cre12.g520500; Cre10.g459250; Cre01.g007700; Cre10.g432800; Cre08.g358556;
	GO:0005840	0.0085	151/17711	14/207	CC	ribosome	Cre14.g621450; Cre12.g504200; Cre06.g308250; Cre17.g701200; Cre13.g573351; Cre09.g388200; Cre06.g289550; Cre06.g272800;

							Cre10.g459250; Cre02.g106600; Cre05.g234637; Cre02.g091100; Cre10.g432800; Cre08.g358556;
	GO:0006520	0.0006	10/17711	2/207	BP	amino acid metabolic process	Cre12.g489700; Cre09.g387726;
	GO:0009058	0.0027	47/17711	3/207	BP	biosynthetic process	Cre03.g175250; Cre09.g387726; Cre10.g451950;
	GO:0005975	0.0043	77/17711	4/207	BP	carbohydrate metabolic process	Cre11.g476650; Cre03.g185550; Cre01.g032650; Cre16.g677450;
	GO:0045454	0.0030	53/17711	8/207	BP	cell redox homeostasis	Cre09.g391900; Cre06.g271200; Cre02.g142351; Cre01.g033550; Cre07.g328150; Cre12.g517150; Cre02.g088200; Cre12.g496700;
	GO:0006094	0.0002	3/17711	2/207	BP	gluconeogenesis	Cre07.g338451; Cre02.g141400;
	GO:0008152	0.0098	173/17711	11/207	BP	metabolic process	Cre17.g699000; Cre12.g507400; Cre06.g295450; Cre02.g088600; Cre01.g071662; Cre07.g343700; Cre12.g537200; Cre09.g396650; Cre16.g675650; Cre12.g517150; Cre07.g353450;
	GO:0055114	0.0253	448/17711	29/207	BP	obsolete oxidation-reduction process	CreMt.g802339; Cre02.g145800; Cre17.g715900; Cre16.g687350; Cre09.g393150; Cre07.g327400; Cre06.g271200; Cre06.g295450; Cre04.g214500; Cre01.g050150; Cre14.g619133; Cre10.g436050; Cre17.g701700; Cre12.g537200; Cre12.g534800;

							Cre03.g194850; Cre16.g675650; Cre06.g268750; Cre06.g251400; Cre06.g272900; Cre09.g417150; Cre11.g476750; Cre09.g405850; Cre06.g278185; Cre06.g278148; Cre14.g614300; Cre02.g114600; Cre02.g087700; Cre10.g434750;
	GO:0006796	0.0002	3/17711	2/207	BP	phosphate-containing compound metabolic process	Cre09.g387875; Cre10.g424100;
	GO:0006457	0.0015	26/17711	3/207	BP	protein folding	Cre01.g038400; Cre02.g080650; Cre03.g178450;
	GO:0006508	0.0080	141/17711	8/207	BP	proteolysis	Cre04.g226850; Cre17.g734900; Cre17.g746597; Cre06.g279400; Cre09.g407700; Cre01.g007700; Cre05.g241650; Cre08.g358522;
	GO:0006979	0.0009	16/17711	2/207	BP	response to oxidative stress	Cre09.g417150; Cre02.g087700;
	GO:0006950	0.0009	16/17711	2/207	BP	response to stress	Cre12.g542350; Cre02.g080650;
	GO:0006412	0.0091	162/17711	15/207	BP	translation	Cre14.g621450; Cre12.g504200; Cre06.g308250; Cre17.g701200; Cre13.g573351; Cre09.g388200; Cre06.g290950; Cre06.g289550; Cre06.g272800; Cre10.g459250; Cre02.g106600; Cre05.g234637; Cre02.g091100; Cre10.g432800; Cre08.g358556;
	GO:0006099	0.0003	6/17711	2/207	BP	tricarboxylic acid cycle	Cre03.g171950; Cre12.g537200;

	GO:0010181	0.0008	15/17711	3/153	MF	FMN binding	Cre16.g683550; Cre12.g531900; Cre16.g691800;
	GO:0005525	0.0065	115/17711	4/153	MF	GTP binding	CreCp.g802267; Cre04.g218250; Cre06.g284750; Cre03.g165000;
	GO:0003924	0.0037	66/17711	4/153	MF	GTPase activity	CreCp.g802267; Cre12.g549550; Cre06.g284750; Cre03.g165000;
	GO:0003676	0.0144	255/17711	8/153	MF	nucleic acid binding	Cre17.g729150; Cre06.g275100; Cre03.g177200; Cre13.g586916; Cre06.g268600; Cre09.g408200; Cre12.g519180; Cre10.g428200;
	GO:0016491	0.0123	217/17711	8/153	MF	oxidoreductase activity	CreCp.g802264; Cre17.g712100; Cre16.g683550; Cre12.g510050; Cre01.g014350; Cre09.g396300; Cre09.g393543; Cre02.g093650;
	GO:0003755	0.0017	30/17711	2/153	MF	peptidyl-prolyl cis-trans isomerase activity	Cre12.g561000; Cre01.g002300;
	GO:0003746	0.0004	7/17711	2/153	MF	translation elongation factor activity	CreCp.g802267; Cre12.g519180;
	GO:0005737	0.0058	103/17711	7/153	CC	cytoplasm	Cre10.g421600; Cre08.g358562; Cre03.g143887; Cre12.g505850; Cre09.g393543; Cre14.g615050; Cre02.g800236;
	GO:0019898	0.0008	15/17711	3/153	CC	extrinsic component of membrane	Cre03.g198850; Cre09.g396213; Cre08.g372450;
	GO:0005622	0.0073	129/17711	4/153	CC	intracellular anatomical structure	CreCp.g802267; Cre13.g581650; Cre12.g519180; Cre16.g666301;
	GO:0009522	0.0008	15/17711	2/153	CC	photosystem I	CreCp.g802312; Cre02.g082500;
	GO:0009523	0.0020	35/17711	4/153	CC	photosystem II	Cre03.g198850; Cre09.g396213; Cre06.g261000;

							Cre08.g372450;
	GO:0009654	0.0010	17/17711	4/153	CC	photosystem II oxygen evolving complex	Cre03.g198850; Cre09.g396213; Cre06.g261000; Cre08.g372450;
	GO:0042651	0.0002	4/17711	2/153	CC	thylakoid membrane	CreCp.g802264; Cre06.g261000;
	GO:0006633	0.0006	10/17711	2/153	BP	fatty acid biosynthetic process	Cre04.g216950; Cre12.g519100;
	GO:0055114	0.0253	448/17711	9/153	BP	obsolete oxidation-reduction process	Cre17.g712100; Cre16.g683550; Cre12.g510050; Cre10.g421700; Cre01.g027550; Cre09.g395650; Cre09.g396300; Cre09.g393543; Cre02.g093650;
	GO:0015979	0.0033	58/17711	7/153	BP	photosynthesis	CreCp.g802312; Cre12.g510050; Cre03.g198850; Cre09.g396213; Cre06.g261000; Cre08.g372450; Cre02.g082500;
	GO:0009765	0.0014	25/17711	4/153	BP	photosynthesis, light harvesting	Cre01.g066917; Cre08.g365900; Cre08.g367400; Cre17.g720250;
	GO:0006457	0.0015	26/17711	2/153	BP	protein folding	Cre08.g358562; Cre12.g505850;
	GO:0000413	0.0016	28/17711	2/153	BP	protein peptidyl-prolyl isomerization	Cre12.g561000; Cre01.g002300;
	GO:0033014	0.0003	6/17711	2/153	BP	tetrapyrrole biosynthetic process	Cre09.g409100; Cre16.g663900;
	GO:0006414	0.0003	6/17711	2/153	BP	translational elongation	CreCp.g802267; Cre12.g519180;

Sup. Table 3: List of primer sequences used for the quantification of the mRNA corresponding to the targeted genes.

Gene Locus (V5.6)	Gene Name	FP	RP
Cre08.g367500	LHCSR3.1	CACAACACCTTGATGCGAGATG	CCGTGTCTTGTCAGTCCCTG
Cre08.g365900	LHCSR1	GAGTCTGAGATCACCCACGG	CCGATCTGCTGGAAGTGGTA
Cre01.g016600	PSBS1	TAAACCGTGTATTGGAACTCCG	CTCTGCACGCGGCGTGTT
Cre06.g309000	LCIA	AGATTTGATAACGGCAGGACC	CCTATCCCATGTCATTCCCAC
Cre10.g452800	LCIB	TGCATAAGAGCGGATGTAGC	CGGTAGTCAGCATCAGTCATC
Cre03.g162800	LCI1	TTGCGGTTTTTGTACGAGCG	GTGCAAAGCCACGTCATCTC
Cre16.g662600	BST1	GCTGTGTGGCATTGAGGAGA	GGATGAGGCTGATGAGTCCG
Cre03.g162800	CAH1	GCTTTGCTTCACGGTTTGGT	CCGGTACTGTGTGTATGCGT
Cre09.g415700	CAH3	AACCTGGAAGGGTGTGTGTG	CACTTCTCGAAGCTGCCGTA
Cre05.g248400	CAH4	CGAAAAGCTGCATGAACTCACC	GCCCGTAGGCTACAGTTTTC
Cre02.g097800	HLA3	CAGTGGCATGTTCCCTTTTG	GGTGCTCATGGTTCTTGTTTG
Cre04.g220200	KEA1	TGGATCTCGGATTTCGCGGTTG	AATGCCGTCACCAGGTCATTCC
Cre04.g220200	KEA1	TGCAGTCTTGCAGACGGAGAAG	ATGCTTAGCAGCAGTGCGTACC
Cre12.g493000	KEA2	CTGTCGCTGTGGTGTTGTGTTG	TCATTAATGCTCTGGGCGTCTCG
Cre12.g493000	KEA2	TGGTGGTGGATGTAGCATTGCAG	ACAACACAACACCACAGCGACAG
Cre16.g687450	CPLD54	AGTGCTTCCTTGAAGCCTTCGG	TTTACACTGTGGCCCGGCTTAG
Cre16.g687450	CPLD54	TACGGTGCGACGCATCATCTTC	ATCACACATGCGACAAGAACGG

Sup. Table 4: Primer sequences used for mating-type determination by single-colony PCR. Primers were bought from EUROGENTEC®.

Gene	FP	RP
fus1	5′-ATG CCT ATC TTT CTC ATT CT-3’	5′-GCA AAA TAC ACG TCT GGA AG-3′
mid	5′- ATG GCC TGT TTC TTA GC-3′	5′-CTA CAT GTG TTT CTT GAC G-3′

Sup. Table 5: Phenotypic and Genetic correlations of photosynthetic traits measured in TAP *versus* TMP.

	Fv/Fm	ETR270	NPQ420	FmDR_1m	FmDR_11m	NPQ_fast_loss	ST_qT	ST_qI
Phenotypic	0.15	0.46	0.22	0.30	0.39	0.04	0.40	0.41
Genotypic	0.43	0.62	0.51	0.66	0.57	0.26	0.55	0.73

Sup. Table 6: List of candidate genes found within each photosynthetic QTL's CI after fine-mapping. The central columns (LOW, MODERATE, HIGH, MODIFIER) refer to the impact of the mutations, predicted by SnpEffect (see materials and methods), and report the number of variants falling within each category.

v6.1._locus	**Description**	**LOW**	**MODER-ATE**	**HIG H**	**MODIFI-ER**	**Associated Traits**	**Group**
Cre09.g390912	—	4	5	1	11	**NPQ130_TMP**	**1**
Cre09.g391097	Cytosolic 80S ribosomal protein L4	1	0	0	7		
Cre09.g391134	—	1	2	0	5		
Cre09.g391171	—	1	1	0	2		
Cre09.g391282	Xylosyl transferase	8	4	0	33		
Cre09.g391319	—	6	7	0	28		
Cre09.g391356	—	1	0	0	3		
Cre09.g391875	—	1	1	0	2		
Cre09.g391912	—	1	0	0	1		
Cre09.g392171	—	2	0	1	8		
Cre09.g392208	—	14	1	0	50		
Cre09.g392245	Dolicol-phosphate mannosyl-transferase	1	1	0	2		
Cre09.g392282	Axonemal Dynein Heavy Chain 2	48	7	0	67		
Cre09.g392319	Hydroxyproline-rich cell wall glycoprotein	9	4	0	46		
Cre09.g392356	—	11	9	1	32		
Cre09.g392393	—	10	26	0	63		
Cre09.g392430	—	6	0	0	34		
Cre09.g392505	—	10	9	0	31		
Cre09.g392542	—	1	0	0	1		
Cre09.g393062	—	21	27	0	58		
Cre09.g393136	—	5	0	0	20		
Cre09.g387023	—	1	1	0	1		
Cre09.g391245	Autophagy related	0	1	0	1		

Cre09.g391578	–	0	2	0	2		
Cre09.g391838	–	0	1	0	2		
Cre09.g392467	copper chaperone	0	1	0	1		
Cre09.g392655	–	0	1	0	2		
Cre09.g390875	–	0	0	0	1		
Cre09.g390949	Flagellar Associated Protein 140	0	0	0	4		
Cre09.g390986	Putative organellar aspartyl-tRNA synthetase	0	0	0	7		
Cre09.g391023	–	0	0	0	3		
Cre09.g391393	–	0	0	0	1		
Cre09.g391615	–	0	0	0	1		
Cre09.g391652	–	0	0	0	2		
Cre09.g391726	–	0	0	0	2		
Cre09.g391801	Hydroxyproline-rich cell wall glycoprotein	0	0	0	2		
Cre02.g800262	–	0	0	0	1		
Cre09.g392134	–	0	0	0	9		
Cre09.g386986	–	0	0	0	2		
Cre09.g396650	Phosphate acetyltransferase	7	0	0	29	**Fv/Fm_TMP**	**3**
Cre09.g396451	Glyoxal oxidase 15	27	10	0	105		
Cre09.g396450	Acid phosphatase	6	5	0	23		
Cre09.g396400	Bi-ubiquitin	3	0	0	14		
Cre09.g396350	–	6	0	0	19		
Cre09.g396300	Protoporphyrinogen oxidase	1	1	0	8		
Cre09.g396250	Phosphatidate cytidylyltransferase	3	2	0	16		
Cre09.g396200	Chlamydomonas-specific family protein	6	2	0	19		
Cre09.g396050	–	10	8	0	62		
Cre09.g395950	Alternative oxidase, mitochondrial	2	0	0	10		
Cre09.g395900	Chlamydomonas-specific family protein	1	1	0	5		
Cre09.g395850	–	11	7	0	16		
Cre09.g395750	–	13	0	0	33		
Cre09.g395700	Sodium:bile acid symporter	10	5	0	36		
Cre09.g395650	–	2	0	0	12		

Cre09.g395600	Factor possibly involved in assembly of the ribosomal 50S subunit	9	1	0	36		
Cre09.g395550	–	5	4	0	25		
Cre09.g395500	Dynein assembly factor HEATR2	8	5	0	20		
Cre09.g395450	–	7	6	0	28		
Cre09.g395400	–	4	2	0	14		
Cre09.g395250	Flagellar Associated Protein 36	11	1	0	44		
Cre09.g395200	–	6	9	0	38		
Cre09.g395150	Dual-specificity protein phosphatase	12	3	0	42		
Cre09.g395100	Dual-specificity protein phosphatase	7	2	1	65		
Cre09.g801012	–	15	19	0	129		
Cre09.g395000	–	5	1	0	41		
Cre09.g394900	Solute-binding protein-like adenylate cyclase	3	2	0	14		
Cre09.g394850	LrgB-like protein	9	0	0	33		
Cre09.g394800	Mitochondrial substrate carrier protein	4	6	0	21		
Cre09.g394700	Ribonuclease Z	5	5	1	34		
Cre09.g801013	–	1	0	0	9		
Cre09.g394400	–	18	13	0	42		
Cre09.g396600	Iron hydrogenase	0	1	0	1		
Cre09.g396550	–	0	0	0	2		
Cre09.g396500	Halo-acid dehalogenase-like hydrolase	0	0	0	16		
Cre09.g396100	Pherophorin-chlamydomonas homolog 15	0	0	0	1		
Cre09.g396000	Nitrate/nitrite transporter	0	0	0	17		
Cre09.g395800	–	0	0	0	7		
Cre09.g395300	–	0	0	0	10		
Cre09.g394750	Chloroplast Ribosomal Protein S1	0	0	0	34		
Cre09.g394550	ribose-phosphate pyrophosphokinase	0	0	0	7		

Cre09.g394450	Ran-binding protein 1	0	0	0	14		
Cre01.g053150	Glycerol-3-phosphate dehydrogenase/dihydroxyacetone-3-phosphate reductase	1	0	0	5	**ST_ETR270_TAP; ST_ETR270_TMP; qI_TMP; NPQ130_TMP**	**5**
Cre01.g053200	–	2	3	0	8		
Cre01.g800139	–	1	0	0	18		
Cre01.g053288	–	1	1	0	6		
Cre01.g053300	Agmatine iminohydrolase	2	4	0	9		
Cre01.g800140	–	13	16	1	31		
Cre01.g053450	Nucleotidyl cyclase	14	0	1	22		
Cre01.g053550	–	1	0	0	1		
Cre01.g053700	–	21	20	0	52		
Cre01.g053800	–	3	6	0	18		
Cre01.g053850	–	8	4	0	28		
Cre01.g053900	–	7	5	1	31		
Cre01.g053950	–	11	13	0	46		

Cre01.g054000	–	8	5	0	35		
Cre01.g054050	–	1	0	0	2		
Cre01.g054100	–	6	1	0	26		
Cre01.g054150	NADPH-dependent thioredoxin reductase C, chloroplastic	1	0	0	27		
Cre01.g054250	Cytochrome P450, CYP5 superfamily, CYP5A family	7	4	0	15		
Cre01.g054500	–	1	0	0	3		
Cre01.g054650	–	5	9	0	27		
Cre01.g054700	–	3	2	0	15		
Cre01.g054800	–	11	2	0	28		
Cre01.g054850	–	2	1	0	10		
Cre01.g054900	–	13	4	0	27		
Cre01.g055000	–	5	2	0	17		
Cre01.g055100	–	1	0	0	11		

Cre01.g055151	—	2	0	0	25		
Cre01.g052850	—	0	1	0	1		
Cre01.g052950	DNA damage checkpoint protein	0	1	0	1		
Cre01.g054200	—	0	3	0	3		
Cre01.g055200	conserved expressed protein related to GIF3	0	1	0	1		
Cre01.g052800	—	0	0	1	2		
Cre01.g053000	Glycerol-3-phosphate dehydrogenase/dihydroxyacetone-3-phosphate reductase	0	0	0	1		
Cre01.g053750	Putative lipoate A/B protein ligase	0	0	0	19		
Cre01.g054550	—	0	0	0	4		
Cre01.g054600	—	0	0	0	7		
Cre01.g054750	—	0	0	0	9		
Cre01.g054950	—	0	0	0	39		
Cre01.g055050	—	0	0	0	7		
Cre03.g176866	conserved protein of unknown function	2	3	0	10	**Fv/Fm_TMP; ST_FmDR_TMP;**	**1**

Cre03.g176900	–	25	29	0	49	**FmDR_11m_TMP**	**1**
Cre03.g176930	–	3	3	0	17		
Cre03.g176961	–	3	9	0	12		
Cre03.g177007	–	3	4	0	9		
Cre03.g177053	–	1	0	0	5		
Cre03.g177100	–	2	0	0	3		
Cre03.g177150	–	7	2	0	20		
Cre03.g177250	Haloperoxidase-like protein	1	0	0	1		
Cre03.g177300	Haloperoxidase-like protein	3	1	0	5		
Cre03.g177350	–	1	0	0	14		
Cre03.g177600	–	4	2	0	14		
Cre03.g177650	–	23	16	0	63		
Cre03.g177700	transcription factor regulating nitrogen metabolism	2	1	0	11		
Cre03.g177750	related to EDS5, enhanced disease susceptibility gene	10	3	0	70		
Cre03.g177826	–	5	4	0	9		
Cre03.g177850	–	8	9	0	21		
Cre03.g177900	subunit of 38 kDa of the the TOB complex	5	2	0	18		
Cre03.g177950	–	24	11	1	60		
Cre03.g178000	–	10	9	0	24		
Cre03.g178014	–	1	0	0	10		
Cre03.g178050	Predicted protein	4	1	0	23		

Cre03.g178100	—	32	2	1	85		
Cre03.g178450	Chaperonin 10	2	0	0	7		
Cre03.g178500	Flagellar protofilament ribbon protein 43	5	1	0	26		
Cre03.g178550	—	2	0	0	21		
Cre03.g178600	DNA topoisomerase I	7	0	0	29		
Cre03.g178650	Minichromosome maintenance protein	7	0	0	23		
Cre03.g178700	—	12	10	0	32		
Cre03.g178750	—	6	0	0	20		
Cre03.g178850	—	8	4	0	21		
Cre03.g178900	putative meiotic recombination protein	17	19	1	50		
Cre03.g178950	DEAD/DEAH box helicase	12	8	0	41		
Cre03.g800341	—	2	1	0	4		
Cre03.g179000	component psaA trans-splicing sub complex II	14	5	1	28		
Cre03.g179050	—	1	2	0	6		
Cre03.g179100	UFD1b homolog	14	2	0	36		
Cre03.g179150	—	5	2	0	16		
Cre03.g179200	—	3	2	0	12		
Cre03.g179250	—	2	1	0	3		
Cre03.g179300	SNF2-related DNA/RNA helicase	15	2	0	32		
Cre03.g179600	—	1	1	0	1		

Cre03.g179650	—	1	0	0	2		
Cre03.g179700	—	2	0	0	3		
Cre03.g179820	NON1 paralog	1	1	0	3		
Cre03.g179880	—	1	1	0	1		
Cre03.g179961	DNA polymerase epsilon subunit 1	1	0	0	1		
Cre03.g181950	—	2	1	0	7		
Cre03.g182200	—	4	2	0	14		
Cre03.g182700	—	1	1	0	1		
Cre03.g183350	SNF2-related DNA/RNA helicase	1	0	0	2		
Cre03.g183700	Glucan synthase-like 3	1	1	0	5		
Cre03.g183850	Apoferredoxin, chloroplast precursor	3	0	0	5		
Cre03.g178400	—	0	1	0	1		
Cre03.g179750	—	0	2	0	3		
Cre03.g179921	—	0	1	0	2		
Cre03.g177200	RNA-binding protein C3, CELF family, subunit of CHLAMY1	0	0	0	8		
Cre03.g177800	—	0	0	0	20		
Cre03.g179350	Major facilitator superfamily transporter	0	0	0	3		
Cre03.g179400	Major facilitator superfamily transporter	0	0	0	2		
Cre03.g179450	Scavenger receptor cysteine rich (SRCR) protein	0	0	0	2		
Cre03.g179500	Prolyl 4-hydroxylase 13	0	0	0	1		

Cre03.g179860	tRNA-(m5C) methyltransferase	0	0	0	4		
Cre03.g179901	mitochondrial ribosome protein mL116, Chlamydomonas-specific	0	0	0	7		
Cre03.g179941	—	0	0	0	3		
Cre03.g180250	Myo-inositol-1-phosphate synthase	0	0	0	1		
Cre03.g180300	Sulfite reductase	0	0	0	1		
Cre03.g180700	BOLA protein	0	0	0	1		
Cre03.g180750	Cobalamin-dependent methionine synthase	0	0	0	1		
Cre03.g181250	conserved protein related to nucleoside diphosphate sugar epimerase	0	0	0	2		
Cre03.g181300	5-enolpyruvylshikimate-3-phosphate (EPSP) synthase (EC 2.5.1.19)	0	0	0	5		
Cre03.g181450	—	0	0	0	1		
Cre03.g181500	4-alpha-glucanotransferase	0	0	0	1		
Cre03.g800344	—	0	0	0	2		
Cre03.g181576	—	0	0	0	1		
Cre03.g181650	—	0	0	0	1		
Cre03.g181700	—	0	0	0	8		
Cre03.g181800	—	0	0	0	1		
Cre03.g181900	—	0	0	0	3		
Cre03.g182150	Thylakoid Lumen Protein 18.3	0	0	0	1		
Cre03.g182300	Phosphoglycerate mutase	0	0	0	2		

Cre03.g182400	–	0	0	0	1		
Cre03.g182650	Phospholipid/glycerol acyltransferase	0	0	0	1		
Cre03.g182750	–	0	0	0	1		
Cre03.g182800	Alanine-glyoxylate transaminase	0	0	0	1		
Cre03.g183100	translocase of inner mitochondrial membrane 22 homolog	0	0	0	1		
Cre03.g183150	–	0	0	0	2		
Cre03.g183400	–	0	0	0	1		
Cre03.g183500	–	0	0	0	1		
Cre03.g183550	–	0	0	0	2		
Cre03.g183650	Glycerophosphoryl diester phosphodiesterase family protein	0	0	0	1		
Cre03.g183750	OctotricoPeptide Repeat protein 16	0	0	0	1		
Cre03.g183800	–	0	0	0	3		
Cre03.g183900	–	0	0	0	8		
Cre03.g184000	–	0	0	0	8		
Cre03.g184050	–	0	0	0	1		
Cre03.g184100	–	0	0	0	1		
Cre03.g184200	–	0	0	0	2		
Cre03.g184250	Calmodulin-like protein	0	0	0	1		
Cre03.g184300	S-adenosyl-L-methionine-dependent methyltransferase	0	0	0	3		

Cre02.g119900	Cysteine endopeptidase	1	0	0	4	**qT_TMP; qT_TAP**	**16**
Cre02.g800251	–	1	1	0	3		
Cre02.g120250	Chloroplast protein kinase required for state transitions	5	1	0	20		
Cre02.g119850	3',5'-cyclic-nucleotide phosphodiesterase	0	0	0	10		
Cre02.g119950	–	0	0	0	15		
Cre02.g120050	–	0	0	0	4		
Cre02.g120100	ribulose-1,5-bisphosphate carboxylase/oxygenase small subunit 1, chloroplastic	0	0	0	5		
Cre02.g120150	ribulose-1,5-bisphosphate carboxylase/oxygenase small subunit 2, chloroplastic	0	0	0	3		
Cre09.g386800	–	0	0	0	1		
Cre03.g189605	–	3	0	0	15	**qT_TAP**	**17**
Cre03.g189650	Histone acetyltransferase	23	4	0	77		
Cre03.g189700	–	2	0	0	61		
Cre03.g189750	–	1	0	0	8		
Cre03.g189850	–	3	2	0	6		
Cre03.g190050	–	1	6	0	9		
Cre03.g190500	Glucosidase IIa	4	0	0	28		
Cre03.g190550	–	12	1	0	36		
Cre03.g190900	–	1	0	0	3		
Cre03.g191150	–	1	0	0	1		
Cre03.g191200	RNA methylase	5	8	0	22		
Cre03.g191250	Low-CO2-inducible protein 34	11	2	0	23		
Cre03.g800357	–	3	0	0	23		
Cre03.g191350	–	8	10	1	12		
Cre03.g191500	–	1	0	0	5		
Cre03.g191550	–	1	1	0	2		
Cre03.g191600	–	1	1	0	1		
Cre03.g191750	–	2	1	0	3		
Cre03.g191800	–	6	0	0	12		
Cre03.g191900	–	12	6	0	17		

Cre03.g192201	Pherophorin-chlamydomonas homolog 51	3	2	0	29		
Cre03.g192250	Pherophorin-chlamydomonas homolog 69	4	3	0	7		
Cre03.g192300	–	6	3	0	5		
Cre03.g192450	Adenylate cyclase	2	2	0	8		
Cre03.g190000	Phosphoprotein phosphatase 2C-related	0	2	0	5		
Cre03.g190850	EnoylCoA hydratase/isomerase	0	1	0	1		
Cre03.g191400	–	0	1	0	2		
Cre03.g191650	–	0	2	0	4		
Cre03.g192400	–	0	1	0	3		
Cre03.g189350	–	0	0	0	1		
Cre03.g189400	Seryl-tRNA(Sec) synthetase	0	0	0	1		
Cre03.g189800	Cyclophilin 38	0	0	0	3		
Cre03.g189950	HSP70-HSP90 organizing protein	0	0	0	1		
Cre03.g800353	–	0	0	0	2		
Cre03.g190100	Eukaryotic translation initiation factor 3, subunit B	0	0	0	1		
Cre03.g190150	Conserved in the Green Lineage	0	0	0	2		
Cre03.g190650	–	0	0	0	2		
Cre03.g191300	Low-CO2-inducible protein 35	0	0	0	32		
Cre03.g191450	–	0	0	0	9		
Cre03.g191700	–	0	0	0	1		
Cre03.g191850	Short-chain dehydrogenase/reductase	0	0	0	28		
Cre03.g192350	–	0	0	0	3		
Cre14.g625300	CAX family cation antiporter, membrane protein	4	3	0	19	**qT_TAP**	**18**
Cre14.g625350	MATE efflux family protein	4	2	0	21		
Cre14.g625400	26S proteasome regulatory subunit	2	0	0	20		
Cre14.g625450	MPBQ/MSBQ methyltransferase, chloroplastic	3	0	0	12		
Cre14.g625600	FtsH-like ATPase	3	3	1	13		

Cre14.g625625	FtsH-like membrane ATPase/metalloprotease	5	4	1	37		
Cre14.g625750	22 kDa translocon at the inner membrane of chloroplasts	1	0	0	13		
Cre14.g625802	—	4	3	0	18		
Cre14.g625850	Matrix metalloproteinase	9	5	0	28		
Cre14.g625901	—	5	10	0	25		
Cre14.g625950	Mitochondrial Class-II RNA nucleotidyl transferase	3	5	0	18		
Cre14.g626000	—	8	2	0	24		
Cre14.g626100	—	1	4	0	11		
Cre14.g626150	—	6	12	0	27		
Cre14.g626200	Prolyl 4-hydroxylase 7	6	1	0	43		
Cre14.g626250	—	1	0	0	26		
Cre14.g626300	—	4	1	0	14		
Cre14.g626350	—	7	0	0	24		
Cre14.g626400	Cytochrome P450, CYP197 superfamily	13	5	0	43		
Cre14.g626433	—	8	2	0	24		
Cre14.g626466	—	10	2	0	51		
Cre14.g626500	—	5	1	0	31		
Cre14.g626550	—	3	1	0	11		
Cre14.g626600	—	6	10	0	18		
Cre14.g801641	—	8	6	0	12		
Cre14.g626667	—	1	1	0	6		
Cre14.g626800	OctotricoPeptide Repeat protein 64	3	9	0	12		
Cre14.g626950	Nicotinate-/nicotinamide-nucleotide adenylyltransferase	3	3	0	12		
Cre14.g627000	—	10	13	0	39		
Cre14.g627050	—	2	0	0	20		
Cre14.g627100	—	22	20	1	75		
Cre14.g627150	—	12	8	0	45		
Cre14.g627200	—	19	21	0	59		
Cre14.g627251	—	2	0	0	4		
Cre14.g627350	Sulfite eporter family protein	15	2	0	28		

Cre14.g627411	–	11	19	1	37		
Cre14.g627422	–	10	2	0	23		
Cre14.g625500	Ankyrin Repeat Flagellar Associated Protein 254	0	0	0	3		
Cre14.g625550	Flagellar Associated Protein 410	0	0	0	3		
Cre14.g625650	–	0	0	0	2		
Cre14.g626700	Chloroplast ferredoxin	0	0	0	2		
Cre14.g626750	ELIP, Maintenance factor for photosystem I	0	0	0	35		
Cre14.g626900	Phophomannomutase	0	0	0	5		
Cre14.g801642	–	0	0	0	1		
Cre01.g050608	–	2	5	0	7	**qI_TAP; ETR270_TAP**	**19**
Cre01.g051174	bZIP transcription factor	1	4	0	6		
Cre01.g051550	DEAD/DEAH box helicase	1	1	0	27		
Cre01.g052150	Flagellar Associated Protein 87	1	1	0	3		
Cre01.g052250	Thioredoxin x, chloroplastic	1	0	1	2		
Cre01.g800135	–	1	2	0	11		
Cre01.g052650	inositol hexakisphosphate kinase	6	7	0	13		
Cre01.g052750	Transient receptor potential ion channel	37	19	2	46		
Cre01.g053150	Glycerol-3-phosphate dehydrogenase/dihydroxyacetone-3-phosphate reductase	2	0	0	6		
Cre01.g053200	–	3	3	0	8		
Cre01.g800139	–	3	0	0	14		
Cre01.g053288	–	1	1	0	4		
Cre01.g053300	Agmatine iminohydrolase	1	4	0	7		
Cre01.g800140	–	13	14	1	33		
Cre01.g053450	Nucleotidyl cyclase	15	0	1	23		
Cre01.g053550	–	2	0	0	3		
Cre01.g053700	–	22	21	0	54		

Cre01.g053800	–	3	6	0	21		
Cre01.g053850	–	10	5	0	30		
Cre01.g053900	–	10	5	1	40		
Cre01.g053950	–	10	11	0	43		
Cre01.g054000	–	7	5	0	33		
Cre01.g054050	–	1	0	0	1		
Cre01.g054100	–	7	2	0	26		
Cre01.g054150	NADPH-dependent thioredoxin reductase C, chloroplastic	1	0	0	31		
Cre01.g054250	Cytochrome P450, CYP5 superfamily, CYP5A family	7	4	0	15		
Cre01.g054650	–	5	10	0	27		
Cre01.g054700	–	4	3	0	17		
Cre01.g054800	–	1	0	0	4		
Cre01.g050650	–	0	1	0	8		
Cre01.g800132	–	0	1	1	1		
Cre01.g051750	–	0	1	0	9		
Cre01.g052850	–	0	1	0	1		
Cre01.g052950	DNA damage checkpoint protein	0	1	0	1		
Cre01.g054200	–	0	4	0	4		
Cre01.g054600	–	0	1	0	7		
Cre01.g800136	–	0	0	1	2		
Cre01.g052800	–	0	0	1	2		
Cre01.g051100	–	0	0	0	2		
Cre01.g051137	–	0	0	0	3		
Cre01.g051625	–	0	0	0	11		
Cre01.g051700	–	0	0	0	16		
Cre01.g051800	Aspartate aminotransferase	0	0	0	2		
Cre01.g051850	–	0	0	0	2		
Cre01.g052000	–	0	0	0	1		
Cre01.g052300	Transcription factor, E2F and DP-related	0	0	0	9		
Cre01.g052350	Mitochondrial ribosomal protein L20	0	0	0	2		
Cre01.g052450	–	0	0	0	5		
Cre01.g052500	–	0	0	0	8		

Cre01.g053000	Glycerol-3-phosphate dehydrogenase/dihydroxyacetone-3-phosphate reductase	0	0	0	2		
Cre01.g053500	–	0	0	0	2		
Cre01.g053750	Putative lipoate A/B protein ligase	0	0	0	16		
Cre01.g054550	–	0	0	0	2		
Cre01.g054750	–	0	0	0	11		
Cre08.g367250	Flagellar Associated Protein 176	37	9	0	94	**NPQ420_TAP; FmDR_1m_TAP; FmDR_11m_TAP ; Fv/Fm_TMP; NPQ130_TMP; NPQ420_TMP; FmDR_1m_TMP; FmDR_11m_TMP ; ST_FmDR_TMP**	**20**
Cre08.g367350	–	7	1	0	55		
Cre08.g367550	Flagellar Associated Protein 291	3	0	0	10		
Cre08.g367600	O-acetylserine (Thiol)-lyase/cysteine synthase	12	3	0	51		
Cre08.g367650	Transcriptional repression protein	1	0	0	32		
Cre08.g367700	–	1	0	0	54		
Cre08.g367750	GT90 family protein 12	8	1	0	37		
Cre08.g367800	Nucleoside diphosphate hydrolase	4	1	0	18		
Cre08.g367950	Cyclic nucleotide-monophosphate binding domain Flagellar Associated Protein 323	12	6	0	29		
Cre08.g368000	–	1	5	0	12		
Cre08.g368100	–	17	26	0	53		
Cre08.g368200	–	2	4	0	9		
Cre08.g368250	–	4	3	0	19		
Cre08.g368300	Putative RNA helicase	20	16	1	95		
Cre08.g368350	–	17	6	0	69		
Cre08.g368400	NADPH-dependent thioredoxin reductase 1, selenoprotein	12	0	0	47		
Cre08.g368450	–	7	0	0	16		
Cre08.g368500	–	2	0	0	15		
Cre08.g368550	–	2	3	0	11		
Cre08.g368600	–	2	2	0	6		
Cre08.g368150	–	0	2	0	2		
Cre08.g367300	–	0	0	0	19		

Cre08.g367400	Stress-related chlorophyll a/b binding protein 3	0	0	0	16		
Cre08.g367500	Stress-related chlorophyll a/b binding protein 2	0	0	0	5		
Cre08.g368050	Methylated-DNA--[protein]-cysteine S-methyltransferase	0	0	0	9		
Cre08.g800915	—	0	0	0	3		
Cre08.g368650	—	0	0	0	2		
Cre17.g802041	—	2	1	0	13	**ST_ETR270_TAP; ETR270_TAP**	**21**
Cre17.g707250	Major facilitator superfamily transporter	13	7	0	42		
Cre17.g707300	Phospholipid/glycerol acyltransferase	2	0	0	29		
Cre17.g707400	—	28	18	0	86		
Cre17.g707500	—	12	5	1	57		
Cre17.g707551	—	24	30	0	68		
Cre17.g707600	—	1	1	0	8		
Cre17.g707650	—	13	1	0	89		
Cre17.g707700	Manganese/metal transporter, NRAMP homolog	6	0	0	46		
Cre17.g707750	—	4	0	0	40		
Cre17.g707800	—	18	3	1	51		
Cre17.g708000	Membrane-associated Flagellar Associated Protein 260	12	2	0	35		
Cre17.g802043	—	2	0	0	5		
Cre17.g708050	—	12	6	0	45		
Cre17.g708100	Similar to Hypoxanthine-Guanine	4	2	0	26		
Cre17.g708150	Histone H3	2	0	0	2		
Cre17.g708250	ARF-like GTPase	2	0	0	18		
Cre17.g708300	26S proteasome regulatory subunit	1	0	1	26		
Cre17.g708350	—	6	1	0	32		
Cre17.g708400	Subtilisin-like protease	39	11	1	123		
Cre17.g708450	Matrix metalloproteinase	21	7	0	103		
Cre17.g708500	—	27	49	0	71		

Cre17.g708850	—	6	1	0	77		
Cre17.g708901	—	2	0	0	66		
Cre17.g708950	—	4	2	0	19		
Cre17.g709000	—	35	12	0	57		
Cre17.g709300	—	1	0	0	13		
Cre17.g709400	—	17	15	0	45		
Cre17.g709450	—	1	0	0	5		
Cre17.g709500	—	15	4	1	83		
Cre17.g709550	—	9	3	0	76		
Cre17.g709600	—	12	7	0	56		
Cre17.g802046	—	2	10	0	27		
Cre17.g709700	—	5	5	0	29		
Cre17.g709750	—	5	12	0	30		
Cre17.g709800	RegA/Rls-like protein	8	1	0	51		
Cre17.g709850	Acetate kinase	16	4	1	139		
Cre17.g709900	—	34	36	1	93		
Cre17.g709950	—	2	1	0	17		
Cre17.g710000	—	19	7	0	53		
Cre17.g710050	—	17	12	0	57		
Cre17.g710100	—	7	0	0	23		
Cre17.g710150	26S proteasome regulatory subunit	3	0	0	23		
Cre17.g710200	Indoleamine 2,3-dioxygenase	4	4	0	19		
Cre17.g710300	Pherophorin-chlamydomonas homolog 31	3	1	0	12		
Cre17.g710351	—	7	7	0	17		
Cre17.g710600	Protein tyrosine kinase	5	0	0	28		
Cre17.g710650	Protein tyrosine kinase	15	13	0	48		
Cre17.g710700	—	7	7	0	57		
Cre17.g710750	—	14	18	0	77		
Cre17.g710800	iron-sulfur cluster assembly protein	3	0	0	43		
Cre17.g711100	—	1	3	0	8		
Cre17.g711150	Fatty acid desaturase, delta-12	5	1	0	25		
Cre17.g711250	Aquaporin	1	0	0	10		
Cre17.g711401	—	6	6	0	17		
Cre17.g711450	Endoplasmic reticulum Qa-SNARE protein	3	2	0	22		
Cre17.g711457	—	4	0	0	13		

Cre17.g711550	Cyclin-related protein	3	2	0	14		
Cre17.g711900	—	6	0	0	25		
Cre17.g711950	Prefoldin-family protein	1	0	0	3		
Cre17.g712100	monodehydroascorbate reductase	3	1	0	11		
Cre17.g712300	—	1	1	0	6		
Cre17.g712450	—	1	3	0	7		
Cre17.g712500	—	1	0	0	1		
Cre17.g712950	—	6	15	0	23		
Cre17.g713000	—	1	0	1	3		
Cre17.g713025	DnaJ-like protein	3	3	0	20		
Cre17.g713600	Subtilisin-like protease	4	0	0	16		
Cre17.g713650	DNA mismatch repair protein, MutS homolog	6	4	0	20		
Cre17.g713674	—	5	9	0	26		
Cre17.g713700	Indoleamine 2,3-dioxygenase	1	2	0	11		
Cre17.g713900	TOR kinase binding protein	1	0	0	10		
Cre17.g714229	—	2	0	0	14		
Cre17.g714300	—	2	5	0	9		
Cre17.g714700	—	8	5	0	23		
Cre17.g714950	—	2	1	0	6		
Cre17.g715000	Heat shock protein 33	2	1	0	10		
Cre17.g715300	Polycystin-2	1	1	0	6		
Cre17.g715350	—	1	0	0	6		
Cre17.g715400	—	1	0	0	4		
Cre17.g715421	—	1	1	1	8		
Cre17.g715450	—	1	1	0	3		
Cre17.g715500	—	1	0	0	7		
Cre17.g715550	—	1	3	0	6		
Cre17.g715600	—	5	9	0	16		
Cre17.g715700	protein phosphatase 2C-like	3	1	0	17		
Cre17.g715750	COP-II coat subunit	1	0	0	7		
Cre17.g715800	—	1	2	1	13		
Cre17.g715801	—	16	13	1	39		
Cre17.g715850	—	2	0	0	4		

Cre17.g715900	Similar to Dihydrofolate Reductase-Thymidylate	1	0	0	14		
Cre17.g716050	–	1	0	0	15		
Cre17.g716101	DNA polymerase lambda	7	11	0	25		
Cre17.g716350	GT90 family protein 32	1	1	0	8		
Cre17.g716450	katanin like protein 3	1	0	0	5		
Cre17.g716600	–	1	3	0	7		
Cre17.g710950	–	0	1	0	1		
Cre17.g711000	–	0	2	0	4		
Cre17.g713150	–	0	1	0	1		
Cre17.g714150	Potassium ion uptake transporter	0	1	0	3		
Cre17.g714400	–	0	1	0	5		
Cre17.g707350	–	0	0	0	9		
Cre17.g707900	–	0	0	0	6		
Cre17.g707950	Hsp70 escorting protein 2, chloroplast	0	0	0	4		
Cre17.g802044	–	0	0	0	3		
Cre17.g708800	Glutathione synthetase	0	0	0	22		
Cre17.g709050	Histone H3	0	0	0	3		
Cre17.g709250	–	0	0	0	11		
Cre17.g709350	Qc-SNARE protein, Syn8/Syntaxin8-family	0	0	0	3		
Cre17.g710850	UDP-xylose transporter	0	0	0	15		
Cre17.g711050	–	0	0	0	9		
Cre17.g711200	Haloacid dehalogenase-like hydrolase (HAD) superfamily protein	0	0	0	8		
Cre17.g711300	–	0	0	0	16		
Cre17.g711600	–	0	0	0	3		
Cre17.g711650	Nuclear distribution/movement family protein	0	0	0	13		
Cre17.g711700	Histone H2A	0	0	0	2		
Cre17.g712000	Serine/arginine-rich pre-mRNA splicing factor	0	0	0	5		
Cre17.g712050	–	0	0	0	6		

Cre17.g712350	conserved protein related to metal-dependent CAAX amino terminal protease family	0	0	0	3		
Cre17.g712400	Thylakoid protein integration factor	0	0	0	4		
Cre17.g712600	—	0	0	0	3		
Cre17.g712850	Thioredoxin-like protein	0	0	0	1		
Cre17.g712900	—	0	0	0	3		
Cre17.g713051	—	0	0	0	5		
Cre17.g713726	—	0	0	0	1		
Cre17.g713850	Serine O-acetyl transferase	0	0	0	4		
Cre17.g714200	Potassium ion uptake transporter	0	0	0	4		
Cre17.g714350	—	0	0	0	5		
Cre17.g714750	—	0	0	0	5		
Cre17.g714800	Hydroxyproline-rich cell wall protein	0	0	0	10		
Cre17.g714900	Conserved in the Green Lineage	0	0	0	14		
Cre17.g715050	Small Rab-related GTPase	0	0	0	11		
Cre17.g715100	—	0	0	0	7		
Cre17.g715150	—	0	0	0	3		
Cre17.g715200	—	0	0	0	11		
Cre17.g715250	Acetyl-CoA biotin carboxyl carrier	0	0	0	9		
Cre17.g715653	—	0	0	0	3		
Cre17.g715950	—	0	0	0	1		
Cre17.g716000	—	0	0	0	3		
Cre17.g716026	—	0	0	0	1		
Cre17.g716150	Similar to Small ubiquitin-like modifier	0	0	0	3		
Cre17.g716400	—	0	0	0	5		
Cre17.g716650	—	0	0	0	11		
Cre17.g716700	—	0	0	0	10		
Cre17.g716750	—	0	0	0	5		

4.4 List of acronyms

2-phosphoglycollate (2PG)
3-phosphoglycerate (3-PGA)
Actinic light (AL), 23
Adenosine triphosphate (ATP)
Advanced intercross lines (AILs), 68
Alternative oxidase (AOX)
Base pairs (bp), 67
Billion years (Gyr)
Calvin-Benson-Bassham cycle (CBB cycle)
Carbon-concentrating mechanism (CCM)
Centimorgans (cM), 67
Chemical gradient (ΔpH)
Chloride channels (CLC), 28
Chlorophyll *a* fluorescence (ChlF), 23
Confidence interval (CI), 85
Cyclic electron-flow (CEF)
Cytochrome b6f (Cyt b6f)
digalactosyl diacylglycerols (DGDG)
Electrical Gradient (ΔΨ)
Electrochromic shift (ECS), 44
Electron-transport chain (ETC)
Electron-transport rate (ETR)
Fatty acids (FAs), 53
Ferredoxin (Fdx)
Ferredoxin-NADP reductase (FNR)
Flavodiiron proteins (FLVs)
Gene Ontology (GO), 53
Genome-wide sequencing (GWS), 71
Glyceraldehyde 3-phosphate (GAP)
Great Oxidation Event (GOE)
Guanosine diphosphate (GDP), 57
Guanosine triphosphate (GTP), 57
High-light (HL)
identical-by-descendant (IBD), 72
identical-by-state (IBS), 75
Internal transcribed spacer (ITS)
KEGG Orthology (KO), 55
Last Universal Common Ancestor (LUCA)
Light-Harvesting Complex (LHC)
Likelihood ratio test (LRT), 89
Linear Electron Flow (LEF)
Loss-of-function (LOF)
Low-light (LL)
MAGIC lines (MLs), 74, 75
Map units (m.u.), 67
Mating-type (MT)
monogalactosyl diacylglycerols (MGDG)

4.5 List of figures

4.6 List of tables

Supplementary

4.7 Acknowledgments

I would like to thank all the people who have accompanied me on this journey. My promoters, Pierre, and Tom, who gave me this great opportunity and the support needed to turn my ideas into valuable scientific knowledge. Marc, for welcoming me into his laboratory and for his guidance through the MAGIC project. Claire, for her constant encouragement and support.

My colleagues and friends Sara, Felix, Anna, Lorenzo, Véronique, Rebecca, Gwenaëlle, Damien, and all the other lab members who have interacted with me during the last 6 years. Through good and hard times, you have always been there by my side. I will always be there for you.

My colleagues from other institutions, Olivier Vallon, Dimitris Petroutsos, Vasco Giovagnetti, Wojciech Nawrocki, Yizhon Yuan, Benjamin Bailleul, Ugo Cenci, Giovanni Finazzi, Massimo Genovese, Davide Califano, and all other scientists who contributed to my success through discussion, advice, support, and experiments. I would not be here without the support of such a beautiful and resourceful community of great scientists.

A special thanks to Véronique Larosa and Dimitris Petroutsos for the uncountable times they helped me across this journey.

My family, for their constant encouragement, even during long periods of not seeing each other, and during all the hard times we have faced during these years. My father Vincenzo and my mother Nelly, my second father Franco, my siblings Valentina e Andrea. The memory of my brother Marco. This is for you all. My sweet Christine, whose support and constant love have been my ultimate source of energy and motivation. You truly are to me what sun is to *Chlamydomonas*!

All my friends from all around the world who have made those years wonderful and full of good memories. I won't name you all because we are already at 180 pages, and I would like to keep it within the 200! ;P

Finally, thank you to me for keeping believing in myself and in my ideas until the very end. Thank you to my curiosity that pushes me to question myself and all the things around me, without putting limits on what is questionable and what is not. There is no wrong question in life. There are only wrong answers.

Liege, May 5th, 2023

Fabrizio Iacono

4.8 References

Águila Ruiz-Sola M, Flori S, Yuan Y, Villain G, Sanz-Luque E, Redekop P, Tokutsu R, Küken A, Tsichla A, Kepesidis G, et al (2023) Light-independent regulation of algal photoprotection by CO2 availability. Nat Commun **14**: 1977

Allen JF (2002) Photosynthesis of ATP—Electrons, Proton Pumps, Rotors, and Poise. Cell **110**: 273–276

Allorent G, Lefebvre-Legendre L, Chappuis R, Kuntz M, Truong TB, Niyogi KK, Ulm R, Goldschmidt-Clermont M (2016) UV-B photoreceptor-mediated protection of the photosynthetic machinery in Chlamydomonas reinhardtii. Proceedings of the National Academy of Sciences **113**: 14864–14869

Allorent G, Tokutsu R, Roach T, Peers G, Cardol P, Girard-Bascou J, Seigneurin-Berny D, Petroutsos D, Kuntz M, Breyton C, et al (2013) A Dual Strategy to Cope with High Light in Chlamydomonas reinhardtii. The Plant Cell **25**: 545–557

Anbar AD, Knoll AH (2002) Proterozoic Ocean Chemistry and Evolution: A Bioinorganic Bridge? Science **297**: 1137–1142

Anderson LE (1971) Chloroplast and cytoplasmic enzymes II. Pea leaf triose phosphate isomerases. Biochimica et Biophysica Acta (BBA) **-** Enzymology **235**: 237–244

Arias C, Obudulu O, Zhao X, Ansolia P, Zhang X, Paul S, Bygdell J, Pirmoradian M, Zubarev RA, Samuelsson G, et al (2020) Nuclear proteome analysis of Chlamydomonas with response to CO2 limitation. Algal Research **46**: 101765

Armbruster U, Carrillo LR, Venema K, Pavlovic L, Schmidtmann E, Kornfeld A, Jahns P, Berry JA, Kramer DM, Jonikas MC (2014) Ion antiport accelerates photosynthetic acclimation in fluctuating light environments. Nat Commun **5**: 5439

Aspatwar A, Haapanen S, Parkkila S (2018) An Update on the Metabolic Roles of Carbonic Anhydrases in the Model Alga Chlamydomonas reinhardtii. Metabolites **8**: 22

Austin JR, Frost E, Vidi P-A, Kessler F, Staehelin LA (2006) Plastoglobules are lipoprotein subcompartments of the chloroplast that are permanently coupled to thylakoid membranes and contain biosynthetic enzymes. Plant Cell **18**: 1693–1703

Badger MR, Kaplan A, Berry JA (1980) Internal Inorganic Carbon Pool of Chlamydomonas reinhardtii: EVIDENCE FOR A CARBON DIOXIDE-CONCENTRATING MECHANISM 1. Plant Physiology **66**: 407–413

Bailey S, Walters RG, Jansson S, Horton P (2001) Acclimation of Arabidopsis thaliana to the light environment: the existence of separate low light and high light responses. Planta **213**: 794–801

Bailleul B, Cardol P, Breyton C, Finazzi G (2010) Electrochromism: a useful probe to study algal photosynthesis. Photosynth Res **106**: 179

Baker NR, Harbinson J, Kramer DM (2007) Determining the limitations and regulation of photosynthetic energy transduction in leaves. Plant, Cell & Environment **30**: 1107–1125

Ballottari M, Dall'Osto L, Morosinotto T, Bassi R (2007) Contrasting Behavior of Higher Plant Photosystem I and II Antenna Systems during Acclimation *. Journal of Biological Chemistry **282**: 8947–8958

Ballottari M, Truong TB, Re ED, Erickson E, Stella GR, Fleming GR, Bassi R, Niyogi KK (2016) Identification of pH-sensing Sites in the Light Harvesting Complex Stress-related 3 Protein Essential for Triggering Non-photochemical Quenching in Chlamydomonas reinhardtii*. Journal of Biological Chemistry **291**: 7334–7346

Banti V, Giuntoli B, Gonzali S, Loreti E, Magneschi L, Novi G, Paparelli E, Parlanti S, Pucciariello C, Santaniello A, et al (2013) Low Oxygen Response Mechanisms in Green Organisms. International Journal of Molecular Sciences **14**: 4734–4761

Bassham JA, Benson AA, Calvin M (1950) The Path of Carbon in Photosynthesis VIII. The Role of MalicAcid. doi: 10.2172/910351

Béal D, Rappaport F, Joliot P (1999) A new high-sensitivity 10-ns time-resolution spectrophotometric technique adapted to in vivo analysis of the photosynthetic apparatus. Review of Scientific Instruments **70**: 202–207

Beer S, Björk M (2000) Measuring rates of photosynthesis of two tropical seagrasses by pulse amplitude modulated (PAM) fluorometry. Aquatic Botany **66**: 69–76

Blaby IK, Blaby-Haas C, Tourasse N, Hom EFY, Lopez D, Aksoy M, Grossman A, Umen J, Dutcher S, Porter M, et al (2014) The Chlamydomonas genome project: a decade on. Trends Plant Sci **19**: 672–680

Blankenship RE (2002) History and Early Development of Photosynthesis. Molecular Mechanisms of Photosynthesis. John Wiley & Sons, Ltd, pp 26–41

Bohne A-V, Schwarz C, Schottkowski M, Lidschreiber M, Piotrowski M, Zerges W, Nickelsen J (2013) Reciprocal Regulation of Protein Synthesis and Carbon Metabolism for Thylakoid Membrane Biogenesis. PLOS Biology **11**: e1001482

Bonente G, Ballottari M, Truong TB, Morosinotto T, Ahn TK, Fleming GR, Niyogi KK, Bassi R (2011) Analysis of LhcSR3, a Protein Essential for Feedback De-Excitation in the Green Alga Chlamydomonas reinhardtii. PLoS Biol. doi: 10.1371/journal.pbio.1000577

Bonente G, Pippa S, Castellano S, Bassi R, Ballottari M (2012) Acclimation of Chlamydomonas reinhardtii to Different Growth Irradiances *. Journal of Biological Chemistry **287**: 5833–5847

Boron WF (1978) Active control of intracellular pH. Respiration Physiology **33**: 59–62

Boynton JE, Harris EH, Burkhart BD, Lamerson PM, Gillham NW (1987) Transmission of mitochondrial and chloroplast genomes in crosses of Chlamydomonas. Proceedings of the National Academy of Sciences **84**: 2391–2395

Bradbury M, Baker NR (1981) Analysis of the slow phases of the in vivo chlorophyll fluorescence induction curve. Changes in the redox state of Photosystem II electron acceptors and fluorescence emission from Photosystems I and II. Biochimica et Biophysica Acta (BBA) **-** Bioenergetics **635**: 542–551

Briantais J-M, Vernotte C, Picaud M, Krause GH (1980) Chlorophyll fluorescence as a probe for the determination of the photo-induced proton gradient in isolated chloroplasts. Biochimica et Biophysica Acta (BBA) **-** Bioenergetics **591**: 198–202

Brzezowski P, Ksas B, Havaux M, Grimm B, Chazaux M, Peltier G, Johnson X, Alric J (2019) The function of PROTOPORPHYRINOGEN IX OXIDASE in chlorophyll biosynthesis requires oxidised plastoquinone in Chlamydomonas reinhardtii. Commun Biol **2**: 1–9

Buchanan BB (2016) The carbon (formerly dark) reactions of photosynthesis. Photosynth Res **128**: 215–217

Burlacot A, Dao O, Auroy P, Cuiné S, Li-Beisson Y, Peltier G (2022) Alternative photosynthesis pathways drive the algal CO2-concentrating mechanism. Nature 1–6

Calatrava V, Chamizo-Ampudia A, Sanz-Luque E, Ocaña-Calahorro F, Llamas A, Fernandez E, Galvan A (2017) How Chlamydomonas handles nitrate and the nitric oxide cycle. Journal of Experimental Botany **68**: 2593–2602

Camp PJ, Randall DD (1985) Purification and Characterization of the Pea Chloroplast Pyruvate Dehydrogenase Complex 1: A Source of Acetyl-CoA and NADH for Fatty Acid Biosynthesis. Plant Physiology **77**: 571–577

Canfield DE (2005) THE EARLY HISTORY OF ATMOSPHERIC OXYGEN: Homage to Robert M. Garrels. Annual Review of Earth and Planetary Sciences **33**: 1–36

Cardoso Esteves SM (2023) Natural variation in nutrient homeostasis mechanisms of Chlamydomonas reinhardtii.

Carraretto L, Formentin E, Teardo E, Checchetto V, Tomizioli M, Morosinotto T, Giacometti GM, Finazzi G, Szabó I (2013) A Thylakoid-Located Two-Pore K+ Channel Controls Photosynthetic Light Utilization in Plants. Science **342**: 114–118

Castillo-Davis CI, Hartl DL (2003) GeneMerge--post-genomic analysis, data mining, and hypothesis testing. Bioinformatics **19**: 891–892

Cavanagh C, Morell M, Mackay I, Powell W (2008) From mutations to MAGIC: resources for gene discovery, validation and delivery in crop plants. Current Opinion in Plant Biology **11**: 215–221

Cenci U, Moog D, Archibald JM (2015) Origin and Spread of Plastids by Endosymbiosis. Algal and Cyanobacteria Symbioses. WORLD SCIENTIFIC (EUROPE), pp 43–81

Chanroj S, Wang G, Venema K, Zhang M, Delwiche C, Sze H (2012) Conserved and Diversified Gene Families of Monovalent Cation/H+ Antiporters from Algae to Flowering Plants. Frontiers in Plant Science 3:

Charlesworth B (2009) Effective population size and patterns of molecular evolution and variation. Nat Rev Genet **10**: 195–205

Chaux F, Burlacot A, Mekhalfi M, Auroy P, Blangy S, Richaud P, Peltier G (2017) Flavodiiron Proteins Promote Fast and Transient O2 Photoreduction in Chlamydomonas. Plant Physiology **174**: 1825–1836

Churchill GA, Airey DC, Allayee H, Angel JM, Attie AD, Beatty J, Beavis WD, Belknap JK, Bennett B, Berrettini W, et al (2004) The Collaborative Cross, a community resource for the genetic analysis of complex traits. Nat Genet **36**: 1133–1137

Cinar O, Viechtbauer W (2022) The poolr Package for Combining Independent and Dependent p Values. Journal of Statistical Software **101**: 1–42

Cingolani P, Platts A, Wang LL, Coon M, Nguyen T, Wang L, Land SJ, Lu X, Ruden DM (2012) A program for annotating and predicting the effects of single nucleotide polymorphisms, SnpEff: SNPs in the genome of Drosophila melanogaster strain w1118; iso-2; iso-3. Fly (Austin) **6**: 80–92

Cordat E, Casey JR (2008) Bicarbonate transport in cell physiology and disease. Biochemical Journal **417**: 423–439

Cox J, Hein MY, Luber CA, Paron I, Nagaraj N, Mann M (2014) Accurate proteome-wide label-free quantification by delayed normalization and maximal peptide ratio extraction, termed MaxLFQ. Mol Cell Proteomics **13**: 2513–2526

Craig RJ, Böndel KB, Arakawa K, Nakada T, Ito T, Bell G, Colegrave N, Keightley PD, Ness RW (2019) Patterns of population structure and complex haplotype sharing among field isolates of the green alga Chlamydomonas reinhardtii. Molecular Ecology **28**: 3977–3993

Craig RJ, Gallaher SD, Shu S, Salomé P, Jenkins JW, Blaby-Haas CE, Purvine SO, O'Donnell S, Barry K, Grimwood J, et al (2022) The Chlamydomonas Genome Project, version 6: reference assemblies for mating type plus and minus strains reveal extensive structural mutation in the laboratory. 2022.06.16.496473

Cross FR, Umen JG (2015) The Chlamydomonas cell cycle. Plant J **82**: 370–392

Curien G, Flori S, Villanova V, Magneschi L, Giustini C, Forti G, Matringe M, Petroutsos D, Kuntz M, Finazzi G (2016) The Water to Water Cycles in Microalgae. Plant and Cell Physiology **57**: 1354–1363

DalCorso G, Pesaresi P, Masiero S, Aseeva E, Schünemann D, Finazzi G, Joliot P, Barbato R, Leister D (2008) A Complex Containing PGRL1 and PGR5 Is Involved in the Switch between Linear and Cyclic Electron Flow in Arabidopsis. Cell **132**: 273–285

Davis GA, Kanazawa A, Schöttler MA, Kohzuma K, Froehlich JE, Rutherford AW, Satoh-Cruz M, Minhas D, Tietz S, Dhingra A, et al (2016) Limitations to photosynthesis by proton motive force-induced photosystem II photodamage. eLife **5**: e16921

Depège N, Bellafiore S, Rochaix J-D (2003) Role of Chloroplast Protein Kinase Stt7 in LHCII Phosphorylation and State Transition in Chlamydomonas. Science **299**: 1572–1575

Dinc E, Tian L, Roy LM, Roth R, Goodenough U, Croce R (2016) LHCSR1 induces a fast and reversible pH-dependent fluorescence quenching in LHCII in Chlamydomonas reinhardtii cells. Proceedings of the National Academy of Sciences **113**: 7673–7678

Druet T, Farnir FP (2011) Modeling of Identity-by-Descent Processes Along a Chromosome Between Haplotypes and Their Genotyped Ancestors. Genetics **188**: 409–419

Druet T, Macleod IM, Hayes BJ (2014) Toward genomic prediction from whole-genome sequence data: impact of sequencing design on genotype imputation and accuracy of predictions. Heredity **112**: 39–47

Dukic E, Herdean A, Cheregi O, Sharma A, Nziengui H, Dmitruk D, Solymosi K, Pribil M, Spetea C (2019) K + and Cl − channels/transporters independently fine-tune photosynthesis in plants. Sci Rep **9**: 8639

Eberhard S, Finazzi G, Wollman F-A (2008) The Dynamics of Photosynthesis. Annual Review of Genetics **42**: 463–515

Ebersold WT (1956) CROSSING OVER IN CHLAMYDOMONAS REINHARDI. doi: 10.1002/J.1537-2197.1956.TB10509.X

Elrad D, Niyogi KK, Grossman AR (2002) A Major Light-Harvesting Polypeptide of Photosystem II Functions in Thermal Dissipation[W]. The Plant Cell **14**: 1801–1816

Engel BD, Schaffer M, Kuhn Cuellar L, Villa E, Plitzko JM, Baumeister W (2015) Native architecture of the Chlamydomonas chloroplast revealed by in situ cryo-electron tomography. eLife **4**: e04889

Eriksson M, Karlsson J, Ramazanov Z, Gardeström P, Samuelsson G (1996) Discovery of an algal mitochondrial carbonic anhydrase: molecular cloning and characterization of a low-CO2-induced polypeptide in Chlamydomonas reinhardtii. Proceedings of the National Academy of Sciences **93**: 12031–12034

Eriksson M, Villand P, Gardeström P, Samuelsson G (1998) Induction and Regulation of Expression of a Low-CO2-Induced Mitochondrial Carbonic Anhydrase inChlamydomonas reinhardtii. Plant Physiology **116**: 637–641

Evans JR (2013) Improving Photosynthesis. Plant Physiology **162**: 1780–1793

Fang W, Si Y, Douglass S, Casero D, Merchant SS, Pellegrini M, Ladunga I, Liu P, Spalding MH (2012) Transcriptome-Wide Changes in Chlamydomonas reinhardtii Gene Expression Regulated by Carbon Dioxide and the CO2-Concentrating Mechanism Regulator CIA5/CCM1. The Plant Cell **24**: 1876–1893

Fei C, Wilson AT, Mangan NM, Wingreen NS, Jonikas MC (2022) Modelling the pyrenoid-based CO2-concentrating mechanism provides insights into its operating principles and a roadmap for its engineering into crops. Nat Plants **8**: 583–595

Fernández-Calleja M, Monteagudo A, Casas AM, Boutin C, Pin PA, Morales F, Igartua E (2020) Rapid On-Site Phenotyping via Field Fluorimeter Detects Differences in Photosynthetic Performance in a Hybrid—Parent Barley Germplasm Set. Sensors **20**: 1486

Ferris PJ (1989) Characterization of a Chlamydomonas Transposon, Gulliver, Resembling Those in Higher Plants. Genetics **122**: 363–377

Ferris PJ, Goodenough UW (1997) Mating Type in Chlamydomonas Is Specified by Mid, the minus-Dominance Gene. Genetics **146**: 859–869

Ferris PJ, Woessner JP, Goodenough UW (1996) A sex recognition glycoprotein is encoded by the plus mating-type gene fus1 of Chlamydomonas reinhardtii. Mol Biol Cell **7**: 1235–1248

Fett JP, Coleman JR (1994) Regulation of Periplasmic Carbonic Anhydrase Expression in Chlamydomonas reinhardtii by Acetate and pH. Plant Physiology **106**: 103–108

Fischer BB, Wiesendanger M, Eggen RIL (2006) Growth Condition-Dependent Sensitivity, Photodamage and Stress Response of Chlamydomonas reinhardtii Exposed to High Light Conditions. Plant and Cell Physiology **47**: 1135–1145

Flood PJ, Harbinson J, Aarts MGM (2011) Natural genetic variation in plant photosynthesis. Trends Plant Sci **16**: 327–335

Flood PJ, Kruijer W, Schnabel SK, van der Schoor R, Jalink H, Snel JFH, Harbinson J, Aarts MGM (2016) Phenomics for photosynthesis, growth and reflectance in Arabidopsis thaliana reveals circadian and long-term fluctuations in heritability. Plant Methods **12**: 14

Flowers JM, Hazzouri KM, Pham GM, Rosas U, Bahmani T, Khraiwesh B, Nelson DR, Jijakli K, Abdrabu R, Harris EH, et al (2015) Whole-Genome Resequencing Reveals Extensive Natural Variation in the Model Green Alga Chlamydomonas reinhardtii. The Plant Cell **27**: 2353–2369

Fukuzawa H, Miura K, Ishizaki K, Kucho K, Saito T, Kohinata T, Ohyama K (2001) Ccm1, a regulatory gene controlling the induction of a carbon-concentrating mechanism in Chlamydomonas reinhardtii by sensing CO2 availability. Proceedings of the National Academy of Sciences **98**: 5347–5352

Gabilly ST, Baker CR, Wakao S, Crisanto T, Guan K, Bi K, Guiet E, Guadagno CR, Niyogi KK (2019) Regulation of photoprotection gene expression in Chlamydomonas by a putative E3 ubiquitin ligase complex and a homolog of CONSTANS. Proceedings of the National Academy of Sciences **116**: 17556–17562

Gallaher SD, Fitz-Gibbon ST, Glaesener AG, Pellegrini M, Merchant SS (2015) Chlamydomonas Genome Resource for Laboratory Strains Reveals a Mosaic of Sequence Variation, Identifies True Strain Histories, and Enables Strain-Specific Studies. The Plant Cell **27**: 2335–2352

Gallaher SD, Fitz-Gibbon ST, Strenkert D, Purvine SO, Pellegrini M, Merchant SS (2018) High-throughput sequencing of the chloroplast and mitochondrion of Chlamydomonas reinhardtii to generate improved de novo assemblies, analyze expression patterns and transcript speciation, and evaluate diversity among laboratory strains and wild isolates. Plant J **93**: 545–565

Geraghty AM, Spalding MH (1996) Molecular and Structural Changes in Chlamydomonas under Limiting CO2 (A Possible Mitochondrial Role in Adaptation). Plant Physiology **111**: 1339–1347

Gfeller RP, Gibbs M (1984) Fermentative Metabolism of Chlamydomonas reinhardtii: I. Analysis of Fermentative Products from Starch in Dark and Light. Plant Physiology **75**: 212–218

Gillham NW (1969) Uniparental Inheritance in Chlamydomonas reinhardi. The American Naturalist. doi: 10.1086/282608

Gnesutta N, Kumimoto RW, Swain S, Chiara M, Siriwardana C, Horner DS, Holt BF, Mantovani R (2017) CONSTANS Imparts DNA Sequence Specificity to the Histone Fold NF-YB/NF-YC Dimer[OPEN]. Plant Cell **29**: 1516–1532

Goodenough UW, Heuser JE (1985) The Chlamydomonas cell wall and its constituent glycoproteins analyzed by the quick-freeze, deep-etch technique. Journal of Cell Biology **101**: 1550–1568

Goto S, Mori H, Uchiyama K, Ishizuka W, Taneda H, Kono M, Kajiya-Kanegae H, Iwata H (2021) Genetic Dissection of Growth and Eco-Physiological Traits Associated with Altitudinal Adaptation in Sakhalin Fir (Abies sachalinensis) Based on QTL Mapping. Genes **12**: 1110

Gounaris K, Barber J (1983) Monogalactosyldiacylglycerol: The most abundant polar lipid in nature. Trends in Biochemical Sciences **8**: 378–381

Gräber P, Witt HT (1976) Relations between the electrical potential, pH gradient, proton flux and phosphorylation in the photosynthetic membrane. Biochimica et Biophysica Acta (BBA) - Bioenergetics **423**: 141–163

Hagino T, Kato T, Kasuya G, Kobayashi K, Kusakizako T, Hamamoto S, Sobajima T, Fujiwara Y, Yamashita K, Kawasaki H, et al (2022) Cryo-EM structures of thylakoid-located voltage-dependent chloride channel VCCN1. Nat Commun **13**: 2505

Hangarter RP, Good NE (1982) Energy thresholds for ATP synthesis in chloroplasts. Biochimica et Biophysica Acta (BBA) - Bioenergetics **681**: 397–404

Harris EH (2008) The Chlamydomonas Sourcebook: Introduction to Chlamydomonas and Its Laboratory Use - 2nd Edition, Second Edition.

Hasan AR, Ness RW (2020) Recombination Rate Variation and Infrequent Sex Influence Genetic Diversity in Chlamydomonas reinhardtii. Genome Biology and Evolution **12**: 370–380

Heifetz PB, Förster B, Osmond CB, Giles LJ, Boynton JE (2000) Effects of acetate on facultative autotrophy in Chlamydomonas reinhardtii assessed by photosynthetic measurements and stable isotope analyses. Plant Physiol **122**: 1439–1445

Herdean A, Nziengui H, Zsiros O, Solymosi K, Garab G, Lundin B, Spetea C (2016a) The Arabidopsis Thylakoid Chloride Channel AtCLCe Functions in Chloride Homeostasis and Regulation of Photosynthetic Electron Transport. Front Plant Sci. doi: 10.3389/fpls.2016.00115

Herdean A, Teardo E, Nilsson AK, Pfeil BE, Johansson ON, Ünnep R, Nagy G, Zsiros O, Dana S, Solymosi K, et al (2016b) A voltage-dependent chloride channel fine-tunes photosynthesis in plants. Nat Commun **7**: 11654

Hodgskiss MSW, Crockford PW, Peng Y, Wing BA, Horner TJ (2019) A productivity collapse to end Earth’s Great Oxidation. Proc Natl Acad Sci U S A **116**: 17207–17212

Höhner R, Galvis VC, Strand DD, Völkner C, Krämer M, Messer M, Dinc F, Sjuts I, Bölter B, Kramer DM, et al (2019) Photosynthesis in Arabidopsis Is Unaffected by the Function of the Vacuolar K+ Channel TPK3. Plant Physiol **180**: 1322–1335

Holland HD (2006) The oxygenation of the atmosphere and oceans. Philos Trans R Soc Lond B Biol Sci **361**: 903–915

Houille-Vernes L, Rappaport F, Wollman F-A, Alric J, Johnson X (2011) Plastid terminal oxidase 2 (PTOX2) is the major oxidase involved in chlororespiration in Chlamydomonas. PNAS **108**: 20820–20825

Hu MY, Yan J-J, Petersen I, Himmerkus N, Bleich M, Stumpp M (2018) A SLC4 family bicarbonate transporter is critical for intracellular pH regulation and biomineralization in sea urchin embryos. eLife **7**: e36600

Huang BE, Verbyla KL, Verbyla AP, Raghavan C, Singh VK, Gaur P, Leung H, Varshney RK, Cavanagh CR (2015) MAGIC populations in crops: current status and future prospects. Theor Appl Genet **128**: 999–1017

HUTAGALUNG AH, NOVICK PJ (2011) Role of Rab GTPases in Membrane Traffic and Cell Physiology. Physiol Rev **91**: 119–149

Inoue K (2007) The Chloroplast Outer Envelope Membrane: The Edge of Light and Excitement. Journal of Integrative Plant Biology **49**: 1100–1111

Jaślan D, Dreyer I, Lu J, O'Malley R, Dindas J, Marten I, Hedrich R (2019) Voltage-dependent gating of SV channel TPC1 confers vacuole excitability. Nat Commun **10**: 2659

Johnson X, Alric J (2013) Central carbon metabolism and electron transport in Chlamydomonas reinhardtii: metabolic constraints for carbon partitioning between oil and starch. Eukaryot Cell **12**: 776–793

Johnson X, Steinbeck J, Dent RM, Takahashi H, Richaud P, Ozawa S-I, Houille-Vernes L, Petroutsos D, Rappaport F, Grossman AR, et al (2014) Proton Gradient Regulation 5-Mediated Cyclic Electron Flow under ATP- or Redox-Limited Conditions: A Study of ΔATPase pgr5 and ΔrbcL pgr5 Mutants in the Green Alga Chlamydomonas reinhardtii1[C][W]. Plant Physiol **165**: 438–452

Johnson X, Vandystadt G, Bujaldon S, Wollman F-A, Dubois R, Roussel P, Alric J, Béal D (2009) A new setup for in vivo fluorescence imaging of photosynthetic activity. Photosynth Res **102**: 85

Juneau P, Harrison PJ (2005) Comparison by PAM Fluorometry of Photosynthetic Activity of Nine Marine Phytoplankton Grown Under Identical Conditions¶. Photochemistry and Photobiology **81**: 649–653

Kanazawa A, Kramer DM (2002) In vivo modulation of nonphotochemical exciton quenching (NPQ) by regulation of the chloroplast ATP synthase. Proceedings of the National Academy of Sciences **99**: 12789–12794

Kanehisa M, Sato Y, Kawashima M, Furumichi M, Tanabe M (2016) KEGG as a reference resource for gene and protein annotation. Nucleic Acids Research **44**: D457–D462

Kang Y, Khan S, Ma X (2009) Climate change impacts on crop yield, crop water productivity and food security – A review. Progress in Natural Science **19**: 1665–1674

Karlsson J, Clarke, Chen (1998) A novel α-type carbonic anhydrase associated with the thylakoid membrane in Chlamydomonas reinhardtii is required for growth at ambient CO2. The EMBO Journal **17**: 1208–1216

Kautsky H, Hirsch A (1931) Neue Versuche zur Kohlensäureassimilation. Naturwissenschaften **19**: 964–964

Kelly G j., Latzko E (1976) Inhibition of spinach-leaf phosphofructokinase by 2-phosphoglycollate. FEBS Letters **68**: 55–58

Kerr RA (2005) The Story of O2. Science **308**: 1730–1732

Kirchhoff H (2019) Chloroplast ultrastructure in plants. New Phytologist **223**: 565–574

Kok B, Forbush B, McGloin M (1970) Cooperation of charges in photosynthetic O2 evolution-I. A linear four step mechanism. Photochem Photobiol **11**: 457–475

Kornberg HL, Krebs HA (1957) Synthesis of Cell Constituents from C2-Units by a Modified Tricarboxylic Acid Cycle. Nature **179**: 988–991

Koroidov S, Shevela D, Shutova T, Samuelsson G, Messinger J (2014) Mobile hydrogen carbonate acts as proton acceptor in photosynthetic water oxidation. PNAS **111**: 6299–6304

Kover PX, Valdar W, Trakalo J, Scarcelli N, Ehrenreich IM, Purugganan MD, Durrant C, Mott R (2009) A Multiparent Advanced Generation Inter-Cross to Fine-Map Quantitative Traits in Arabidopsis thaliana. PLOS Genetics **5**: e1000551

Kramer DM, Cruz JA, Kanazawa A (2003) Balancing the central roles of the thylakoid proton gradient. Trends in Plant Science **8**: 27–32

Kramer DM, Sacksteder CA, Cruz JA (1999) How acidic is the lumen? Photosynthesis Research **60**: 151–163

Kroymann J, Schneider W, Zetsche K (1995) Opposite Regulation of the Copy Number and the Expression of Plastid and Mitochondrial Genes by Light and Acetate in the Green Flagellate Chlorogonium. Plant Physiology **108**: 1641–1646

Kubo T, Abe J, Saito T, Matsuda Y (2002) Genealogical relationships among laboratory strains of Chlamydomonas reinhardtii as inferred from matrix metalloprotease genes. Curr Genet **41**: 115–122

Kunz H-H, Gierth M, Herdean A, Satoh-Cruz M, Kramer DM, Spetea C, Schroeder JI (2014) Plastidial transporters KEA1, -2, and -3 are essential for chloroplast osmoregulation, integrity, and pH regulation in Arabidopsis. PNAS **111**: 7480–7485

Lacour T, Babin M, Lavaud J (2020) Diversity in Xanthophyll Cycle Pigments Content and Related Nonphotochemical Quenching (NPQ) Among Microalgae: Implications for Growth Strategy and Ecology. Journal of Phycology **56**: 245–263

Lander ES, Botstein D (1989) Mapping mendelian factors underlying quantitative traits using RFLP linkage maps. Genetics **121**: 185–199

Lee C-K, Cheong H-K, Ryu K-S, Lee JI, Lee W, Jeon YH, Cheong C (2008) Biotinoyl domain of human acetyl-CoA carboxylase: Structural insights into the carboxyl transfer mechanism. Proteins: Structure, Function, and Bioinformatics **72**: 613–624

Leebens-Mack JH, Barker MS, Carpenter EJ, Deyholos MK, Gitzendanner MA, Graham SW, Grosse I, Li Z, Melkonian M, Mirarab S, et al (2019) One thousand plant transcriptomes and the phylogenomics of green plants. Nature **574**: 679–685

Leffler EM, Bullaughey K, Matute DR, Meyer WK, Ségurel L, Venkat A, Andolfatto P, Przeworski M (2012) Revisiting an Old Riddle: What Determines Genetic Diversity Levels within Species? PLOS Biology **10**: e1001388

Leiser M, Gromet-Elhanan Z (1977) Comparison of the electrochemical proton gradient and phosphate potential maintained by Rhodospirillum rubrum chromatophores in the steady state. Archives of Biochemistry and Biophysics **178**: 79–88

Leister D (2020) Alternative electron pathways in photosynthesis: strength in numbers. New Phytologist **228**: 1166–1168

Li JB, Gerdes JM, Haycraft CJ, Fan Y, Teslovich TM, May-Simera H, Li H, Blacque OE, Li L, Leitch CC, et al (2004) Comparative Genomics Identifies a Flagellar and Basal Body Proteome that Includes the BBS5 Human Disease Gene. Cell **117**: 541–552

Li X, Zhang R, Patena W, Gang SS, Blum SR, Ivanova N, Yue R, Robertson JM, Lefebvre PA, Fitz-Gibbon ST, et al (2016) An Indexed, Mapped Mutant Library Enables Reverse Genetics Studies of Biological Processes in Chlamydomonas reinhardtii[OPEN]. Plant Cell **28**: 367–387

Liang M, Nielsen R (2014) The Lengths of Admixture Tracts. Genetics **197**: 953–967

Li-Beisson Y, Beisson F, Riekhof W (2015) Metabolism of acyl-lipids in Chlamydomonas reinhardtii. The Plant Journal **82**: 504–522

Lippert C, Listgarten J, Liu Y, Kadie CM, Davidson RI, Heckerman D (2011) FaST linear mixed models for genome-wide association studies. Nat Methods **8**: 833–835

Liu X, Nawrocki W, Croce R (2022) The role of LHCBM1 in non-photochemical quenching in Chlamydomonas reinhardtii. 2022.01.13.476201

Lubitz W, Chrysina M, Cox N (2019) Water oxidation in photosystem II. Photosynth Res **142**: 105–125

Lynch M, Walsh B (1999) Genetics and Analysis of Quantitative Traits. The Quarterly Review of Biology **74**: 225–225

Lyons TW, Reinhard CT, Planavsky NJ (2014) The rise of oxygen in Earth's early ocean and atmosphere. Nature **506**: 307–315

Machingura MC, Bajsa-Hirschel J, Laborde SM, Schwartzenburg JB, Mukherjee B, Mukherjee A, Pollock SV, Förster B, Price GD, Moroney JV (2017) Identification and characterization of a solute carrier, CIA8, involved in inorganic carbon acclimation in Chlamydomonas reinhardtii. Journal of Experimental Botany **68**: 3879–3890

Mackinder LCM, Chen C, Leib RD, Patena W, Blum SR, Rodman M, Ramundo S, Adams CM, Jonikas MC (2017) A Spatial Interactome Reveals the Protein Organization of the Algal CO2-Concentrating Mechanism. Cell **171**: 133-147.e14

Mackinder LCM, Meyer MT, Mettler-Altmann T, Chen VK, Mitchell MC, Caspari O, Freeman Rosenzweig ES, Pallesen L, Reeves G, Itakura A, et al (2016) A repeat protein links Rubisco to form the eukaryotic carbon-concentrating organelle. Proceedings of the National Academy of Sciences **113**: 5958–5963

Malosetti M, Ribaut JM, Vargas M, Crossa J, van Eeuwijk FA (2008) A multi-trait multi-environment QTL mixed model with an application to drought and nitrogen stress trials in maize (Zea mays L.). Euphytica **161**: 241–257

Marchand J, Heydarizadeh P, Schoefs B, Spetea C (2018) Ion and metabolite transport in the chloroplast of algae: lessons from land plants. Cell Mol Life Sci **75**: 2153–2176

Marmagne A, Vinauger-Douard M, Monachello D, de Longevialle AF, Charon C, Allot M, Rappaport F, Wollman F-A, Barbier-Brygoo H, Ephritikhine G (2007) Two members of the Arabidopsis CLC (chloride channel) family, AtCLCe and AtCLCf, are associated with thylakoid and Golgi membranes, respectively. J Exp Bot **58**: 3385–3393

May RM (2010) Tropical Arthropod Species, More or Less? Science **329**: 41–42

Mekhedov S, de Ilárduya OM, Ohlrogge J (2000) Toward a Functional Catalog of the Plant Genome. A Survey of Genes for Lipid Biosynthesis1. Plant Physiology **122**: 389–402

Merchant SS, Prochnik SE, Vallon O, Harris EH, Karpowicz SJ, Witman GB, Terry A, Salamov A, Fritz-Laylin LK, Maréchal-Drouard L, et al (2007) The Chlamydomonas Genome Reveals the Evolution of Key Animal and Plant Functions. Science. doi: 10.1126/science.1143609

Meyer K, Houle D (2013) Sampling based approximation of confidence intervals for functions of genetic covariance matrices.

Mirkovic T, Ostroumov EE, Anna JM, van Grondelle R, Govindjee, Scholes GD (2017) Light Absorption and Energy Transfer in the Antenna Complexes of Photosynthetic Organisms. Chem Rev **117**: 249–293

Misztal I, Tsuruta S, Strabel T, Auvray B, Druet T, Lee DH (2002) BLUPF90 AND RELATED PROGRAMS (BGF90). 2

Mitchell P (1961) Coupling of Phosphorylation to Electron and Hydrogen Transfer by a Chemi-Osmotic type of Mechanism. Nature **191**: 144–148

Mittelmeier TM, Boyd JS, Lamb MR, Dieckmann CL (2011) Asymmetric properties of the Chlamydomonas reinhardtii cytoskeleton direct rhodopsin photoreceptor localization. Journal of Cell Biology **193**: 741–753

Miura K, Yamano T, Yoshioka S, Kohinata T, Inoue Y, Taniguchi F, Asamizu E, Nakamura Y, Tabata S, Yamato KT, et al (2004) Expression Profiling-Based Identification of CO2-Responsive Genes Regulated by CCM1 Controlling a Carbon-Concentrating Mechanism in Chlamydomonas reinhardtii. Plant Physiol **135**: 1595–1607

Mooney BP, Miernyk JA, Randall DD (1999) Cloning and Characterization of the DihydrolipoamideS-Acetyltransferase Subunit of the Plastid Pyruvate Dehydrogenase Complex (E2) from Arabidopsis1. Plant Physiology **120**: 443–452

Moroney JV, Husic HD, Tolbert NE, Kitayama M, Manuel LJ, Togasaki RK (1989) Isolation and Characterization of a Mutant of Chlamydomonas reinhardtii Deficient in the CO(2) Concentrating Mechanism. Plant Physiol **89**: 897–903

Moroney JV, Ma Y, Frey WD, Fusilier KA, Pham TT, Simms TA, DiMario RJ, Yang J, Mukherjee B (2011) The carbonic anhydrase isoforms of Chlamydomonas reinhardtii: intracellular location, expression, and physiological roles. Photosynth Res **109**: 133–149

Moroney JV, Ynalvez RA (2007) Proposed Carbon Dioxide Concentrating Mechanism in Chlamydomonas reinhardtii. Eukaryotic Cell **6**: 1251–1259

Morsy FM (2011) Acetate Versus Sulfur Deprivation Role in Creating Anaerobiosis in Light for Hydrogen Production by Chlamydomonas reinhardtii and Spirulina platensis: Two Different Organisms and Two Different Mechanisms. Photochemistry and Photobiology **87**: 137–142

Mukherjee A, Lau CS, Walker CE, Rai AK, Prejean CI, Yates G, Emrich-Mills T, Lemoine SG, Vinyard DJ, Mackinder LCM, et al (2019) Thylakoid localized bestrophin-like proteins are essential for the CO2 concentrating mechanism of Chlamydomonas reinhardtii. PNAS **116**: 16915–16920

Nakada T, Shinkawa H, Ito T, Tomita M (2009) Recharacterization of Chlamydomonas reinhardtii and its relatives with new isolates from Japan. J Plant Res **123**: 67

Nawrocki WJ, Bailleul B, Cardol P, Rappaport F, Wollman F-A, Joliot P (2019a) Maximal cyclic electron flow rate is independent of PGRL1 in Chlamydomonas. Biochimica et Biophysica Acta (BBA) - Bioenergetics **1860**: 425–432

Nawrocki WJ, Bailleul B, Picot D, Cardol P, Rappaport F, Wollman F-A, Joliot P (2019b) The mechanism of cyclic electron flow. Biochimica et Biophysica Acta (BBA) - Bioenergetics **1860**: 433–438

Nawrocki WJ, Santabarbara S, Mosebach L, Wollman F-A, Rappaport F (2016) State transitions redistribute rather than dissipate energy between the two photosystems in Chlamydomonas. Nature Plants **2**: 1–7

Nawrocki WJ, Tourasse NJ, Taly A, Rappaport F, Wollman F-A (2015) The Plastid Terminal Oxidase: Its Elusive Function Points to Multiple Contributions to Plastid Physiology. Annual Review of Plant Biology **66**: 49–74

Ness RW, Morgan AD, Colegrave N, Keightley PD (2012) Estimate of the Spontaneous Mutation Rate in Chlamydomonas reinhardtii. Genetics **192**: 1447–1454

Neusius D, Kleinknecht L, Teh JT, Ostermeier M, Kelterborn S, Eirich J, Hegemann P, Finkemeier I, Bohne A-V, Nickelsen J (2022) Lysine acetylation regulates moonlighting activity of the E2 subunit of the chloroplast pyruvate dehydrogenase complex in Chlamydomonas. The Plant Journal **111**: 1780–1800

Nicholls DG, Ferguson SJ, eds (1992) 2 - ION TRANSPORT ACROSS ENERGY-CONSERVING MEMBRANES. Bioenergetics 2. Academic Press, pp 22–37

Odell SG, Hudson AI, Praud S, Dubreuil P, Tixier M-H, Ross-Ibarra J, Runcie DE (2022) Modeling allelic diversity of multiparent mapping populations affects detection of quantitative trait loci. G3 Genes|Genomes|Genetics **12**: jkac011

Ögren E, Baker NR (1985) Evaluation of a technique for the measurement of chlorophyll fluorescence from leaves exposed to continuous white light. Plant, Cell & Environment **8**: 539–547

Ohad I, Adir N, Koike H, Kyle DJ, Inoue Y (1990) Mechanism of photoinhibition in vivo. A reversible light-induced conformational change of reaction center II is related to an irreversible modification of the D1 protein. Journal of Biological Chemistry **265**: 1972–1979

Orthwein T, Scholl J, Spät P, Lucius S, Koch M, Macek B, Hagemann M, Forchhammer K (2021) The novel PII-interactor PirC identifies phosphoglycerate mutase as key control point of carbon storage metabolism in cyanobacteria. Proceedings of the National Academy of Sciences **118**: e2019988118

Papageorgiou GC, Govingjee (2004) Chlorophyll a Fluorescence.

Pazour GJ, Dickert BL, Vucica Y, Seeley ES, Rosenbaum JL, Witman GB, Cole DG (2000) Chlamydomonas IFT88 and Its Mouse Homologue, Polycystic Kidney Disease Gene Tg737, Are Required for Assembly of Cilia and Flagella. Journal of Cell Biology **151**: 709–718

Pazour GJ, Sineshchekov OA, Witman GB (1995) Mutational analysis of the phototransduction pathway of Chlamydomonas reinhardtii. Journal of Cell Biology **131**: 427–440

Peers G, Truong TB, Ostendorf E, Busch A, Elrad D, Grossman AR, Hippler M, Niyogi KK (2009) An ancient light-harvesting protein is critical for the regulation of algal photosynthesis. Nature **462**: 518–521

Petroutsos D, Busch A, Janßen I, Trompelt K, Bergner SV, Weinl S, Holtkamp M, Karst U, Kudla J, Hippler M (2011) The Chloroplast Calcium Sensor CAS Is Required for Photoacclimation in Chlamydomonas reinhardtii[W]. Plant Cell **23**: 2950–2963

Petroutsos D, Tokutsu R, Maruyama S, Flori S, Greiner A, Magneschi L, Cusant L, Kottke T, Mittag M, Hegemann P, et al (2016) A blue-light photoreceptor mediates the feedback regulation of photosynthesis. Nature **537**: 563–566

Plancke C, Vigeolas H, Höhner R, Roberty S, Emonds-Alt B, Larosa V, Willamme R, Duby F, Onga Dhali D, Thonart P, et al (2014) Lack of isocitrate lyase in Chlamydomonas leads to changes in carbon metabolism and in the response to oxidative stress under mixotrophic growth. The Plant Journal **77**: 404–417

Pröschold T, Harris EH, Coleman AW (2005) Portrait of a Species: Chlamydomonas reinhardtii. Genetics **170**: 1601–1610

Puzanskiy R, Shavarda A, Romanyuk D, Shishova M (2021) The role of trophic conditions in the regulation of physiology and metabolism of Chlamydomonas reinhardtii during batch culturing. J Appl Phycol **33**: 2897–2908

Qu Z, Hartzell HC (2008) Bestrophin Cl− Channels are Highly Permeable to HCO3−. Am J Physiol Cell Physiol **294**: C1371–C1377

Rai AK, Chen T, Moroney JV (2021) Mitochondrial carbonic anhydrases are needed for optimal photosynthesis at low CO2 levels in Chlamydomonas. Plant Physiology **187**: 1387–1398

Raven JA (2001) A role for mitochondrial carbonic anhydrase in limiting CO2 leakage from low CO2-grown cells of Chlamydomonas reinhardtii. Plant, Cell & Environment **24**: 261–265

Raven JA, Cockell CS, De La Rocha CL (2008) The evolution of inorganic carbon concentrating mechanisms in photosynthesis. Philosophical Transactions of the Royal Society B: Biological Sciences **363**: 2641–2650

Rawat M, Moroney JV (1995) The Regulation of Carbonic Anhydrase and Ribulose-1,5-Bisphosphate Carboxylase/Oxygenase Activase by Light and CO2 in Chlamydomonas reinhardtii. Plant Physiol **109**: 937–944

Redekop P, Sanz-Luque E, Yuan Y, Villain G, Petroutsos D, Grossman AR (2022) Transcriptional regulation of photoprotection in dark-to-light transition—More than just a matter of excess light energy. Science Advances **8**: eabn1832

Rifkin SA (2012) Quantitative Trait Loci (QTL). Springer

Roach T (2022) Chlorophyll fluorescence of Chlamydomonas reinhardtii; insights into the complexities. doi: 10.26124/MITOFIT:2022-0023.V2

Roach T, Sedoud A, Krieger-Liszkay A (2013) Acetate in mixotrophic growth medium affects photosystem II in Chlamydomonas reinhardtii and protects against photoinhibition. Biochimica et Biophysica Acta (BBA) - Bioenergetics **1827**: 1183–1190

Rochaix J-D (2016) The Dynamics of the Photosynthetic Apparatus in Algae. Applied Photosynthesis - New Progress. doi: 10.5772/62261

Runcie DE, Crawford L (2019) Fast and flexible linear mixed models for genome-wide genetics. PLOS Genetics **15**: e1007978

Rungrat T, Awlia M, Brown T, Cheng R, Sirault X, Fajkus J, Trtilek M, Furbank B, Badger M, Tester M, et al (2016) Using Phenomic Analysis of Photosynthetic Function for Abiotic Stress Response Gene Discovery. Arabidopsis Book **14**: e0185

Russell JM, Boron WF (1976) Role of chloride transport in regulation of intracellular pH. Nature **264**: 73–74

Sack L, Zeyl C, Bell G, Sharbel T, Reboud X, Bernhardt T, Koelewyn H (1994) Isolation of Four New Strains of Chlamydomonas Reinhardtii (chlorophyta) from Soil Samples. Journal of Phycology **30**: 770–773

Sager R (1955) Inheritance in the Green Alga Chlamydomonas Reinhardi. Genetics **40**: 476–489

Sager R, Granick S (1953) Nutritional Studies with Chlamydomonas Reinhardi. Annals of the New York Academy of Sciences **56**: 831–838

Salomé PA, Merchant SS (2019) A Series of Fortunate Events: Introducing Chlamydomonas as a Reference Organism. The Plant Cell **31**: 1682–1707

Santabarbara S, Villafiorita Monteleone F, Remelli W, Rizzo F, Menin B, Casazza AP (2019) Comparative excitation-emission dependence of the FV/FM ratio in model green algae and cyanobacterial strains. Physiologia Plantarum **166**: 351–364

Satoh K, Katoh S (1983) Induction Kinetics of Millisecond-Delayed Luminescence in Intact Bryopsis Chloroplasts. Plant and Cell Physiology **24**: 953–962

Schaffner SF, Taylor AR, Wong W, Wirth DF, Neafsey DE (2018) hmmIBD: software to infer pairwise identity by descent between haploid genotypes. Malaria Journal **17**: 196

Scholz M, Gäbelein P, Xue H, Mosebach L, Bergner SV, Hippler M (2019) Light-dependent N-terminal phosphorylation of LHCSR3 and LHCB4 are interlinked in Chlamydomonas reinhardtii. The Plant Journal **99**: 877–894

Schreiber U (2004) Pulse-Amplitude-Modulation (PAM) Fluorometry and Saturation Pulse Method: An Overview. *In* GC Papageorgiou, Govindjee, eds, Chlorophyll a Fluorescence: A Signature of Photosynthesis. Springer Netherlands, Dordrecht, pp 279–319

Seaton GGR, Walker DA (1990) Chlorophyll fluorescence as a measure of photosynthetic carbon assimilation. Proceedings of the Royal Society of London Series B: Biological Sciences. doi: 10.1098/rspb.1990.0099

Sedlar A, Zupin M, Maras M, Razinger J, Šuštar-Vozlič J, Pipan B, Meglič V (2020) QTL Mapping for Drought-Responsive Agronomic Traits Associated with Physiology, Phenology, and Yield in an Andean Intra-Gene Pool Common Bean Population. Agronomy **10**: 225

Seelert H, Poetsch A, Dencher NA, Engel A, Stahlberg H, Müller DJ (2000) Proton-powered turbine of a plant motor. Nature **405**: 418–419

Semchonok DA, Sathish Yadav KN, Xu P, Drop B, Croce R, Boekema EJ (2017) Interaction between the photoprotective protein LHCSR3 and C2S2 Photosystem II supercomplex in Chlamydomonas reinhardtii. Biochimica et Biophysica Acta (BBA) **-** Bioenergetics **1858**: 379–385

Seydoux C, Storti M, Giovagnetti V, Matuszyńska A, Guglielmino E, Zhao X, Giustini C, Pan Y, Blommaert L, Angulo J, et al (2022) Impaired photoprotection in Phaeodactylum tricornutum KEA3 mutants reveals the proton regulatory circuit of diatoms light acclimation. New Phytologist **234**: 578–591

Sharkey TD (1988) Estimating the rate of photorespiration in leaves. Physiologia Plantarum **73**: 147–152

Shutova T, Kenneweg H, Buchta J, Nikitina J, Terentyev V, Sergey C (2008) The photosystem II-associated Cah3 in Chlamydomonas enhances the O2 evolution rate by proton removal. The EMBO Journal **27**: 782–791

Slatkin M (2008) Linkage disequilibrium — understanding the evolutionary past and mapping the medical future. Nat Rev Genet **9**: 477–485

Sonoike K (2011) Photoinhibition of photosystem I. Physiologia Plantarum **142**: 56–64

de Souza MP, Hoeltz M, Gressler PD, Benitez LB, Schneider RCS (2019) Potential of Microalgal Bioproducts: General Perspectives and Main Challenges. Waste Biomass Valor **10**: 2139–2156

Sproles AE, Fields FJ, Smalley TN, Le CH, Badary A, Mayfield SP (2021) Recent advancements in the genetic engineering of microalgae. Algal Research **53**: 102158

Steen CJ, Burlacot A, Short AH, Niyogi KK, Fleming GR (2022) Interplay between LHCSR proteins and state transitions governs the NPQ response in Chlamydomonas during light fluctuations. Plant, Cell & Environment **45**: 2428–2445

Sung W, Ackerman MS, Miller SF, Doak TG, Lynch M (2012) Drift-barrier hypothesis and mutation-rate evolution. Proceedings of the National Academy of Sciences **109**: 18488–18492

Tang R-J, Zhao F-G, Yang Y, Wang C, Li K, Kleist TJ, Lemaux PG, Luan S (2020) A calcium signalling network activates vacuolar K+ remobilization to enable plant adaptation to low-K environments. Nat Plants **6**: 384–393

Tardif M, Atteia A, Specht M, Cogne G, Rolland N, Brugière S, Hippler M, Ferro M, Bruley C, Peltier G, et al (2012) PredAlgo: A New Subcellular Localization Prediction Tool Dedicated to Green Algae. Molecular Biology and Evolution **29**: 3625–3639

Tashiro T, Ishida A, Hori M, Igisu M, Koike M, Méjean P, Takahata N, Sano Y, Komiya T (2017) Early trace of life from 3.95 Ga sedimentary rocks in Labrador, Canada. Nature **549**: 516–518

Teardo E, Frare E, Segalla A, Marco VD, Giacometti GM, Szabò I (2005) Localization of a putative ClC chloride channel in spinach chloroplasts. FEBS Letters **579**: 4991–4996

Teuscher F, Guiard V, Rudolph PE, Brockmann GA (2005) The Map Expansion Obtained With Recombinant Inbred Strains and Intermated Recombinant Inbred Populations for Finite Generation Designs. Genetics **170**: 875–879

The Gene Ontology Consortium (2008) The Gene Ontology project in 2008. Nucleic Acids Research **36**: D440–D444

Theeuwen TPJM, Logie LL, Harbinson J, Aarts MGM (2022) Genetics as a key to improving crop photosynthesis. Journal of Experimental Botany **73**: 3122–3137

Thelen JJ, Ohlrogge JB (2002) The multisubunit acetyl-CoA carboxylase is strongly associated with the chloroplast envelope through non-ionic interactions to the carboxyltransferase subunits. Archives of Biochemistry and Biophysics **400**: 245–257

Thomas RC (1977) The role of bicarbonate, chloride and sodium ions in the regulation of intracellular pH in snail neurones. The Journal of Physiology **273**: 317–338

Tian L, Nawrocki WJ, Liu X, Polukhina I, Stokkum IHM van, Croce R (2019) pH dependence, kinetics and light-harvesting regulation of nonphotochemical quenching in Chlamydomonas. PNAS **116**: 8320–8325

Tikhonov AN (2018) The Cytochrome b6f Complex: Biophysical Aspects of Its Functioning in Chloroplasts. *In* JR Harris, EJ Boekema, eds, Membrane Protein Complexes: Structure and Function. Springer, Singapore, pp 287–328

Tikhonov AN (2013) pH-Dependent regulation of electron transport and ATP synthesis in chloroplasts. Photosynth Res **116**: 511–534

Tikhonov AN (2015) Induction events and short-term regulation of electron transport in chloroplasts: an overview. Photosynth Res **125**: 65–94

Tikhonov AN, Khomutov GB, Ruuge EK, Blumenfeld LA (1981) Electron transport control in chloroplasts. Effects of photosynthetic control monitored by the intrathylakoid pH. Biochimica et Biophysica Acta (BBA) - Bioenergetics **637**: 321–333

Tirumani S, Kokkanti M, Chaudhari V, Shukla M, Rao BJ (2014) Regulation of CCM genes in Chlamydomonas reinhardtii during conditions of light–dark cycles in synchronous cultures. Plant Mol Biol **85**: 277–286

Tokutsu R, Fujimura-Kamada K, Matsuo T, Yamasaki T, Minagawa J (2019) The CONSTANS flowering complex controls the protective response of photosynthesis in the green alga Chlamydomonas. Nat Commun **10**: 4099

Tovar-Méndez A, Miernyk JA, Randall DD (2003) Regulation of pyruvate dehydrogenase complex activity in plant cells. European Journal of Biochemistry **270**: 1043–1049

Trouillard M, Shahbazi M, Moyet L, Rappaport F, Joliot P, Kuntz M, Finazzi G (2012) Kinetic properties and physiological role of the plastoquinone terminal oxidase (PTOX) in a vascular plant. Biochimica et Biophysica Acta (BBA) - Bioenergetics **1817**: 2140–2148

Tsai Y-C, Chen K-C, Cheng T-S, Lee C, Lin S-H, Tung C-W (2019) Chlorophyll fluorescence analysis in diverse rice varieties reveals the positive correlation between the seedlings salt tolerance and photosynthetic efficiency. BMC Plant Biology **19**: 403

Tulin F, Cross FR (2014) A Microbial Avenue to Cell Cycle Control in the Plant Superkingdom. The Plant Cell **26**: 4019–4038

Ueki N, Ide T, Mochiji S, Kobayashi Y, Tokutsu R, Ohnishi N, Yamaguchi K, Shigenobu S, Tanaka K, Minagawa J, et al (2016) Eyespot-dependent determination of the phototactic sign in Chlamydomonas reinhardtii. Proceedings of the National Academy of Sciences **113**: 5299–5304

Uniacke J, Zerges W (2007) Photosystem II Assembly and Repair Are Differentially Localized in Chlamydomonas. The Plant Cell **19**: 3640–3654

United Nations, Department of Economic and Social Affairs, Population Division (2019) World population prospects Highlights, 2019 revision Highlights, 2019 revision.

Vecchi V, Barera S, Bassi R, Dall'Osto L (2020) Potential and Challenges of Improving Photosynthesis in Algae. Plants **9**: 67

Veerabadhran M, Natesan S, MubarakAli D, Xu S, Yang F (2021) Using different cultivation strategies and methods for the production of microalgal biomass as a raw material for the generation of bioproducts. Chemosphere **285**: 131436

Wakao S, Shih PM, Guan K, Schackwitz W, Ye J, Patel D, Shih RM, Dent RM, Chovatia M, Sharma A, et al (2021) Discovery of photosynthesis genes through whole-genome sequencing of acetate-requiring mutants of Chlamydomonas reinhardtii. PLOS Genetics **17**: e1009725

Walker BJ, VanLoocke A, Bernacchi CJ, Ort DR (2016) The Costs of Photorespiration to Food Production Now and in the Future. Annual Review of Plant Biology **67**: 107–129

Wang C, Yamamoto H, Shikanai T (2015) Role of cyclic electron transport around photosystem I in regulating proton motive force. Biochimica et Biophysica Acta (BBA) - Bioenergetics **1847**: 931–938

Wang L, Yamano T, Takane S, Niikawa Y, Toyokawa C, Ozawa S-I, Tokutsu R, Takahashi Y, Minagawa J, Kanesaki Y, et al (2016) Chloroplast-mediated regulation of CO2-concentrating mechanism by Ca2+-binding protein CAS in the green alga Chlamydomonas reinhardtii. Proc Natl Acad Sci U S A **113**: 12586–12591

Wienkoop S, Weiß J, May P, Kempa S, Irgang S, Recuenco-Munoz L, Pietzke M, Schwemmer T, Rupprecht J, Egelhofer V, et al (2010) Targeted proteomics for Chlamydomonas reinhardtii combined with rapid subcellular protein fractionation, metabolomics and metabolic flux analyses. Mol BioSyst **6**: 1018–1031

Wilson S, Johnson MP, Ruban AV (2021) ΔpH dominates proton motive force in plant photosynthesis in both low and high light. Plant Physiology. doi: 10.1093/plphys/kiab270

Xu F, Wu X, Jiang L-H, Zhao H, Pan J (2016) An organelle K+ channel is required for osmoregulation in Chlamydomonas reinhardtii. Journal of Cell Science **129**: 3008–3014

Xu S (2022) Quantitative Genetics. doi: 10.1007/978-3-030-83940-6

Xue H, Tokutsu R, Bergner SV, Scholz M, Minagawa J, Hippler M (2015) PHOTOSYSTEM II SUBUNIT R Is Required for Efficient Binding of LIGHT-HARVESTING COMPLEX STRESS-RELATED PROTEIN3 to Photosystem II-Light-Harvesting Supercomplexes in Chlamydomonas reinhardtii. Plant Physiology **167**: 1566–1578

Yalcin B, Flint J, Mott R (2005) Using Progenitor Strain Information to Identify Quantitative Trait Nucleotides in Outbred Mice. Genetics **171**: 673–681

Yamano T, Tsujikawa T, Hatano K, Ozawa S, Takahashi Y, Fukuzawa H (2010) Light and Low-CO2-Dependent LCIB–LCIC Complex Localization in the Chloroplast Supports the Carbon-Concentrating Mechanism in Chlamydomonas reinhardtii. Plant and Cell Physiology **51**: 1453–1468

Yamori W, Shikanai T (2016) Physiological Functions of Cyclic Electron Transport Around Photosystem I in Sustaining Photosynthesis and Plant Growth. Annual Review of Plant Biology **67**: 81–106

Yamori W, Shikanai T, Makino A (2015) Photosystem I cyclic electron flow via chloroplast NADH dehydrogenase-like complex performs a physiological role for photosynthesis at low light. Sci Rep **5**: 13908

Yan X, Shen Y (2021) Rab-like small GTPases in the regulation of ciliary Bardet-Biedl syndrome (BBS) complex transport. The FEBS Journal. doi: 10.1111/febs.16232

Yang W, Catalanotti C, D'Adamo S, Wittkopp TM, Ingram-Smith CJ, Mackinder L, Miller TE, Heuberger AL, Peers G, Smith KS, et al (2014) Alternative Acetate Production Pathways in Chlamydomonas reinhardtii during Dark Anoxia and the Dominant Role of Chloroplasts in Fermentative Acetate Production[W]. Plant Cell **26**: 4499–4518

Yin Z, Meng F, Song H, He X, Xu X, Yu D (2010) Mapping quantitative trait loci associated with chlorophyll a fluorescence parameters in soybean (Glycine max (L.) Merr.). Planta **231**: 875–885

Yocum CF (2022) Photosystem 2 and the oxygen evolving complex: a brief overview. Photosynth Res. doi: 10.1007/s11120-022-00910-1

Zhang X, Smits AH, van Tilburg GB, Ovaa H, Huber W, Vermeulen M (2018) Proteome-wide identification of ubiquitin interactions using UbIA-MS. Nat Protoc **13**: 530–550

Zhang Y, Gu Z, Ren Y, Wang L, Zhang J, Liang C, Tong S, Wang Y, Xu D, Zhang X, et al (2021) Integrating Transcriptomics and Metabolomics to Characterize Metabolic Regulation to Elevated CO2 in Chlamydomonas Reinhardtii. Mar Biotechnol **23**: 255–275

Zhu Y, Orre LM, Zhou Tran Y, Mermelekas G, Johansson HJ, Malyutina A, Anders S, Lehtiö J (2020) DEqMS: A Method for Accurate Variance Estimation in Differential Protein Expression Analysis. Mol Cell Proteomics **19**: 1047–1057

Zou Y, Wenzel S, Müller N, Prager K, Jung E-M, Kothe E, Kottke T, Mittag M (2017) An Animal-Like Cryptochrome Controls the Chlamydomonas Sexual Cycle. Plant Physiology **174**: 1334–1347